UNIVERSITY OF CALIFORNIA

Santa Barbara

Correlating Structure, Properties, and Performance in Sodium Metal Fluoride Battery Cathodes

A dissertation submitted in partial satisfaction of the

requirements for the degree Doctor of Philosophy

in Materials

by

Emily Eileen Foley

Committee in charge:

Professor Raphaële Clément, Chair

Professor Ram Seshadri

Professor Anton Van der Ven

Professor Gabriel Ménard, University of Calgary

June 2023

The dissertation of Emily Eileen Foley is approved.

Ram Seshadri

Anton Van der Ven

Gabriel Ménard

Raphaële Clément, Committee Chair

June 2023

Correlating Structure, Properties, and Performance in Sodium Metal Fluoride Battery Cathodes

by

Emily Eileen Foley

DEDICATION

To Toothless, Olive, and Brandon.

ACKNOWLEDGEMENTS

I would like to first thank Prof. Raphaële Clément for her unwavering support, guidance, ideas, and patience in the pursuit of this research and over the last five years. It has been a privilege working with and learning from her. Despite all the learning curves associated with a new lab, I cannot imagine having done my PhD with anyone else.

I would also like to thank my committee for all the scientific discussions and questions over the years – Prof. Ram Seshadri for welcoming me into the MRL and his group, Prof. Anton Van der Ven for the great introduction to quantum mechanics and first-principles calculations, and Prof. Gabriel Ménard for helping me get started with understanding (and now managing) Mössbauer spectroscopy. It has been a great opportunity to learn from you all as well as all the other great faculty at UCSB. Additionally, I would also like to thank all the great administrators and staff at UCSB who help keep our research facilities and department running behind the scenes – in particular, Amanda Strom for keeping the MRL going despite all the leaks, Nathan "Fuzzy" Rogers for dealing with my constant badgering, Bob Hansen for somehow managing all of Elings, and all the staff that keep the X-ray and spectroscopy facilities running.

Importantly, I must thank my group members and officemates, past and present, that have helped keep me sane throughout this process and talked through many scientific questions, problems, and ideas with me. A PhD is truly a team effort, and I am grateful to have learned from all of you. To this end it has been a pleasure being part of

such a great Materials program and being able to learn from such brilliant students – many of which I now consider lifelong friends.

I would be remiss if I did not thank my family for helping me get started on this path and supporting me along the way. Specifically I'd like to acknowledge both of my grandfathers who were material scientists before it was called that. Finally, thank you Brandon for being my rock throughout the last four years. I'm so thankful we crossed paths here and look forward to many years to come with you, Olive, Toothless, and our yet to be realized orange kitty.

Curriculum Vitæ

Emily Eileen Foley

Education

Ph.D. Materials, University of California Santa Barbara — June 2023
Emphasis: *Functional & Quantum Materials* — 4.0/4.0
Advisor: Professor Raphaële Clément

B.S. in Materials Science & Eng., University of Illinois Urbana-Champaign — May 2018
Emphasis: *Electronic Materials* — 3.72/4.0

Publications

9. **E.E. Foley**, V.C. Wu, W. Jin, W. Cui, E. Yoshida, A. Manche, and R.J. Clément, "Polymorphism in Weberite $Na_2Fe_2F_7$ and its Effects on Electrochemical Properties as a Na-ion Cathode", *Chem. Mater.* **35** (2023) 3614-3627. doi:10.1021/acs.chemmater.3c00233

8. Y. Ji, C. Palmer, **E.E. Foley**, R. Giovine, E. Yoshida, E. Sebti, A.R. Patterson, E. McFarland, and R.J. Clément, "Valorizing the carbon byproduct of methane pyrolysis in batteries", *Carbon* **204** (2023) 26-35. doi:10.1016/j.carbon.2022.12.044

7. V.C. Wu, R. Giovine, **E.E. Foley,** J. Finzel, M. Balasubramanian, E. Sebti, E. M. Mozur, A.H. Kwon, and R.J. Clément, "Unlocking New Redox Activity in Alluaudite Cathodes through Compositional Design", *Chem. Mater.* **34** (2022) 4088-4103. doi:10.1021/acs.chemmater.2c00324

6. Z. Cai, H. Ji, Y. Ha, J. Liu, D.-H. Kwon, Y. Zhang, A. Urban, **E.E. Foley**, R. Giovine, H. Kim, Z. Lun, T.-Y. Huang, G. Zeng, Y. Chen, J. Wang, B.D. McCloskey, M. Balasubramanian, R.J. Clément, W. Yang, and G. Ceder, "Realizing continuous cation order-to-disorder tuning in a class of high-energy spinel-type Li-ion cathodes", *Matter* **4** (2021) 3897–3916. doi:10.1016/j.matt.2021.10.013

5. **E.E. Foley**, A. Wong, R.C. Vincent, A. Manche, A. Zaveri, E. Gonzalez-Correa, G. Ménard, and R.J. Clément, "Probing reaction processes and reversibility in Earth-abundant Na_3FeF_6 for Na-ion batteries", *Phys. Chem. Chem. Phys.* **23** (2021) 20052–20064. doi:10.1039/D1CP02763H

4. Z. Lun, B. Ouyang, D.H. Kwon, Y. Ha, **E.E. Foley**, T.Y. Huang, Z. Cai, H. Kim, M. Balasubramanian, Y. Sun, J. Huang, Y. Tian, H. Kim, B.D. McCloskey, W. Yang, R.J. Clément, H. Ji, and G. Ceder, "Cation-disordered rocksalt-type high-entropy cathodes for Li-ion batteries", *Nat. Mater.* **20** (2021) 214-221. doi: 10.1038/s41563-020-00816-0

3. Y. Yue, N. Li, L. Li, **E.E. Foley**, Y. Fu, V.S. Battaglia, R.J. Clément, C. Wang, and W. Tong, "Redox Behaviors in a Li-Excess Cation-Disordered Mn–Nb–O–F Rocksalt Cathode", *Chem. Mater.* **32** (2020) 4490-4498. doi:10.1021/acs.chemmater.9b05221

2. H. Ji, J. Wu, Z. Cai, J Liu, D.-H. Kwon, H. Kim, A. Urban, J.K. Papp, **E.E. Foley**, Y. Tian, M. Balasubramanian, H. Kim, R.J. Clément, B.D. McCloskey, W. Yang, and G. Ceder, "Ultrahigh Power and Energy Density in Partially Ordered Lithium-ion Cathode Materials", *Nature Energy* **5** (2020) 213-221. doi:10.1038/s41560-020-0573-1

1. H. Ji, D. Kitchaev, Z. Lun, H. Kim, **E.E. Foley,** D.H. Kwon, Y. Tian, M. Balasubramanian, M. Bianchini, Z. Cai, R.J. Clément**,** J. Kim, and G. Ceder, "Computational Investigation and Experimental Realization of Disordered High-Capacity Li-ion Cathodes Based on Ni Redox", *Chem. Mater.* **31** (2019) 2431-2442. doi:10.1021/acs.chemmater.8b05096

ABSTRACT

Correlating Structure, Properties, and Performance in Sodium Metal Fluoride Battery Cathodes

by

Emily Eileen Foley

The continued reliance on a select few elements, namely Li, Ni, and Co, for rechargeable battery cathodes is untenable with the increasing demand for batteries in electric vehicles, grid-scale energy storage, and portable electronics. In this dissertation we have explored three alternative cathode classes exhibiting improved sustainability: 1) Li-ion disordered rocksalt oxyfluorides, 2) cryolite-like Na_3FeF_6, and 3) weberite $Na_2Fe_2F_7$. The first class enables a greater variety of transition metals to be utilized, but their long-range disorder necessitates short-range characterization which we have accomplished using ^{7}Li and ^{19}F solid-state nuclear magnetic resonance (ss-NMR). The second and third class, forming the bulk of this dissertation, completely depart from Li as the intercalant ion and instead utilize Na.

While Na-ion batteries have emerged as a clear alternative for Li-ion batteries in select applications, their energy densities are still largely limited by the cathode materials. Thus, a paradigm shift in the development of competitive Na cathodes hinges on the investigation of new structural frameworks and anion chemistries. Here, we investigated two sodium iron fluoride materials whose differing structures lead to

significantly different cycling mechanisms – conversion in cryolite-like Na_3FeF_6 due to its dense structure, and intercalation in weberite $Na_2Fe_2F_7$ due to its more open framework structure. The former material, Na_3FeF_6, we find via an *ex situ* analytical method based on ^{23}Na NMR and *operando* magnetometry, forms NaF and Fe on discharge, which is only moderately reversible due to sluggish conversion reaction kinetics. In the latter material, weberite $Na_2Fe_2F_7$, we find more reversible electrochemical intercalation behavior, but a phase transformation to perovskite $NaFeF_3$ still occurs upon cycling. Through compositional tuning and synthetic control, this phase transformation can be suppressed leading to a promising new Na-ion cathode material. Additional computational characterization highlights the complex phase stability landscape inherent to weberite materials, leading to polymorphism and metastability as observed experimentally. Thus, we have developed a set of computationally informed design rules to guide further exploration of the weberite structure class.

Table of Contents

1. Introduction 1

1.1 The Drive for Sustainable Energy Storage 1

1.2 Rechargeable LIBs and NIBs 3

1.2.1 Battery Metrics 4

1.2.2 Electrochemical Cycling 7

1.3 Na-Fe-F Cathodes for Na-ion Batteries 10

1.3.1 The Case for Fluoride Cathodes 11

1.4 Aims & Outline of this Dissertation 13

2. Methods 16

2.1 Diffraction 16

2.1.1 Bragg Diffraction 17

2.1.2 Fitting the XRD Pattern 19

2.2 Nuclear Magnetic Resonance 20

2.2.1 Overview 20

2.2.2 Magic Angle Spinning (MAS) – Solution to Solid-State 22

2.2.3 Hyperfine Interactions 24

2.2.3.1 Fermi Contact Interaction 25

2.2.3.2 Spin Density Transfer Pathways 27

2.2.3.3 The Dipolar Hyperfine Interaction 29

2.2.4 Quadrupolar Interactions 30

2.2.5 NMR Experiments 33

2.2.5.1 Hahn-Echo 34
2.2.5.2 Measuring T_1 and T_2 Relaxation Times 38
2.2.5.3 Quantitative NMR 42
2.2.5.4 pj-MATPASS 43
2.2.5.5 Frequency Stepping 44
2.3 Mössbauer Spectroscopy 44
2.3.1 The Mössbauer Effect 45
2.3.2 Mössbauer Spectroscopy Experiments 47
2.3.2.1 The Electric Monopole Interaction 48
2.3.2.2 The Electric Quadrupole Interaction 49
2.3.2.3 The Magnetic Dipole Interaction 50
2.4 Magnetometry 52
2.5 Computational Methods 54
2.5.1 Theoretical Background – Density Functional Theory 55
2.5.1.1 Approximating Electron Exchange and Correlation 56
2.5.1.2 Calculating Periodic Structures with VASP 57
2.5.2 DFT Calculations of Formation Energies & Voltages 58
2.5.3 First Principles Calculations of NMR Parameters 61
3. $^{19}F/^{7}Li$ NMR Study of Disordered Rocksalt (DRX) Oxyfluorides 65
3.1 Introduction 66
3.1.1 d^0 Incorporation 66
3.1.2 Li-Excess in Disordered Rocksalts 68
3.1.3 Fluorination in Disordered Rocksalts 69

3.1.4 Outlook 69
3.2 Experimental 70
3.3 Results & Discussion 73
3.3.1 Suppression of Short-Range Ordering via High-Entropy DRX 73
3.3.2 Computational Investigation and Experimental Realization of Ni-based Disordered Rocksalts 77
3.3.3 Structure & Redox Characterization of a Model Disordered Rocksalt 86
3.3.4 Improved Performance in Partially-Disordered Spinel Cathodes 88
3.3.4.1 Demonstration of High Performance Partially-Ordered Spinels 89
3.3.4.2 Order-to-Disorder Tuning in Partially-Ordered Spinels 93
3.4 Conclusion 97
3.5 Appendix 99
4. Probing Reaction Processes & Reversibility in Na_3FeF_6 103
4.1 Introduction 104
4.2 Experimental 108
4.3 Results & Discussion 114
4.3.1 Characterization of as-synthesized Na_3FeF_6 114
4.3.2 Electrochemical Properties 121
4.3.3 Characterization of Conversion Processes 125
4.3.4 Na_3FeF_6 Conversion Process & Insights into Performance Limitations 132
4.3.5 Confirmation of Conversion Mechanism via *Operando* Magnetometry 137
4.4 Conclusion 141
4.5 Appendix – Supplemental Material 143

5. Polymorphism in Weberite $Na_2Fe_2F_7$ & its Effects on Electrochemical Properties..157

5.1 Introduction 158

5.2 Experimental 160

5.3 Results & Discussion 166

5.3.1 Weberite Structure and its Variants 166

5.3.2 $Na_2Fe_2F_7$ Polymorphism and Energetics 169

5.3.3 Synthesis and Long-range Structural Characterization of $Na_2Fe_2F_7$ 171

5.3.4 Insights into Fe & Na local environments from Mössbauer and solid-state NMR spectroscopy 174

5.3.5 Electrochemical properties of $Na_2Fe_2F_7$ 181

5.3.6 *Ex Situ* Characterization of the Charge-Discharge Mechanism 185

5.3.7 Computational Investigation of the Electrochemical Properties of $Na_2Fe_2F_7$ Weberite Variants 191

5.4 Conclusion 196

5.5 Appendix – Supplemental Material 198

6. Exploration of Weberite Compositions Outside of $Na_2Fe_2F_7$ 210

6.1 Mn^{2+}-substitution in $Na_2Mn_xFe_{2-x}F_7$ 211

6.2 Al^{3+}-substitution in $Na_2Fe_{2-x}Al_xF_7$ 217

6.3 Mg^{2+}-substitution in $Na_2Mg_xFe_{2-x}F_7$ 220

6.4 Weberite Material Design Rules 227

6.4.2 Weberite Polymorphism 229

6.4.3 Weberite Metastability 232

6.4.4 Weberite Redox Behavior 233

6.4 Weberite Material Design Rules....235
6.6 Appendix – Weberite Material Synthesis....236
6.6.1 Traditional Solid-State Synthesis....236
6.6.1.1 Microwave Synthesis....239
6.6.2 Topochemical/Hydrothermal Synthesis....240
6.6.3 Mechanochemically-Assisted Solid-State Synthesis....242
6.6.4 PTFE-Assisted Fluorination Synthesis....243
7. Conclusions....247
References....250

Chapter 1– Introduction

1.1 The Drive for Sustainable Energy Storage

The climate crisis, largely driven by the burning of fossil fuels, is accelerating and without rapid action will cause even more catastrophic consequences.[1] Already intense floods, droughts, hurricanes, forest fires, and heat waves have increased in intensity and frequency globally contributing to significant human suffering and financial damages. While implementation of renewable energy sources (e.g., solar and wind) on the grid has caused a significant decrease in anthropogenic CO_2 emissions (approximately 28% of which stems from transportation), the intermittency of these sources limits the efficacy of these renewables and their competitivity with fossil fuels. A grid capable of storing renewables for later use is desperately needed. In this regard, rechargeable batteries have emerged as a solution, the most commercially successful of these batteries being Li-ion (LIBs)–routinely used to power portable electronic devices and more recently in electric and hybrid electric vehicles.

While the performance of LIBs has improved significantly since their first commercialization in the early 1990s—through electrolyte additives, electrode fabrication and cell design—it remains limited by the cathode material. Indeed, present

day commercial batteries largely rely on the family of layered cathode materials first realized by John B. Goodenough in 1980 with $LiCoO_2$.[2] However, the sourcing of Co—and to a lesser extent Li—is an expensive, unsustainable, and ethically-complicated process: significant work has been directed towards decreasing the Co content of the cathode, leading to the development of NMC-based (e.g. $LiNi_xMn_yCo_zO_2$ ($x + y + z = 1$), $LiFePO_4$ (olivine), and $Li_2Mn_2O_4$ (spinel) chemistries. These compositions rely on a limited number of elements—notably all Li-ion-based. A greater diversity of battery chemistries is needed to enable a just energy transition. In recent years, Na-ion batteries (NIBs) have emerged as a clear alternative for certain applications—for example, in grid scale energy storage as well as in low-end transportation applications, having already been commercialized by CATL and Natron—due to the very similar physicochemical properties of Na and Li, and their greater exploration compared to other alkali (K^+) and alkaline-earth (Mg^{2+}, Ca^{2+}) battery chemistries.

This dissertation focuses on the exploration of new battery chemistries including Li-ion disordered rocksalts (DRX, Chapter 3), which enable a greater variety of transition metals to be incorporated into high energy Li-ion cathodes; and novel Na-ion fluoride cathodes (Chapters 4-6), which rely on Na-ion conversion or intercalation, and leverage low-cost transition metal chemistries and electronegative fluorine. This latter topic forms the core of this dissertation and will be further discussed below. This dissertation endeavors to better understand the evolution of complex structure-property relationships during electrochemical cycling of these novel, sustainable battery cathodes.

1.2 Rechargeable LIBs and NIBs

Batteries convert electrical energy to and from chemical energy. The three main components of a battery include the anode, cathode, and electrolyte (Figure 1.1). On charge, Na^+ ions travel from the cathode to the anode with coupled oxidation and reduction reactions occurring in the cathode and anode, respectively. Discharge is the reverse process. Thus, as both electrodes transfer ions and electrons, they need to be ionically and electronically conductive, while the highly ionically conductive electrolyte, often including a separator to physically isolate the anode and cathode, must be electronically insulating to decouple electron-ion motion and force the electrons generated by the electrode redox reactions to travel through the external circuit. To ensure maximum battery efficiency and lifetime, these ion and electron transfer processes must occur with high reversibility. However, these charge transfer processes inherently lead to bulk structural changes, affecting the reversibility of the electrochemical processes.

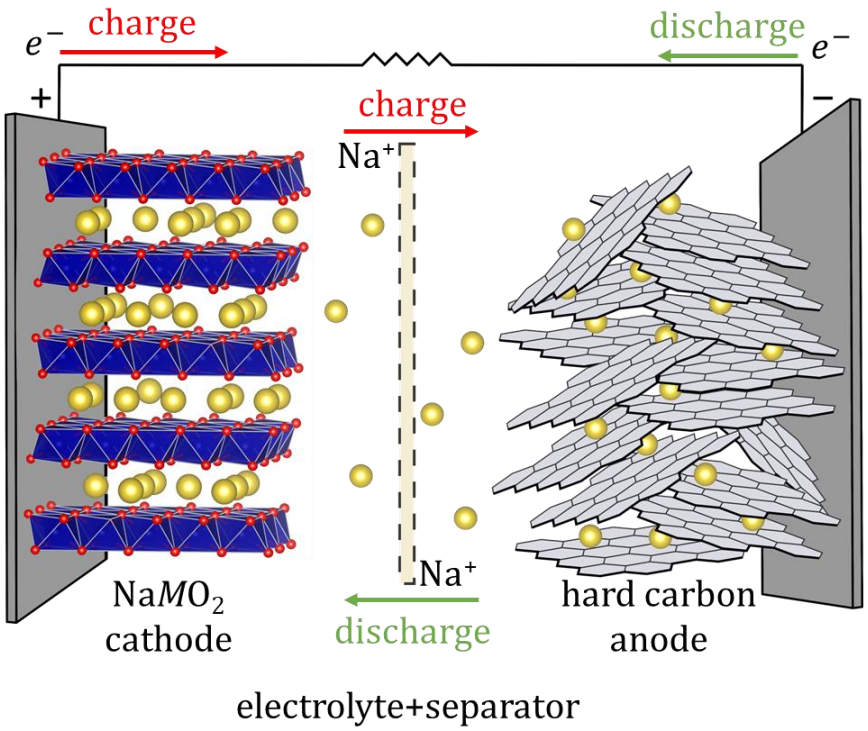

Figure 1.1 – Na-ion battery schematic with a representative layered NaMO_2 cathode (left), liquid electrolyte with a separator (center, light yellow box), and a representative hard carbon anode (right).[a] The direction of Na^+ ion and $\boldsymbol{e}^-$ flow is labeled for charge and discharge.

1.2.1 Battery Metrics

One of the key metrics characterizing a battery is its energy density (units Wh/kg), the product of the cell potential (E^0_{cell} or V) and cell specific capacity (Q, units C/g or mAh/g with 1mAh/g = 3.6 C) shown as

$$E = Q * V \tag{1.1}$$

Note that the quantities here are gravimetric—i.e., the energy density and specific capacity are normalized to the mass of the electrode material. One can likewise

[a] As Na does not readily intercalate into graphite (commonly used in LIBs as an anode), hard carbon is instead used in NIBs.

define volumetric metrics, as often used in grid-scale energy storage as well as in electric vehicles.[3]

The cell potential is defined as the potential difference of the anode and cathode given as

$$\Delta G^0_{\text{cell}} = \Delta G^0_{\text{cathode}} - \Delta G^0_{\text{anode}} = -nFE^0_{\text{cell}} \quad 1.2$$

with

$$E^0_{\text{cell}} = E^0_{\text{anode}} + E^0_{\text{cathode}} \quad 1.3$$

where ΔG^0_{cell} is the Gibbs Free Energy of the cell, *n* the number of electrons transferred, and *F* is Faraday's constant. A positive cell potential indicates a spontaneous reaction, as occurs during the discharging of a battery. By applying a potential, the reverse reaction can be driven, as occurs during the charging of a battery. The voltage of a battery is typically referenced against the potential of their pure metal, which is offset from the standard hydrogen electrode (SHE)—by −3.04 V for Li/Li^+ or −2.7 V for Na/Na^+).[b]

The specific capacity represents the total charge able to be stored and transferred and is defined as

$$Q = \frac{F*n}{M} \quad 1.4$$

where *M* is the molecular weight of the electrode. Note that *n*, the number of electrons transferred per formula unit (f.u.), is necessarily an assumption when calculating the theoretical capacity and should be clearly defined for a given electrode material.

Another important battery metric is its power density (again, can be volumetric or gravimetric) which describes the rate at which energy can be transferred given as

[b] Note that Li metal has a 0.34 V lower potential *vs*. the SHE than Na metal, which results in analogous Na-ion electrodes exhibiting a ≈ 0.3 V lower voltage than their Li-ion counterparts.

$$P = \frac{\partial E}{\partial t} = \frac{\partial Q}{\partial t} * V = I * V \quad 1.5$$

with I being the applied current. This metric describes how quickly the battery can be charged or discharged and is highly relevant for electric vehicle applications. The applied current rate is typically defined in terms of C, meaning the amount of current required to fully charge/discharge the cell in an hour. Thus, a rate of $C/20$ is the current required to charge/discharge the cell in 20 h while a rate of $20C$ is the current required to charge/discharge the cell in 1/20 hours (3 min).

Additional battery metrics include its cycle life, Coulombic efficiency, and voltaic efficiency. Cycle life describes the change in cycling performance with respect to cycle number. This is commonly described as capacity retention—the ratio of a given cycle capacity over the first cycle capacity. The Coulombic (also termed Faradaic) efficiency describes how efficiently electrons are transferred within the cell and is defined as the ratio of the amount of charge extracted on discharge *vs*. the amount of charge input on charge. Similarly, voltaic efficiency is the ratio of the discharge to charge voltage with the overall energy efficiency of a cell being the product of the Coulombic and voltaic efficiencies. While Coulombic efficiencies can theoretically be 100%, voltaic efficiencies are inherently limited to < 100% due to the nonspontaneous nature of the charge process. In practice, this is manifested by voltage polarization and voltage hysteresis. Voltage polarization, also considered as overpotentials, is the potential difference between the thermodynamic and experimental voltage and arises due to the extra energy required to drive a given kinetic process. Voltage hysteresis is the difference between the charge and discharge voltage and can be related to the overpotentials, and thereby kinetics, and/or asymmetric charge/discharge processes.[4]

Note that these metrics typically focus on the discharge performance (*e.g.*, reporting discharge capacity retention, defining Coulombic efficiencies as discharge over charge capacity) as this pertains to energy extraction from the cell and is most practically relevant. Regardless, in an ideal cell the charge and discharge processes should be identical, providing high Coulombic efficiencies and small overpotentials.

1.2.2 Electrochemical Cycling

Batteries are typically tested in an academic setting *via* galvanostatic cycling, meaning constant current cycling between set voltage limits.[5] These voltage limits are typically set to minimize adverse side-reactions from occurring in the cell, such as electrolyte decomposition (commonly occurring > 4.3 V vs. Na/Na^+ for carbonate-based electrolytes[6]). The galvanostatic cycling data can be further analyzed by taking the derivative of the capacity with respect to voltage (dQ/dV). The resulting dQ/dV data enables the discrete electrochemical processes to be more clearly elucidated. Additional electrochemical tests include variable rate cycling (cycling at different current rates over several cycles to assess the power capability of a cell) and galvanostatic intermittent titration technique (GITT) cycling (application of short current pulses and long relaxation steps to monitor the voltage response of the cell throughout charge and discharge).[7] All three of these electrochemical tests have been utilized in this dissertation and are depicted in Figure 1.2.

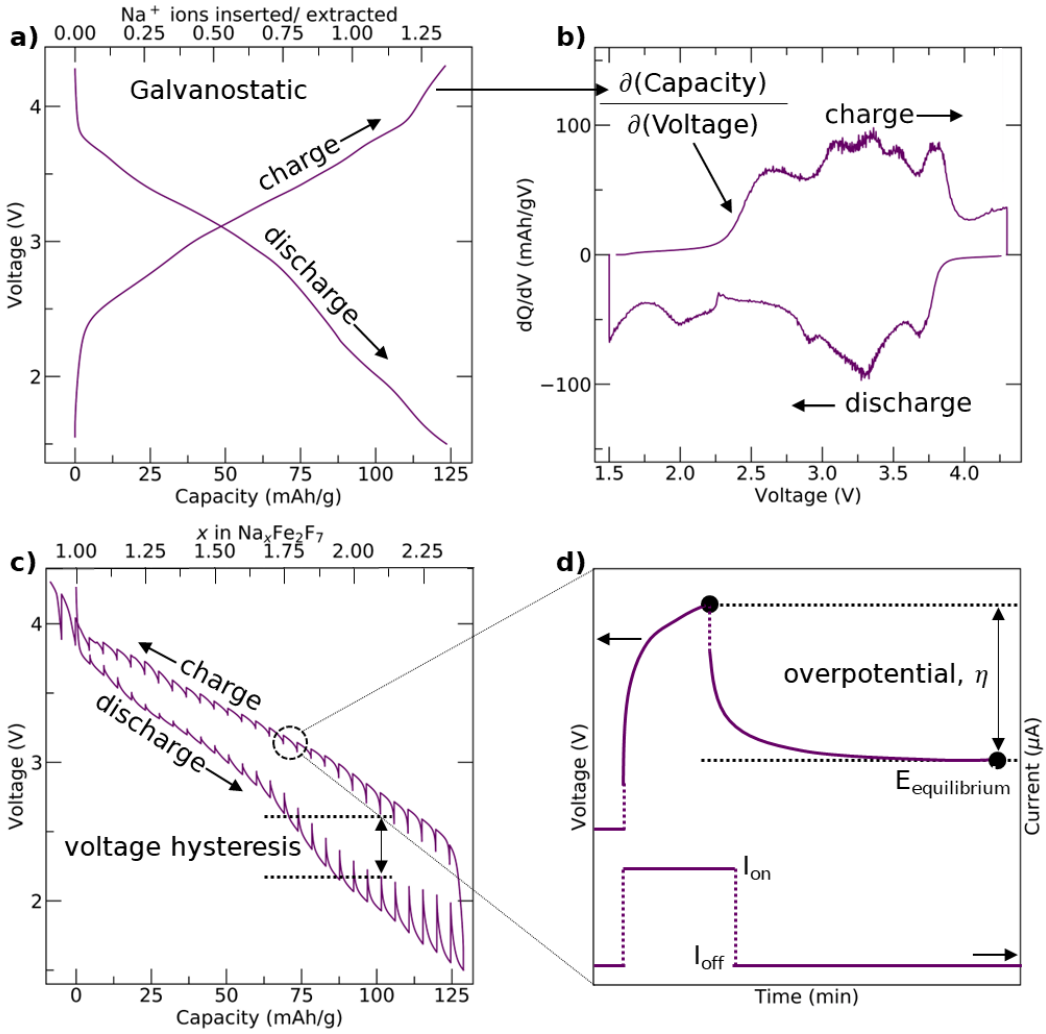

Figure 1.2 – Schematic of electrochemical tests used in this dissertation. a) Galvanostatic (i.e., constant current) charge-discharge cycling between set voltage limits (here, 1.5 V and 4.3 V). **b)** dQ/dV data for the galvanostatic data in **(a)** obtained by taking the derivative of voltage with respect to capacity. **c)** Galvanostatic intermittent titration technique (GITT) voltage *vs.* capacity profile with the corresponding voltage and current vs. time data shown in **(d)**. The charge data in **(c)** is shown "flipped" (i.e., multiplied by −1 and shifted by the preceding discharge capacity) to connect the charge-discharge profiles, which better illustrates voltage hysteresis between cycles. Note that **(a)** and **(c)** have the same bottom *x*-axis (capacity in mAh/g) but different top *x*-axis formats.

An intercalation reaction, also known as a topotactic phase transformation, occurs when the host crystal structure remains largely unchanged upon ion insertion or extraction. An intercalation reaction can manifest itself through either a solid solution or two-phase like reaction (Figure 1.3).[8] In the former, the chemical potential (Na stoichiometry) varies continuously upon Na insertion or extraction while the electrode

structure is preserved, giving a sloping voltage profile. In the latter, insertion/extraction of Na^+ ions cause a new phase with a differing Na stoichiometry to nucleate. Here, as Na insertion/extraction proceeds, the phase fractions of the original and new phase vary as their Na contents (chemical potentials) remain constant. This manifests as a plateau in the electrochemical profile. The input energy is instead put towards converting between the two phases. To be reversible, both intercalation mechanisms must involve minimal structural changes throughout electrochemical cycling. As a two-phase reaction fundamentally involves a transition between two, albeit related, structures, these reactions can be less reversible and kinetically hindered.

Similar to two-phase intercalation reactions, conversion reactions involve the formation of new phases on Na extraction/insertion and thus also manifest themselves as a plateau in the electrochemical profile.[8] However, in conversion reactions, the new phases formed constitute fundamentally new phases that share little to no structural similarities with the original phase. These reactions can be represented as

$$M_aX_b + (b \times c)A^+ + (b \times c)e^- \leftrightarrow aM^0 + bA_cX \qquad 1.6$$

where M corresponds to a transition metal, X to an anion, and A to an alkali ion. Thus, these reactions tend to involve multi-electron redox where M is reduced from M^{b+} to M^0, thus delivering large capacities.[9–11] However, as these reactions rely on the displacement of all constitutive species—not only the mobile alkali ion as in intercalation reactions—and induce significant structural changes, these reactions tend to be less reversible and more kinetically-hindered than intercalation reactions.

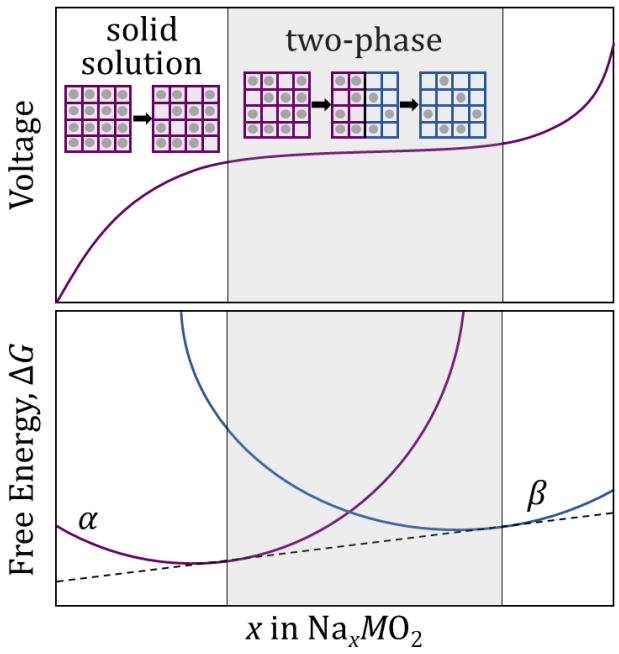

Figure 1.3 – Schematic of a galvanostatic electrochemical voltage curve and free energy change of a solid solution in the ***α*** phase and two-phase (shaded in blue) reaction between the ***α*** and ***β*** phases.

Note that materials that undergo intercalation reactions can also evolve over time to irreversibly form another new, related structure at the expense of the original phase.[8,12–14] This can be described as a phase transformation and may occur if the material begins and/or becomes metastable upon alkali-ion insertion and extraction. The reversibility of this transformation depends on the specific system but can be both favorable and unfavorable.

1.3 Na-Fe-F Cathodes for Na-ion Batteries

The higher atomic weight and larger ionic radius of Na^+ compared to Li^+, as well as 0.3 V higher potential of the Na^+/Na redox couple compared to Li^+/Li, leads to inherently lower theoretical energy densities for NIBs compared to their Li-ion analogues. While significant work has gone towards developing layered oxide,[15–17] polyanion,[18–20] and Prussian Blue[21,22] cathodes for NIBs, viable Na alternatives to current

Li systems have proven elusive.[23] A paradigm shift in the development of competitive Na cathodes hinges on the investigation of new structural frameworks and anion chemistries.

In keeping with the low-cost and sustainable ethos of NIBs, earth-abundant transition metals—Mn and Fe in particular (Figure 1.4), whose operating voltages lie within the electrolyte decomposition window[13,19,24]—should be utilized as much as possible in NIB cathode materials.

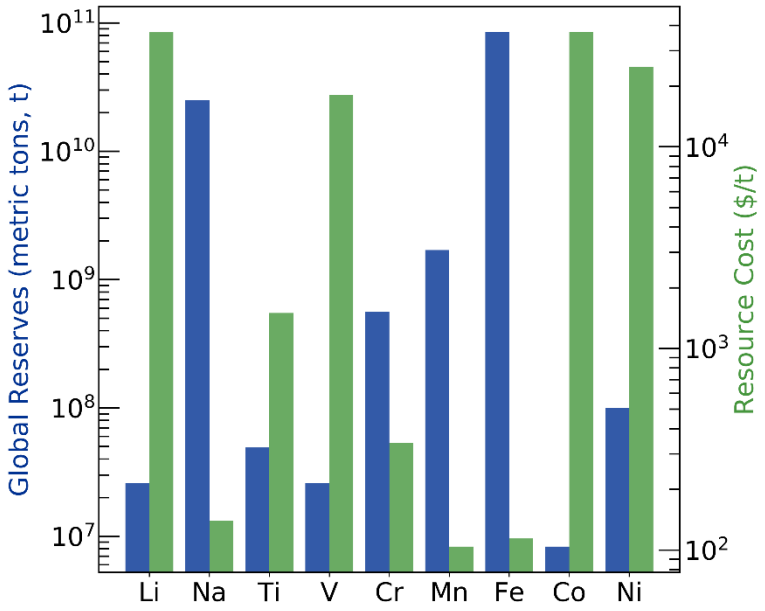

Figure 1.4 – Global reserves and cost for battery-relevant elements. Values from the 2023 U.S. Geological Survey.[26]

1.3.1 The Case for Fluoride Cathodes

In John B. Goodenough's seminal paper on $LiCoO_2$,[2] which was a departure from the previously studied layered-$LiTiS_2$,[25] it was stated that "a larger negative free energy change for a reaction, $xA + MX_n = A_xMX_n$, is expected when A is small and electropositive, MX_n contains a metal atom M in a high oxidation state, and X is small and

electronegative."[2] This effect is generally referred to as the inductive effect and refers to the increase in polarity of the *A*-*X* and *M*-*X* bonds when *X* becomes more electronegative, causing a decrease in the overall band energy for A_xMX_n and an increase in the redox potential for *M* and extraction potential for *A*. Thus, fluorides tend to have large operating potentials.

While having a higher operating voltage is beneficial for high power applications (assuming it is still within the electrochemical stability window), the increase in anion electronegativity causes increased electronic localization that decreases the electronic conductivity. For example, many transition metal oxides are semiconducting or metallic, but all transition metal fluorides are insulating. Consequently, methods to improve the electronic conductivity of fluorides are needed. Additionally, *M*-F bonds tend to be much weaker than *M*-O bonds often resulting in fluorine being unable to stabilize metals of high oxidation states and therefore forming less stable structures (with respect to decomposition) overall. This is due to O^{2-} being able to form more covalent bonds than F^- owing to its higher negative charge, as well as fluorides requiring twice as many anions as oxides for charge balance, thereby resulting in metal environments with a higher average coordination number.[c]

In practice, fluorine substitution has been shown to successfully increase the operating voltage (and thereby the energy density) of both oxide[27,28] and polyanion-based[29,30] cathodes. As alluded to above, pure transition metal fluorides are infrequently used as cathodes due to their generally poor electronic, and in some cases ionic,

[c] For example, OsO_4 is a stable molecule with tetrahedrally coordinated Os^{8+} whereas OsF_8 is very unstable.

conduction properties.[31–34] While electronic conduction can be partially mitigated by carbon-coating, particle downsizing, and nanostructuring,[35–37] ionic conduction is an intrinsic requirement for a topotactic Na (de)intercalation process. Often for poor ionic conductors—as well as for metastable compounds—structure-preserving Na extraction and reinsertion processes are replaced by conversion or phase transformation reactions.

As will be demonstrated in Chapter 4 for Na_3FeF_6,[38] conversion reactions can in theory result in high capacities but are poorly reversible in practice,[39,40] as also seen for rutile MF_2[41,42], and for perovskite-type MF_3[31,43,44] and $NaMF_3$[45,46] on deep discharge. Thus, to prevent electrochemical conversion reactions from occurring, transition metal fluoride structures containing fast Na-ion transport pathways are needed. In this regard, weberite compounds (with general formula $Na_2M^{2+}M'^{3+}F_7$) have been shown to exhibit an open framework structure that holds promise for facile Na-ion diffusion and topotactic Na-ion (de)intercalation.[47–49] These weberite compounds will be discussed in Chapters 5 and 6.

1.4 Aims & Outline of this Dissertation

This dissertation aims to investigate several new structure-types for use as sustainable battery cathodes. We have used both experimental—including complementary long-range and short-range structural techniques—and computational methods to characterize the behaviour of these materials and these methods will be discussed next in Chapter 2.

In Chapter 3, we investigate Li-ion disordered rocksalt (DRX) oxyfluorides, which enable a greater variety of transition metals to be utilized, thereby reducing the dependence on both Ni and Co. Due to their long-range disorder, we investigate their local structures through ^{7}Li and ^{19}F solid-state nuclear magnetic resonance (ss-NMR) to complement data obtained by collaborators. We find that while there is bulk incorporation of ^{7}Li and ^{19}F in the structure, there is a nuanced effect of short-range ordering in DRX materials.

In Chapter 4, we carry out a comprehensive study of the cycling behavior of cryolite-like Na_3FeF_6 using synchrotron X-ray diffraction (XRD), *ex situ* ^{23}Na and ^{19}F NMR, ^{57}Fe Mössbauer spectroscopy, and electrochemical cycling. We identify using a novel *ex situ* analytical method that Na_3FeF_6 undergoes largely irreversible conversion on discharge to NaF and Fe, despite the rapid oxidation of the Fe nanoparticles. This is further confirmed by *operando* magnetometry which highlights the sluggish reaction kinetics and irreversibility intrinsic to this system.

Chapters 5 and 6 investigate weberites (with general formula $Na_2M^{2+}M'^{3+}F_7$), an emerging class of NIB cathodes, informed by first-principles thermodynamic and NMR calculations paired with SXRD, ^{23}Na and ^{19}F NMR, ^{57}Fe Mössbauer spectroscopy, and electrochemical cycling. Chapter 5 focuses on $Na_2Fe_2F_7$, which has been demonstrated to be a very high performance NIB cathode, but we highlight the need for high-quality long- and short-range structural characterization. We further identify complex thermodynamic relationships in this phase space that lead to the formation of polymorphic $Na_2Fe_2F_7$ materials that show a phase transformation to $NaFeF_3$. Chapter 6 further investigates $Na_2Fe_2F_7$ and doped $Na_2M_xFe_{2-x}F_7$ (M = Mg^{2+}, Al^{3+}, and Mn^{2+}, $0 \leq x \leq$

1), providing additional insight into the phase transformation behavior and tendency towards polymorphism exhibited by this cathode class. Chapter 6 also contains final insights and conclusions towards the design of high-performance Na-Fe-F cathode materials, focusing on the weberite structure class.

Overall, this dissertation endeavors to better understand the complex structure-property relationships informing the electrochemical cycling of these novel, sustainable cathode materials to enable the rational design of high performance NIBs.

Chapter 2 – Methods

2.1 Diffraction

Diffraction relies on the scattering of a beam of light from an object and on the subsequent interference pattern created between the scattered waves. It is a ubiquitous characterization technique capable of reporting on a plethora of chemical structures, from proteins to quantum materials. The method predominantly used throughout this dissertation is powder X-ray diffraction (XRD). Here, an X-ray beam[d] is directed onto a material, and then interacts with and scatters from the material's electron density.[e] Consequently, atoms with larger electron densities will strongly diffract, giving more intense scattered waves and resultant diffraction patterns. The materials studied in this dissertation, however, predominantly contain "light" elements (e.g., Li, Na and F), which necessitate the use of synchrotron X-ray sources[f] that produce higher flux, higher

[d] This beam is typically created in-house by firing an electron beam at a metal target resulting in the generation of X-rays due to electronic excitations. The X-rays used in-house here are Cu K-α with a wavelength of *ca*. 1.54 Å.

[e] Neutrons and electrons can also be used for diffraction where they instead scatter off nuclei, thus providing complementary data.

[f] Synchrotrons produce X-rays by accelerating electrons around a circular particle accelerator (a synchrotron) at speeds approaching the speed of light that when deflected through a magnetic field, produce a beam of high-energy, high-flux X-rays. An X-ray wavelength

resolution X-rays (the latter is a consequence of the shorter wavelength produced by synchrotron sources).

X-ray diffraction is invaluable in characterizing the long-range structure of the cathode materials studied throughout this dissertation.

2.1.1 Bragg Diffraction

Crystalline materials are a convolution of a lattice—a periodic set of points in space—and a motif—a set of atoms centered at each lattice point, and which comprise the material in question. At its simplest, the entire crystal can be represented with a unit cell (with lattice vectors a, b, c, α, β, γ) that contains at least one lattice point, and upon tiling through three-dimensional space creates the full crystal. To describe the diffraction process, one must consider the interaction of the incident irradiation with the crystal. Once a dauting challenge to compute all possible interactions, William Bragg devised a simple scheme to describe this process where the crystal can be represented by parallel lattice places defined by the Miller indices h, k, and l, where the distance between a given set of (hkl) planes (d_{hkl}) is given as

$$\frac{1}{d_{hkl}^2} = \frac{h^2}{a^2} + \frac{k^2}{b^2} + \frac{l^2}{c^2} \tag{2.1}$$

When X-rays are shone on a crystalline material, the X-rays can be thought to reflect off individual lattice planes. Destructive interference between these reflected waves results in no signal intensity, while constructive interference, the condition for which is given by Bragg's Law, gives a peak in the diffraction pattern (Figure 2.1):

of 0.485 Å is obtained from 11-BM at Argonne National Lab, as significantly used throughout this dissertation.

$$n\lambda = 2d_{hkl}\sin(\theta) \qquad 2.2$$

where n is an integer describing the order of diffraction,[g] λ is the wavelength of X-ray radiation, and θ the angle of incidence of the X-ray on a given lattice plane.

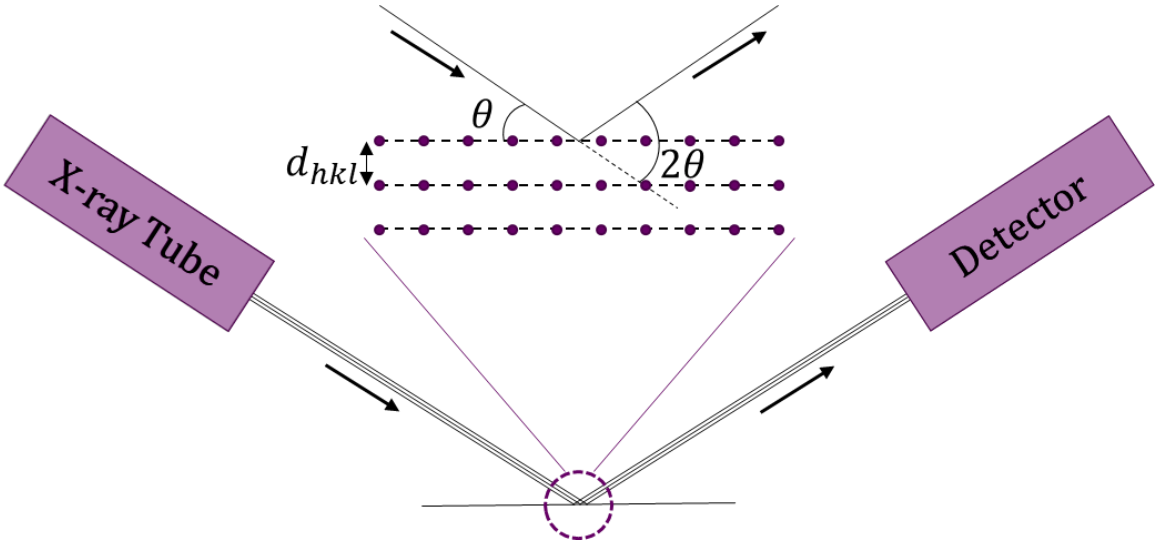

Figure 2.1 – Upper, illustration of Bragg's law with the incident X-rays diffracting from a set of lattice planes. Lower, schematic of X-ray diffraction in a Bragg-Brentano geometry.

The XRD experiments in this work measure the intensity of the diffracted beam with respect to the angular position of the detector relative to the X-ray beam, 2θ, in a Bragg-Brentano geometry as shown in Figure 2.1. A wealth of information can be gleaned from each diffraction pattern: the position of the resultant peaks provides structural information (size, shape, and symmetry of the unit cell) while the peak intensity provides chemical information (e.g., atom identity and position).

As the peak position given as 2θ has a wavelength dependence given by Bragg's Law, and each diffractometer has a subtly different operating wavelength, the scattering vector, Q, is used throughout this work:

[g] For the X-ray diffraction described in this work, *n* is set to 1.

$$Q = \frac{4\pi \sin(\theta)}{\lambda} = \frac{2\pi}{d_{hkl}}, \quad 2.3$$

2.1.2 Fitting the XRD Pattern

To extract the information contained in a diffraction pattern, the data must be fit to an appropriate model. XRD data is commonly fit using a Pawley[50] (purely structural model) and/or Rietveld[51] refinement[h] (structural and chemical model). These parameters which define the model can be experimental in nature (e.g., sample height, background intensity) or relate to a physical property of the system, such as the lattice parameters, atomic positions and site occupancies, size, and strain within particles.

In a Pawley refinement, only the lattice parameters and symmetry of the lattice (i.e., space group) are provided. The peak intensities are then arbitrarily fit to the data enabling one to obtain a theoretical best fit—i.e., one with no assumptions about the chemical species in the material. This method is useful for obtaining the appropriate peak shape parameters to then be fixed and used in a Rietveld refinement. The peak shape parameters are largely influenced by the crystallite distribution and are often described using Gaussian, Lorentzian, and/or Pseudo-Voigt functions.

In a Rietveld refinement, however, the lattice parameters and space group of the lattice are provided along with all the chemical information pertaining to the crystal structure—for example, atomic positions, atomic identities, and site occupancies. As previously described, X-rays diffract off electron density and thus, diffracted peak intensities are influenced by the type and number of atoms present on that specific

[h] Note that these refinements are least squares refinements: the sum of the squares of all residuals (the difference between the calculated and observed intensities) are minimized.

diffraction plane. For example, assuming all atoms to be the same, the closest packed plane in a lattice will provide the highest peak intensity. In this way, Rietveld refinements can quantify the amount of crystalline phases present in each material's diffraction pattern. As there are many refinable variables in a Rietveld refinement, care must be taken to ensure the data is not being overfit and the resultant model is physically meaningful.[i] Additionally, an understanding of what constitutes a "good" fit should be known rather than solely relying on refinement residuals.[52]

2.2 Nuclear Magnetic Resonance

2.2.1 Overview

Both nuclei and electrons possess a quantum property called spin, defined by quantum numbers I and S, respectively. This spin is an intrinsic form of angular momentum so that nuclei and electrons act as minute bar magnets in the presence of a magnetic field. For a given nuclear spin, there are $2I + 1$ spin microstates, defined by the magnetic nuclear spin quantum number, m_I. This quantity takes values from $-I, \ldots, +I$ in integer steps. When a sample is placed inside a magnetic field, as in an NMR experiment, these m_I microstates split due to the nuclear Zeeman interaction (Figure 2.2a). The energy separation of these microstates, ΔE, is given by:

[i] It has been said that "a refinement is never truly finished, simply abandoned."

$$\Delta E = -\hbar\,\gamma_I B_0 = \hbar\omega_0 \tag{2.4}$$

where $\hbar$ is the reduced Plank's constant, γ_I is the gyromagnetic ratio of the nuclear spin, B_0 the applied field strength, and $\omega_0 = -\gamma_I B_0$ the Larmor frequency. The nuclear transition selection rules dictate only $\Delta m_I = \pm 1$ transitions can occur.

To compare transitions observed at different field strengths, we must remove the field-dependence; this is conventionally done using the chemical shift of a nucleus relative to an agreed reference compound:

$$\delta = \frac{\omega - \omega_{\mathrm{ref}}}{\omega_{\mathrm{ref}}} * 10^6 \tag{2.5}$$

where ω_{ref} is the angular frequency of the reference. Note, these values are multiplied by 10^6 to prevent $\delta \ll 1$, and thus chemical shifts are given in parts per million (ppm).[53] The chemical shift interaction arises from the shielding of the applied magnetic field by electrons surrounding the nucleus – which are dependent on several factors, including the local chemical, structural, and electronic environment around the nucleus.

The total Hamiltonian representing NMR interactions can be written as

$$\hat{H} = \hat{H}_{\mathrm{ext}} + \hat{H}_{\mathrm{int}} \tag{2.6}$$

where $\hat{H}_{\mathrm{ext}} = \hat{H}_0 + \hat{H}_1$ is the sum of the Zeeman term, $\hat{H}_0$, and the term resulting from the interaction with the RF field (B_1), $\hat{H}_1$. The internal contribution,

$$\hat{H}_{\mathrm{int}} = \hat{H}_{\mathrm{CS}} + \hat{H}_{\mathrm{SC}} + \hat{H}_{\mathrm{D}} + \hat{H}_{\mathrm{Q}} + \hat{H}_{\mathrm{hyp}} \tag{2.7}$$

contains contributions from chemical shift interactions ($\hat{H}_{\mathrm{CS}}$), scalar couplings between two nuclei ($\hat{H}_{\mathrm{SC}}$), dipolar interactions between two nuclei ($\hat{H}_{\mathrm{D}}$), quadrupolar interactions ($\hat{H}_{\mathrm{Q}}$), and hyperfine interations between an electron and a nucleus ($\hat{H}_{\mathrm{hyp}}$). In the paramagnetic cathode materials studied in the bulk of this dissertation, the

dominant interactions are hyperfine—and quadrupolar for ^{23}Na—interactions. The remaining interactions can be neglected but descriptions may be found in ref. [53] and [54].

The key NMR properties of the nuclei probed in this dissertation are summarized in Table 2.1. Both ^{1}H and ^{19}F are spin-½, high-γ_I nuclei enabling them to be high sensitivity nuclei. However, as will be discussed, mainly for ^{19}F, their high-γ_I's lead to significant interactions of their nuclear moments with unpaired electrons causing significant hyperfine shifts and line broadening. Only ^{7}Li and ^{23}Na exhibit non-zero quadrupole moments and hence are the only nuclei that are affected by quadrupolar interactions. However, as the quadrupole moment for ^{7}Li is quite small, quadrupolar interactions are typically considered negligible, especially in the presence of hyperfine interactions as encountered in this dissertation.

Table 2.1 – NMR Properties of Nuclei Probed in this Dissertation. Taken from the *Encyclopedia of Magnetic Resonance* article, Nuclear spin properties and conventions for chemical shifts (IUPAC Recommendations 2001).[55]

Nucleus	I	Quadrupole Moment, Q (fm^2)	Gyromagnetic Ratio, γ_I ($* 10^7$ $^{\mathrm{rad}}/_{\mathrm{T}\cdot s}$)	Natural Abundance (%)
^{1}H	$^{1}/_{2}$	---	26.75221	99.9885
^{7}Li[j]	$^{3}/_{2}$	−4.01	10.39717	92.41
^{19}F	$^{1}/_{2}$	---	25.18148	100
^{23}Na	$^{3}/_{2}$	10.40	7.08085	100

2.2.2 Magic Angle Spinning (MAS) – Solution to Solid-State

In solution-state NMR, the rapid tumbling of molecules at rates faster than the NMR timescale averages out the spatially anisotropic interactions (e.g. nuclear-nuclear

[j] Note that ^{6}Li ($I = 1$, $Q = -0.0808\ \mathrm{fm}^2$, $\gamma_I = 3.9371 * 10^7\ ^{\mathrm{rad}}/_{T\cdot s}$, 7.59% natural abundance), is occasionally done in tandem to ^{7}Li due to its even lower quadrupole moment. However, this was not pursued here due to the dominant hyperfine interactions and gain in sensitivity when using ^{7}Li.

dipolar, chemical shift anisotropy, quadrupolar, electron-nuclear dipolar) that arise between the nucleus of interest and its surrounding environment. However, in solid-state NMR, crystallites are fixed with respect to the applied magnetic field, such that their spatially anisotropic interactions are no longer averaged out. Thus, the resonant frequency of the nucleus depends on the orientation of the nucleus inside the crystallite with respect to the applied field. The spectra of these samples are a sum of each crystallite orientation's spectra, giving rise to a broad distribution of shifts known as a powder pattern (Figure 2.2c).

As the breadth of the powder pattern can prevent extraction of useful information from the spectrum, magic angle spinning (MAS) is typically employed. As most of the anisotropic interactions encountered in NMR have an orientation dependence of $3\cos^2(\theta) - 1$, with θ describing the orientation of the nucleus with respect to the applied field, spinning the sample about the "magic angle", approximately 54.74° (e.g. the body diagonal of a cube), averages out these interactions (Figure 2.2b).[k] Under sufficiently fast MAS (typically three to four times the size of the anisotropic interaction),[54] a sharp resonance at the isotropic chemical shift is observed. At "slow" MAS speeds (relative to the size of the anisotropic interaction(s)),[l] the broad NMR

[k] Notably, not all anisotropic interactions are able to be averaged by MAS due to a differing angular dependence. Specifically, second-order interactions, such as the 2nd order quadrupole of ^{23}Na, are not averaged under MAS as such interactions evolve in a more complex manner with respect to the relative orientation of particles and the applied field.

[l] In many of the systems studied in this dissertation with dominate hyperfine interactions, the maximum attainable spinning speed of 60 kHz (60,000 revolutions per second!) is slow relative to the hyperfine interactions.

spectrum is broken up into spinning sidebands separated by integer multiples of the MAS speed. Due to the strong hyperfine, and in some cases quadrupolar, interactions encountered in the cathode materials investigated in this dissertation, all spectra were acquired under MAS.

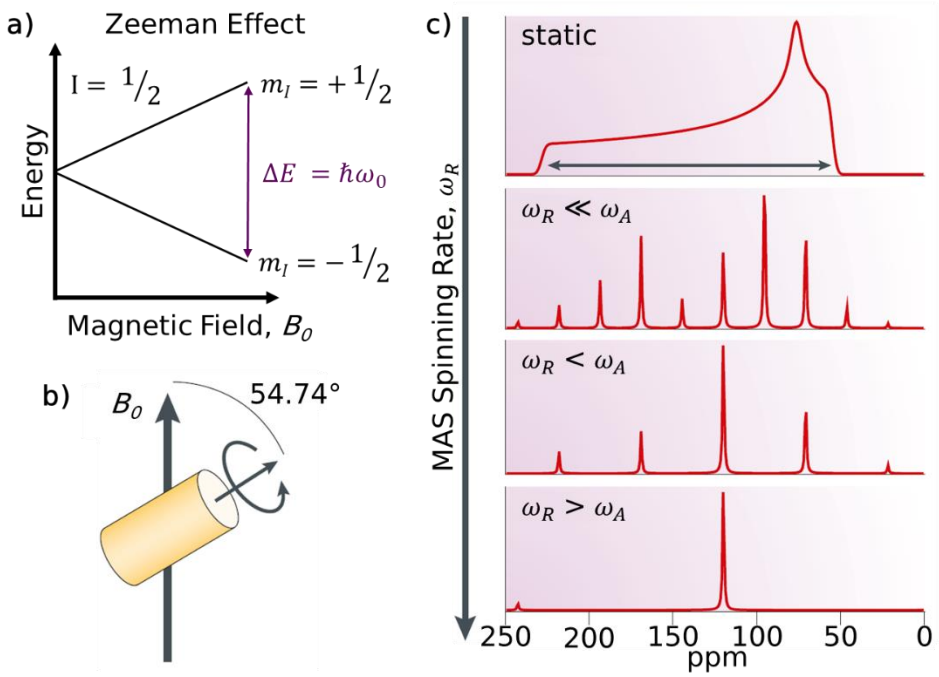

Figure 2.2 – a) Schematic of the Zeeman Effect where a nucleus' $\boldsymbol{m_I}$ microstates are split in the presence of a magnetic field. **b)** Diagram of magic angle spinning (MAS) where a rotor (represented as a cylinder) containing a polycrystalline sample is spun at an angle of 54.74° and with a frequency of $\boldsymbol{\omega_R}$ inside the external static magnetic field, $\boldsymbol{B_0}$, to average out anisotropic interactions. **c)** Effect of spinning speed of the chemical shift anisotropy (CSA) for an anisotropically broadened spectrum of width $\boldsymbol{\omega_A}$. Figure **(b)** and **(c)** are adapted with permission from Watts,[56] © 2005 Springer Nature.

2.2.3 Hyperfine Interactions

The materials examined in this work contain paramagnetic transition metals, most commonly $Fe^{2+/3+}$ ions. The unpaired electrons on these centers are also split by the Zeeman effect within an applied field and interact with nearby nuclear magnetic moments. On the NMR timescale (10^{-4} to 10^{1} s), the electron microstates relax rapidly (10^{-13} to 10^{-7} s)[57] allowing them to be treated as a time-averaged magnetic moment,

$\langle \mu_e \rangle$, rather than individual electron spin microstates, when considering interactions between it and the nuclear magnetic moment. This interaction (depicted in Figure 2.3) is known as hyperfine coupling, or paramagnetic coupling, and can result in significant shifts and broadening of the NMR signal. The hyperfine Hamiltonian takes the form:

$$\hat{H}_{\text{hyp}} = \hat{\boldsymbol{I}} \cdot \boldsymbol{A} \cdot \langle \boldsymbol{S_z} \rangle \qquad 2.8$$

where $\boldsymbol{A}$ is the hyperfine coupling tensor, $\hat{\boldsymbol{I}}$ the nuclear spin operator, and $\langle \boldsymbol{S_z} \rangle$ the time-averaged local field due to unpaired electrons from a nearby paramagnetic transition metal. This coupling can be a through-bond (Fermi contact) or through-space (dipolar coupling) process.

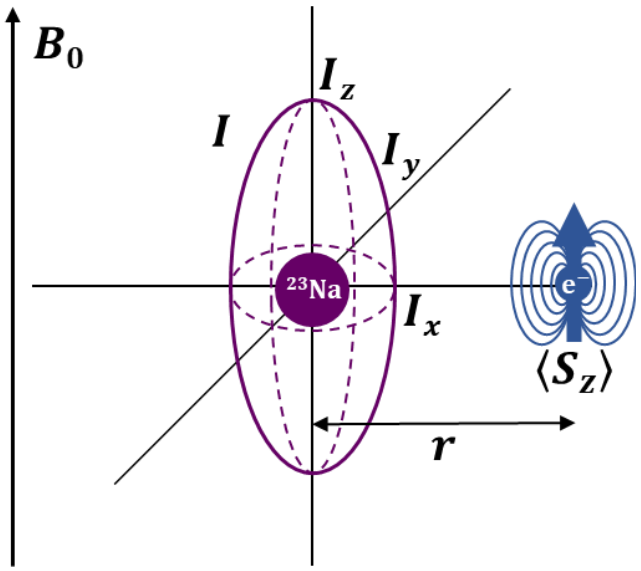

Figure 2.3 – Illustration of the hyperfine interaction between a ^{23}Na nuclear magnetic moment $\boldsymbol{I}$ and the time-averaged electron magnetic moment $\langle \boldsymbol{S_z} \rangle$ resulting from unpaired transition metal *d* electrons, with a distance $\boldsymbol{r}$ between the moments.

2.2.3.1 Fermi Contact Interaction

The Fermi contact interaction is an orbital-mediated process where unpaired electron spin density is transferred from the orbitals containing unpaired electrons to

the *s* orbitals of the nucleus of interest, *A*. This interaction is spatially isotropic and can be represented as

$$\hat{H}_{FC} = A_{FC} \langle \hat{\boldsymbol{S}} \rangle \cdot \hat{\boldsymbol{I}} \tag{2.9}$$

where $\hat{\boldsymbol{S}}$ is the spin angular momentum operator and $\hat{\boldsymbol{I}}$ is the nuclear spin angular moment operator. A_{FC} is the hyperfine coupling constant[58] given as

$$\frac{A_{FC}}{\hbar} = \frac{g_e \mu_0 \mu_B \gamma_I \rho(r=0)}{3S} \tag{2.10}$$

where g_e is the free-electron g-factor, μ_0 the permittivity of free space, μ_B the Bohr magneton, $\rho(r = 0)$ the unpaired spin density at the nuclear position where r is a position vector originating at the nucleus of interest, and S the total transition metal (M) electron spin.

The Fermi contact shift, δ_{FC} in ppm, is obtained by dividing the contact coupling energy by the nuclear Zeeman energy:

$$\delta_{FC} = \frac{10^6 \Delta\omega}{\omega_0} = -\frac{10^6 A_{FC}}{\hbar \omega_0} \langle \boldsymbol{S_z} \rangle \tag{2.11}$$

where $\langle \boldsymbol{S_z} \rangle$ is the average electron spin along B_0 and can be expressed in terms of its molar magnetic susceptibility, χ_m, as:

$$\langle \boldsymbol{S_z} \rangle = -\frac{\chi_m B_0}{\mu_0 \mu_B g_e N_A} \tag{2.12}$$

where N_A is Avogadro's number. Thus, δ_{FC}, in ppm, can be given as:

$$\delta_{FC} = \left(-\frac{10^6 A_{FC}}{\hbar \omega_0}\right) * \left(-\frac{\chi_m B_0}{\mu_0 \mu_B g_e N_A}\right) = \frac{10^6 A_{FC} \chi_m}{\mu_0 \mu_B g_e N_A} * \frac{B_0}{\hbar \omega_0} = \frac{10^6 A_{FC} \chi_m \hbar}{\mu_0 \mu_B g_e N_A \gamma_I} \tag{2.13}$$

Based on the equation for δ_{FC}, the following conclusions can be made regarding the Fermi contact shift: a lower γ_I results in lower sensitivity but also in smaller paramagnetic shifts; paramagnetic M ions that exhibit large magnetic susceptibilities also give rise to larger Fermi contact shifts; and the magnitude and sign of A_{FC}

determines the magnitude and direction, respectively, of the observed chemical shift.[58,59] Finally, through its dependence on A_{FC}, which is proportional to the unpaired electron spin density at the nuclear position ($\rho(r = 0)$), δ_{FC} necessarily results from a non-zero unpaired electron spin density at the nuclear position *via* an electron delocalization and/or polarization mechanism. These mechanisms can be qualitatively described by the Goodenough-Kanamori rules, as discussed in the next section.

2.2.3.2 Spin Density Transfer Pathways

In the paramagnetic cathodes studied in this work, the Fermi contact hyperfine coupling overwhelmingly dominates the isotropic chemical shift and thus δ can be approximated as δ_{FC}. Several ssNMR studies on paramagnetic materials[60,61] have shown that in this case, the observed chemical shift is given by the sum of the individual *M*-*X*-*A* bond pathway shift contributions, denoted P_i, where *M* is a transition metal in the first coordination shell of *A*:

$$\delta_{FC} = \sum_i P_i \qquad 2.14$$

The extent of spin transfer along each bond pathway—and therefore the value of P_i—depends on the degree of orbital overlap along the bond pathway between the paramagnetic center and the nucleus of interest, and thus is highly sensitive to the *M* orbital occupancy and bond geometry.[60,62–64] The sign and magnitude of δ_{FC} can be qualitatively rationalized using the Goodenough-Kanamori rules[65–67] as depicted in Figure 2.4 for the limiting 90° and 180° interactions for an $Fe^{2+/3+}$-F-Na bond pathway.

A careful assignment of the features in paramagnetic ssNMR spectra can provide a wealth of information, ranging from the local environments experienced by the NMR nucleus to the extent of spin transfer.[68] In practice, individual *M-X-A* shift contributions are first obtained on model compounds with well-known structures and are then used to understand the shifts of more complex materials. A detailed explanation of the way these shift contributions are obtained is outside the scope of this dissertation but we direct the reader to the work by Middlemiss *et al.*[63] for more information.

We note that in quadrupolar systems (here, ^{23}Na), the quadrupole-induced shift (δ_{QIS}) must also be accounted for, which will be discussed in section 2.2.4 , but due to the additive nature of NMR chemical shifts, this can be added onto the shift deduced from the δ_{FC}.

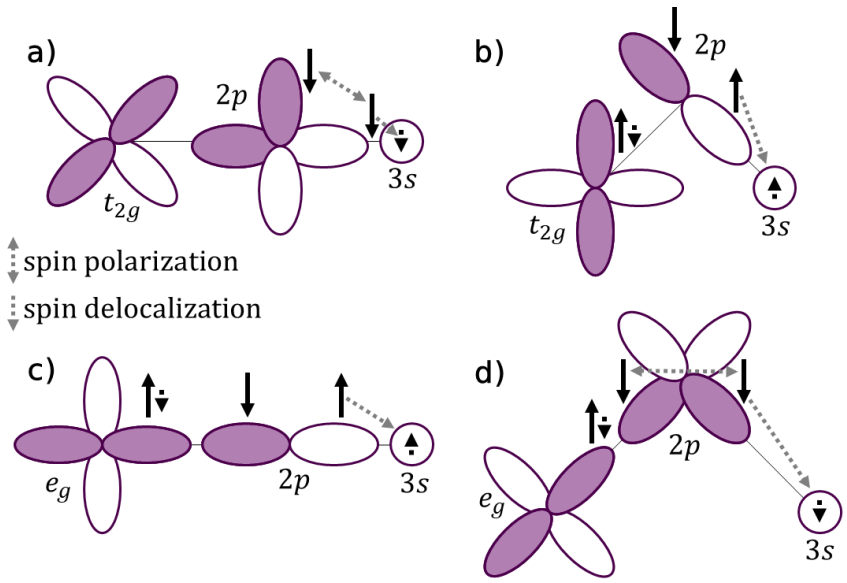

Figure 2.4 – Spin density transfer pathways for limiting 90° and 180° interactions for Na (empty 3*s*) - $Fe^{2+/3+}$ (half-filled $\boldsymbol{t_{2g}}$ and $\boldsymbol{e_g}$) – F (filled 2*p*) bond interactions. **(b)** and **(c)** depict a delocalization-type mechanism where net positive spin density is transferred to the Na *s* orbital. **(a)** and **(d)** depict a polarization-type spin density transfer mechanism where negative spin density is transferred to the Na *s* orbital. As this mechanism requires two intervening F 2*p* orbitals, it is considered a "weak" interaction. The dashed double-headed grey arrows denote spin polarization, and the dashed single-headed grey arrows note spin delocalization.

2.2.3.3 The Dipolar Hyperfine Interaction

The dipolar hyperfine interaction is a through-space electron spin density transfer process describing the interaction of electron and nuclear magnetic moments. The magnitude of this interaction depends on the distance and orientation of the vector relating the two interacting spins relative to the external field. The Hamiltonian for this interaction is:

$$\hat{H}_{\mathrm{dd}} = \langle \hat{\boldsymbol{S}} \rangle \cdot \boldsymbol{D} \cdot \hat{\boldsymbol{I}} \tag{2.15}$$

where $\boldsymbol{D}$ is the second-rank dipolar coupling tensor given as:

$$\boldsymbol{D} = \hbar \left(\frac{\mu_0}{4\pi}\right) \gamma_I \gamma_S \begin{pmatrix} \frac{1}{r^3} & 0 & 0 \\ 0 & \frac{1}{r^3} & 0 \\ 0 & 0 & \frac{1}{r^3} \end{pmatrix} \tag{2.16}$$

where r is now the electron-nucleus separation. As this tensor is traceless and has no isotropic component, dipolar coupling is purely anisotropic. Thus, the orientation-dependence of the chemical shift leads to significant broadening of the observed signal—parameterized by the dipolar anisotropy (Δ_δ) and the dipolar asymmetry (η) which will be quantitatively defined in Section 2.5.3—that appears as spinning sidebands under intermediate MAS (Figure 2.2*c*). The magnitude of this interaction scales with r^{-3}, and thus decreases with increasing electron-nucleus separation, with $r = 20$ Å typically treated as the upper cutoff.

The hyperfine dipolar coupling may also generate a pseudo-contact shift (PCS) interaction, provided that the magnetic susceptibility is anisotropic (as can be the case for Fe^{2+}). This PCS interaction contains both isotropic and anisotropic components, but is frequently much smaller than the Fermi contact shift.[59,69] Anisotropic bulk magnetic

susceptibility (ABMS) effects can also lead to inhomogeneous line broadening that MAS cannot average out. For further discussion of PCS and ABMS interactions, the reader is directed to a recent review by Pell *et al.*[59]

2.2.4 Quadrupolar Interactions

As shown in Table 2.1, both ^{7}Li and ^{23}Na are I = 3/2 nuclei. However, ^{7}Li quadrupolar interactions are typically considered negligible compared with the much larger hyperfine interactions present in paramagnetic compounds.[60] Thus, the present discussion will focus on quadrupolar interactions in ^{23}Na.

Nuclei with $I > ½$ possess a nuclear electric quadrupole moment, Q, arising from the non-spherical charge distribution in their nucleus. This quadrupole moment interacts with the local electric field gradient (EFG)—if present—at the nucleus, which is directly related to the anisotropy of the local electronic and nuclear charge distribution (i.e., the local bonding environment). The quadrupolar interaction is described by a second-rank tensor, $\boldsymbol{V}$, and the quadrupolar Hamiltonian takes the form:

$$\hat{H}_Q = \frac{eQ}{2I(I-1)} \hat{\boldsymbol{I}} \cdot \boldsymbol{V} \cdot \hat{\boldsymbol{I}} \qquad 2.17$$

where e is the electron charge and eQ is the nuclear quadrupole moment. The EFG tensor can be described by two terms—the anisotropy, eq, and the asymmetry, η_Q given as:

$$eq = V_{ZZ} \qquad 2.18$$

$$\eta_Q = \frac{V_{XX} - V_{YY}}{V_{ZZ}} \qquad 2.19$$

where V_{ii} are the principal components of the EFG tensor with $|V_{ZZ}| \geq |V_{XX}| \geq |V_{YY}|$. The asymmetry, η_Q, describes the degree of axial symmetry of the local coordination environment with $\eta_Q = 0$ being axially symmetric. The degree of spherical symmetry

and overall strength of the quadrupolar interaction is given by the nuclear quadrupolar coupling constant, C_Q:

$$C_Q = \frac{e^2qQ}{\hbar} = \frac{eQ}{\hbar}V_{ZZ} \qquad 2.20$$

Highly symmetric sites (e.g. cubic) have $C_Q = 0$, while less symmetric environments will have $C_Q > 0$.[70,71]

If the quadrupolar coupling constant is much smaller than the nuclear Zeeman splitting, then the quadrupolar interaction can be considered as a perturbation of the Zeeman interaction. This shifts the Zeeman-split microstates so that they are no longer evenly spaced, generating several single-quantum ($\Delta m_I = \pm 1$) transitions. For half-integer nuclear spin quantum numbers—such as ^{23}Na (I = 3/2)—these transitions can be split into two classes shown in Figure 2.5: the central transition (CT) corresponding to $m_I = -\frac{1}{2} \leftrightarrow +\frac{1}{2}$, and the satellite transition (ST), corresponding to all other single-quantum transitions (for ^{23}Na this is only $m_I = -\frac{3}{2} \leftrightarrow -\frac{1}{2}$ and $m_I = \frac{1}{2} \leftrightarrow +\frac{3}{2}$). To first order, the CT frequency is unaffected by the quadrupolar interactions, but the ST frequencies exhibit an orientation-dependence that can be partially averaged under MAS.

When the quadrupolar splitting is ≈ 10% of the Zeeman splitting (as the case for ^{23}Na at low fields),[54,72] both first-and second-order quadrupolar interactions must be considered as shown in Figure 2.5. Here, both the CT and STs' resonant frequencies are orientation-dependent, leading to broad lineshapes which can only partially be averaged out under MAS. However, the second-order term cannot be averaged out due to a different angular dependence of this interaction, which leads to broadening of the

observed CT line.[73] Regardless, first-order line broadening of the ST can be so significant that only the CT is seen in the spectrum. The ^{23}Na NMR experiments in this dissertation were done with low[m] enough pulse strengths to ensure that we are CT-selective (i.e. the STs are not excited). In the absence of other sources of line broadening, the first-order quadrupolar lineshape can be fitted to determine the quadrupolar NMR parameters. The second-order terms lead to a typically small quadrupole induced shift, δ_{QIS}, defined as[74]:

$$\delta_{\mathrm{QIS}} = -\frac{1*10^6}{30}\frac{3}{\nu_0}\left(\frac{3C_{\mathrm{Q}}}{2I(2I-1)}\right)^2\left(\frac{1+\eta_{\mathrm{Q}}^2/3}{\nu_0}\right) \qquad 2.21$$

where ν_0 is the nuclear Larmor frequency. The ν_{Q} is the quadrupolar frequency, in Hz, is defined as:

$$\nu_{\mathrm{Q}} = \frac{\omega_{\mathrm{Q}}}{2\pi} = \frac{3C_{\mathrm{Q}}}{2I(2I-1)} \qquad 2.22$$

Thus, the overall experimental shift, δ_{exp}, is the sum of the field-independent isotropic shift, δ_{iso} (typically in paramagnetic systems $\delta_{\mathrm{iso}} \cong \delta_{\mathrm{FC}}$), and of the field-dependent δ_{QIS}:

$$\delta_{\mathrm{exp}} = \delta_{\mathrm{iso}} + \delta_{\mathrm{QIS}} \qquad 2.23$$

As δ_{QIS} is proportional to $\frac{C_{\mathrm{Q}}^2}{\nu_0^2}$, this second-order term can be suppressed by using larger magnetic field strengths, enabling δ_{QIS} to be made negligible at high fields.[72] These high fields also enable suppression of the additional broadening caused by the quadrupolar interaction and are typically preferred for quadrupolar experiments. However, the electron-nuclear hyperfine interaction varies linearly with B_0. Thus, due

[m] To ensure the pulse strength is low enough, "CT only" fits can be done in SOLA in Topspin.

to the competing quadrupolar and hyperfine effects present in the Na-ion cathodes studied here, an intermediate field strength—and in some cases a low field—was used to avoid significant line broadening induced by the hyperfine interaction. Regardless, this line broadening caused by the hyperfine interaction prevents details on the EFG tensor from being obtained *via* peak fitting.

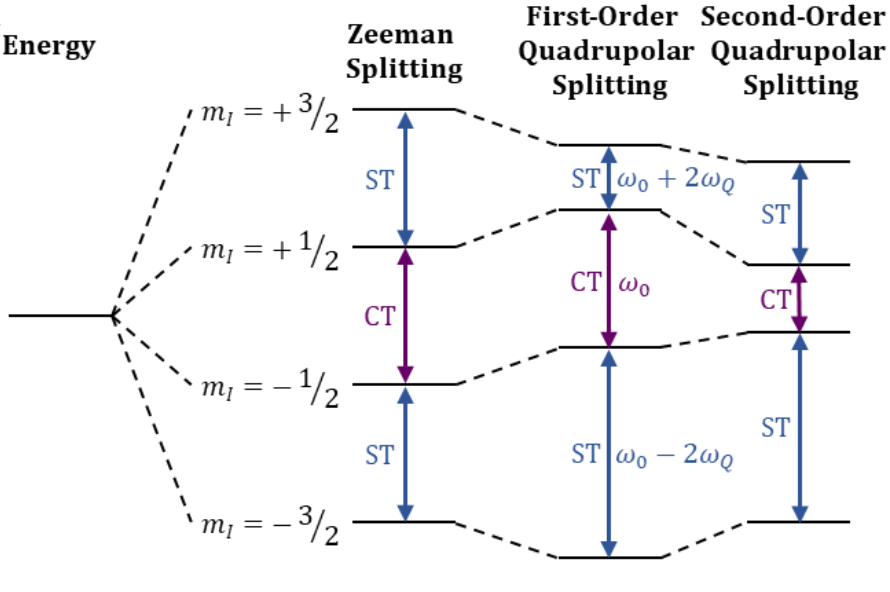

Figure 2.5 – Schematic energy level diagram for a spin $\boldsymbol{I} = \frac{3}{2}$ nucleus within an external magnetic field, $\boldsymbol{B_0}$. The diagram shows the effect of the Zeeman effect and first- and second- order quadrupolar interactions on the energy level of the four $\boldsymbol{m_I}$ states. The central transition (CT) and satellite transitions (ST) are unaffected and affected, respectively, by the first-order quadrupolar interaction, whereas all transitions are affected by the second-order quadrupolar interaction.

2.2.5 NMR Experiments

The strong hyperfine and quadrupolar interactions encountered in the paramagnetic cathode materials investigated in this dissertation complicate analysis of the NMR spectrum. Specifically, hyperfine, and in some cases quadrupolar, interactions can induce large shifts (~10^3 ppm)[28,38,64] and rapid relaxation of the NMR signals, necessitating fast MAS, frequency stepping,[75–78] and isotropic-resonance isolating NMR

techniques.[79] These will be briefly discussed here, first involving quantification *via* the Hahn-echo pulse sequence with some discussion as well on advanced NMR techniques utilized throughout this dissertation.

We note that typical quadrupolar NMR experiments (e.g. multiple-quantum MAS or MQMAS)[80,81] were not performed here as they require moderate spinning speeds and long pulsing times leading to poor spectral resolution and loss of signal due to T_2 losses, respectively, when the samples are also strongly paramagnetic.

2.2.5.1 Hahn-Echo

In an NMR experiment, a sample is placed inside a magnetic field and due to the Zeeman effect, a net magnetization (***M***) is produced parallel to the external magnetic field, B_0. This net magnetization is proportional to the population difference of the different nuclear spin microstates given by a Boltzmann distribution of

$$\boldsymbol{M}\alpha \left(N_{+1/2} - N_{-1/2}\right) \approx N\frac{\gamma_I \hbar B_0}{2k_B T} \qquad 2.24$$

where $N_{+1/2}$ and $N_{-1/2}$ is the number of spins with $m_I = +1/2$ and $m_I = -1/2$, respectively, and k_B is the Boltzmann constant.[58] Thus, the highest ***M*** is produced using a high field, high γ_I nucleus, and at low temperature. However, even under these conditions, an exceedingly small net nuclear magnetization is generated. Thus, while NMR is a very high-resolution technique, its sensitivity is inherently low.

Upon generation of this net magnetization, ***M***, the comprising spins are rotated to the *xy* plane by a transverse radiofrequency (RF) pulse[n] with an oscillating magnetic

[n] Brief note on energy scales… the RF pulses that are used have a wavelength of 10^{-1} to 10^{1} m, energies of 10^{-8} to 10^{-6} eV, and frequencies of 10^{3} to 10^{1} MHz. Therefore, NMR is a relatively low energy technique—especially compared to Mössbauer spectroscopy which uses

field, B_1, of frequency, ω_{rf}. These spins begin to precess about B_0 with their characteristic ω_0 due to the torque applied by the B_1 field. Once the RF pulse is removed, there is now a driving force for the system to return to equilibrium (i.e., $\boldsymbol{M}$ will begin to move towards the z-axis). The time taken for $\boldsymbol{M}$ to return to the z-axis is known as the longitudinal relaxation time (T_1). However, during that time $\boldsymbol{M}$ is simultaneously precessing about the z-axis and when the sample is placed inside a conducting coil, the components of $\boldsymbol{M}$ in the *xy* plane generate a voltage in the coil, which can be measured as a function of time. This decaying magnetization detected in the coil is known as the free induction decay (FID). This FID is then Fourier transformed to separate the various Larmor frequencies (in Hz), or chemical shifts (in ppm) in the final NMR spectrum.

The net magnetization $\boldsymbol{M}$ comprises all the individual nuclear spins in the sample and as each spin exhibits different Larmor frequencies, due to their different chemical environments and thereby different relative orientations of spins with respect to B_0, each individual nuclear spin precesses about the z-axis at a slightly different frequency. This can be described as a phase shift between the precession frequency of each spin. As a result, the *xy* components of $\boldsymbol{M}$ also decay due to the different phases of the individual nuclear spins (along with the decay as $\boldsymbol{M}$ returns to the z-axis). This *xy* decay process is known as dephasing, or transverse relaxation, and is described by the time constant T_2.

Note that the same conductive coil that generates the RF pulse also detects the *xy* magnetization. Due to the finite time taken to switch from RF generation to magnetization detection ("dead time"), there is a brief period where no signal can be

gamma-rays (14 keV). This makes NMR a high-resolution technique, enabling it to detect small changes to the local chemical, electronic, and/or structural environment.

detected, leading to (partial) signal loss. To avoid this, a Hahn echo pulse sequence may be used (Figure 2.6).[82] Here, a 90° flip-angle pulse (also called a $\frac{\pi}{2}$ pulse) is applied to the sample, flipping $\boldsymbol{M}$ into the *xy* plane, and the magnetization is allowed to evolve for a time τ before a 180° flip-angle pulse (also called a π pulse) is applied. The effect of this second pulse is to flip $\boldsymbol{M}$ towards $-z$ and then back to the *xy* plane to reverse the direction of precession of the individual spins. This leads to a build-up of net magnetization in the *xy* plane, up to a maximum at a time τ after the π pulse, at which point $\boldsymbol{M}$ is fully rephased. At this point, the acquisition begins and provided that τ is greater than the dead time of the detector (and that the nucleus does not have an incredibly short T_2) no signal is lost. Note that the delay, τ, is chosen to be rotor synchronized, so that information about the anisotropic interactions (contained in the sideband manifold) is retained in the spectrum.

For nuclei with large quadrupolar coupling (i.e., quadrupolar interaction ≈ 10% of the Zeeman interaction) as encountered in this dissertation for ^{23}Na, the STs are inefficiently excited by a typical $\frac{\pi}{2}$ or π pulse and only the CT is excited (known as a selective pulse), as the strong quadrupolar coupling creates a large energy separation between the CT and ST transitions. In this strong coupling limit, the nucleus can be considered as a spin-½ nucleus whose nutation frequency (frequency that $\boldsymbol{M}$ rotates about the *y*- or *x*-axis with respect to RF pulse power) is increased by a factor of $I + \frac{1}{2}$ (Figure 2.7). Therefore, the optimal radiofrequency pulse length is decreased by a factor of $I + \frac{1}{2}$ compared to an environment with $C_\mathrm{Q} = 0$ (known as the liquid limit where all quadrupolar interactions are averaged out—e.g., ^{23}Na in aqueous NaCl).[72] For ^{23}Na

signals with a small to moderate C_Q, the optimal pulse length is thus one half the liquid pulse length.

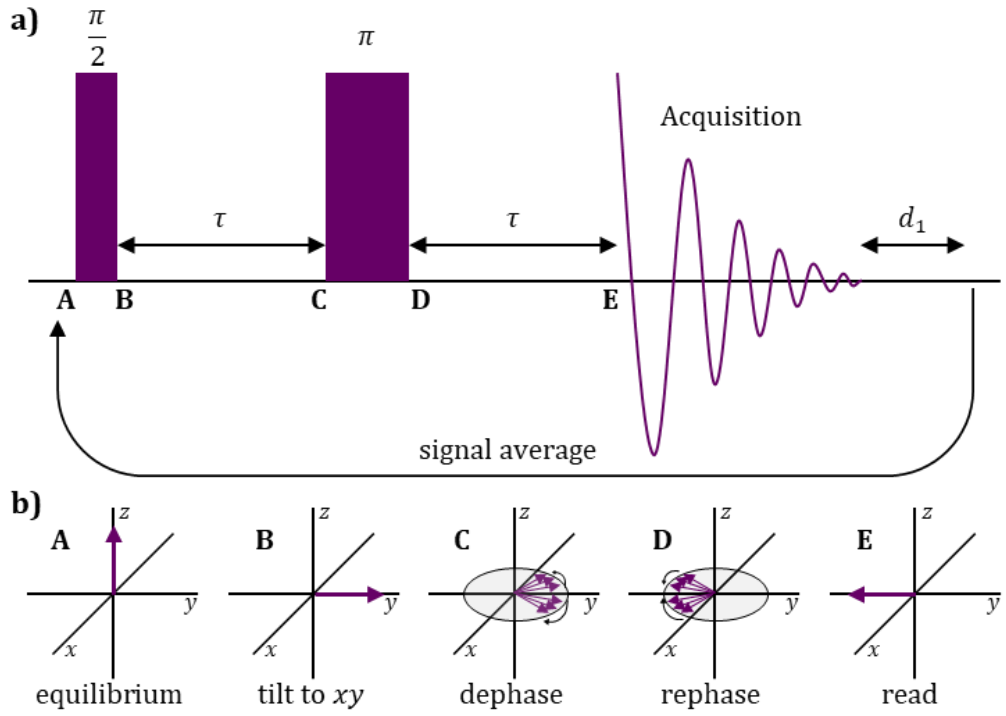

Figure 2.6 – a) Hahn echo pulse sequence highlighting the $\frac{\pi}{2}$ and $\boldsymbol{\pi}$ pulses, time delays ($\boldsymbol{\tau}$), and recycling delay ($\boldsymbol{d_1}$). **b)** Vector model description of the net magnetization (arrow(s) shown in purple) evolution throughout the Hahn echo pulse sequence with labels corresponding to location within the pulse sequence shown in **(a)**.

Due to the large variation in ^{23}Na sites in the weberite materials explored in Chapter 5 of this dissertation, there is a large distribution of different nutation profiles. To quantitatively compare all sites in these materials, shorter pulse lengths must be used so that all sites are in the linear regime. Thus, when studying weberite materials *via* ^{23}Na NMR, $\frac{\pi}{6}$ and $\frac{\pi}{2}$ pulses were used to equally excite and selectively excite, respectively, ^{23}Na signals to qualitatively separate the range of local environments by the relative magnitude of their C_Q.

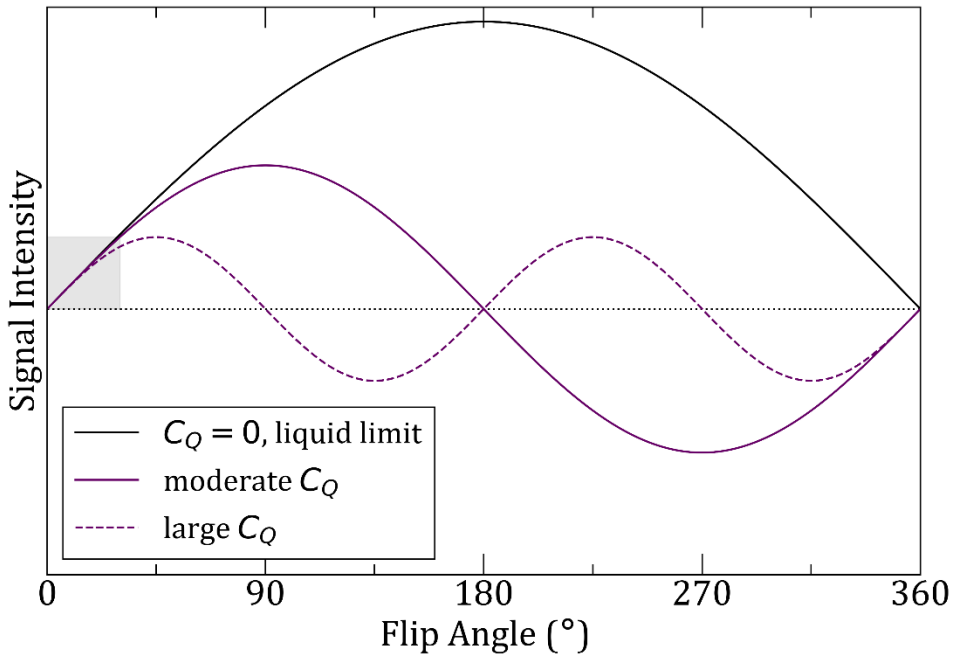

Figure 2.7 – Variation in the NMR signal intensity *vs*. RF pulse flip angle for a spin-$^3/_2$ nucleus (e.g., ^{23}Na) depending on the magnitude of its quadrupolar interactions. $\boldsymbol{C_Q = 0}$ effectively denotes the liquid limit (all anisotropy averaged out by molecular tumbling), whereas a "moderate" and "large" $\boldsymbol{C_Q}$ is most readily encountered in solid-state samples which experience non-negligible quadrupolar interactions. The shaded grey box highlights the region where all environments are equally excited, typically requiring a 30° ($\frac{\pi}{6}$) pulse or less.

2.2.5.2 Measuring T_1 and T_2 Relaxation Times

The longitudinal (T_1) and transverse (T_2) relaxation times provide valuable information regarding the electronic, transport, and other physical properties of a given system. Longitudinal relaxation (T_1)—also called spin-lattice relaxation—describes the drive for the net magnetization to orient along the *z*-axis to reach equilibrium. For spin-½ nuclei, the magnetization evolution is given as

$$M = M_0 \left[1 - \exp\left(-\frac{t}{T_1}\right)\right] \qquad 2.25$$

where M is the magnitude of magnetization at time t and M_0 the magnetization at time $t = 0$. Note that for quadrupolar nuclei, the magnetization depends on the populations of both the CT and ST and thus cannot be described by a single relaxation parameter.

However, due to the many factors influencing longitudinal relaxation and often comparable relaxation rates of the CT and ST, it is reasonable to fit the magnetization *vs*. time data using either a single or multiexponential.[72]

By measuring the *z* magnetization of the sample as a function of time and fitting this evolution to Equation 2.25, the T_1 can be extracted. This can be done using either a saturation-recovery or inversion-recovery pulse sequence, although when working with a broad signal it is best to use a saturation recovery experiment.[o] Thus, a saturation recovery pulse sequence was used in this dissertation to measure T_1 values. In this sequence, a train of saturating $\frac{\pi}{2}$ pulses are first applied to force all magnetization into the *xy* plane (Figure 2.8a,b). The magnetization is then allowed to evolve towards equilibrium along *z*, the direction of the external magnetic field, *via* longitudinal relaxation during a time τ, after which a single $\frac{\pi}{2}$ "read" pulse is applied and the magnetization is measured in the *xy* plane. This is repeated several times with varying τ periods and the data (Figure 2.8e) is then fitted to Equation 2.25. As much as possible, this fitting is performed for each individual peak in the spectrum, allowing the T_1 of each nuclear environment in the system to be extracted.

Longitudinal relaxation is typically caused by fluctuations of the local electric and magnetic fields on the order of the Larmor frequency (tens of MHz), originating from quadrupolar interactions, hyperfine coupling, and/or electron/ion transport. The materials studied in this dissertation experience large hyperfine coupling with unpaired

[o] An inversion recovery pulse sequence first applies a π pulse, waits for a time τ, and a final "read" $\frac{\pi}{2}$ pulse before acquisition. This sequence is less efficient for broad signals due to the lower efficiency of π pulses compared to $\frac{\pi}{2}$ pulses, which is why it was not used here.

electrons from $Fe^{2+/3+}$ (and other paramagnetic centers depending on the material), causing very short T_1s—typically at most a few milliseconds. Additionally, ^{23}Na nuclei generally experience shorter T_1s than $^{7}Li/^{19}F$ due to its quadrupolar moment.

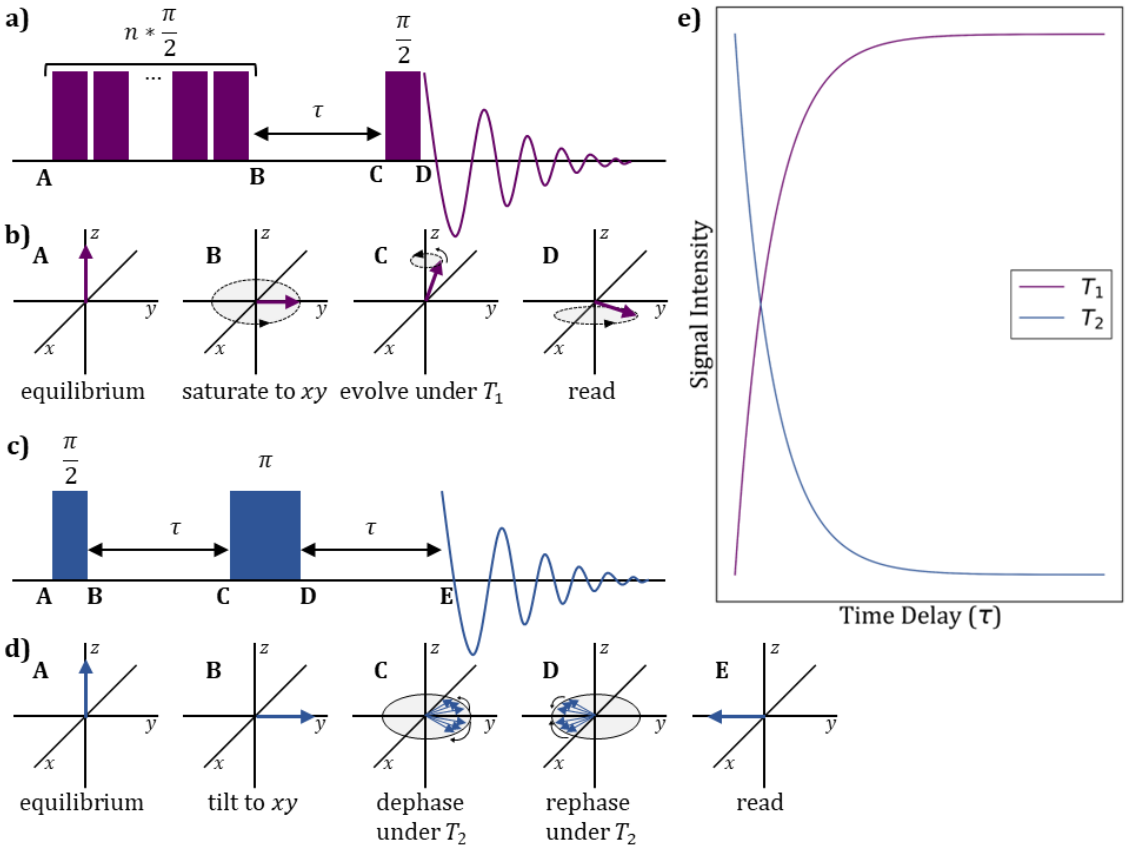

Figure 2.8 – Pulse sequences and vector model illustrations for **(a)** $\boldsymbol{T_1}$ saturation recovery and **(b)** $\boldsymbol{T_2}$ modified Hahn echo relaxation measurements where their vector model representations are shown in **(b)** and **(d)**, respectively, with labels corresponding to the location within the corresponding pulse sequence. **e)** Evolution of signal intensity detected throughout $\boldsymbol{T_1}$ (purple) and $\boldsymbol{T_2}$ (blue) relaxation measurements.

Transverse relaxation (T_2)—also called spin-spin relaxation—describes spin dephasing (also termed coherence loss) in the *xy* plane caused by random fluctuations of the local electric and magnetic fields (due to quadrupolar interactions, hyperfine coupling, and/or ion motion) in the kHz regime leading to variations in a spin's precession frequency. T_2 relaxation is typically significantly faster than T_1 relaxation as it can occur through rapid, adiabatic flip-flop transitions in which one spin undergoes a

transition from m_I to $m_1 + 1$, the "flip", while a nearby spin undergoes a transition from m_I to $m_I - 1$, the "flop". As the system neither gains nor loses energy, this process is rapid.[54]

Transverse relaxation influences the linewidth of signals in a spectrum. However, in solids, the linewidth of a signal is also affected by a distribution in local environments and/or field inhomogeneities in a sample—known as inhomogeneous broadening, characterized by the time constant T_2^*. Thus, T_2 can no longer be measured from the linewidth at full-width-half-maximum (FWHM), as is done for well-behaved solution samples which undergo homogeneous broadening. Instead, the T_2 is measured using a modified Hahn-echo experiment, as shown in Figure 2.8c,d, where the time delay τ is varied[p] while maintaining rotor synchronization. In this experiment, a $\frac{\pi}{2}$ pulse is first applied to tilt the magnetization into the *xy* plane, the system then undergoes dephasing during a time delay τ, then a π pulse is applied, and a time τ passes before acquisition to refocus the dephased magnetization. The signal decay measured in this way is a combination of the intrinsic T_2 and of all the NMR interactions not refocused by the echo π pulse.[83] Thus, the overall relaxation time is denoted T_2'. The magnetization in this experiment follows:

$$M = M_0 \exp\left(-\frac{\tau}{T_2'}\right) \qquad 2.26$$

where M_0 is the magnetization at time $t = 0$ and τ is the delay between the first and second pulses and between the second pulse and acquisition. By fitting the variation in

[p] T_2 filters (using longer τ delays to eliminate quickly relaxing signals) can be used in a standard Hahn-echo to better separate signals with T_2 values whose difference exceed one rotor period.

M with τ (Figure 2.8e) as a single exponential (or multiexponential for quadrupolar systems), the T_2' can be extracted. Like the analysis done for T_1 relaxation, this fitting can be done for individual peaks allowing individual T_2' values to be extracted for each signal.

2.2.5.3 Quantitative NMR

The Hahn-echo pulse sequence is well-suited for quickly-relaxing species (i.e., those with short T_1 and T_2 times), as encountered in the paramagnetic cathode materials investigated in this dissertation, due to the large number of scans that can be recorded over a relatively short time frame. However, to ensure acquisition of quantitative spectra, the net magnetization, ***M***, must be allowed to return to equilibrium at the end of the pulse sequence before another measurement is run (typically the same sequence is run multiple times to increase the signal-to-noise ratio[q]). Thus, a time delay called the recycle delay (d_1) is added to the end of the pulse sequence to ensure the net magnetization reaches equilibrium. To be fully quantitative (i.e., all nuclei returned to equilibrium prior to pulsing), the recycle delay should be set to at least $5T_1$.

Additionally, a Hahn-echo pulse sequence should be used to prevent signal loss during the finite time needed for the conducting coil to switch from RF generation to magnetization detection. However, in systems with very short T_2s (on the order of hundreds of nanoseconds or less), signal can still be lost prior to the start of acquisition. Thus, to be fully quantitative, these losses—termed T_2 losses—must be considered. This is typically done by scaling the signal intensity by a relaxation factor:

[q]The signal-to-noise ratio increases roughly as (time)$^{-2}$ or (# of scans)$^{-2}$ so if the signal is too low initially, there will likely be significant noise present in your final spectrum regardless of how long you signal average. This is an issue encountered in Chapter 5.

$$f = \exp\left(-\frac{T}{T_2'}\right) \quad 2.27$$

where T is the total time between the last RF pulse application and the start of the signal acquisition. Finally, for significantly quadrupolar systems (e.g. ^{23}Na NMR as discussed in Chapter 5) a small flip angle should be used to ensure that all ^{23}Na environments are equally excited by the RF pulse.

2.2.5.4 pj-MATPASS

Solid-state NMR spectra—especially of quadrupolar nuclei in paramagnetic materials—can become extremely complex due to the presence of overlapping signals from multiple nuclear environments in the sample, which exhibit broad resonances with spinning sideband manifolds spanning hundreds to thousands of ppm. Hence, identifying the isotropic resonances of the nucleus under investigation is nearly impossible in some cases without the use of (pseudo-)two-dimensional NMR experiments capable of separating the isotropic and anisotropic components of the spin interactions. In this dissertation, isotropic resonances were separated using the projected magic angle turning phase-adjusted sideband separation (pj-MATPASS) experiment.[79] This pulse sequence will be briefly explained here but for a detailed description the reader is directed to the work by Hung et al.[79]

The pj-MATPASS pulse sequence is a pseudo-two-dimensional experiment, where delays between $\frac{\pi}{2}$ pulses are calculated according to the PASS equations[84,85] and are designed to isolate sidebands in different slices in the indirect dimension of the spectrum. For each individual signal in the dataset, the intensity transferred from the isotropic resonance to the sidebands at a finite sample spinning speed can be restored in an isotropic spectrum (containing no sidebands) by shearing the two-dimensional

dataset and summing the sideband intensities in each of the indirect increments of the experiment in the central increment. We note that due to the very short relaxation times observed for ^{23}Na in select paramagnetic cathodes, application of this pulse sequence and others is complicated by the significant signal loss experienced during the duration of the experiment.

2.2.5.5 Frequency Stepping

In the presence of significant spectral broadening (e.g., the spectrum is wider than the excitation bandwidth of the RF pulse), broadband NMR techniques may be necessary to capture the full NMR spectrum. This problem was encountered in Chapter 3 for ^{19}F spectra collected on Li-excess disordered rocksalt oxyfluoride materials. The method used in this dissertation to collect the full spectrum is termed "frequency stepping",[75,76] "spin echo mapping",[77] or "variable offset cumulative spectrum" (VOCS),[78] where the entire spectrum is collected in a series of frequency steps, set to be slightly lower than the excitation bandwidth of the RF pulse. The individual sub-spectra are then processed using a zero-order phase correction and finally added to give an overall sum spectrum in absorption mode that requires no further phase correction.

2.3 Mössbauer Spectroscopy

Mössbauer spectroscopy is based on the Mössbauer effect as first discovered by Rudolf Mössbauer in 1958, earning him the Nobel Prize in Physics in 1961.[86] The Mössbauer effect is the nearly recoil-free emission and absorption of gamma rays which occurs in solid materials allowing one to achieve nuclear resonance between the source

(radioactive material emitting gamma rays) and absorber (sample) material.[87,88] This effect enables very small changes in the chemical environment as well as local magnetic fields at the nucleus under investigation to be detected, making Mössbauer spectroscopy a very useful local spectroscopic technique.

2.3.1 The Mössbauer Effect

To understand this technique, first consider a gaseous system consisting of a radioactive source and sample. The energy of an emitted gamma ray (E_γ) from this source is:

$$E_{\gamma,\text{transmitted}} = E_{\text{resonance}} + D - R \tag{2.28}$$

where $E_{\text{resonance}}$ is the energy difference between the ground and first excited state of the source nucleus, D is the Doppler shifted energy due to translational motion of the nucleus, and R is the recoil energy. This recoil energy is a natural consequence of conservation of momentum and is given as

$$R = \frac{E_\gamma^2}{2mc^2} \tag{2.29}$$

with m the emitting/absorbing mass and c the speed of light. The energy for an absorbed gamma ray is then given as

$$E_{\gamma,\text{absorbed}} = E_{\text{resonance}} + D + R \tag{2.30}$$

where now the recoil energy is added. The energy for gamma ray absorption and emission are shifted apart by $2R$ which tends to be on the order of 10^{-3}eV, while the natural linewidth for emission/absorption lines are only on the order of 10^{-9}eV. Thus it is very unlikely to observe emission/absorption of gamma rays in this set-up as the source would have to be moving on the order of 10^4 cm/s for the Doppler energy to

cause significant overlap of the emission/absorption lines. This effect is shown in Figure 2.9 along with representative values for ^{57}Fe shown in Table 2.2, the most studied nucleus in Mössbauer spectroscopy and the nucleus studied in this dissertation.

Table 2.2 – Typical Mossbauer properties for a ^{57}Fe nucleus. Values from Drago, 1992.[88]

	E_γ (keV)	R (eV)	Linewidth (eV)	Linewidth (mm/s)	Lifetime of 1st excited state (ns)
^{57}Fe	14.4	$2 * 10^{-3}$	$4.7 * 10^{-9}$	0.097	140

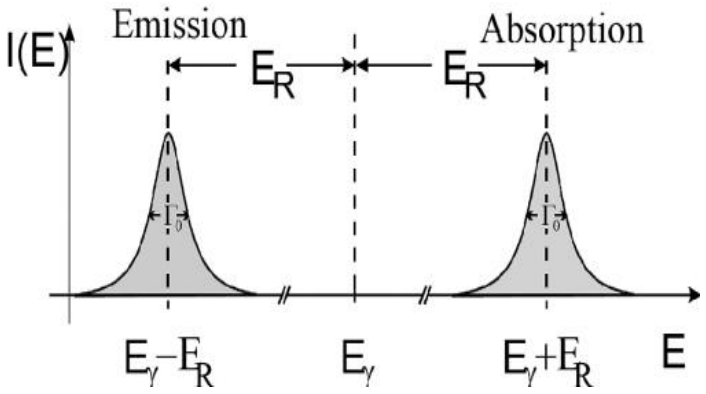

Figure 2.9 – Difference between emitted and absorbed gamma ray in a system with significant recoil energy change. Figure adapted with permission from Gütlich © 1992 Wiley VCH.[87]

However, if the source and sample are both solid materials, R decreases substantially as the mass considered in Equation 2.29 becomes the mass of the entire solid material rather than just the emitting/absorbing atom. Thus, nearly recoil-free emission/absorption is obtained and is termed the Mössbauer Effect. However, it should be noted that in some systems part of the recoil energy is converted into phonons which prevents nuclear resonance of the source and sample from occurring (most commonly a problem for molecular solids). However, for systems where emission/absorption of gamma-rays does not cause quantized lattice vibrations (termed zero-phonon processes) the Mössbauer effect is observable. The Lamb-Mössbauer factor f (or the elastic incoherent structure factor, EISF)[89,90] describes the occurrence of these zero-

phonon processes for a system and is used to define the system's ability to exhibit recoilless nuclear resonance absorption, and hence the Mössbauer effect.

2.3.2 Mössbauer Spectroscopy Experiments

For a Mössbauer experiment probing ^{57}Fe, a radioactive ^{57}Co source is utilized (270 day half-life) which decays by electron capture to the $I = 5/2$ excited state of ^{57}Fe (with I the nuclear spin angular momentum) that then decays within ≈ 10 ns to the $I = 3/2$ or $1/2$ state with 85% and 15% probability, respectively. Finally, the $I = 3/2$ state decays to the $I = 1/2$ state after 100 ns emitting a gamma-ray of 14.4 keV, which is then used to perform Mössbauer spectroscopy. This relatively long lifetime and reasonable transition energy are some of the key reasons (along with convenient production of the ^{57}Co source isotope with a practical lifetime) that have led to ^{57}Fe being the most studied Mössbauer nucleus, along with of course the accompanying interesting chemical properties, abundance, and utility of Fe-containing materials.

The Mössbauer source is accelerated through a range of velocities allowing for the emitted gamma-ray to probe a variety of nuclear energies in the sample. Typical values for an experimental setup are ± 11 mm/s corresponding to ± 530 neV away from the energy of the emitted gamma-ray. This energy range is on the order of the hyperfine interactions (≈ 10^{-8} eV) occurring for nuclear moments in electric and magnetic fields allowing for very sensitive detection of local chemical environments.[r] These interactions

[r]Note that, while NMR and Mössbauer spectroscopy both probe the nuclear spin, Mossbauer spectroscopy probes nuclear spin, I, transitions making it a much higher energy technique (10s of keV) *vs.* NMR (≈ 10^{-10} keV). However, the energy transitions probed in Mössbauer spectroscopy (e.g. the hyperfine interaction) are still quite small making Mössbauer spectroscopy a relatively low-resolution technique.

can be broken down into three parts arising from the electric monopole, electric quadrupole, and magnetic dipole.

2.3.2.1 The Electric Monopole Interaction

The electric monopole interaction originates from the Coulombic interaction between the charge density in the nucleus and surrounding electron density. Since *s* electrons are the only electrons with a finite probability of existing at the nucleus, they are the only ones that are included in this interaction. However, the *s* electron density can be influenced by other orbitals (*p* and *d*) as these orbitals tend to be closer to the nucleus (although not at the nucleus) so they are able to screen the nuclear charge from the outer *s* electrons. This interaction leads to a corresponding shift, termed the isomer shift.

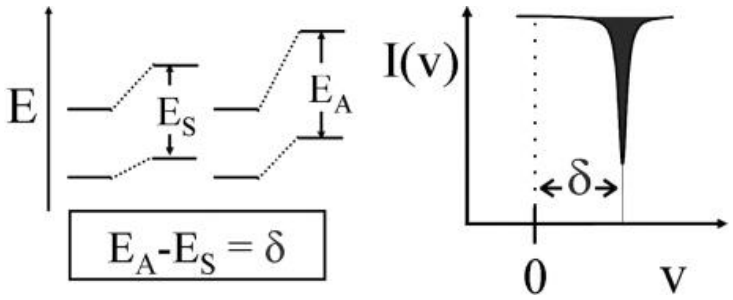

Figure 2.10 – Isomer shift caused by the difference in source and absorber (sample) electric monopole interactions resulting in a singlet signal (right). Figure adapted with permission from Gütlich © 1992 Wiley VCH.[87]

Since the source and sample will generally have different *s* electron densities, their electric monopole interactions will be different. This will lead to a shift in energy of the ground and excited state that is measured by the isomer shift, *δ*, as shown in Figure 2.10. Since *p* and *d* orbitals can screen the electron density (thereby changing the *s* electron density), the isomer shift is sensitive to the oxidation state, spin state, and

bonding properties (thereby degree of covalency and electronegativity of the surrounding ligands) of the nucleus.

2.3.2.2 The Electric Quadrupole Interaction

The previous example in Figure 2.10 shows a system with only two accessible states: the ground and excited state. However, if the system has a nuclear quadrupole moment (which occurs for nuclear spins with $I > 1/2$) and an inhomogeneous electric field at the nucleus (i.e., an EFG), the electric quadrupole interaction will split the states into $\pm m_I$ (the magnetic spin quantum number). Like quadrupolar interactions in NMR, as discussed in Section 2.2.4, this splitting occurs due to an EFG at the nucleus that causes the nuclear spin to precess about the EFG axis, thereby raising/lowering the substates' energy. This EFG can be described in the same manner as the EFG in NMR (see Equations 2.18 and 2.19). Figure 2.11 shows an example for an $I = 1/2$ nucleus (like ^{57}Fe) with the isomer shift at the average of the doublet. The energy splitting between these two substates is called the electric quadrupole splitting, ΔE_Q, and is defined as

$$\Delta E_Q = \frac{1}{2} e Q V_{ZZ} \left(1 + \frac{\eta^2}{3}\right)^{1/2} \qquad 2.31$$

where Q is the quadrupole moment, V_{ZZ} the largest principal component of the EFG tensor, and η the EFG asymmetry. ΔE_Q, in a system can give one information regarding the EFG that the nucleus experiences, which may arise due to non-cubic electron density at the nucleus caused by non-cubic valence electron distribution and/or non-cubic ligand field interactions. Thus, ΔE_Q can provide information regarding oxidation state, spin state, local symmetry, and coordination of the nucleus of interest.

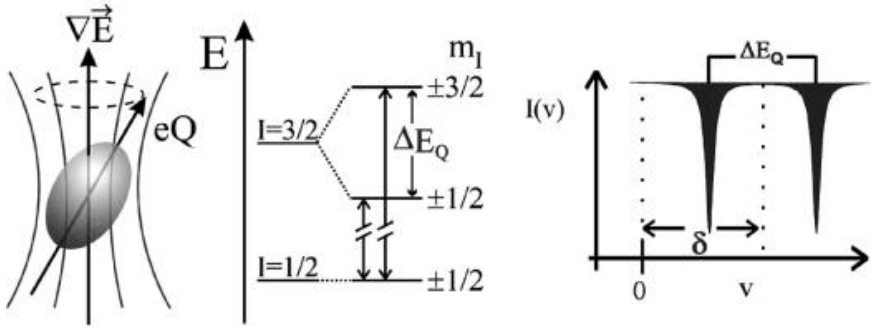

Figure 2.11 – Nuclear spin with a quadrupole moment precessing about the EFG axis (left) causing the $I = 3/2$ state to split into two substates, $m_I = \pm 1/2$ and $\pm 3/2$ (center) that has equal probability of being transitioned to and therefore equal intensity resulting in a doublet signal (right).Figure adapted with permission from Gütlich © 1992 Wiley VCH.[87]

2.3.2.3 The Magnetic Dipole Interaction

While the measurements performed in this dissertation were done at zero field as our in-house Mössbauer spectrometer is unable to apply a magnetic field, discussion of the magnetic dipole interaction is included here for completeness. While some degeneracy has been lifted in the previous example, each state is still doubly degenerate. However, if the states have $I > 1/2$, the $\pm m_I$ states can be split in the presence of a magnetic field (B, either applied or intrinsic) due to the nuclear Zeeman effect (also known as the magnetic dipole interaction). This can be viewed as the nuclear magnetic dipole moment (μ_I) precessing about the magnetic field (B) as shown in Figure 2.12. Thus for ^{57}Fe, the ground $I = 1/2$ state will split into two and the excited $I = 3/2$ state into four substates. However, the only allowed transitions due to the selection rules for magnetic dipoles are those with $\Delta I = \pm 1$ and $\Delta m_I = \pm 0,1$ so for ^{57}Fe there are only six allowed transitions resulting in a sextet pattern as shown in Figure 2.12. The isomer shift will always still lie at the average of the sextet pattern. The electric quadrupole interaction does not necessarily always occur when the magnetic dipole interaction is

present but if it does the energies of the substates will now be shifted by ΔE_Q depending on the direction of the EFG.

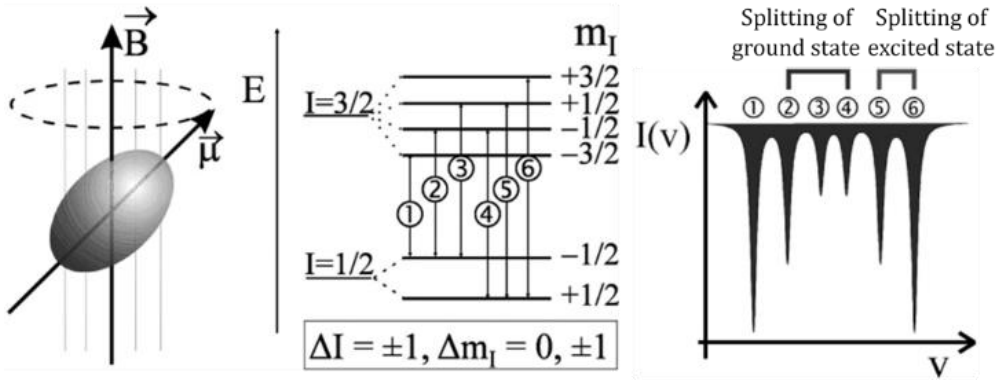

Figure 2.12 – Precession of the nuclear magnetic dipole moment about the magnetic field (left) causing the + and – m_I microstates to split (center). Due to the selection rules $\Delta I = \pm 1$ and $\Delta m_I = \pm 0{,}1$ there are only six allowed transitions resulting in a sextet (right) with unequal transition probability. Figure adapted with permission from Gütlich © 1992 Wiley VCH.[87]

The magnetic hyperfine splitting shown on the right in Figure 2.12 can be found by applying a known magnetic field in different directions. This enables one to determine the effective size and direction of the internal magnetic field at the nucleus, thereby determining the average electron distribution around the nucleus. This effective magnetic field can be composed of several components including the external applied field (B_{ext}), Fermi contact field (B_C, due to net spin up/down *s* electron density that occurs due to spin polarized valence electrons as in NMR, see Section 0), a spin-dipolar field (B_D, associated with electron spin angular momentum), and a field associated with the electron angular momentum (B_L) as shown below:

$$B_{\text{eff}} = B_{\text{ext}} + B_{\text{C}} + B_{\text{D}} + B_{\text{L}} \qquad 2.32$$

By carefully altering sample conditions including crystallite size (powder vs. single crystal), temperature, applied field and direction, along with including information from other complementary characterization techniques and computational

methods, the separate components of the internal magnetic field in a material can be elucidated to understand the various contributions to the magnetic moment.

2.4 Magnetometry

Cathode materials for LIBs and NIBs often contain paramagnetic *M* centers that undergo redox during electrochemical cycling. These redox state changes can affect several properties, including the material's magnetic response. Thus, magnetometry can be used to understand the redox processes occurring on charge and discharge, as used in Chapter 4 of this dissertation. Additionally, characterization of the paramagnetic behavior of a material is necessary to scale the computed NMR parameters as discussed in Section 2.5.3 to the experimentally relevant temperature. Some basic magnetic properties will be briefly discussed.[91,92]

The magnetization, *M*, of a material is the sum of all individual magnetic moments, μ, which can be normalized by volume, mass, or moles. Here, we are predominantly interested in the molar magnetization. The magnetic susceptibility of a material, χ, is then defined as the total magnetization over the applied field, *H*,

$$\chi = M/H \tag{2.33}$$

Thus, the magnetic susceptibility represents the tendency for a material to align with the magnetic field. All materials demonstrate a diamagnetic response to an applied field, exhibiting a χ that is small and negative—i.e., the material repels the applied field. However, this contribution to the susceptibility is often nearly negligible in systems with unpaired electrons, but should be included in the analysis for optimal results.

In a paramagnetic material, χ is often relatively large and positive as the unpaired electrons in these sytems tend to align with the external magnetic field. The majority of the materials studied in this dissertation are paramagnetic at room temperature, although they may exhibit more complex magnetic phenomena at lower temperatures which is largely outside the scope of this dissertation. Briefly, spins that tend to align parallel to each other and to the applied magnetic field are considered ferromagnetic ($\chi \gg 0$), whereas spins that align antiparallel to one another are considered to be antiferromagnetic ($\chi \ll 0$). The magnetic susceptibility of a paramagnetic material is well described by the Curie-Weiss Law[s] given as

$$\chi = \frac{C}{T-\Theta} + \chi_{\text{dia}} \qquad 2.34$$

where χ_{dia} is the temperature-independent diamagnetic contribution to the susceptibility (defined by Pascal's constants, tabulated for several compounds and elements in ref. [93]), T is the temperature, C is the Curie constant (units emu K mol^{-1}), and Θ is the Weiss constant (units K) with $\Theta > 0$ corresponding to a ferromagnetic material and $\Theta < 0$ an antiferromagnetic material below the ordering temperature (these materials order at the Curie or Néel temperature, T_{C} or T_{N}, for ferromagnetic or antiferromagnetic materials, respectively). To determine the Curie and Weiss constants a plot of $\frac{1}{\chi-\chi_{dia}}$ *vs.* temperature can be fitted with the intercept corresponding to $-\Theta/C$ and the slope $1/C$. Note that only the linear (high temperature) region of the $\frac{1}{\chi-\chi_{dia}}$ vs. T data should be fitted as any region below that is outside of the paramagnetic-regime.

[s]Curie's Law describes paramagnetism in non-interacting spin systems. The materials studied in this dissertation contain many interacting moments near each other and therefore are better described by Curie-Weiss' Law.

Once the Curie constant, C, is known, the effective magnetic moment, μ_{eff} (units of Bohr magneton, μ_{B}), can be calculated as

$$\mu_{\text{eff}} = \sqrt{8C} \tag{2.35}$$

This value can then be compared to the the spin-only magnetic moment, μ_{SO}, given as

$$\mu_{\text{SO}} = 2\sqrt{S(S+1)} \tag{2.36}$$

where S is the spin quantum number. Note that this equation is valid only when spin-orbit coupling[t] is small and/or quenched, as is the case for most 3*d Ms*.

Magnetic susceptibility data is typically taken at a set field against temperature either in zero-field cooled (ZFC) or field-cooled (FC) manner, with the former corresponding to cooling of the sample down to near 0 K (typically ≈ 2 K) without a field and the latter cooling in an applied field. Any differences between the two measurements can be indicative of magnetic hysteresis present, although this is not studied in this dissertation. The resulting data can then be fit as described above.

2.5 Computational Methods

First-principles calculations are an invaluable complement to experimental characterization as they provide a rigorous basis for expected properties and trends one may observe experimentally. In this dissertation, calculations were used for several applications: 1) thermodynamic stability assessment of the NaF-FeF_2-FeF_3 phase space and for (de)intercalation of $Na_2Fe_2F_7$, and 2) prediction of ^{23}Na and ^{19}F NMR parameters.

[t] Meaning, the interaction between an electron spin's angular momentum and its orbital angular momentum.

The theoretical background of these first-principles calculations will be briefly reviewed and then each of these topics will be discussed. However, the latter calculations were performed by a collaborator and so the methodology will not be thoroughly described, and rather this discussion will focus on analysis of the resulting computational output.

2.5.1 Theoretical Background – Density Functional Theory

The energy of a system can be calculated using the time-independent, nonrelativistic Schrödinger equation:[94]

$$\widehat{H}|\psi\rangle = E|\psi\rangle \tag{2.37}$$

where $\widehat{H}$ is the Hamiltonian operator, $|\psi\rangle$ the state vector, and E containing the energy eigenvalues. For a simple system, like a H_2 molecule, the Schrödinger equation can be solved completely. However, for more complex systems, like the crystals studied in this dissertation, this equation quickly becomes intractable.

Fortunately, several approximations simplify the problem and allow for the Schrödinger equation to be applied to larger systems. First, the Born-Oppenheimer approximation[95] states that, due to the size and speed of electrons compared to atomic nuclei, the electrons can be treated dynamically while the nuclei are treated statically. Hohenberg and Kohn[96] then showed that the ground state of a system (the lowest energy state) is a unique functional of the electron density, $\rho(\vec{r})$, and that the electron density that minimizes the energy is the ground state electron density. The treatment of individual electrons as a total electron density thus greatly reduces the complexity and leads to the name "density functional theory" (DFT). Finally, Kohn and Sham[97] showed that the charge density of interacting electrons could be replaced with a charge density

of non-interacting electrons, thus allowing the many-body Schrödinger equation to be recast as a set of single-electron equations. Combined with splitting the Hamiltonian into four contributions, the Schrödinger equation (in this form referred to as the Kohn-Sham equations) is now:

$$[T_S[\rho(\vec{r})] + V_{Nn}[\rho(\vec{r})] + V_H[\rho(\vec{r})] + V_{XC}[\rho(\vec{r})]]\psi_i(\vec{r}) = E_i\psi_i(\vec{r}), \qquad 2.38$$

with $T_S[\rho(\vec{r})]$ the electron kinetic energy, $V_{Nn}[\rho(\vec{r})]$ the electron-nuclei interaction potential energy, $V_H[\rho(\vec{r})]$ the electron-electron potential energy (known as the Hartree potential), and $V_{XC}[\rho(\vec{r})]$ the exchange-correlation correction. Thus, the Kohn-Sham equation solutions, and therefore ground state electron density, can be found by solving a set of equations each containing a single electron. However, while the three leading terms can be solved exactly, a precise description of the electron exchange-correlation is not yet known. Several approximations of electron exchange-correlation have been proposed, such as the generalized gradient approximation (GGA), which has been used in this dissertation. In GGA, both the local electron density and gradient of the local electron density are used to calculate V_{XC}.[98]

2.5.1.1 Approximating Electron Exchange and Correlation

The GGA functional uses a plane-wave basis set which leads to a delocalization of the valence and core electron states over the entire crystal. Thus, GGA poorly describes the localized valence states of *M*s and must be corrected to provide realistic results. Two corrections are employed in this work. The first correction is known as DFT+*U*[99–101] where the electron self-interaction error is accounted for by adding a parameter, *U*, that acts as an energy penalty for *d* electron delocalization, while all remaining valence electrons are treating using standard DFT. The *U* in DFT+*U* includes both the Hubbard *U*

Coulombic energy penalty for spin-pairing and Hund's rule requirement that all degenerate orbitals must be singly occupied before being doubly occupied. Typically, U is obtained semi-empirically and has been shown to be successfully applied in the study of battery materials' properties.[102,103] The second correction combines DFT with Hartree-Fock theory, which states that the potential experienced by the electrons is equal to the nuclear potential and an electronic potential that contains a self-interaction term. Thus Hartree-Fock functionals better represent electron self-interaction but poorly represent electron correlation, leading to overrepresentation of electron localization. Thus, a combination of both DFT and Hartree-Fock in what is called a "hybrid functional" can lead to a more appropriate representation of both electron exchange and correlation.[104,105] However, hybrid functionals are more computational expensive than DFT+U.

2.5.1.2 Calculating Periodic Structures with VASP

Electrons in crystalline materials occupy bands which contain contributions from all atoms (though it is noted some atoms may have negligible contributions). To describe such states and conserve lattice periodicity, one can construct Bloch waves:

$$\psi(\vec{r}) = e^{-i\vec{k}\cdot\vec{r}}u(\vec{r}), \tag{2.39}$$

where k is the wave vector and $u(\vec{r})$ is a function with the same periodicity as the lattice. The density and energy of these waves are computationally restricted by the k-point mesh and basis set energy cutoff, respectively. However, calculating wavefunctions for all electrons is computationally prohibitive and thus only the valence electrons are calculated using this method while the core electrons are treated as a pseudopotential. The pseudopotential is designed to mimic the potential experienced by the valence

electrons due to the core electrons and nucleus. The *k*-point density, energy cutoff, and pseudopotentials, as well as other computational parameters, are specified when relevant as these parameters can have significant implications on the results.

We used the Vienna Ab Initio Simulation Package (VASP)[106,107] for DFT+*U* calculations. VASP uses an iterative approach of first making a guess at the electron density, solving the Kohn-Sham equations to find the wavefunctions, and then using the wavefunctions to calculate a new electron density. If the initial and final electron densities (and therefore total energies) are within a set convergence criteria (i.e., specified differences in the energy and ionic forces of the system) then a minimum energy state and minimum energy geometry have been found. Otherwise, the process is repeated until the convergence criteria are met.

2.5.2 DFT Calculations of Formation Energies & Voltages

The total energy calculated within VASP for a given unit cell does not provide much meaning at first. However, comparison of total DFT energies (in units of eV/f.u.) for atomic arrangements containing the same number and identity of atoms per formula unit (f.u.) enables determination of what given arrangement(s) is most stable, However, to assess stability compared to competing phases, the formation energy must be calculated from the DFT energy. Typically, formation energy is defined as the energy evolved or absorbed during the formation of one mole of a compound formed from its constituent elements.[u] However, within DFT, any two or more reference compounds that

[u] The constituent elements can still be used to calculate formation energies based on DFT computed energies. However, this is not pursued here due to the difficulty of calculating $F_{2(g)}$.

span the compositional range of interest can be used to calculate a series of relative formation energies for compounds in that range.

This method has been used in this dissertation to a) assess the thermodynamic stability in the NaF-FeF_2-FeF_3 compositional space and b) understand the Na (de)intercalation behavior of a given intercalation material, $Na_xM_2X_7$, upon Na (de)intercalation from Fe_2F_7 to $Na_yFe_2F_7$ ($y \geq x$). The formation energy of a given compound in each case can be calculated as

$$E_f(\mathrm{Na}_a\mathrm{Fe^{II}}_b\mathrm{Fe^{III}_c F}_d) = E(\mathrm{Na}_a\mathrm{Fe^{II}}_b\mathrm{Fe^{III}_c F}_d) - aE(\mathrm{NaF}) - bE(\mathrm{FeF_2}) - cE(\mathrm{FeF_3}) \quad 2.40$$

and

$$E_f(\mathrm{Na}_x\mathrm{Fe_2F_7}) = E(\mathrm{Na}_x\mathrm{Fe_2F_7}) - \left(\frac{x}{y}\right)E\left(\mathrm{Na}_y\mathrm{Fe_2F_7}\right) - \left(1 - \frac{x}{y}\right)E(\mathrm{Fe_2F_7}), \quad 2.41$$

respectively, where E refers to DFT energy and E_f is the formation energy, both in units of eV/f.u. In equation 2.40, $d = a + 2b + 3c$. A plot of formation energy *vs.* composition for case (b) is shown in Figure 2.13, where a negative formation energy indicates that the compound is stable against phase separation into the reference compounds. By comparing this series of formation energies, one can deduce the lowest energy structures across the compositional range. These low-energy structures and the two-phase regions between two adjacent minima form the convex hull (or thermodynamic minimum) across the compositional range. Structures that are $\leq$ 30 meV/atom[v] above the hull are typically considered metastable.

[v] This value is chosen as thermal fluctuations (i.e., k_BT) at room temperature are on the order of 30 meV/atom.

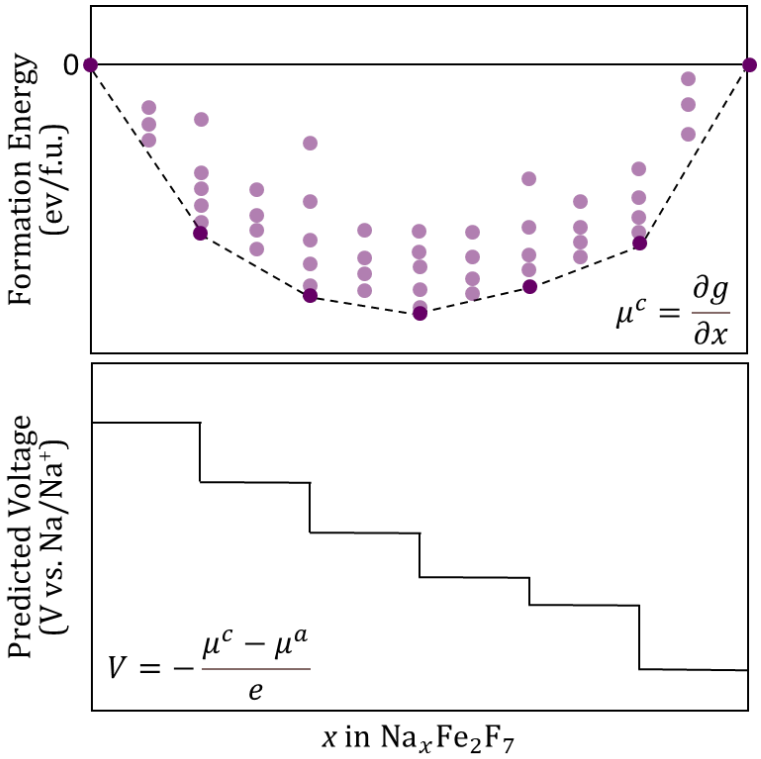

Figure 2.13 – Plots showing relation between predicted formation energy and voltage as outlined for case (b) in the text. The convex hull (top, dashed line) has been plotted for the lowest energy structures.

Thermodynamic stability can be additionally understood as the decomposition energy (E_d), or the energy evolved upon decomposition of a given compound A defined as:

$$E_d^A = E(\text{decomposition products}) - E^A \qquad 2.42$$

This analysis relies on determining all possible decomposition reaction pathways with the pathway that results in the most negative E_d being the thermodynamically favored pathway. Compounds that form the convex hull for a given phase space (e.g., the NaF-FeF_2-FeF_3 compositional space described for case (a) above) should give $E_d \geq 0$ while compounds above the convex hull have $E_d \leq 0$.

In case (b) described above, it can be useful to further analyze this data to understand whether the calculated energy landscape accurately captures the observed

experimental behavior. This can be done by converting the DFT energies (E) of the computed ground state structures to a voltage. The derivation of the relationship between voltage and chemical potential is shown elsewhere[8] and results in the final relationship of

$$V = \frac{\eta^c - \eta^a}{e} = -\frac{\mu^c - \mu^a}{e} \quad 2.43$$

where η is the electrochemical potential (i.e., chemical potential in the presence of an applied potential), μ is the chemical potential (defined below), e is the charge of an electron,[w] and n is the charge transferred (for Na^+, $n = 1$) with the superscripts of c and a denoting the cathode and anode, respectively. The cathode chemical potential, μ_c, can be approximated as the set of slopes along the convex hull resulting in

$$\mu^c = \frac{\partial g}{\partial x} = \frac{E(\mathrm{Na}_{X_1}\mathrm{Fe_2F_7}) - E(\mathrm{Na}_{X_2}\mathrm{Fe_2F_7})}{(X_1 - X_2)} \quad 2.44$$

where $X_1 < X_2$. As most electrochemical tests are performed using an anode of Na metal,[x] μ^a can be treated as the DFT energy of Na metal (eV/f.u.). The relationship between formation energy and calculated voltage is summarized in Figure 2.13.

2.5.3 First Principles Calculations of NMR Parameters

As described, DFT uses single-electron wavefunctions—represented by plane waves—generated from several potential terms to approximate the total wavefunction of the system. While plane-wave DFT does a relatively good job at predicting structures and bonding, and at assessing the total energy of a system—because those properties

[w] When the DFT energies used are in units of electronvolts (eV), e is already included.

[x] This is because the composition and chemical potential of Na does not change during cycling.

depend on the valence electronic states—it fails to provide accurate predictions of spectroscopic properties that depend on core electron states as the core electronic states are represented by only a pseudopotential, thereby losing orbital specificity. Thus for NMR calculations, as we are interested in the core electron states of our nucleus and how spin density is transferred from paramagnetic *M*s to our nucleus of interest, a different wavefunction representation must be used. *s* orbitals, the only orbitals present at the nuclear position, has a form best approximated by a Slater determinant ($e^{-\xi r}$). However, these are computationally expensive so a linear combination of Gaussian-type ($e^{-\alpha r^2}$) orbitals are used instead.

This orbital description scheme is done here using CRYSTAL which represents all electrons (both core and valence) using a linear combination of Gaussian-type orbitals. These calculations rely on a combination of both DFT and Hartree-Fock functionals to better represent electron exchange and correlation, as a U value cannot be readily included in the calculations. Specifically, 20% and 35% Hartree-Fock (with the remainder being DFT) —known has H20 and H35, respectively—was used, as these levels of theory have previously been shown to provide adequate lower and upper bounds to the shifts, respectively.[60,61,63] Thus, both H20 and H35 CRYSTAL calculations were performed in this thesis to determine the ^{23}Na and ^{19}F NMR parameters. Using the output spin densities at the nuclear positions ($|\psi(r_n)|^2$) and electric field gradient tensor, the hyperfine and quadrupolar parameters, respectively could be calculated.

As described in Section 0, the Fermi Contact shift, δ_{FC}, is represented by:

$$\delta_{\mathrm{FC}} = \frac{10^6 \mu_o \mu_{\mathrm{B}} g_{\mathrm{e}} \gamma_I}{3\hbar\omega_0} \phi |\psi(r_n)|^2 \qquad 2.45$$

with $|\psi(r_n)|^2$ output from the CRYSTAL calculation when all spins are ferromagnetically aligned[y]. ϕ represents the magnetic scaling parameter applied to the computed shifts to scale the magnetic state of the system to the temperature of the NMR experiment where:

$$\phi(T) = \frac{B_0 \mu_{\mathrm{eff}}^2}{3k_{\mathrm{B}} g_{\mathrm{e}} \mu_{\mathrm{B}} S(T-\Theta)} \qquad 2.46$$

with χ_m the magnetic susceptibility, S the average spin per transition metal site, and μ_{eff} the experimentally determined effective magnetic moment.

The electron-nuclear dipolar tensor, in ppm, is described as:

$$\delta_{ij} = -\frac{10^6 \mu_o \mu_{\mathrm{B}} g_e \gamma_I}{8\pi\hbar\omega_0} \phi \sum_{\kappa\tau} \sum_{\boldsymbol{G}} P_{\kappa\tau G}^{\alpha-\beta} \int \varphi_\kappa(\boldsymbol{r}) \frac{r^2 \Delta_{ij} - 3 r_i r_j}{r^5} \varphi_\tau^G(\boldsymbol{r}) d\boldsymbol{r} \qquad 2.47$$

where i and j label Cartesian components, κ and τ atomic orbitals, $\boldsymbol{G}$, the set of lattice vectors, $\boldsymbol{r}$ a position vector originating at the nucleus of interest, $P_{\kappa\tau G}^{\alpha-\beta}$ the real space unpaired electron density matrix, $\varphi_\kappa(\boldsymbol{r})$ an orbital in the reference cell ($\boldsymbol{G} = \boldsymbol{0}$), $\varphi_\tau^G(\boldsymbol{r})$ an orbital in the cell originating at lattice vector $\boldsymbol{G}$, and Δ_{ij} the Kronecker delta. By diagonalizing the tensor, as performed in the CRYSTAL calculation, the principal components δ_{kk} are achieved such that $|\delta_{ZZ}| \geq |\delta_{XX}| \geq |\delta_{YY}|$. The dipolar anisotropy (Δ_δ), in ppm, and the dipolar asymmetry (η) are then given, respectively, as

$$\Delta_\delta = \delta_{ZZ} - \frac{1}{2}(\delta_{XX} + \delta_{YY}) \qquad 2.48$$

and

[y] While this is not the true ground state in most materials, it is a good approximation as most electrons will tend to align with the applied magnetic field used in NMR.

$$\eta = \left|\frac{\delta_{XX}-\delta_{YY}}{\delta_{ZZ}}\right|. \quad 2.49$$

The quadrupolar parameters are evaluated from the ground state electric field gradient (EFG) tensor, $\boldsymbol{V}$, calculated by the CRYSTAL calculation. These parameters have been previously described in Section 2.2.4, and will be briefly summarized here for completeness. The quadrupole coupling constant (C_{Q}), in MHz, and the quadrupolar asymmetry parameter (η_{Q}) are given as

$$C_{\mathrm{Q}} = \frac{e^2qQ}{\hbar} = \frac{eQ}{h}V_{ZZ} \quad 2.50$$

and

$$\eta_{\mathrm{Q}} = \frac{V_{XX}-V_{YY}}{V_{ZZ}}, \quad 2.51$$

respectively, with V_{ii} the principal components of the EFG tensor with $|V_{ZZ}| \geq |V_{XX}| \geq |V_{YY}|$. The second-order quadrupolar shift, in ppm, is then:

$$\delta_{\mathrm{QIS}} = -\frac{1*10^6}{30}\frac{3}{\nu_0}\left(\frac{3C_{\mathrm{Q}}}{2I(2I-1)}\right)^2\left(\frac{1+\eta_{\mathrm{Q}}^2/3}{\nu_0}\right) \quad 2.52$$

with $\nu_0 = \omega_0/2\pi$.

Chapter 3 – $^{19}F/^{7}Li$ NMR Study of Disordered Rocksalt Oxyfluorides

Li-excess disordered rocksalt (DRX) oxyfluoride materials are a promising new Li-ion cathode class exhibiting rich structural and compositional playgrounds. However, their disordered nature complicates structural characterization, necessitating complementary nuclear-specific local characterization techniques. Here, I highlight my ^{7}Li and ^{19}F NMR characterization contributions to five DRX studies[108–112] performed in collaboration with a team of researchers on these DRX materials. Through this work we can better understand the incorporation of Li and F in diamagnetic- vs. paramagnetic-like environments and begin to understand the role of short-range ordering in DRX materials.

3.1 Introduction

Li-excess cation-disordered rocksalt (DRX) oxyfluorides cathodes have recently emerged as high energy density Li-ion cathode materials with reversible capacities > 300 mAh/g and energy densities near 1000 Wh/kg.[108,111,113] These materials retain the same close-packed rocksalt framework as layered LiMO$_2$, but now exhibit cation disordering (structure comparison shown in Figure 3.1a), as well as anion disordering when fluorine is incorporated. In contrast to ordered layered rocksalts where only Ni and Co metals can be redox active, the disordered rocksalt structure allows a broad array of transition metals to be utilized, such as Fe, Mn, Cr, and V, enabling sustainable, high energy density cathodes. Typically, these materials take on the formula of $Li_{1+x}M_{1-x-y}M'_yO_{2-z}F_z$, where x denotes the amount of Li excess, y the d^0 element content, and z the fluorination level in the DRX material. The impact of these three compositional variables will be briefly summarized.

3.1.1 d^0 Incorporation

DRX materials are inherently metastable due to the significant cation size differences between Li (r = 0.76 Å) and commonly used transition metals (r ranging from 0.6 to 0.8 Å). Rather than being segregated to separate layers (as occurs for layered LiMO$_2$), these cations now occupy a variety of randomly distributed, distorted octahedral sites within the rocksalt structure. The distortion of transition metal octahedra introduces energy penalties that can be predicted from their d shell filling and has been shown to directly govern the propensity of a given Li-M-O to disorder.[114] The energetic cost to disorder can be partially mitigated through incorporation of a d^0

element, which can buffer octahedral distortions due to its empty *d* shell that renders it largely insensitive to site distortions. Many different d^0 elements have been incorporated in DRX materials including Ti^{4+}, Zr^{4+}, V^{5+}, Nb^{5+}, and Mo^{6+}.[115–118] Ji *et al.* showed through DFT cluster expansions that, in general, d^0 elements with smaller ionic radii favor Li segregation into Li-rich clusters, which leads to more favorable Li percolation properties.[119] Regardless, the metastability of these materials necessitates energy and time-intensive synthesis methods, often requiring long high temperature anneals or mechanochemical syntheses, although recent developments in microwave synthesis have shown promise.[120] The impact of DRX metastability on the electrochemical performance will be explored in Section 3.3.2 of this chapter.

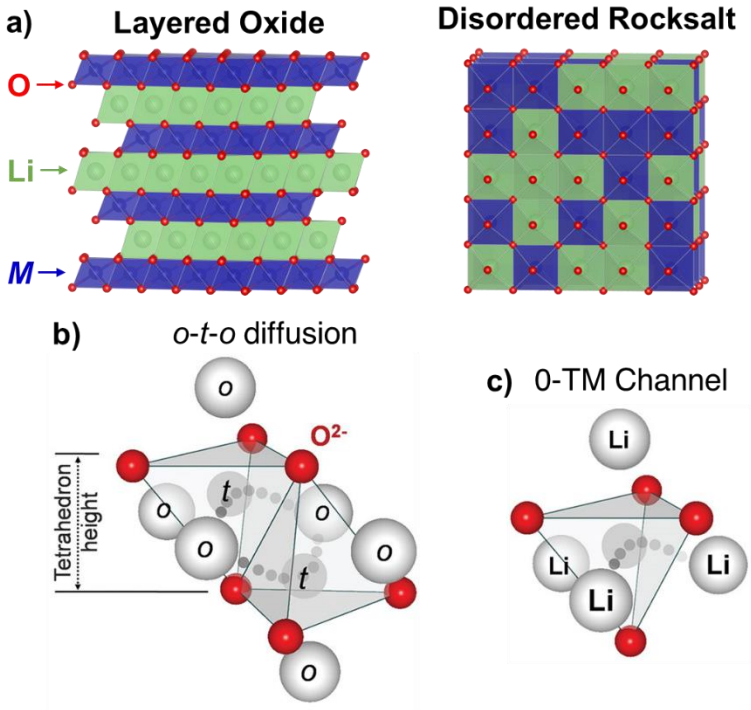

Figure 3.1 – a) Comparison between layered oxide (left) and disordered rocksalt (right) structures. **b)** Schematic of o-t-o diffusion path where two tetrahedral paths connect each pair of neighboring octahedral sites. **c)** 0-TM channel where the intermediate tetrahedral state shares no faces with octahedral transition metals. **b,c** from Lee et al.[116] Reprinted with permission from AAAS.

3.1.2 Li-Excess in Disordered Rocksalts

In traditional layered oxide materials, two-dimensional Li diffusion readily occurs throughout the Li-plane. However, upon disordering, this long-range Li diffusion is disrupted. Thus, to enable long-range Li diffusion, Li-excess is required to create a three-dimensional percolation network. In layered oxides and DRX materials, Li diffusion locally occurs between two Li octahedral sites through an intermediate tetrahedral site, a phenomenon referred to as *o-t-o* diffusion (Figure 3.1b),[121] where the migration barrier to move through an intermediate tetrahedral site is dependent on the tetrahedron height. In layered oxides, this tetrahedron height is quite large as it is roughly equivalent to the Li layer height and thus, Li ions can diffuse through tetrahedra that face-share with one transition metal (termed a 1-TM (transition metal) channel). However, in DRX materials these tetrahedra are much smaller and thus, Li diffusion only readily occurs through 0-TM channels (Figure 3.1c), where now the tetrahedra does not face share with any transition metals, due to the large energy barrier introduced by even a single transition metal.[116,122] As these sites infrequently occur in stoichiometric DRX materials, Li-excess is required to increase the proportion of Li-rich 0-TM channels and create a percolating three-dimensional network. Using Monte Carlo Percolation Simulations, Urban *et al.* showed that ≈ 15% Li-excess is required to create a 0-TM percolation network.[122] However, as will be explored in section 3.3.4 of this chapter, a spinel-like cation order can improve the Li^+ percolation properties in disordered materials due to the presence of 0-TM sites in the ordered spinel structure.[116,122]

3.1.3 Fluorination in Disordered Rocksalts

Unlike traditional layered oxides, DRX materials can incorporate fluorine due to the presence of lithium-rich environments in the disordered structure, thus preventing the formation of high energy fluorine-transition metal bonds, which prevents fluorination of layered oxides.[123] Through fluorination, the average transition metal valence state can be reduced, thereby increasing the redox reservoir, which has enabled a decreased dependence on irreversible oxygen redox.[27,28,124]. However, as will be explored in Section 3.3.4.1, fluorination can lead to somewhat limited Li extraction due to a "Li-gettering" phenomenon where F ions trap some of its coordinating Li ions to avoid forming high-energy undercoordinated states.[109] Thus, the extent that fluorination affects the cation long- and short-range order is unclear and thereby the electrochemical performance of DRX materials, especially considering the necessity of locally Li-rich environments for F incorporation

3.1.4 Outlook

DRX materials present a promising method to increase the energy density of Li-ion cathodes, but their structural and compositional complexity requires thorough characterization for practical realization. Thus, we have worked in collaboration with a team of researchers to better understand several DRX compounds. Specifically, due to the difficulty in differentiating oxygen and fluorine in most characterization techniques, we have utilized ssNMR to gain an understanding of the ^{19}F and ^{7}Li local environments. Here, I highlight my contributions to five DRX-related studies[108–112] with additional results from collaborators included where necessary to complement the information

obtained via ssNMR. All work besides the $^{7}Li/^{19}F$ NMR was performed by collaborators. However, the reader is directed to the published articles for full details. These studies can be categorized into three categories: high-entropy DRX,[108] traditional DRX,[109,110] and partially-ordered spinel-like DRX,[111,112] which exhibit increasing degrees of short-range ordering. Overall, we find that short-range ordering has a significant effect on the electrochemical performance of DRX materials and can impact the performance in both a positive and negative manner depending on its extent.

3.2 Experimental

In the second study to be discussed,[109] a Bruker Avance 500 MHZ (11.7 T) wide-bore NMR spectrometer with Larmor frequencies of −470.6 and −194.4 MHz was used to collect ssNMR data. However, in the all other studies,[108,110–112] a Bruker Avance 300 MHz (7.05 T) wide-bore NMR spectrometer with Larmor frequencies of 282.40 and 116.64 MHz was used to minimize the strength of the paramagnetic interactions. In all cases, measurements were performed at room temperature.

The data were obtained using 60 kHz[108,109,111] or 50 kHz[110] magic-angle spinning (MAS) with a 1.3 mm double-resonance probe or 30 kHz[112] MAS with a 2.5-mm double-resonance HX probe. The slower speeds were utilized due to unstable spinning at 60 kHz or to increase the sample volume and thereby signal intensity, respectively. ^{19}F and ^{7}Li NMR data were referenced against either lithium fluoride (LiF, $\delta(^{19}F)$ = −204 ppm and $\delta(^{7}Li)$ = −1 ppm) or 1M aqueous solutions of sodium fluoride (NaF, $d(^{19}F)$ = −118 ppm) and lithium chloride (LiCl, $d(^{7}Li)$ = 0 ppm). These samples were also used for pulse

calibration. Lineshape analysis was carried out within the Bruker Topspin software using the SOLA lineshape simulation package.

The resonant frequency range of ^{19}F nuclei in the DRX cathode materials studied here using a 300 MHz spectrometer was larger than the excitation bandwidth of the radiofrequency pulse used in the NMR experiment. To obtain the full spectrum, 6 to 11 spin echo spectra were collected using frequency steps between 140 ppm (73.95 kHz) to 300 ppm (84.73 kHz) across several thousand ppm, where the step size was slightly lower than the excitation bandwidth of the radiofrequency pulse. Individual sub-spectra were processed using a zero-order phase correction and then added to give an overall sum spectrum in absorption mode that required no further phase correction. Individual ^{19}F spin echo spectra were collected using a 90° and a 180° radiofrequency pulse calibrated for each set of experiments. The 90° pulses ranged from 1.95 μs at 190 W to 5.2 μs at 100 W with the 180° pulses being two times that calibrated for the 90° pulse. The measurements performed on the 500 MHz spectrometer did not require frequency stepping as the excitation bandwidth of the radiofrequency pulse was sufficiently broad (we note that this was mainly a hardware limitation). Thus, for the experiments performed on the 500 MHz, the ^{19}F spin echo spectra[109] were collected using a 90° pulse of 1 μs and 180° pulse of 2 μs at 76.3 W and a ^{19}F pj-MATPASS spectra was able to be obtained which used the same 90° pulse. Recycle delays were calibrated for each sample to ensure full relaxation of the ^{19}F paramagnetic and diamagnetic signals. In cases where relaxation of the ^{19}F diamagnetic signal was longer than 100 ms, an additional spin echo spectrum was obtained using a recycle delay optimized for the ^{19}F paramagnetic signals

to ensure a high signal to noise ratio spectrum was obtained. Additionally, ^{19}F LiF reference spin echo spectra were obtained using a recycle delay between 5 to 30 s.

^{7}Li spin echo spectra were collected using a 90° and a 180° radiofrequency pulse calibrated for each set of experiments. The 90° pulses ranged from 0.43 μs at 300 W to 0.7 μs at 100 W with the 180° pulses being two times that calibrated for the 90° pulse. pj-MATPASS spectra were also collected on all samples using the same 90° pulse length. Recycle delays were calibrated for each sample to ensure full relaxation of the ^{7}Li paramagnetic and diamagnetic signals for quantification purposes. In cases where relaxation of the ^{7}Li diamagnetic signal was longer than 1 s, an additional spin echo spectrum was obtained using a recycle delay optimized for the ^{7}Li paramagnetic signals to ensure a high signal to noise ratio spectrum was obtained. pj-MATPASS spectra were also collected using a recycle delay optimized for the ^{7}Li paramagnetic signal as these spectra were mainly used to understand the nature of the ^{7}Li paramagnetic environments. Additionally, ^{7}Li LiF reference spin echo spectra were obtained using a recycle delay between 14 to 30 s. Fits of the ^{7}Li spin echo spectra were performed using a minimum number of components (at least one diamagnetic and paramagnetic component) to prevent overfitting of the broad spectra.

3.3 Results & Discussion

3.3.1 Suppression of Short-Range Ordering via High-Entropy DRX[z]

High-entropy materials have been pursued in a number of fields, initially as multi principal element alloys,[125,126] where several unique elements are combined to create new single-phase materials. These materials are believed to exhibit large configurational entropy that enhances the solubility of the individual components, which can be used to optimize target properties. Here, the goal of creating high-entropy DRX materials was to suppress short-range ordering, thereby improving the overall Li transport properties, as several prior studies have linked certain kinds of short-range ordering with reduced Li percolation compared to a random arrangement of cation species.[28,119,122,127,128] This work is the result of a collaboration with Prof. Gerd Ceder's group at the University of California Berkeley (UCB) and Lawrence Berkely National Laboratory (LBNL). Dr. Zhengyan Lun synthesized the materials, performed the X-ray diffraction, and prepared and tested the electrochemical cells. Dr. Deok-Hwang Kwon acquired and analyzed the TEM data. I acquired and analyzed the NMR data.

Three compositions with increasing numbers of transition metal species, but constant Li-excess and F-doping, were prepared via solid-state synthesis: $Li_{1.3}Mn^{3+}_{0.4}Ti_{0.3}O_{1.7}F_{0.3}$ (TM2), $Li_{1.3}Mn^{2+}_{0.2}Mn^{3+}_{0.2}Ti_{0.1}Nb_{0.2}O_{1.7}F_{0.3}$ (TM4), and $Li_{1.3}Mn^{2+}_{0.1}Co^{2+}_{0.1}Mn^{3+}_{0.1}Cr^{3+}_{0.1}Ti_{0.1}Nb_{0.2}\ O_{1.7}F_{0.3}$ (TM6). These materials were

[z]The contents of this section have substantially appeared in reference [110]: Z. Lun, B. Ouyang, D.H. Kwon, Y. Ha, **E.E. Foley**, T.Y. Huang, Z. Cai, H. Kim, M. Balasubramanian, Y. Sun, J. Huang, Y. Tian, H. Kim, B.D. McCloskey, W. Yang, R.J. Clément, H. Ji, and G. Ceder, "Cation-disordered rocksalt-type high-entropy cathodes for Li-ion batteries", *Nat. Mater.* **20** (2021) 214-221. doi: 10.1038/s41563-020-00816-0

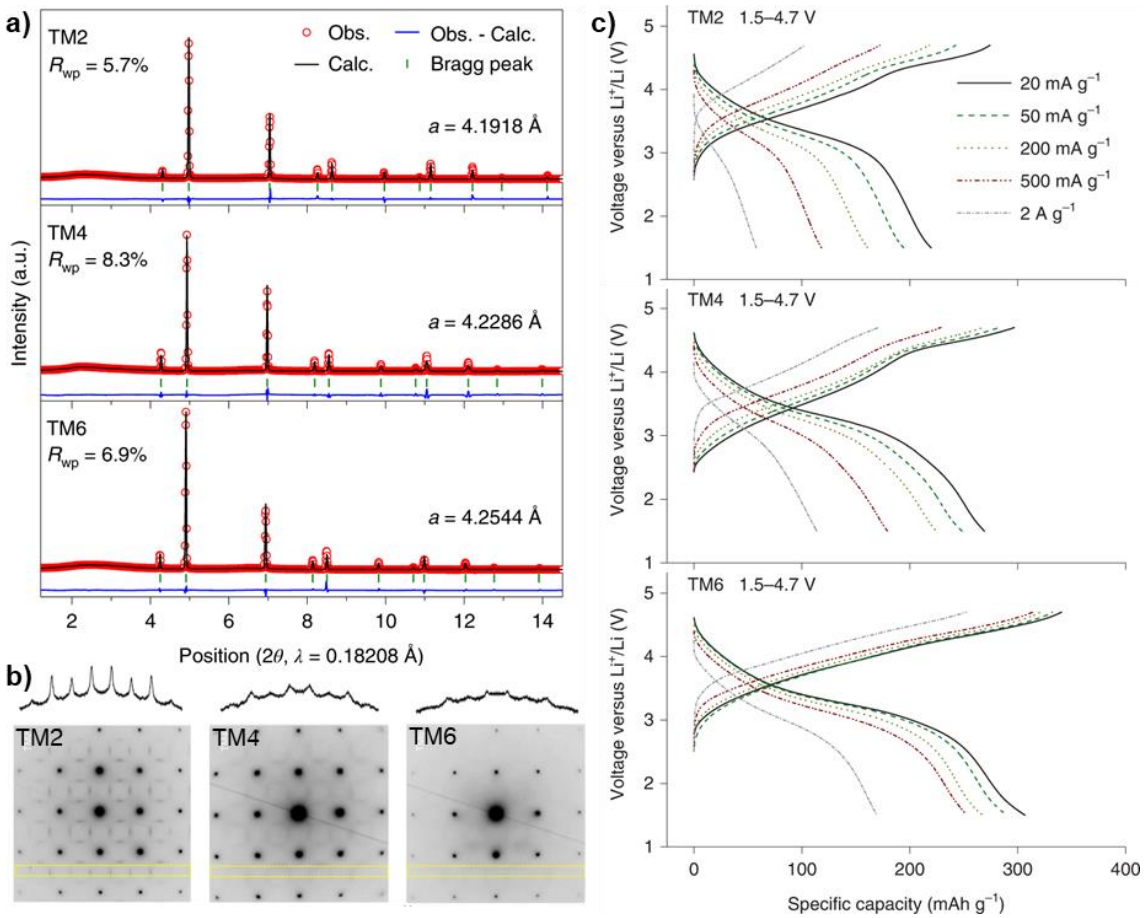

Figure 3.2 – High-entropy effect on structure & electrochemistry in DRX. a) SXRD patterns and refined lattice constants of the as-synthesized materials, where *a* is the refined lattice constant and R_{wp} is the R-factor of the refinement. **b)** TEM ED patterns collected on as-synthesized TM2, TM4, and TM6 along the [100] zone axis. The round spots, originating from the long-range order in the materials, are indexed to the *Fm*-3*m* space group. The square-like diffuse scattering patterns are attributed to the short-range ordering. The short-range order pattern intensity was quantified by integrating the counts within the dashed rectangular regions and is displayed above the ED patterns. **c)** Rate capability of TM2, TM4, and TM6 showing the first-cycle voltage profiles of all three compounds. The legend for TM2 also applies to TM4 and TM6.

characterized by several techniques including SXRD, transmission electron microscopy (TEM) electron diffraction (ED), and $^{7}Li/^{19}F$ ssNMR, which are shown below in Figure 3.2 and Figure 3.3. The SXRD patterns and corresponding fits in Figure 3.2.a show that each material has the same long-range DRX structure. However, TEM ED (Figure 3.2. b) shows decreasing short-range ordering (evidenced by the square-like diffuse scattering between the main DRX Bragg reflection spots) as the number of transition metal species

increases. Similarly, the electrochemistry (Figure 3.2.c) shows increasing first-cycle capacities and improved rate performance with increasing amounts of transition metal species. These results are consistent with the hypothesis that decreasing short-range ordering through formation of a high- entropy DRX improves the electrochemical performance.

As diffraction techniques are unable to identify amorphous phases, $^{7}Li/^{19}F$ ssNMR was utilized to understand the local, nuclear-specific structure in the as-synthesized materials. ^{19}F NMR measurements were conducted to confirm the bulk incorporation of F into the DRX lattice rather than the formation of a separate LiF impurity phase. The ^{19}F NMR spectra shown in Figure 3.3a collected on the as-synthesized DRX materials differ significantly from the sharp spectrum obtained on the LiF reference. Strong paramagnetic interactions between unpaired *d* electrons on the *M* ions (Mn^{2+}, Co^{2+}, Mn^{3+}, and Cr^{3+} in this case) and F nuclei lead to a shift of the ^{19}F resonant frequency away from that of diamagnetic LiF at −204 ppm and significant spectral broadening. Hence, the broad ^{19}F spectra obtained on the as-synthesized DRX cathodes indicate bulk incorporation of F into the paramagnetic cathodes, as well as a distribution of resonant frequencies due to the formation of a range of local F environments in the disordered lattice. As discussed in previous work[27,129] when F ions are directly bonded to *M* ions with unpaired *d* electrons, very strong paramagnetic interactions are generated, which result in signals that are too broad and/or decay too quickly to be observed. As a result, quantitative information on the distribution of the different F coordination environments (paramagnetic vs. diamagnetic) cannot be obtained from the integration of the ^{19}F spectra. We also note that these spectra were acquired using a

short recycle delay of 30 ms to maximize the signal-to-noise ratio, but which may not allow the ^{19}F NMR signal from diamagnetic sites in the sample to fully return to equilibrium between successive scans and may lead to a reduced apparent ^{19}F NMR signal from these environments. However, our previous ^{19}F ssNMR work on related DRX cathodes indicates that most of the diamagnetic ^{19}F signal is observed under such experimental conditions. Hence, the presence of a very low intensity diamagnetic signal in the spectra collected on TM2, TM4, and TM6 samples suggests that most F ions are incorporated in the DRX phase.

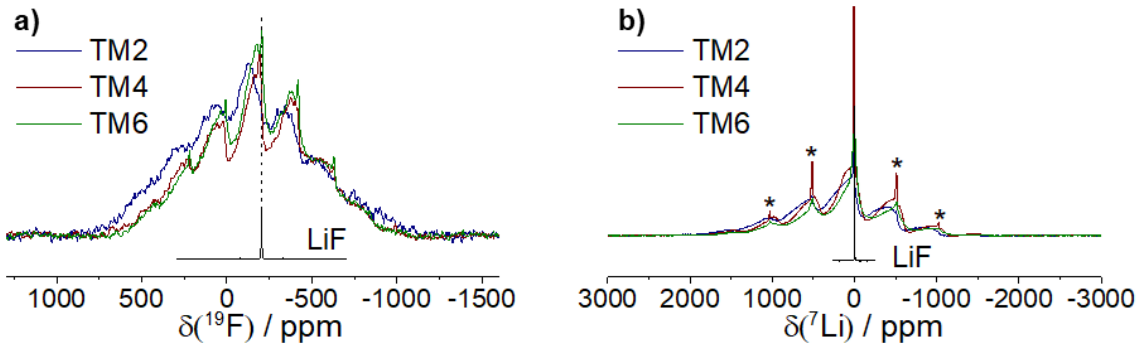

Figure 3.3 – ssNMR spectra obtained on the as-synthesized materials. a) ^{19}F ssNMR spectra obtained by summing over multiple spin echo sub-spectra acquired at different excitation frequencies to ensure homogeneous excitation of the broad lineshape. The spectra were scaled according to the amount of sample in the rotor and number of scans. For comparison, a ^{19}F spin echo spectrum collected on LiF powder is overlaid. **b)** ^{7}Li spin echo NMR spectra of the as-synthesized materials. For comparison, the ^{7}Li spin echo spectrum collected on LiF powder is overlaid. Spinning sidebands of the sharp, diamagnetic ^{7}Li signals (e.g., LiF, Li_2O, Li_2CO_3) are indicated with asterisks.

The ^{7}Li spin echo NMR spectra collected on the three as-synthesized compounds and LiF powder are presented in Figure 3.3b. Integration of the sharp signal at approximately 0 ppm in each of the spectra indicates that the fraction of Li present in diamagnetic environments (e.g., in LiF, Li_2O, or Li_2CO_3 impurity phases) is less than 10%, 19%, and 11% (+/− 5%) in TM2, TM4, and TM6, respectively. This integration was performed on quantitative ^{7}Li spectra collected using optimized recycle delays of 0.5 s

for TM2 and 3 s for TM4/TM6. We note that the intensity of the diamagnetic ^{7}Li signal gives the upper limits for the amount of impurity phases present in the samples because this signal could also be due to the formation of diamagnetic Li-rich (*M*-poor) domains within the disordered oxide matrix.[123] Hence, both impurity particles and structurally integrated diamagnetic domains arising from local segregation of cations in our compounds can, in theory, give rise to diamagnetic ^{7}Li environments. The absence of additional signals in the XRD and neutron scattering patterns suggests that the amount of impurities in the as-synthesized materials, if any, is small and amorphous.

Thus, using ^{19}F and ^{7}Li ssNMR we confirm bulk incorporation of F into the DRX phase and identify a relatively consistent amount of diamagnetic Li-rich domains present in each as-synthesized compound, supporting the overall conclusions of this study that the main factor affecting improved electrochemical behavior is the formation of a high-entropy DRX structure which acts to suppress short-range ordering. For a more thorough investigation of the cycling mechanism in these high-entropy DRX materials, as well as a computational investigation of high-entropy DRX design rules, the reader is directed to the published study.[108]

3.3.2 Computational Investigation and Experimental Realization of Ni-based Disordered Rocksalts[aa]

While the ability of DRX materials to form a variety of chemistries, especially when considering various fluorination levels, presents an opportunity to finely tune the

[aa]The contents of this section have substantially appeared in reference [109]: H. Ji, D. Kitchaev, Z. Lun, H. Kim, **E.E. Foley,** D.-H. Kwon, Y. Tian, M. Balasubramanian, M. Bianchini, Z. Cai, R.J. Clément, J. Kim, and G. Ceder, "Computational Investigation and Experimental Realization of

electrochemical performance, it also presents a complex challenge to rational design of DRX compositions. Thus, compositional prediction provides an opportunity to make informed decisions regarding theoretical capacities (influenced by both Li and Ni content, which is further influenced by the fluorination level) and material synthesizability. This work is the result of a collaboration with Prof. Gerd Ceder's group at UCB and LBNL. Dr. Huiwen Ji synthesized the materials, performed the X-ray diffraction, and prepared and tested the electrochemical cells. Dr. Daniil Kitchaev performed the DFT calculations. I acquired and analyzed the NMR data.

Here, compositional prediction was used to identify two compositions (predicted ternary phase diagram for NiO-Li_3NbO_4-LiF is shown in Figure 3.5): $Li_{1.13}Ni_{0.57}Nb_{0.3}O_{1.75}F_{0.25}$ (LNNOF25) and $Li_{1.19}Ni_{0.59}Nb_{0.22}O_{1.46}F_{0.54}$ (LNNOF54), which both exhibit sufficient Li excess, balanced Li and Ni theoretical capacities, and are likely to be synthesizable. However, the latter composition exhibits an increase in fluorination, decrease in d^0 content, and decrease in overall thermodynamic stability, providing an opportunity to investigate the effect of fluorination and metastability on Ni electrochemistry in a DRX compound. For a detailed investigation of the redox mechanism in these compounds the reader is directed to the full manuscript although some insight via *ex situ* NMR on the reversibility of the cycling mechanism is presented in Appendix 3.5.1. The present discussion will focus on structural characterization of the

Disordered High-Capacity Li-ion Cathodes Based on Ni Redox", *Chem. Mater.* **31** (2019) 2431-2442. doi:10.1021/acs.chemmater.8b05096

ball-milled and annealed materials and the impact of annealing – and thereby thermodynamic stability – on electrochemical behavior.

Both LNNOF25 and LNNOF54 were synthesized via mechanochemical synthesis and a nearly phase-pure, chemically homogenous DRX phase was prepared as evidenced by XRD and TEM/EDS mapping, as done for the previously discussed high-entropy DRX study. To further prove the bulk substitution of fluorine, ^{19}F ssNMR experiments were performed on LNNOF25 and LNNOF54 to study the local chemical environments of fluorine. If fluorine exists in a segregated LiF phase, then the ^{19}F NMR data are expected to show a sharp peak at −204 ppm. On the contrary, if fluorine is incorporated into the targeted DRX phase, then a wide variety of chemical environments are expected. ^{19}F spin echo and pj-MATPASS spectra collected for the two compounds are shown in Figure 3.4. Both materials show signals that span a wide range of chemical shift, as evidenced from the pj-MATPASS data (shaded areas in the top and middle spectra), indicating the presence of various local environments of fluorine. The significant broadening of the peaks also suggests that the fluorine ions are in proximity (<5 Å) to paramagnetic ions (Ni^{2+} in this case). Specifically, the pj-MATPASS spectrum of LNNOF25 shows a broad peak centered around −155 ppm, with a slight asymmetry toward −204 ppm, suggesting the close to complete F integration in the bulk of the material, with only a small proportion of F nuclei in LiF-like environments. The pj-MATPASS spectrum of LNNOF54 shows a slightly higher signal intensity at −204 ppm than that of LNNOF25. These observations confirm that most F ions in both materials are incorporated into the paramagnetic DRX phases with the low-F substituted LNNOF25 containing almost no LiF, and the high-F substituted LNNOF54 containing a small amount of LiF. As previously

discussed, the exact quantification of LiF-like environments in these compounds is complicated by the ambiguous multicomponent fit of the broad, overlapping peaks in the spin echo spectra, as well as the absence of the signal from F nuclei directly bonded to Ni.[27,28,130] Thus, we refrain from quantification but conclude that the ball-milled materials contain few LiF-like domains with LNNOF54 exhibiting more than LNNOF25.

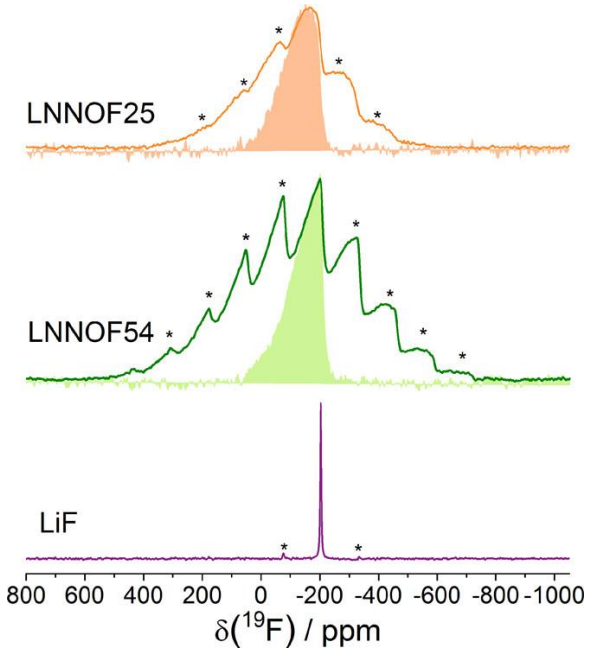

Figure 3.4 – ^{19}F spin echo NMR spectra obtained at 60 kHz MAS for LNNOF25 (orange, top), LNNOF54 (green, middle), and LiF (purple, bottom). Spinning sidebands in the spin echo spectra are labeled with asterisks. The shaded areas in the top and middle spectra correspond to ^{19}F pj-MATPASS isotropic spectra collected on LNNOF25 and LNNOF54 and indicate the presence of broad, overlapping signals spanning a wide range of resonant frequencies. The spectra obtained on LNNOF25 and LNNOF54 are scaled according to the number of scans in the experiment and the amount of sample in the NMR rotor.

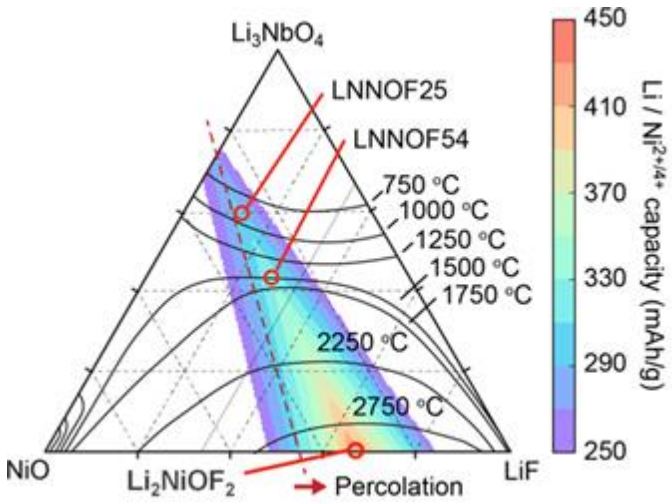

Figure 3.5 – Computed phase diagram and theoretical capacity of the Li_3NbO_4–NiO–LiF system, constrained to solid phases on a rocksalt lattice. The temperature contours denote the extent of the binodal at the marked temperature, starting from the NiO and Li_3NbO_4 endpoints. The color-coded overlay maps the minimum of the theoretical Li and $Ni^{2+/4+}$ gravimetric capacity, and the red dashed lines represent compositions with at least 9% Li excess required for percolative Li transport.

Given that mechanochemical synthesis often results in a considerable amount of local strain in the material structure, the as-ball-milled samples were annealed (at 700°C for 30 min followed by a quench to room temperature) to relax this strain and study the effect of annealing on the cathode cyclability. XRD patterns are shown in Figure 3.6a,b and exhibit significant peak sharpening, suggesting particle size growth and/or relaxation of lattice strain. The XRD pattern of a-LNNOF25 is well fit by the DRX structural model, whereas a-LNNOF54 exhibits a significant increase in the amount of NiO present (19.9 wt.% compared to 2.3% before annealing).

However, as XRD is only sensitive to crystalline phases, we characterized the amount of LiF in both annealed samples using more sensitive ^{19}F ssNMR (Figure 3.6c,d). While the spectrum of a-LNNOF25 largely retains the broad span of the chemical shift with slightly more contribution from LiF-like environments after annealing, the spectrum of a-LNNOF54 shows significant peak sharpening and shifting toward –204

ppm after annealing. These results indicate that LNNOF25 is stable enough at 700°C to retain the DRX structure and compositional homogeneity, whereas LNNOF54 is not sufficiently stable, as it tends to phase-separate when annealed, which is consistent with the extremely high temperature we compute to be necessary to achieve this high level of fluorination. In addition, the increased ^{19}F NMR signal intensity presumably originates from structural changes in the materials during annealing, leading to a decreased proportion of F nuclei with at least one Ni–F bond that are invisible in the spectra. Hence, a possible scenario is that annealing the samples leads to the replacement of high-energy Ni–F bonds with lower-energy Li–F bonds,[123] resulting in a more thermodynamically stable structure.

To assess the amount of diamagnetic-like Li environments present, we used ^{7}Li ssNMR. ^{7}Li pj-MATPASS and spin echo ssNMR spectra are shown in Figure 3.6e,f for LNNOF25, a-LNNOF25, LNNOF54, and a-LNNOF54. A sharp peak was seen around −1 to 0 ppm in all spectra indicating a significant diamagnetic signal that increases in intensity upon annealing and with higher fluorine content. This peak could be attributed to a combination of $LiCO_2$, LiO_2, and LiF environments as these are all commonly occurring signals in ^{7}Li ssNMR within the −1 to 0 ppm range. However, it is impossible to differentiate the diamagnetic signals as they so closely overlap each other. We further quantified the diamagnetic Li environment by fitting each ^{7}Li spectrum with one paramagnetic peak and one diamagnetic peak using the Topspin software where the fraction of each Li environment is determined from the integrated intensity. The diamagnetic Li environment accounts for roughly 16%, 22.5%, 18.6%, and 62.1% of total Li in LNNOF25, a-LNNOF25, LNNOF54, a-LNNOF54, respectively. As previously

discussed, these diamagnetic-like Li signals does not only include contributions from Li_2Co_3, Li_2O, and LiF, but also from Li in a disordered-rocksalt environment where the first and second coordination shells are made exclusively of diamagnetic Li^+ or Nb^{5+}.[115] Regardless, the significant increase in the diamagnetic-like Li environments in a-LNNOF54 is in line with the XRD and ^{19}NMR results that show partial decomposition of the metastable LNNOF54 DRX phase.

The voltage profiles of the two annealed samples for the first 10 cycles are presented in Figure 3.7a,c. The a-LNNOF25 cathode delivers a first-cycle capacity of ~200 mAh/g when cycled over the range of 1.5–4.6 V, with a similar voltage profile to the as-ball-milled cathode (see Appendix 0). However, its capacity retention is significantly improved, as shown in Figure 3.7b. Roughly 83% of the original capacity is retained after 20 cycles compared with 40% for the ball-milled LNNOF25. In contrast, the voltage profile of a-LNNOF54 changes substantially compared with that of the as-ball-milled cathode, with its high-voltage plateau region significantly shortened, leading to a limited first-cycle capacity of 133 mAh/g. This reduced capacity is likely associated with the phase segregation observed via XRD and NMR. Nevertheless, a-LNNOF54 retains ~94% of its original capacity after 20 cycles (Figure 3.7d). The exact reason why the capacity retention improves significantly after annealing needs further investigation. Three possible mechanisms are (i) the enhanced crystallinity after annealing leads to better structural retention during cycling, (ii) annealing leads to larger particles and reduced surface area and thus less surface side reactions (e.g., oxygen loss and densification), and (iii) annealing leads to a different cation short-range order from that of the ball-milled samples, resulting in different electrochemical performance.

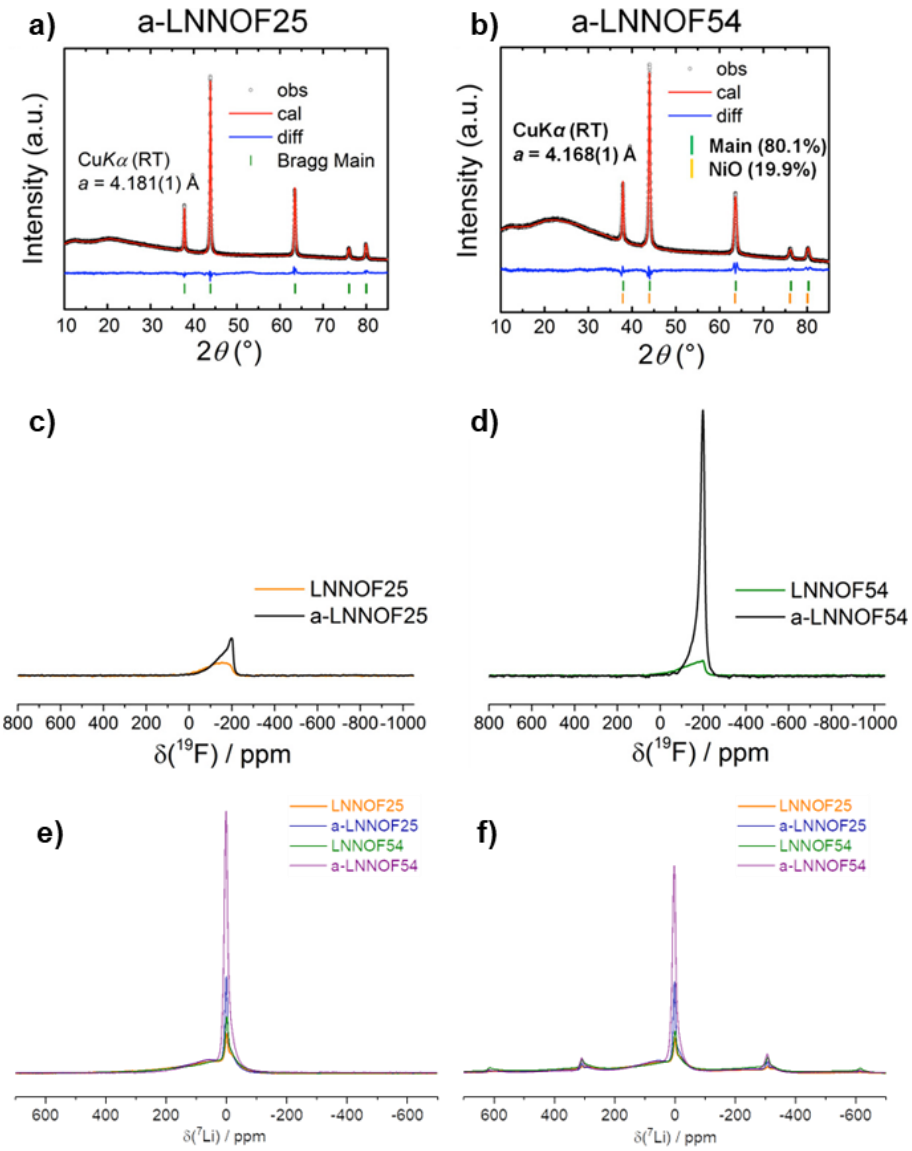

Figure 3.6 – Room-temperature XRD patterns and Rietveld refinement results for **a)** a-LNNOF25 and **b)** a-LNNOF54. ^{19}F pj-MATPASS isotropic NMR spectra of **c)** LNNOF25 and **d)** LNNOF54 before and after annealing obtained at 60 kHz MAS. The spectra are scaled according to the number of scans in the experiment and the amount of sample in the NMR rotor. ^{7}Li **e)** pj-MATPASS and **f)** spin echo ssNMR spectra obtained at 60 kHz MAS for LNNOF25 (orange), a-LNNOF25 (blue), LNNOF54 (green), and a-LNNOF54 (purple). A sharp peak occurs around –1 to 0 ppm in all spectra, indicating the presence of diamagnetic Li environments in each sample. All spectra have been scaled to have equal paramagnetic signal intensities so that the diamagnetic peaks can be appropriately compared.

Overall, annealing for LNNOF25 has a large positive impact on the reversibility of the electrochemical behavior while the metastability of LNNOF54 ultimately presents a large challenge as it begins to decompose when subjected to a short anneal. The exact

cause for this behavior improvement is unknown, and a closer investigation of changes in cation short-range order is crucial for determining distinctly how Li transport is changing upon annealing in these DRX materials. Again, we direct the reader to the published study for a detailed investigation of the redox mechanism, although some insight via *ex situ* NMR on the reversibility of the cycling mechanism is presented in Appendix 3.5.1.

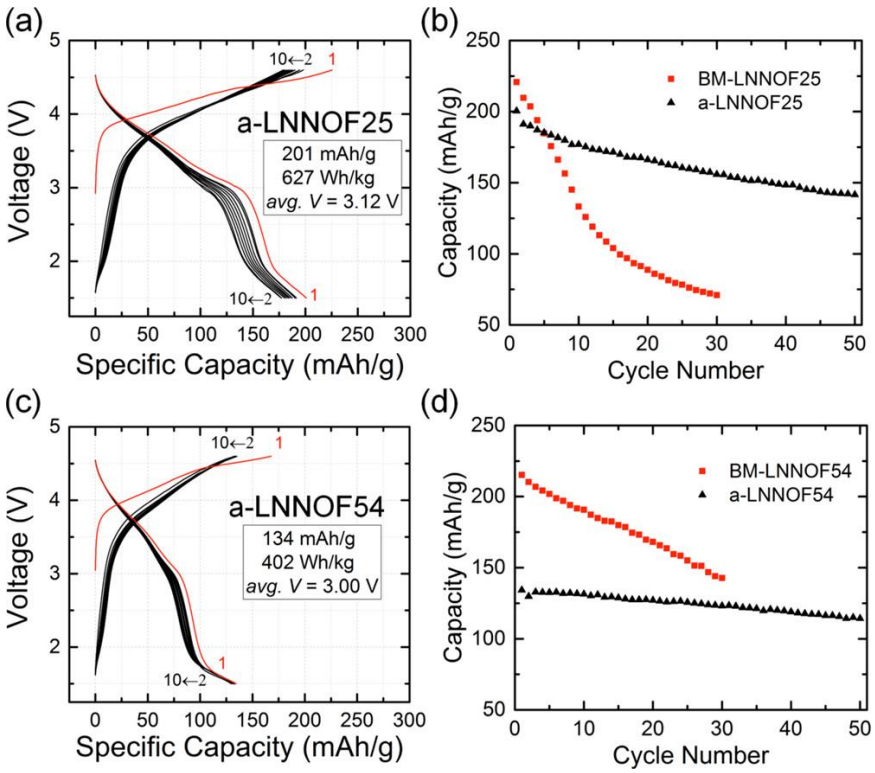

Figure 3.7 – Voltage profiles for the first 10 cycles for **(a)** a-LNNOF25 and **(c)** a-LNNOF54. Capacity retention over 50 cycles for **(b)** a- LNNOF25 and **(d)** a-LNNOF54. The capacity retention of the ball-milled samples (BM-LNNOF25 and BM-LNNOF54) over 30 cycles is also shown for comparison. The cycling rate for all tests is 20 mA/g.

3.3.3 Structure & Redox Characterization of a Model Disordered Rocksalt[bb]

DRX materials frequently deliver exceptionally high capacities (> 250 mAh/g),[113] which may imply the occurrence of both cationic transition metal redox and anionic oxygen redox.[129,131] Studies on non-fluorinated DRX materials observed significant oxygen gas evolution at high voltages indicating irreversible oxygen redox.[129,131] However, this affect is largely suppressed upon F-substitution, yet prolonged performance decay is nevertheless still observed.[27,129,132] Thus, this study endeavored to investigate a representative fluorinated DRX compound, $Li_{1.2}Mn_{0.625}Nb_{0.175}O_{1.95}F_{0.05}$ (LMNOF), and utilize an electroanalytical method – complemented with X-ray absorption spectroscopy – to precisely identify the Mn and O redox behaviors on charge and discharge. The work presented in this section is the result of a collaboration with Dr. Wei Tong's group at LBNL. Dr. Yuan Yue synthesized the materials, performed the X-ray diffraction, and prepared and tested the electrochemical cells. I acquired and analyzed the NMR data.

Characterization of the as-prepared materials[110] shows formation of a highly crystalline, chemically homogeneous DRX phase exhibiting short-range ordering, typical of similar DRX cathodes.[119,127] ^{19}F ssNMR experiments were conducted to monitor the incorporation of F in the bulk LMNOF lattice. The ^{19}F spectra (Figure 3.8b) exhibit a broad range of resonant frequencies, indicating the bulk incorporation of F in a wide range of local environments within the DRX materials. The absence of a sharp signal

[bb]The contents of this section have substantially appeared in reference [110]: Y. Yue, N. Li, L. Li, **E. E. Foley**, Y. Fu, V. S. Battaglia, R. Le, R. J. Clément, C. Wang, and W. Tong, Redox Behaviors in a Li-Excess Cation-Disordered Mn–Nb–O–F Rocksalt Cathode. *Chem. Mater.* **32** (2020) 4490–4498. doi:10.1021/acs.chemmater.9b05221.

centered around −204 ppm in the ^{19}F NMR spectra further demonstrates the absence of residual LiF in the sample. The phase purity and bulk fluorination are not affected by the additional carbon processing, the purpose of which is to reduce the large particle size and increase the electrical conductivity of the LMNOF electrode (Figure 3.8). The ^{7}Li spectra (Figure 3.8c) exhibit a broad range of resonant frequencies corresponding to the Li environments in bulk LMNOF and a sharp diamagnetic peak around 0 to −1 ppm corresponding to either Li_2CO_3, Li_2O, or LiF. Based on the integration of spin echo ^{7}Li NMR data, the diamagnetic Li peak accounts for 2 and 8% (±5%) of the total ^{7}Li signal in pristine and carbon-processed LMNOF, respectively.

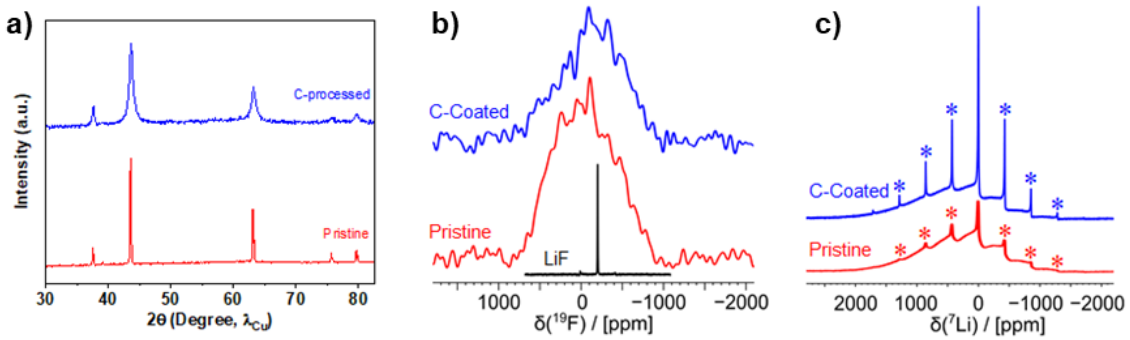

Figure 3.8 – XRD & ssNMR spectra obtained on the as-synthesized materials. a) XRD patterns and **b)** ^{19}F ssNMR spectra of pristine and carbon-processed LMNOF. ssNMR spectra are obtained by summing over multiple spin echo sub-spectra acquired at different excitation frequencies to ensure homogeneous excitation of the broad lineshape. The spectra are scaled according to the amount of sample in the rotor and number of scans. For comparison, a ^{19}F spin echo spectrum collected on LiF powder is overlaid. **c)** ^{7}Li spin echo ssNMR spectra of pristine and carbon-processed LMNOF. Spinning sidebands of the sharp, diamagnetic ^{7}Li signals (e.g., Li_2CO_3 and Li_2O with $\delta(^{7}Li)$ = 0 to −1 ppm) are indicated with asterisks.

As F-substitution in DRX materials has been shown to have a large impact on the anionic redox behavior, the ^{19}F ssNMR results confirming bulk F incorporation in the DRX material here are essential to the following analysis of the redox processes in LMNOF. While the exact details of the electroanalytical characterization of the redox behavior is outside the scope of this dissertation, both Mn and oxygen redox was

suggested (pictorially represented in Figure 3.9) with the latter being largely irreversible and asymmetric (occurring around 4.6 V on charge but active down to 3 V on discharge), contributing to the sluggish kinetics and large voltage hysteresis observed throughout cycling.[110]

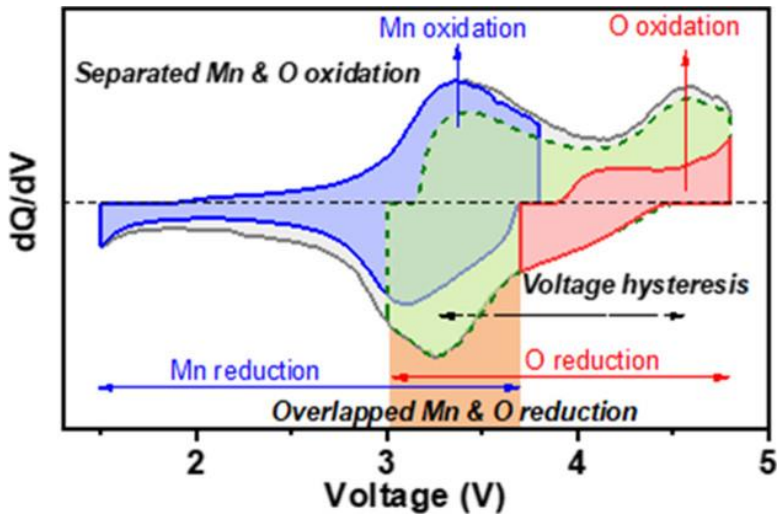

Figure 3.9 – Pictorial representation of proposed manganese and oxygen redox regions in LMNOF investigated using cyclic voltammetry and complementary electroanalytical techniques.

3.3.4 Improved Performance in Partially-Disordered Spinel Cathodes

An extensive network of 0-TM channels is required for high performance DRX materials as they create an interconnecting network of low-energy migration pathways. Spinels exhibit the same anion framework as DRX materials, and thereby layered oxides, but show a distinct cation order where cations now occupy both octahedral and tetrahedral sites. This spinel-like cation order (both short-range and long-range) has been shown to create more of these 0-TM channels favoring fast Li diffusion.[122] These 0-TM pathways are highlighted in Figure 3.10 along with the ordered stoichiometric spinel where the tetrahedral 8*a* and octahedral 16*d* sites are fully occupied by Li and *M*, respectively, leaving the 8*b* and 16*c* sites vacant. However, these materials have limited

capacities as they exhibit two-phase reactions and Li-vacancy orderings outside of the $Li_xMn_2O_4$ x = 0 to 1 range, limiting their accessible capacity.[133,134] Thus, to target the optimal cation-ordering intrinsic to spinels and overcome these capacity limitations, partially-ordered spinel-like materials are a promising solution. Partial-ordering of the spinel structure is achieved through both Li-excess and F-substitution. The first study in this series demonstrates a proof-of-concept formation of a Li-*M*-O-F disordered spinel[111] exhibiting ultrahigh power and energy density validating the design strategy of increasing the 0-TM content through cation-order. The second study furthers this work by investigating cation order-to-disorder tuning through increasing Li contents further paving the way for this DRX-variant.

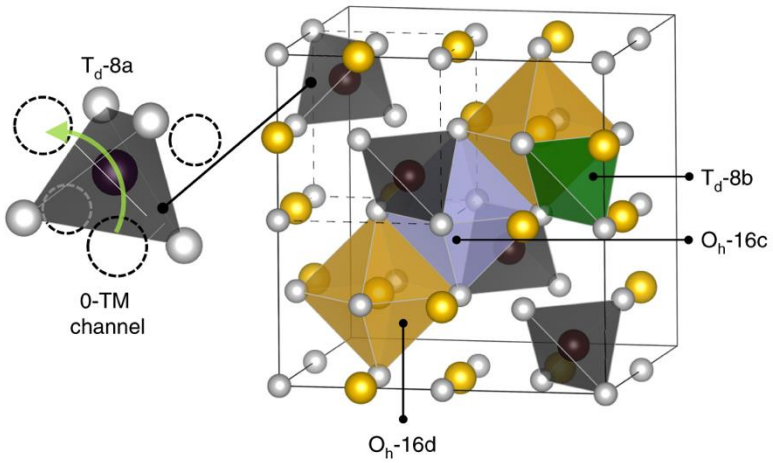

Figure 3.10 – Crystal structure fragment of a perfectly ordered spinel LiM_2O_4 (M = non-Li metal ions), with the high-symmetry Wyckoff positions T_d-8*a*, T_d-8*b*, O_h-16*c*, O_h-16d highlighted as colored polyhedra. A pseudo face-centered-cubic anion framework is outlined with black dashed lines. The black, yellow, and silver spheres represent the occupying Li, *M* and F/O atoms, respectively. Inset: the enlarged T_d-8*a* site illustrates a 0-TM channel, in which none of its four face-sharing octahedral sites (dashed circles) is occupied by a *M*.

3.3.4.1 Demonstration of High Performance Partially-Ordered Spinels[cc]

[cc]The contents of this section have substantially appeared in reference [111]: H. Ji, J. Wu, Z. Cai, J Liu, D.-H. Kwon, H. Kim, A. Urban, J.K. Papp, **E.E. Foley**, Y. Tian, M. Balasubramanian, H. Kim, R.J. Clément, B.D. McCloskey, W. Yang, and G. Ceder, "Ultrahigh Power and Energy Density in

This study demonstrated the first synthesis and characterization of partially-ordered spinel materials: $Li_{1.68}Mn_{1.6}O_{3.7}F_{0.3}$ (LMOF03) and $Li_{1.68}Mn_{1.6}O_{3.4}F_{0.6}$ (LMOF06). The reader is directed to the published study[111] regarding characterization of the cycling mechanism and high-rate behavior. This work is the result of a collaboration with Prof. Gerd Ceder's group at UCB and LBNL. Dr. Huiwen Ji and Dr. Zijian Cai synthesized the materials, performed the X-ray diffraction, and prepared and tested the electrochemical cells. I acquired and analyzed the NMR data.

Here, we focus on the information provided by ssNMR regarding the local structure and influence on cycling behavior. Long-range structural characterization of the two spinel-like oxyfluorides shows that complete cation order is not observed[111] and instead (1) Mn is distributed between the 16*c* and 16*d* sites, with 14-16% of the total Mn content occupying 16*c* sites, and (2) only half of the 8*a* sites are occupied by Li with the remaining Li content being distributed between the 16*c* and 16*d* sites. The LMOF06 contains more Li in the 16*c* site than LMOF03 and is thus considered to be more disordered.

To determine the distribution of Li local environments in the material, ssNMR measurements were carried out. The ^{7}Li NMR spectra (shown in Figure 3.11a) indicate that, both in LMOF06 and LMOF03, the great majority of Li atoms are in paramagnetic environments associated with a range of chemical shifts, leading to very broad and overlapping signals, although a small number of diamagnetic Li environments can also be detected at ≈ 0 ppm. The 0 ppm signal is stronger in LMOF06 (9 ± 2 % of the overall

Partially Ordered Lithium-ion Cathode Materials", *Nature Energy* **5** (2020) 213-221. . doi:10.1038/s41560-020-0573-1

^{7}Li NMR signal intensity) than in LMOF03 (1 ± 2 % of the overall ^{7}Li NMR signal intensity) suggesting more diamagnetic-like Li environments. While this signal could arise from a small amount of diamagnetic impurity phases (e.g., Li_2CO_3, Li_2O or LiF) in the sample, we cannot exclude the possibility of diamagnetic Li in local LiF-like domains in the target phases as previously discussed.[109,123] We note that while in an ordered spinel material different Li coordination environments are readily distinguished,[135] we are unable to be separate these environments due to the broad distribution of local environments within each coordination-type, caused by the partial-disordering of the structure.

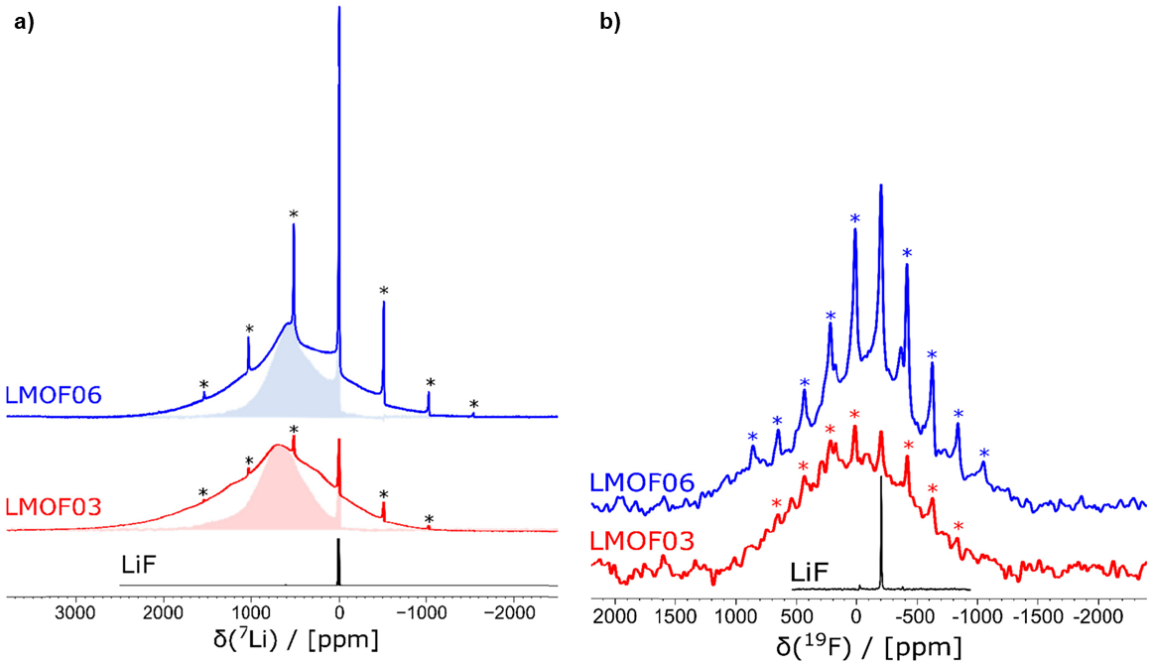

Figure 3.11 – ^{7}Li (**a**) and ^{19}F (**b**) spin echo NMR spectra obtained at 60 kHz for LMOF03 (middle, red), LMOF06 (top, blue) and LiF (bottom, black), with spinning sidebands labeled with asterisks. ^{7}Li pj-MATPASS isotropic spectra for LMOF03 and LMOF06 are presented as the shaded areas underneath the corresponding spin echo NMR spectra. All spectra are scaled by the number of scans and the amount of sampled packed in the NMR rotor

Similarly, the ^{19}F NMR spectra (Figure 3.11b) of LMOF03 and LMOF06 reveal broad, overlapping signals with a wide range of chemical shifts that are entirely different from the ^{19}F shift of LiF, indicating bulk incorporation of F in the spinel structure. A small diamagnetic signal observed at –204 ppm corresponds to a segregated LiF impurity phase and/or to LiF-like domains in the bulk of the material. This diamagnetic signal grows in intensity as the fluorination level increases, like the increase in diamagnetic-like environments identified via ^{7}Li NMR. As F nuclei directly bonded to a paramagnetic center (here Mn) are essentially invisible in the NMR spectrum, as previously discussed and shown in our previous work,[28,123] our ^{19}F NMR data are not quantitative and the proportion of F in paramagnetic environments is larger than our experimental data suggest.

Both spinel-like-ordered oxyfluorides demonstrate remarkable gravimetric capacity and energy density, as shown in Figure 3.12. A full discussion of the electrochemical behavior of these materials is outside the scope of this dissertation but we note that the voltage profile of LMOF06 is steeper than that of LMOF03, which results in a slightly lower capacity of 305 mAh/g (931 Wh/kg) over the range 1.5-4.8 V compared to 363 mAh/g (1103 Wh/kg) for LMOF03. Given that the additional $Mn^{3+/4+}$ capacity in LMOF06 is unlikely to cause this difference, plausible origins include a greater diversity of Li local environments and more F-bonded Li^{+} ions with a higher site energy, induced by the larger F content in LMOF06, a phenomenon commonly referred to as "Li gettering".[130] This speculation about the Li-site distribution is also corroborated by the ^{7}Li NMR data, as the ^{7}Li pj-MATPASS (projected magic-angle turning and phase-

adjusted sideband separation) spectrum obtained for LMOF06 is slightly broader than that obtained for LMOF03 (Figure 3.11a).

Thus, this study exhibits the successful synthesis and electrochemical testing of a partially ordered spinel-like Li-ion cathode material exhibiting bulk F incorporation and a broad range of Li and F local environments, which directly impacts the electrochemical performance.

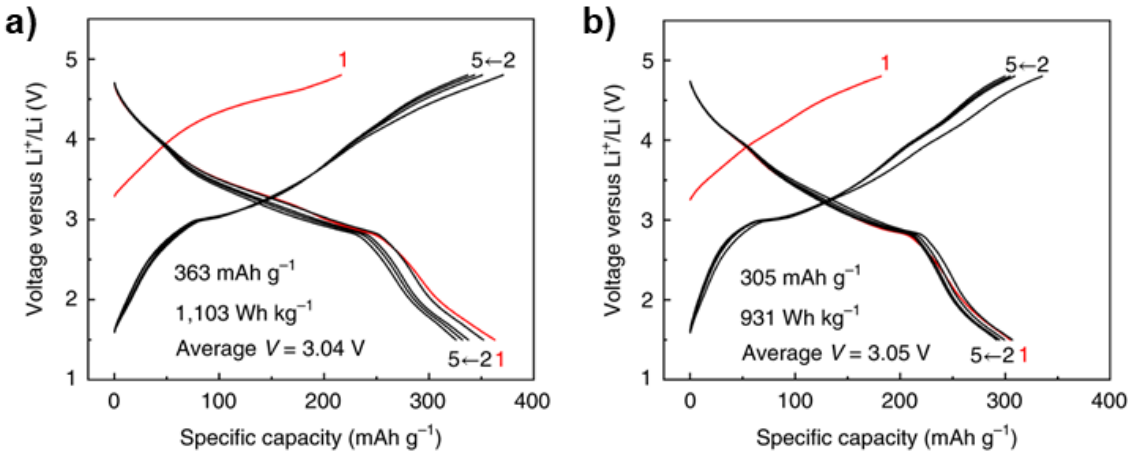

Figure 3.12 – Voltage profiles, started in charge, for the first five cycles obtained over the 1.5–4.8 V range for LMOF03 (**a**) and LMOF06 (**b**).

3.3.4.2 Order-to-Disorder Tuning in Partially-Ordered Spinels[dd]

Following on the success of the proof-of-concept partially-ordered spinel investigation, this study aimed to tune the order-to-disorder nature of a spinel-like Li-Mn-O-F composition more finely through increasing Li contents. In doing so, the goal

[dd]The contents of this section have substantially appeared in reference [112]: Z. Cai, H. Ji, Y. Ha, J. Liu, D.-H. Kwon, Y. Zhang, A. Urban, **E.E. Foley**, R. Giovine, H. Kim, Z. Lun, T.-Y. Huang, G. Zeng, Y. Chen, J. Wang, B.D. McCloskey, M. Balasubramanian, R.J. Clément, W. Yang, and G. Ceder, "Realizing continuous cation order-to-disorder tuning in a class of high-energy spinel-type Li-ion cathodes", *Matter* **4** (2021) 3897–3916. . doi:10.1016/j.matt.2021.10.013 © 2021 Elsevier Inc., reprinted with permission.

was to further limit the irreversible two-phase and Li-vacancy ordering transitions observed in the ordered spinel.[133,134] This work is the result of a collaboration with Prof. Gerd Ceder's group at UCB and LBNL. Dr. Huiwen Ji and Dr. Zijian Cai synthesized the materials, performed the X-ray diffraction, and prepared and tested the electrochemical cells. Dr. Raynald Giovine acquired the NMR data while I analyzed it.

Here, three compositions were prepared via mechanochemical synthesis: $Li_{1.47}Mn_{1.6}O_{3.7}F_{0.3}$ (0.07 excess cations per formula unit), $Li_{1.68}Mn_{1.6}O_{3.7}F_{0.3}$ (0.28 excess cations), and $Li_2Mn_{1.6}O_{3.7}F_{0.3}$, (0.6 excess cations). Characterization via X-ray and neutron diffraction concluded that the material increasingly disorders (e.g. Li ions increasingly occupy the octahedral 16*d* and 16*c* sites) as the Li content increases such that the highest Li content material exhibits a hybrid spinel rocksalt-type disorder. A schematic illustrating this trend is shown in Figure 3.13.

^{19}F and ^{7}Li solid-state nuclear magnetic resonance (ssNMR) measurements were conducted to further verify the integration of F in the bulk structure and distribution of Li environments (Figure 3.14). The ^{19}F spectra obtained on the $Li_{1.47}Mn_{1.6}O_{3.7}F_{0.3}$ and $Li_2Mn_{1.6}O_{3.7}F_{0.3}$ pristine powders show two distinct components: a broad, paramagnetic signal and a sharp, diamagnetic signal. The broad signal corresponds to ^{19}F nuclei in the bulk of the cathode materials. Their interaction with nearby paramagnetic Mn ions leads to a shift of the ^{19}F resonant frequency away from that of diamagnetic LiF at −204 ppm and to significant spectral broadening. In addition, for both compounds, the observed paramagnetic lineshape comprises several broad and overlapping ^{19}F signals assigned to a wide variety of ^{19}F local environments in the partially (dis)ordered spinel lattice. The sharp signal centered at −204 ppm is assigned to a diamagnetic LiF impurity phase

present in small amounts in these two samples. Once again, signals from ^{19}F nuclei directly bonded to paramagnetic centers are invisible in these spectra which prevents the exact quantification of the LiF impurity phase in these samples. Regardless, the amount of LiF impurity phase obtained from ^{19}F NMR data is overestimated due to the invisible paramagnetically-bonded F ions, indicating that most F ions are incorporated into the bulk of the partially disordered spinel compounds.

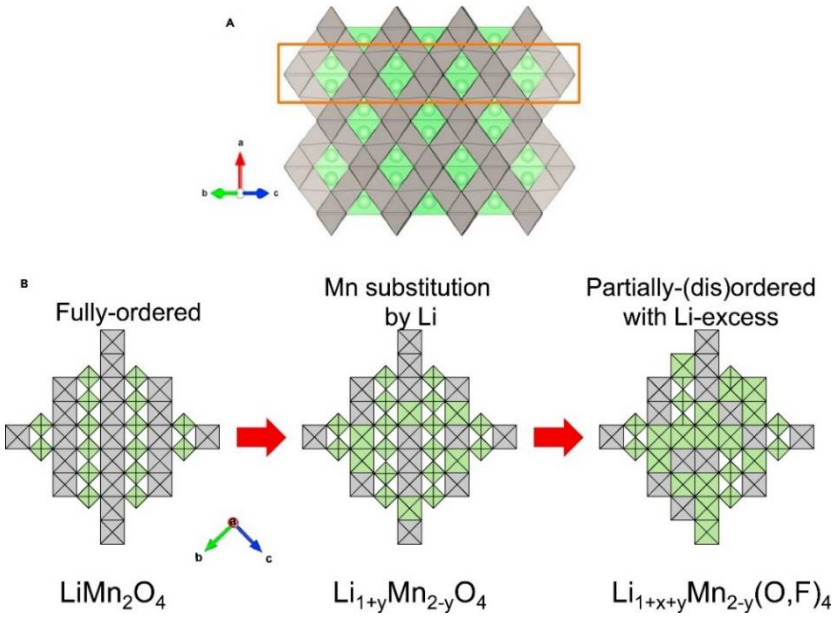

Figure 3.13 – Design of partially (dis)ordered spinel cathodes with Li over-stoichiometry *x* and Mn substitution by Li *y*. (**a**) Structure of fully ordered $LiMn_2O_4$ (gray octahedra = MnO_6, green tetrahedra = LiO_4, green spheres = Li). The slab outlined by the orange square is viewed from above and depicted in detail in (**b**) as fully ordered (left), with some Mn substituted by Li (middle), and with partial disorder and Li over-stoichiometry. The bold green squares represent face sharing Li_{tet}-Li_{oct}.

The integration on quantitative ^{7}Li spin-echo spectra was performed to further characterize the Li local environments. By integrating the sharp signal close to 0 ppm in each spectrum, the fraction of Li present in diamagnetic environments (e.g., in Li_2CO_3, Li_2O, or LiF) was found to be 2% and 1% (± 1%) for $Li_{1.47}Mn_{1.6}O_{3.7}F_{0.3}$ and $Li_2Mn_{1.6}O_{3.7}F_{0.3}$, respectively. This intensity provides the upper limit for the amount of impurity phases present in the samples, as the signal could also arise from the formation

of large diamagnetic Li-rich (Mn-poor) domains within the disordered oxide matrix.[123] Overall, the fraction of diamagnetic ^{7}Li environments in these disordered spinel samples is no more than 3% of the total Li content indicating that there is excellent F solubility in the $Li_{1.47}Mn_{1.6}O_{3.7}F_{0.3}$ and $Li_2Mn_{1.6}O_{3.7}F_{0.3}$ spinel compositions.

A full understanding of the Li site occupancy is once again complicated by the presence of intrinsic disorder in the system that leads to a broad range of local environments, and thereby a broad range of overlapping signals observed via ^{7}Li NMR. However, $Li_2Mn_{1.6}O_{3.7}F_{0.3}$ exhibits a slightly broader pj-MATPASS (projected magic-angle turning and phase-adjusted sideband separation) spectrum consistent with the larger range of local environments expected for this more disordered material.

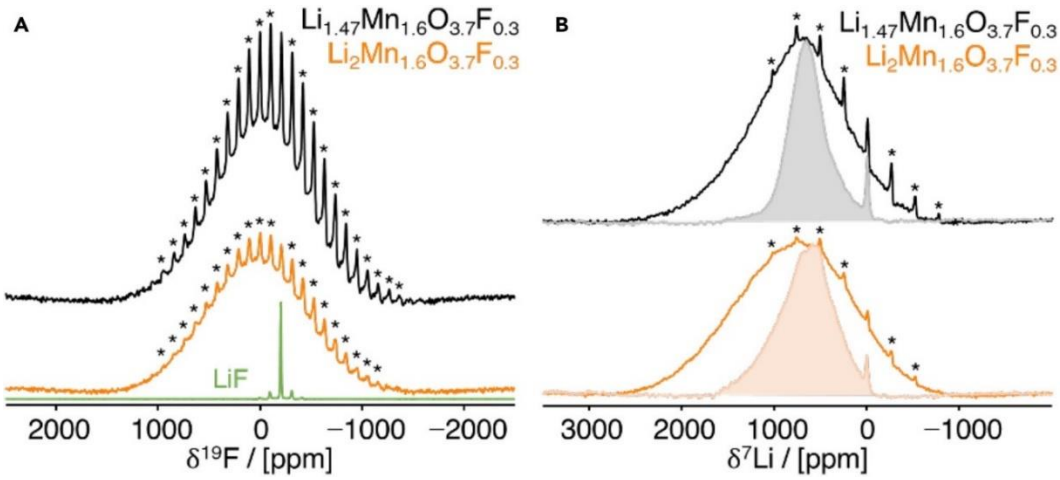

Figure 3.14 – ssNMR spectra obtained on the as-synthesized partially (dis)ordered spinel materials. (**a**) ^{19}F ssNMR spectra obtained by summing multiple spin-echo sub-spectra acquired at different excitation frequencies to ensure homogeneous excitation of the broad lineshape. For comparison, a ^{19}F spectrum collected on LiF powder is overlaid. (**b**) ^{7}Li spin-echo (line) and pj-MATPASS (shaded, for clarity) ssNMR spectra of the as-synthesized materials. All spectra are scaled according to the moles of Li in the rotor and number of scans. The asterisks indicate the spinning sidebands.

For full discussion of the electrochemical behavior and cycling mechanism, the reader is directed to the published study. Briefly, the electrochemical curves for the prepared materials are shown in Figure 3.15 demonstrating smoothing out of the voltage curve with increasing Li contents, consistent with the order-to-disorder tuning of this series of compositions. While there is still much to be understood regarding both the short- and long-range nature of these materials, this study demonstrates the effect of tunable cation order on the electrochemical performance of spinel-like Li-ion

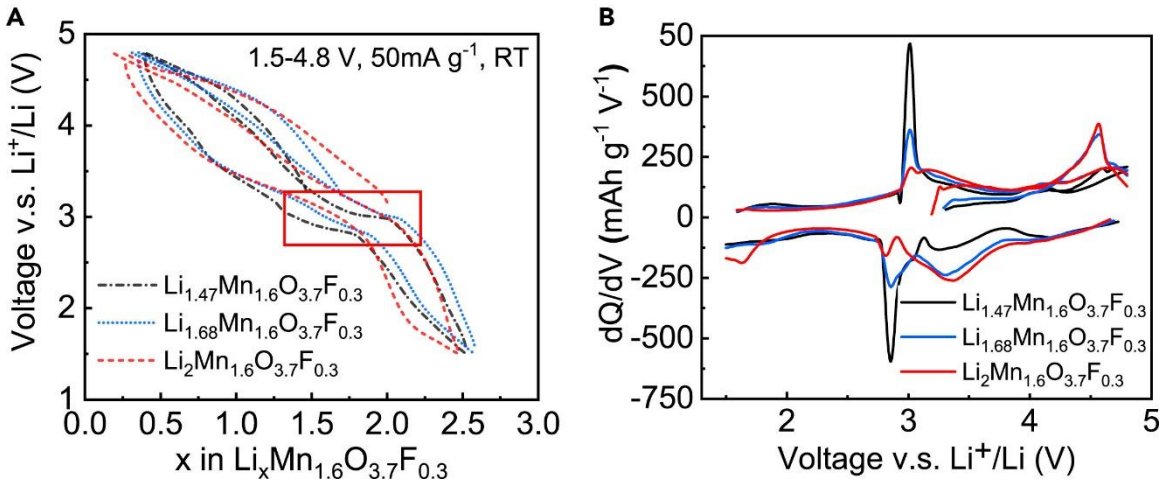

Figure 3.15 – Galvanostatic charge and discharge performance for Li-Mn-O-F series. (A) Voltage profile during first cycle and the second charge of $Li_{1.47}Mn_{1.6}O_{3.7}F_{0.3}$ (black dash dot), $Li_{1.68}Mn_{1.6}O_{3.7}F_{0.3}$ (blue dot), and $Li_2Mn_{1.6}O_{3.7}F_{0.3}$ (red dash). **(B)** Corresponding dQ/dV curves when cycled between 1.5 and 4.8 V at 50 mA g^{-1}.

cathodes.

3.4 Conclusion

In conclusion, DRX materials are a promising new Li-ion cathode class exhibiting high capacities and rich structural and compositional playgrounds. However, due to their disordered nature, structural characterization of these compounds is complicated preventing a full understanding of the reaction mechanisms at play. Regardless, ^{7}Li and ^{19}F NMR are a necessary component of the structural characterization due to their ability

to detect amorphous phases and assess the incorporation of Li and F in diamagnetic- vs. paramagnetic-like environments, which is especially relevant for these metastable DRX materials, as exemplified in the study on DRX metastability. Beyond that, a better understanding of the actual composition of the DRX phase and of the purity of the DRX samples is essential to develop structure/composition-property relationships. Additionally, we have shown here that both decreasing short-range order (as done for the high-entropy DRX study) and increasing short-range order (as done for the partially-ordered spinels) can have positive effects on the electrochemical behavior, yet the nature of this order is only somewhat understood. Thus, careful tuning and design of the short-range order is necessary to realize the potential of Li-excess DRX oxyfluoride cathode materials.

3.5 Appendix

3.5.1 *Ex situ* characterization of LNNOF25 and LNNOF54

The cyclability of the LNNOF25 and LNNOF54 before annealing was tested for 20 continuous cycles at 20 mA/g with a 1 min rest step between charge and discharge cycles. The voltage profiles for the first five cycles in two voltage ranges and their capacity evolution upon further cycles are shown in Figure 3.16. Clearly, LNNOF54 exhibits better capacity retention than LNNOF25. For example, when cycled between 1.5 and 4.6 V, LNNOF25 only retains 40% of its initial capacity after 20 cycles, whereas LNNOF54 retains 78% of its initial capacity. In addition, upon cycling, a more pronounced polarization increase is observed for the voltage profile of LNNOF25 than that of LNNOF54. Finally, for both materials, during discharge, the low-voltage region

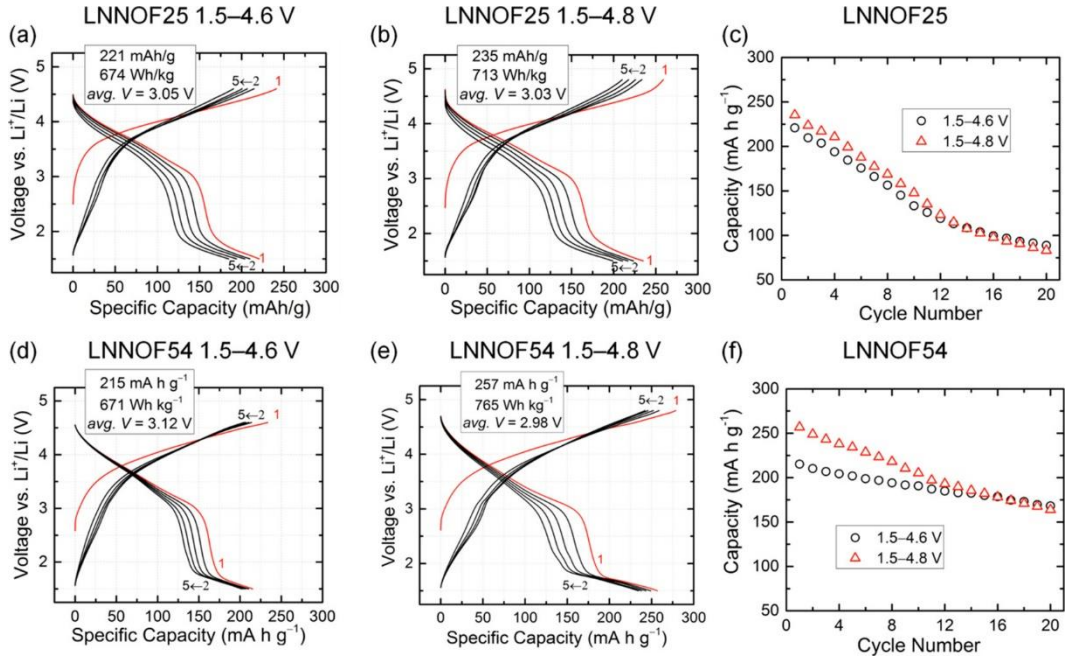

Figure 3.16 – Capacity retention of as-ball-milled **(a–c)** LNNOF25 and **(d–f)** LNNOF54 within two different voltage windows, 1.5–4.6 and 1.5–4.8 V. The first-cycle discharge capacity, energy density, and average voltage are provided at the top of each diagram. The voltage profiles for the first 5 cycles and the capacity evolution over 20 cycles for LNNOF25 and LNNOF54 are shown. The cycling rate for all tests is 20 mA/g.

below 2 V, which is associated with a pronounced polarization, evolves faster when charging to a higher upper cutoff voltage, consistent with the fact that oxygen loss and the subsequent surface densification are more significant at high voltages.

We performed ssNMR tests on both materials at the end of charge and discharge on the first cycle and at the end of discharge on the second cycle. The *ex situ* ^{19}F ssNMR spectra of LNNOF25 and LNNOF54, shown in Figure 3.17, show a predominant signal at −120 ppm attributed to the PTFE binder as well as a signal at −76 ppm attributed to decomposed electrolyte species containing PF_6^- in the charged samples. Considerable paramagnetic broadening is observed for all spectra, indicating that F remains incorporated in the bulk of the DRX material. Note that the spectrum of LNNOF25 upon discharge to 1.5 V in the first cycle is not included because the measurement was performed with a different instrument parameter and therefore cannot be directly compared to the other charge/discharge states. Notably, more significant signal loss is observed upon charge for the low-F LNNOF25 than for the high-F LNNOF54, a phenomenon that suggests more pronounced F migration to paramagnetic environment upon charging in LNNOF25 than in LNNOF54. Such F migration appears largely reversible as the ^{19}F signal is restored upon discharge. The *ex situ* ^{7}Li ssNMR spectra of the two materials, shown in Figure 3.18, both show a sharp peak around −1 to 0 ppm, attributed to a combination of Li_2CO3, Li_2O, LiF impurities and diamagnetic bulk environments in the disordered rocksalt phases. As expected, the signal observed for the charged samples has less intensity compared to the pristine and discharged samples as they contain less Li. The signal at −1 to 0 ppm slightly increases upon cycling, which ls

likely due to reactions occurred at the cathode-electrolyte interface and does not necessarily reflect changes in the bulk of the cathodes.

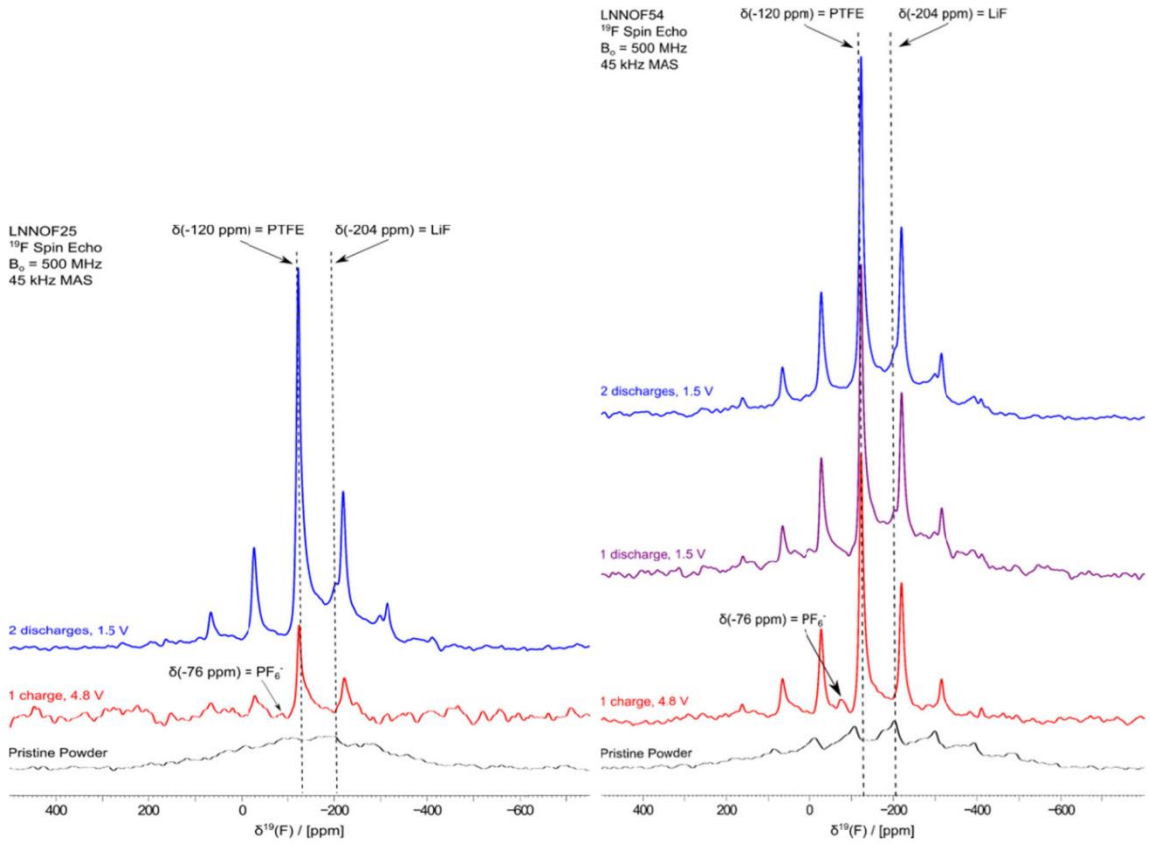

Figure 3.17 – ^{19}F spin echo ssNMR spectra obtained at 45 kHz MAS for LNNOF25 (left) and LNNOF54 (right) on cathode films at various charge/discharge states as well as on pristine powder.

These *ex situ* NMR results, along with the complementary *ex situ* XRD with shows that the two materials retain the rocksalt structure during cycling and that the lattice parameters are restored to the pristine states after discharge, indicate that the two materials undergo largely reversible changes during cycling.

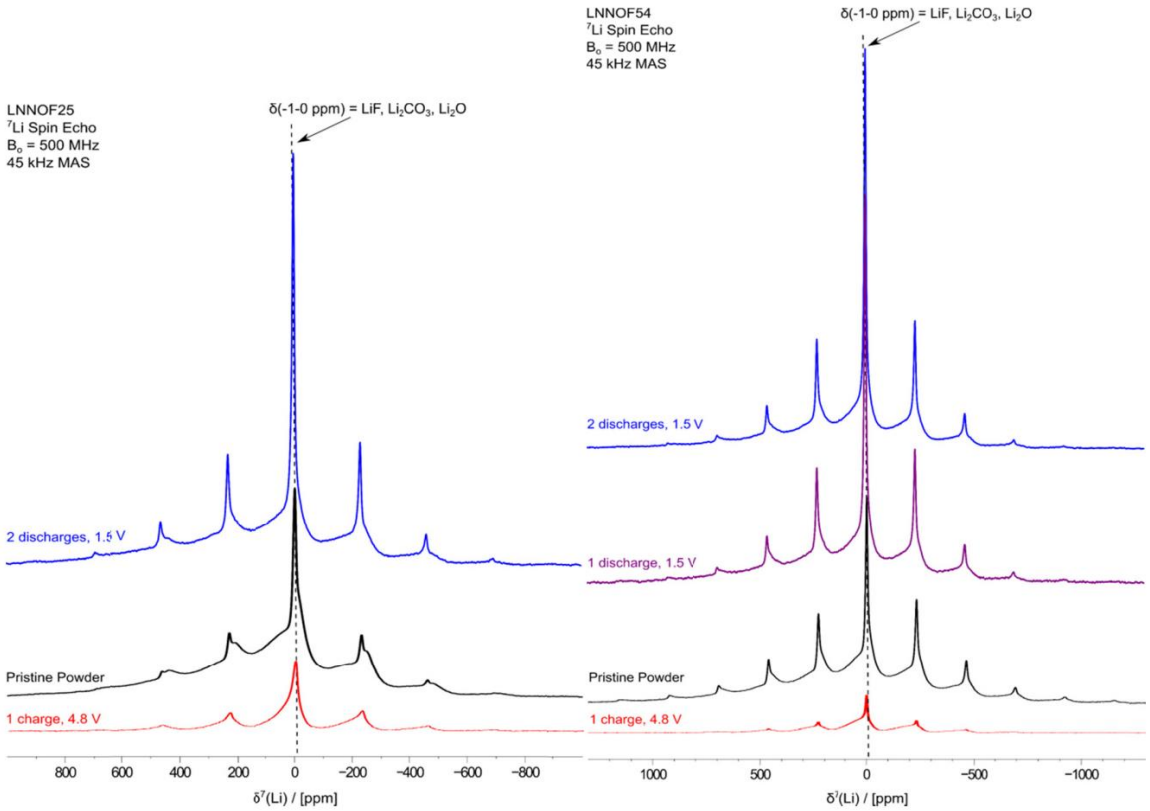

Figure 3.18 – ^{7}Li spin echo ssNMR spectra obtained at 45 kHz MAS for LNNOF25 (left) and LNNOF54 (right) on cathode films at various charge/discharge states as well as on pristine powder.

Chapter 4 – Probing Reaction Processes & Reversibility in Na_3FeF_6

[ee]Na_3FeF_6 is a promising Earth-abundant electrode that operates through a conversion-type charge-discharge reaction associated with a high theoretical capacity (336 mAh/g). In practice, however, only a third of this capacity is achieved during electrochemical cycling. In this study, we demonstrate a new rapid and environmentally friendly assisted-microwave method for the preparation of Na_3FeF_6. A comprehensive understanding of charge-discharge processes and of the reactivity of the cycled electrode samples is achieved using a combination of electrochemical tests, synchrotron X-ray diffraction, ^{57}Fe Mössbauer spectroscopy, X-ray photoelectron spectroscopy, magnetometry, and ^{23}Na/^{19}F solid-state nuclear magnetic resonance (NMR) complemented with first principles calculations of NMR properties. We find that the primary performance limitation of the Na_3FeF_6 electrode is the sluggish kinetics of the conversion reaction, while the methods employed for materials synthesis and electrode

[ee]The contents of this chapter have substantially appeared in reference [38]: **E. E. Foley**, A. Wong, R. C. Vincent, A. Manche, A. Zaveri, E. Gonzalez-Correa, G. Ménard, and R. J. Clément. Probing Reaction Processes and Reversibility in Earth-Abundant Na_3FeF_6 for Na-Ion Batteries. *Phys. Chem. Chem. Phys.* **2021**, 23 (36), 20052–20064. doi: 10.1039/d1cp02763h

preparation do not have a significant impact on the conversion efficiency and reversibility. Our work confirms that Na_3FeF_6 undergoes conversion into NaF and $Fe_{(s)}$ nanoparticles. The latter are found to be prone to oxidation prior to *ex situ* measurements, thus necessitating a robust analysis of the stable phases (here, NaF) formed upon conversion. We further confirm the conversion mechanism through *operando* magnetometry.

4.1 Introduction

Fluoride-based conversion-type NIB electrodes may reach energy densities up to 1400 Wh/kg on account of multi-electron redox processes[136] and thus present a promising direction for NIB electrodes. Yet, conversion reactions lead to a redistribution of all species in the electrode material, as recently shown by Grey and coauthors for $Li_xFe_yF_3$.[11] Thus, these materials generally require a greater driving force (overpotential) and cause more irreversible behavior than intercalation reactions. Further, conversion-type electrodes are often more kinetically-limited than intercalation-type electrodes, leading to sluggish redox reaction kinetics that are exacerbated by the insulating fluoride compounds. As a result, significant discrepancies are observed between theoretically-computed thermodynamic pathways and the experimentally-observed kinetically-limited phenomena, making it difficult to identify conversion reaction mechanisms.[137,138] Furthermore, the structural changes that occur on cycling often result in the formation of amorphous and metastable phases that are difficult to capture via diffraction and *ex situ* methods. For these reasons, the majority of fluoride-based conversion electrodes for NIBs do not have well-established reaction pathways.[136] In

turn, a poor understanding of reaction mechanisms makes it difficult to distinguish between intrinsic limitations imposed by the conversion reaction, and practical losses due to the starting particle morphology and electrode preparation. Thus, to understand the reaction mechanisms and limitations of current conversion materials in NIBs, and to enable the rational design of next-generation systems combining high capacity and long cycle life, local structure probes are warranted.

Na_3FeF_6 is a particularly attractive candidate electrode material for NIBs, as it is exclusively composed of Earth-abundant species. This compound was first explored as a conversion-type NIB electrode by Shakoor et al. and displayed a first discharge capacity of 125 mAh/g with very low reversibility.[139] Two follow-up studies used solution-phase syntheses and obtained more stable cycling with initial reversible capacities of 140 mAh/g and ≈ 64% capacity retention after 400 cycles.[140,141] These studies have focused on electrochemical characterization of Na_3FeF_6, with the only additional characterization reported being *ex situ* X-ray diffraction (XRD) by Shakoor et al.[139] The *ex situ* XRD data collected on cycled electrode samples were used as evidence that NaF and Fe formed on discharge, and the following conversion reaction was proposed:

$$Na_3FeF_6 + 3Na \rightleftarrows 6NaF + Fe.$$

However, the NaF and Fe peaks in the *ex situ* XRD are nearly indistinguishable from the baseline and incommensurate with the reported capacity, which suggests an incomplete understanding of the conversion mechanism at play. Thus, a closer investigation of the reaction process and limitations of Na_3FeF_6 is warranted.

In the present work, we revisit Na_3FeF_6 and aim for a complete understanding of key performance limitations to inform the design of next-generation NIB conversion electrodes. Here, Na_3FeF_6 is prepared through a similar mechanochemical method as Shakoor et al.,[139] as well as a new assisted-microwave synthesis method. The latter is a rapid, environmentally-friendly, all solid-state synthesis method allowing for the facile preparation of inorganic materials,[142] and this work demonstrates its promise for the preparation of battery electrode materials. Inspired by the need to test NIB materials in practical electrode setups and determine the intrinsic charge storage capacity of the conversion material in composite electrodes, we investigate the dependence of the electrochemical reversibility of Na_3FeF_6 on the electrode loading density and separate the capacity contributions associated with Na_3FeF_6 and with the conductive carbon matrix. We answer the question of why this material cannot reach its full conversion capacity based on Shakoor et al.'s proposed mechanism[139] through an in-depth characterization of the long- and short-range chemical changes occurring on cycling. For this, we employ a suite of tools sensitive to both amorphous and crystalline phases, including synchrotron X-ray diffraction (SXRD), $^{23}Na/^{19}F$ solid-state nuclear magnetic resonance (NMR) complemented with first principles calculations of NMR parameters, ^{57}Fe Mössbauer spectroscopy, magnetometry, and X-ray photoelectron spectroscopy (XPS). Our results indicate that the primary performance bottleneck of Na_3FeF_6 is the kinetic limitations of the conversion process due to the formation of insulating NaF domains that are also poorly Na^+ conducting on discharge, leading to a low discharge capacity and rapid capacity decay on subsequent cycles. Interestingly, the impact of the electrode film thickness on the capacity and its retention is minimal, indicating that the

kinetic limitations are already present at the (≤ 100 nm) particle scale. We also find that *ex situ* characterization of the electrode samples is complicated by the spontaneous oxidation of metastable Fe conversion phases during cell disassembly and sample handling (even in an inert environment) and develop a novel and robust analytical framework based on local structure probes and galvanostatic cycling to determine the true underlying conversion processes. An additional *operando* magnetometry experiment was done to confirm the mechanism deduced via *ex situ* methods.

The work presented in this chapter was lead and designed by me with a team of collaborators aiding with characterization. Dr. Anthony Wong in Prof. Gabriel Ménard's group collected the Mössbauer data and performed the chemical reduction of Na_3FeF_6. Rebecca Vincent in Prof. Ram Seshadri's group collected and analyzed the X-ray photoelectron spectroscopy (XPS) data. Within Prof. Raphaële Clément's group, Eliovardo Gonzalez-Correa collected the scanning electron microscope (SEM) data; Aryan Zaveri and Alexis Manche performed first-principles calculations of NMR parameters; and Howie Nguyen acquired and aided in the analysis of the *operando* magnetometry results. Dr. Molleigh Preefer at the Stanford Linear Accelerator Center (SLAC) aided in the X-ray absorption spectroscopy (XAS) measurements. All other work in this chapter (including material synthesis; analysis of the Mössbauer data; acquisition and analysis of the electrochemical, diffraction, NMR, and *ex situ* magnetometry results) was completed by me and I did most of the writing of the submitted manuscript.

4.2 Experimental

4.2.1 Materials Synthesis

Na_3FeF_6 was prepared via both microwave-assisted and mechanochemical methods using stoichiometric ratios of NaF (Strem, 99.99%) and FeF_3 (Sigma, 99.5%). For the microwave-assisted synthesis method, 300 mg of a ground stoichiometric mixture of the precursors was pressed into 6 mm pellets, placed inside BN crucibles, and sealed in vitreous silica ampules under 0.25 atm of Ar. The ampules were placed in a carbon-filled crucible and heated in a 1200 W domestic microwave oven (Panasonic, model NN-SN651WAZ) at 30% power (360 W) for 6 min. For the mechanochemical synthesis method, 1 g of a ground stoichiometric mixture of the precursors was placed in a 50 mL ZrO_2 ball-milling jar along with five 10 mm ZrO_2 balls and ten 5 mm ZrO_2 balls and sealed inside an Ar glovebox. The material was then ball-milled at 500 rpm for 24 h.

4.2.2 Electrochemical Characterization

For all samples the Na_3FeF_6 active material was ball-milled for 24 hrs at 300 rpm with five 10 mm ZrO_2 balls with 34 wt.% carbon (0.5 g in total) to form an electronically conductive carbon nanocomposite[36]. This nanocomposite was then hand-ground with polytetrafluoroethylene (PTFE) for 15 minutes and made into electrodes with a 63:32:5 weight ratio of Na_3FeF_6:C Super P:PTFE. The thick electrodes were prepared by pressing the electrode material into a thin 10 mm diameter pellet whereas for the thin electrodes the electrode material was hand-rolled into a film and punched into 6 mm disks. Their loading densities were 12 mg/cm^2 and 3 mg/cm^2, respectively. Blank cells were prepared in an analogous manner but now replacing the Na_3FeF_6 with NaF. All

electrochemical testing occurred in Swagelok-type cells with an excess of 1 M $NaPF_6$ (≥ 99% Strem Chemicals) in EC:DMC (1:1 w/w, ≥ 99% Sigma-Aldrich) electrolyte with < 25 ppm water content, a Na metal (Sigma-Aldrich) counter-electrode, and a glass fiber separator (Whatman GF/D).

Chemical reduction of the BM Na_3FeF_6 material was achieved by stirring a suspension of BM Na_3FeF_6 (25.0 mg, 0.1046 mmol) in anhydrous THF (2 mL) followed by the addition of Na metal (14.4 mg, 0.6281 mmol) and naphthalene (80.5 mg, 0.6281 mmol). The resulting green mixture was stirred at room temperature under an inert nitrogen atmosphere for three days, until the green coloration of the sodium naphthalenide had faded. The volatile components were then removed in vacuo, and the crude solid residue was analyzed spectroscopically.

4.2.3 Structural Characterization

X-Ray Diffraction. High-resolution synchrotron powder diffraction patterns were collected on Beamline 11-BM at the Advanced Photon Source (APS), Argonne National Laboratory using an average wavelength of 0.457897 Å. Room temperature data were collected between 2θ of 0.5° and 50°. Resulting patterns were refined using the Rietveld method in GSAS-II.[143]

Solid-State Nuclear Magnetic Resonance. ^{23}Na and ^{19}F ssNMR data were collected on the Na_3FeF_6 pristine and ex situ samples using a Bruker Avance 300 MHz (7.05 T) super wide-bore NMR spectrometer with Larmor frequencies of 79.48 MHz and 282.40 MHz, respectively, at room temperature. The data were obtained at 60 kHz magic-angle spinning (MAS) using a 1.3 mm double-resonance HX probe. ^{23}Na and ^{19}F

NMR data were referenced against 1M aqueous solutions of sodium chloride (NaCl, $\delta(^{23}Na) = 0$ ppm) and sodium fluoride (NaF, $\delta(^{19}F) = -118$ ppm) and these samples were also used for pulse calibration. Lineshape analysis was carried out within the Bruker Topspin software using the SOLA lineshape simulation package. ^{23}Na spin echo spectra were acquired on all samples using a 90° radiofrequency (RF) pulse of 0.38 μs and a 180° RF pulse of 0.76 μs at 200 W. A recycle delay between 10 ms and 2 s was used with the exact value optimized for each sample to ensure the full ^{23}Na signal was fully relaxed between pulses. ^{23}Na pj-MATPASS (projected Magic-Angle Turning Phase-Adjusted Sideband Separation)[79] isotropic spectra were also acquired on the pristine samples using a 90° RF pulse of 0.38 μs at 200 W, with a recycle delay of 500 ms. Transverse (T_2') relaxation times were obtained for each Na environment from an exponential fit of the decay of the signal intensity for each site as the echo delay was increased in an NMR spin echo pulse sequence, using an in-house MATLAB code written by Prof. Andrew Pell. ^{19}F spin echo spectra were acquired on all samples using a 90° RF pulse of 4.9 μs and a 180° RF pulse of 9.8 μs at 200 W. A recycle delay between 500 ms and 2 s was used where the exact value was optimized for each sample to ensure the ^{19}F NaF signal was fully relaxed between pulses. Further details on the analysis of the NMR results are provided in the Supplementary Information.

Mössbauer Spectroscopy. ^{57}Fe Mössbauer spectroscopy was performed using a SEECo Model W304 resonant gamma-ray spectrometer (activity = 100 mCi +/- 10 %, $^{57}Co/Rh$ source manufactured by Ritverc) equipped with a Janis Research Model SVT-400 cryostat system. The source linewidth was < 0.12 mm/s for the innermost lines of a 25-micron α-Fe foil standard. Isomer shifts were referenced to α-Fe foil at room

temperature. All ^{57}Fe Mössbauer samples contained 10-20 mg of electrode material prepared inside an Ar filled glovebox. The sample was loaded into a plastic holder, coated with oil, capped, and then measured under a positive flow of N_2 at 298 K. The data were fit using MossA, a program developed by Clemens Prescher at the University of Bayreuth.[144]

Magnetometry. Magnetic susceptibility measurements of pristine and ex situ samples of Na_3FeF_6 were measured with a Quantum Design Magnetic Property Measurement System 3 (MPMS) superconducting quantum interference device (SQUID) magnetometer. Samples of about 2 mg of Na_3FeF_6 were packed into a polypropylene holder in an Ar glovebox, snapped into a brass rod, and wrapped with a single layer of Kapton tape. Zero field-cooled (ZFC) and field-cooled (FC) susceptibility was measured on warming from 2 to 350 K in an applied field of 2000 Oe. Magnetic hysteresis curves were obtained at 2 K in the range of -7 T to 7 T.

X-Ray Photoelectron Spectroscopy. X-ray photoelectron spectroscopy was performed on select pristine and ex situ samples. The samples were loaded onto an air-free sample holder in an Ar-filled glovebox. The powder was spread onto double-sided scotch tape attached to a stainless steel sample holder. A lid with an O-ring seal was secured onto the sample holder to transfer the samples into the XPS chamber. Once under vacuum, the lid was removed such that the samples were never exposed to air. The samples were measured using a Thermo Fisher Escalab Xi+ XPS equipped with a monochromated Al anode (E = 1486.7 eV). Survey scans were collected at 100 eV pass energy with 50 ms of dwell time; two scans were averaged. High resolution scans were collected for Fe from the pristine active material sample of Na_3FeF_6 at 20 eV pass energy

with 100 ms of dwell time; five scans were averaged. Anticipating lower resolution from the discharged and charged ex situ Na_3FeF_6 samples, which were ground with carbon and polymeric binder for cycling, the Fe high resolutions scans were collected at a 20 eV pass energy with 100 ms of dwell time, and ten scans were averaged. Fits were executed using CasaXPS with Tougaard backgrounds and 60% Gaussian and 40% Lorentzian peak shapes. The spectrum for the pristine Na_3FeF_6 was referenced to the adventitious carbon C 1*s* peak at 284.8 eV. The spectra for the *ex situ* samples were referenced to the C 1*s* peak of graphite at 284.4 eV.[145]

4.2.4 Calculation of NMR Parameters

Spin-unrestricted hybrid density functional theory (DFT) / Hartree Fock (HF) calculations were performed using the CRYSTAL17 all-electron linear combination of atomic orbital code[146,147] to determine ^{23}Na and ^{19}F NMR parameters in Na_3FeF_6. Two spin-polarized exchange-correlation functionals based upon the B3LYP form,[104,148–150] and with Fock exchange weights of F_0 = 20% (B3LYP or H20) and 35% (H35) were chosen for their good performance for the electronic structure and band gaps of transition metal compounds (B3LYP or H20),[151,152] and for their accurate description of the magnetic properties of related compounds (H35).[153–155] Besides, previous studies have shown that the hyperfine shifts calculated with the H20 and the H35 functionals on similar compounds are in good agreement with experiment.[60,63]

All-electron atom-centered basis sets comprising fixed contractions of Gaussian primitive functions were employed throughout. Two types of basis sets were used: a smaller basis set (BS-I) was employed for structural optimizations, and a larger basis set

(BS-II) was used for computing ^{23}Na and ^{19}F NMR parameters which require an accurate description of the occupation of core-like electronic states. For BS-I, individual atomic sets are of the form (15*s*7*p*)/[1*s*3*sp*] for Na, (20*s*12*p*5*d*)/[1*s*4*sp*2*d*] for Fe, and (10*s*6*p*1*d*)/[4*s*3*p*1*d*] for F the values in parentheses denote the number of Gaussian primitives and the values in square brackets the contraction scheme. All BS-I sets were obtained from the CRYSTAL online repository and were unmodified from their previous use in a broad range of compounds.[146] For BS-II, modified IGLO-III and (10*s*6*p*2*d*)/[6*s*5*p*2*d*] sets were adopted for F, a flexible and extended TZDP-derived (11*s*7*p*)/[7*s*3*p*] set was used for Na, and an Ahlrichs DZP-derived[156] (13*s*9*p*5*d*)/[7*s*5*p*3*d*] was adopted for Fe.

NMR parameters were computed on the fully optimized (atomic positions and cell parameters) Na_3FeF_6 structure ($P2_1$).[157] All first principles structural optimizations were carried out in the ferromagnetic (FM) state, after removal of all symmetry constraints (within the *P*1 space group) and using the H20 and H35 hybrid functionals. A 160 atom 2 x 2 x 2 supercell was used throughout. Structural optimizations were pursued using the quasi-Newton algorithm with RMS convergence tolerances of 10^{-7}, 0.0003, and 0.0012 au for total energy, root-mean-square (rms) force, and rms displacement, respectively. Tolerances for maximum force and displacement components were set to 1.5 times the respective rms values. Sufficient convergence in total energies and spin densities was obtained by application of integral series truncation thresholds of 10^{-7}, 10^{-7}, 10^{-7}, 10^{-7}, and 10^{-14} for Coulomb overlap and penetration, exchange overlap, and g- and n-series exchange penetration, respectively, as defined in the CRYSTAL17 documentation.[146] The final total energies and spin and

charge distributions were obtained in the absence of any spin and eigenvalue constraints. NMR parameters were obtained on ferromagnetically aligned supercells, and on supercells in which one Fe spin was flipped, using BS-II sets and a method identical to that described in Middlemiss et al.'s work.[63] Anisotropic Monkhorst-Pack reciprocal space meshes[158] with shrinking factors 6 9 3 were used for both H20 and H35 calculations. The lattice parameters for the Na_3FeF_6 structures relaxed using the H20 and H35 functionals are compared to the experimental (EXP) unit cell parameters[157] in Table S4.

4.3 Results & Discussion

4.3.1 Characterization of as-synthesized Na_3FeF_6

Na_3FeF_6 forms a distorted ordered double perovskite structure, more clearly written as $(Na2)_2(Na1)FeF_6$, with space group $P2_1$. This structure (Figure 4.1) characterized by tilted corner-sharing $(Na1)F_6$ and FeF_6 octahedra, with the two remaining Na atoms filling the Na2 sites between the octahedral chains. Synchrotron XRD (SXRD) patterns collected on pristine and C-coated Na_3FeF_6 samples prepared via mechanochemical/ball-mill (BM) and microwave (MW) synthesis are shown in Figure 4.2a along with their Rietveld refinements. A small NaF precursor impurity phase is seen at Q = 2.71 $Å^{-1}$ for the MW samples and a ZrO_2 impurity is seen at Q = 1.98 and 2.12 $Å^{-1}$ for the BM samples from the jars used for the milling. As summarized in Appendix 4.5.1, the Na_3FeF_6 lattice parameters for the as-synthesized materials show little variation between samples and are in good agreement with previously reported structures. The peak broadening observed for the BM and C-coated samples obtained by ball-milling

with a conductive carbon additive is attributed to the formation of ≤ 100 nm particles upon high-energy milling, as shown in the SEM micrographs in Figure 4.2b-e. This procedure may also result in strained particles and an overall decrease in crystallinity, which could also contribute to peak broadening. The greater size of the particle agglomerates in the C-coated materials (Figure 4.2c,e) indicates successful formation of a C nanocomposite.[36]

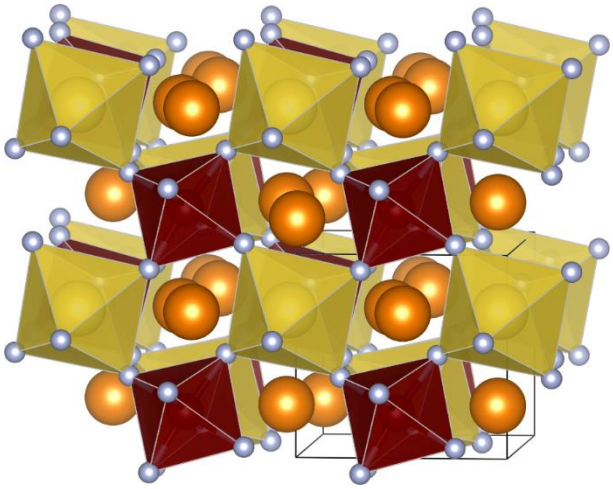

Figure 4.1 – Structure of Na_3FeF_6 = $(Na2)_2(Na1)FeF_6$. The two distinct Na sites, Na1 and Na2, are labeled in yellow and orange, respectively. Fluorine is shown in grey and iron in burgundy.

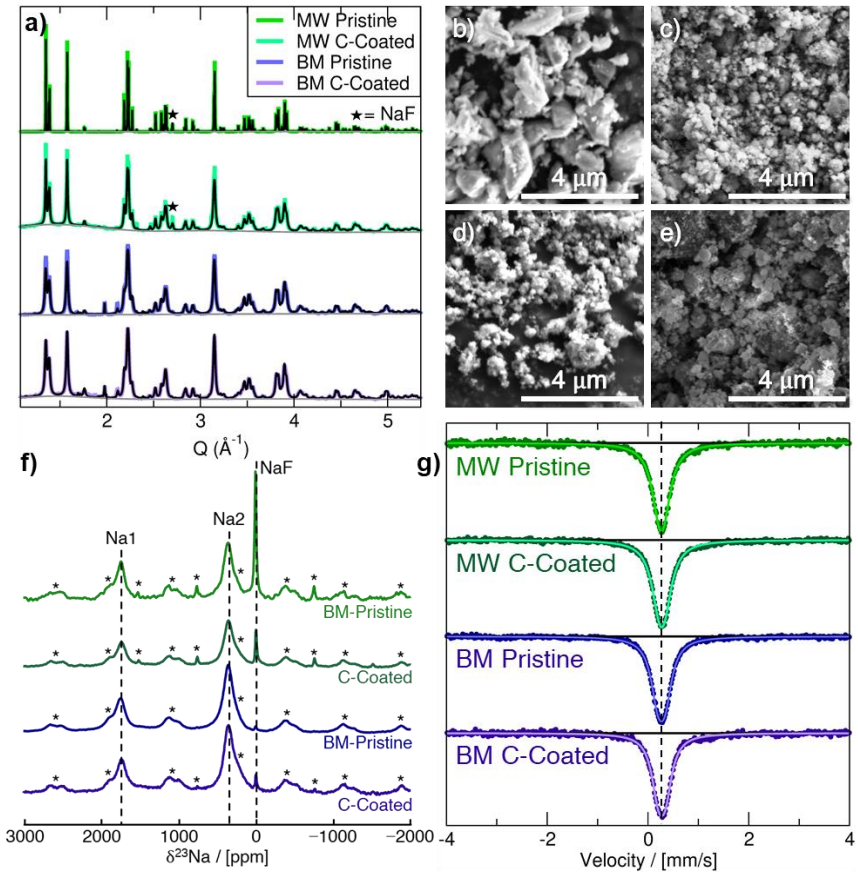

Figure 4.2 – Structural Characterization of As-Prepared Na_3FeF_6 Materials. a) SXRD pattern and Rietveld refinement (black) for each sample. **b-e)** SEM images obtained of MW pristine **(b),** MW C-coated **(c),** BM pristine **(d)**, and BM C-coated **(e)** samples. **f)** ^{23}Na spin echo NMR spectra collected on the as-prepared materials. Each spectrum is scaled according to the number of moles of material in the rotor and the number of scans collected during the experiment. Spinning sidebands are indicated by an asterisk (*). **g)** Zero-field, 298 K ^{57}Fe Mössbauer spectra obtained on the as-prepared materials. The dashed line corresponds to an isomer shift (δ) of 0.27 mm/s typical of an Fe^{3+} ion in an octahedral environment.

^{23}Na and ^{19}F solid-state NMR experiments were conducted to obtain further insights into the local structure of Na_3FeF_6. The presence of open-shell Fe^{3+} species in these compounds results in strong paramagnetic interactions between unpaired electron spins nominally present in the Fe 3*d* orbitals and $^{23}Na/^{19}F$ nuclear spins. These strong interactions result in significant NMR line broadening and large chemical shifts, complicating the attribution of spectral features to specific local environments in the material. Here, the assignment of the complex NMR spectra is assisted by first principles

hybrid density functional theory (DFT) / Hartree Fock (HF) calculations of paramagnetic ^{23}Na and ^{19}F NMR parameters using the CRYSTAL17 code on the optimized Na_3FeF_6 structure (details of the analysis in Appendix 4.5.2). The isotropic chemical shift (δ_{iso}) of ^{23}Na and ^{19}F nuclei in Na_3FeF_6 is dominated by the paramagnetic (Fermi contact) shift resulting from delocalization of unpaired electron spin density from the Fe 3*d* orbitals to the $^{23}Na/^{19}F$ *s* orbitals. For an $I = 3/2$ quadrupolar nucleus such as ^{23}Na, the interaction between the nuclear quadrupole moment and the electric field gradient (EFG) present at the nucleus leads to a further broadening of the spectrum and to a shift of the ^{23}Na resonant frequency due to second-order effects (denoted δ_Q). The observed chemical shift (δ_{obs}) is then the sum of the isotropic Fermi contact shift and of the second-order quadrupolar shift: $\delta_{obs} = \delta_{iso} + \delta_Q$. In contrast, ^{19}F is a spin-1/2 nucleus with no quadrupole moment and so $\delta_{obs} = \delta_{iso}$.

Table 4.1 - First principles ^{23}Na paramagnetic NMR parameters computed on Na_3FeF_6. Calculations performed using the B3LYP hybrid functional with 20% (H20) and 35% (H35) Hartree-Fock exchange, respectively, as implemented in the CRYSTAL17 code. The predicted NMR properties were computed on ferromagnetically-aligned cells and subsequently scaled using a magnetic scaling factor $\mathbf{\Phi} = 0.0328$ to compare with the room temperature (paramagnetic) ^{23}Na solid-state NMR data obtained at an external magnetic field of $B_0 = 7.05$ T. δ_{iso} is the isotropic Fermi contact shift, δ_Q the second-order quadrupolar shift, and $\delta_{obs} = \delta_{iso} + \delta_Q$ the observed chemical shift.

Environment	Parameter	OPT H20	OPT H35
Na1 (x1)	δ_{iso} / ppm	2564	1923
	δ_Q / ppm	−20	−20
	δ_{obs} / ppm	2544	1903
Na2 (x2)	δ_{iso} / ppm	484	148
	δ_Q / ppm	−27	−28
	δ_{obs} / ppm	457	120

^{23}Na NMR characterization of the as-synthesized and C-coated materials is shown in Figure 4.2f. There are three main signals in the ^{23}Na NMR spectra: a diamagnetic signal at 0 ppm assigned to NaF and two paramagnetic signals near 350

ppm and 1750 ppm. The 350 and 1750 ppm signals observed experimentally are consistent with the computed NMR shifts for Na2 and Na1 sites in the Na_3FeF_6 structure, respectively, as summarized in Table 4.1 . We note that two calculations were performed using two different hybrid DFT/HF exchange-correlation functionals (H20 and H35) as it has been shown that paramagnetic NMR shifts computed using the H20 and H35 functionals provide approximate upper and lower bounds to the observed shift, respectively. This is confirmed here with, *e.g.*, the 350 ppm experimental shift lying in between the 120 ppm (H35) and 457 ppm (H20) values computed for Na2. By fitting the spectra in Figure 4.2f to extract the relative integrated intensity of each ^{23}Na resonance, scaled by the transverse relaxation time (T_2') to account for signal loss over the course of the experiment, we can deduce the population of NaF, Na1 and Na2 environments in the sample. We find that < 1% of the integrated ^{23}Na signal intensity corresponds to NaF for the two BM samples, whereas about 7% (± 3%) of the integrated ^{23}Na signal intensity corresponds to NaF for the two MW samples. In all spectra, the ratio of Na2:Na1 present is 2(± 0.2):1, consistent with the multiplicity of Na1 and Na2 sites in the Na_3FeF_6 = $(Na2)_2(Na1)FeF_6$ crystal structure.

The only signal observed in ^{19}F NMR data shown in in Figure 4.3a is the NaF impurity phase at −224 ppm. In agreement with the SXRD and ^{23}Na NMR data, this impurity does not appear for the BM samples and decreases for the MW samples after C-coating. No paramagnetic ^{19}F NMR signal attributable to the Na_3FeF_6 phase is observed in the spectra. While this result may be surprising at first, it can easily be explained by the fact that NMR resonances associated with ^{19}F nuclei directly bonded to paramagnetic

species (here, Fe^{3+}) are too broad and too short lived to be observed, as we recently showed in related electrode compounds.[28]

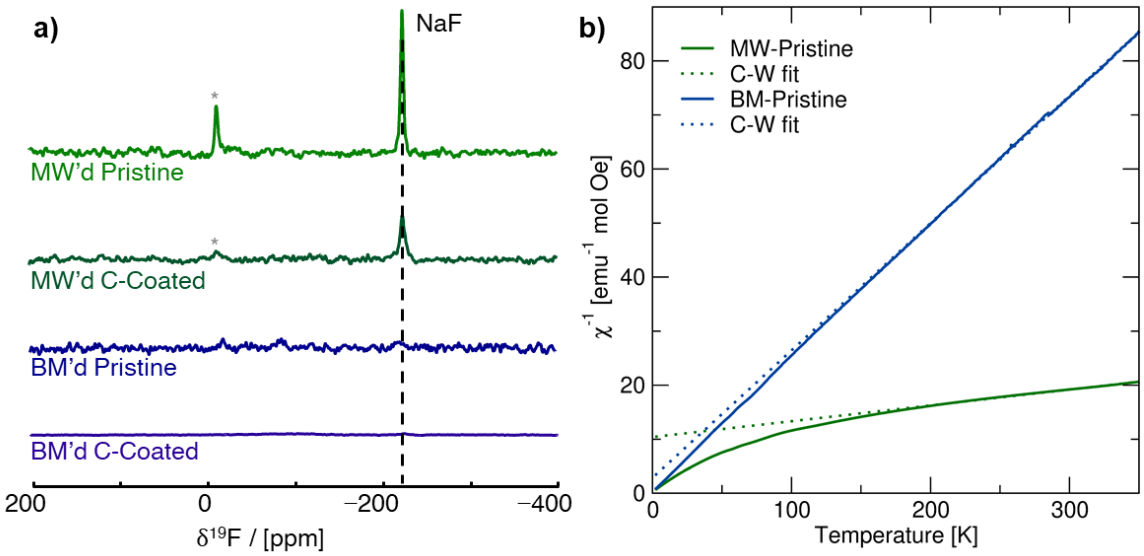

Figure 4.3 – ^{19}F ssNMR and Magnetic Data collected on the As-Prepared Na_3FeF_6 Samples. a) ^{19}F spin echo NMR spectra obtained on the as-prepared materials. Each spectrum is scaled according to the number of moles of material in the rotor and the number of scans collected during the NMR experiment. Spinning sidebands are indicated by an asterisk (*). **b)** Inverse magnetic susceptibility curves obtained at 2000 Oe on the pure pristine Na_3FeF_6 samples (solid lines), and associated Curie-Weiss fits (dashed lines).

^{57}Fe Mössbauer spectra are shown in Figure 4.2g for the as-synthesized materials. All Mössbauer spectra exhibit a singlet with an isomer shift (δ) of about 0.27 mm/s and a small quadrupole splitting (ΔE_Q) of 0.1 to 0.15 mm/s (exact values shown in Appendix 4.5.3. This signal can be assigned to octahedrally-coordinated Fe^{3+} (O_h-Fe^{3+}) surrounded by six F^- anions,[87] in good agreement with the Na_3FeF_6 crystal structure. The slightly larger quadrupole splitting in the BM samples is likely due to an increased amount of structural disorder, as expected from high-energy milling.

The magnetic susceptibility data collected on the pristine BM and MW Na_3FeF_6 powders are shown in Figure 4.3b. The susceptibility χ of the BM sample exhibits Curie-

Weiss-like behavior, *i.e.*, $\chi = \frac{C}{T-\theta}$, where C is the Curie constant, T is the temperature, and θ is the Weiss constant. A fit of the susceptibility data obtained between 150 and 350 K yields C = 4.211 emu K mol^{-1} Oe^{-1} and θ = −10 K. The value of C correlates with an effective magnetic moment (μ_{eff}) of 5.85 μ_B per Fe atom, indicating the presence of high-spin Fe^{3+} (theoretical spin-only magnetic moment $\mu_{SO}^{theo}(Fe^{3+})$ = 5.92 μ_B), which is consistent with the ^{57}Fe Mössbauer results. The small and negative θ = −10 K obtained for BM-Na_3FeF_6 is consistent with the previously reported value of θ = −12 K[159] and suggests that this material is weakly antiferromagnetic. In contrast to BM-Na_3FeF_6, attempts to fit the susceptibility of MW-Na_3FeF_6 with the Curie-Weiss equation resulted in nonphysical properties. We suspect that this sample contains a small amount of an amorphous, unreacted FeF_3 phase compensating for the NaF impurity phase observed via NMR. This impurity is impossible to distinguish from the major Na_3FeF_6 phase via ^{57}Fe Mössbauer spectroscopy, as both compounds have similar local Fe^{3+} environments and therefore similar resonances.

In summary, we have demonstrated that high-energy ball-milling and assisted-microwave synthesis are two possible preparation routes for Na_3FeF_6. While BM-Na_3FeF_6 is almost completely phase pure (with less than 1 % of the total Na molar content in NaF domains), MW-Na_3FeF_6 has a moderate amount of NaF and FeF_3 impurities detected by ^{23}Na/^{19}F NMR and magnetometry, respectively. Thus, despite being a fast and environmentally-friendly synthesis method,[142] the assisted-microwave synthesis protocol used here is unable to produce as high purity of a material as mechanochemical synthesis.

4.3.2 Electrochemical Properties

To determine the role of the electrode loading density on performance, the electrochemical properties of thin and thick (3 and 12 mg/cm^2 loading density, respectively) electrode films composed of BM and MW C-coated Na_3FeF_6 were investigated using galvanostatic cycling at a rate of C/20 (full (dis)charge in 20 hours) between 0.65 and 4 V vs. Na^+/Na. Negligible capacity (< 14 mAh/g) was observed when the cells were charged first (Figure 4.12a), indicating that a very small amount of Na (if any) can be extracted from the pristine structure. A rate of C/20 was used throughout as faster rates resulted in decreased capacities and reversibility (Figure 4.12a). Hence, all the data shown in Figure 4.4 and Figure 4.12b-d were obtained on cells discharged first at a rate of C/20. As shown in Figure 4.12b, particle size reduction and C-coating is required to achieve appreciable electrochemical activity from the intrinsically insulating Na_3FeF_6 phase.

Galvanostatic electrochemical profiles are shown in Figure 4.4a,b for the BM thin and BM thick electrodes, and Figure 4.12c for the MW thin and MW thick electrodes. All cells exhibit first discharge capacities between 160 and 190 mAh/g, with significant capacity fade (> 36%) on second discharge. The discharge capacity retention of BM and MW thin and thick electrodes over the first 20 cycles is shown in Figure 4.4c. For each electrode type, the total capacity and the actual Na_3FeF_6 active material capacity obtained after subtracting the capacity of a thin or thick blank cell (as appropriate) are depicted. The blank cells (NaF in place of Na_3FeF_6) provide an estimate of the capacity due to the presence of a significant amount of conductive carbon additive in the composite Na_3FeF_6 electrodes (32 wt.%). Galvanostatic cycling (Figure 4.12d) of these

blank cells results in sloping electrochemical profiles with an average potential of 1.3 V and an initial reversible capacity of 75 and 100 mAh/g for the thick and thin blank cells, respectively, that gradually decays on subsequent cycles. Thus, a significant fraction of the capacity observed for the Na_3FeF_6 electrodes arises from Na intercalation into the C matrix rather than the conversion process, as shown in Figure 4.4c, with more Na intercalation into C expected for the thin electrodes. MW Na_3FeF_6 electrodes feature higher initial discharge capacities, but also faster capacity fade compared to their BM counterparts, likely due to the presence of an electrochemically active FeF_3 impurity.[44,160] Notably, the BM thin cell exhibits less capacity fade and a higher average potential (1.2 V vs. 1.1 V) compared to all other electrode formulations, and a more sloping discharge profile compared to that of the BM thick cell, as supported by the dQ/dV comparison shown in Figure 4.12f. Hence, for the high purity BM Na_3FeF_6 electrodes, thinner electrode films appear to enhance the reversibility of the charge-discharge reactions.

To investigate the origin of this loading density-dependent performance, galvanostatic intermittent titration technique (GITT) tests were conducted on BM-Na_3FeF_6 thin and thick electrodes, as shown in Figure 4.4d. Following a 30 minute C/20 current pulse, the voltage was allowed to equilibrate for 4 hours to obtain an estimate of the equilibrium voltage and overpotential. A clear equilibrium voltage plateau is observed at 1.4 V for both electrodes in the GITT tests. In contrast, this plateau is only clearly visible in the galvanostatic voltage profile of the thick electrode cell and at a lower voltage of 0.95 V (see Figure 4.4b), presumably due to the significant polarization upon galvanostatic discharge at a rate of C/20.

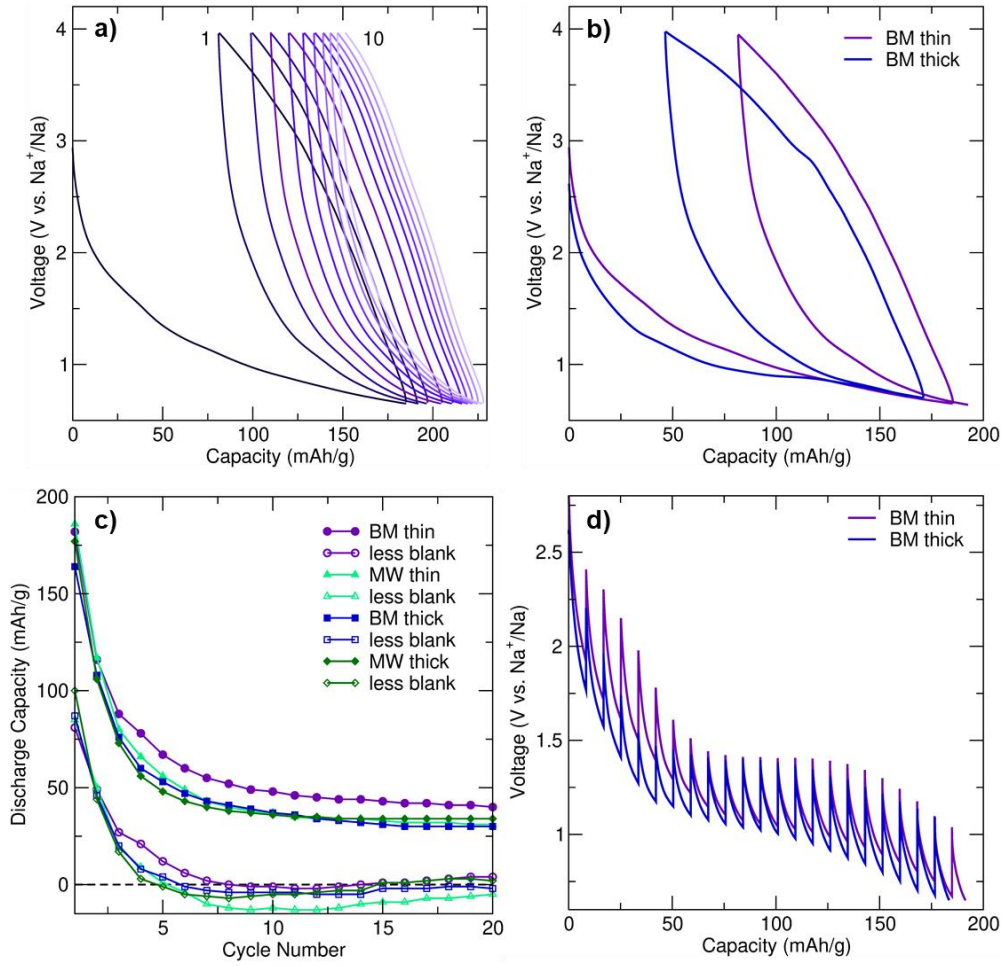

Figure 4.4. Electrochemical Characterization of Na_3FeF_6. a) First ten cycles for BM-Na_3FeF_6 thin cells (C/20 rate). **b)** First two charge and discharge cycles for BM-Na_3FeF_6 thin and thick cells (C/20 rate). **c)** Discharge capacity retention for Na_3FeF_6 cells (filled symbols) and for Na_3FeF_6 cells with the corresponding blank cell capacity subtracted (unfilled symbols). Three cells were averaged for each point. **d)** GITT test (C/20 rate) for the first discharge cycle of BM thin and thick cells.

The evolution of the polarization or overpotential during the first discharge process as obtained from the GITT tests is plotted in Figure 4.12e. For the thick electrode, the overpotential initially decreases from 0.55 V at 10 mAh/g to 0.3 V at 50 mAh/g. For the thin electrode, a similar albeit delayed decrease in the overpotential is observed from 30 mAh/g to 60 mAh/g. We attribute this electrochemical region (≤ 50-60 mAh/g of capacity) to Na intercalation into the C matrix and explain the decrease in overpotential to gradually more facile Na insertion upon discharge. The delay in the

overpotential decrease in the case of the BM thin electrode may be due to side reactions and/or greater Na intercalation into C during the initial stages of discharge (at high voltage), which is consistent with the higher average potential observed for the thin BM electrode (Figure 4.4b). Furthermore, greater Na intercalation into the C matrix of the thin BM electrode is consistent with its more sloping voltage profile and the absence of a clear electrochemical plateau in its galvanostatic profile.

The 1.4 V equilibrium voltage plateau region (50-60 to 150 mAh/g of capacity) of the GITT curves in Figure 4.4d is assigned to bulk Na_3FeF_6 conversion, and the steady increase in the overpotential up to 0.45 V for both electrodes is attributed to a kinetically-hindered conversion process and the build-up of insulating NaF domains that are also poorly Na^+ conducting, as will be discussed later. Perhaps unsurprisingly, the 0.45 V overpotential value matches the voltage difference between the 0.95 V electrochemical plateau observed during galvanostatic cycling for the thick BM electrode and the 1.4 V equilibrium voltage obtained from GITT tests, indicating that kinetic limitations are important when cycling at a rate of C/20. The thin BM electrode results suggest that, at low electrode loading densities, Na intercalation into the C matrix is kinetically-preferred over Na_3FeF_6 conversion over the plateau region. Indeed, Na intercalation into C is more prevalent when the cell is discharged at C/20 without resting periods, resulting in a sloping galvanostatic profile and no voltage plateau (Figure 4.4b). Yet, when the cell is allowed to rest at regular intervals (GITT results), or for thicker electrode films, differences in the rate of Na intercalation and Na_3FeF_6 conversion are reduced, and a clear electrochemical plateau is observed (Figure 4.4d).

In summary, the electrochemical performance is improved in the higher purity BM electrodes although the rapidly prepared MW electrodes perform comparably. While electrodes prepared with a lower loading density (e.g., BM thin) result in greater Na intercalation into the carbon matrix at practical C rates, leading to more sloping profiles and a greater average potential, the electrode loading density does not seem to affect the Na_3FeF_6 conversion mechanism nor its efficiency. The capacity fades quickly for all cells, likely due to the significant kinetic limitations and irreversibility of the conversion process. Our comparison of the electrochemical activity of the C-coated Na_3FeF_6 cells with blank cells is particularly informative in this regard (Figure 4.4c), as it clearly shows some electrochemical activity from the Na_3FeF_6 active material for the first 5 cycles, but past cycle 5 most of the capacity is attributable to Na intercalation into carbon. Thus, we conclude that Na_3FeF_6 suffers from severe charge-discharge irreversibility and is only electrochemically-active for about 5 cycles.

4.3.3 Characterization of Conversion Processes

To elucidate the reaction processes and causes of charge-discharge irreversibility for the Na_3FeF_6 conversion-type electrode, we carried out an in-depth characterization of *ex situ* electrode samples collected over the first 10 cycles, through a combination of solid-state NMR, SXRD, XPS, magnetometry and ^{57}Fe Mössbauer measurements.

High resolution *ex situ* SXRD was performed on several MW thick Na_3FeF_6 electrodes at various states of charge to identify the crystalline phases forming on (dis)charge as shown in Figure 4.5. All patterns can be successfully fitted with contributions from Na_3FeF_6 ($P2_1$) and NaF (Fm-3m) phases. The amount of NaF

increases on discharge and decreases on charge, consistent with a conversion process. Moreover, low intensity reflections at Q ≈ 1.3, 1.9, 2.1, 2.4, 3.1, and 3.8 $Å^{-1}$ indicate the formation of a small amount of (a) crystalline phase(s) on discharge that is only partially reversible on subsequent charge. Yet, none of our attempts to match these reflections to any of the known Na-, Fe-, O- or F-containing phases in the International Crystal Structure Database (ICSD) database were successful (full list of attempted phases in Appendix 4.5.1). The unidentifiable crystalline phase(s) appear(s) to only account for a small fraction of the sample and could potentially arise from side-reactions (*e.g.*, electrolyte decomposition). A broad baseline is noticeable in all but the pristine sample due to its significantly higher signal intensity. This baseline is predominantly attributed to the Kapton capillary used to hold the sample, although contributions from amorphous phase(s) formed during the conversion process cannot be excluded for patterns collected on *ex situ* cycled sample. Notably, we could not detect any crystalline α-Fe in our *ex situ* samples, in contrast to Shakoor et al.'s findings.[139] Yet, in this previous study, the claimed Fe reflections are extremely difficult to discern from the noise in the *ex situ* patterns.

Overall, our results exemplify the limited utility of long-range diffraction techniques to monitor conversion processes and warrant the implementation of more local and quantitative probes to gain insights into nano-sized and disordered/amorphous phases during cycling. Specifically, our *ex situ* SXRD results indicate the conversion of Na_3FeF_6 to NaF on discharge, yet are unable to identify any Fe-containing crystalline phase and cannot rule out the possibility of forming

amorphous Fe nanoparticles, as has been reported in related conversion electrodes.[161,162]

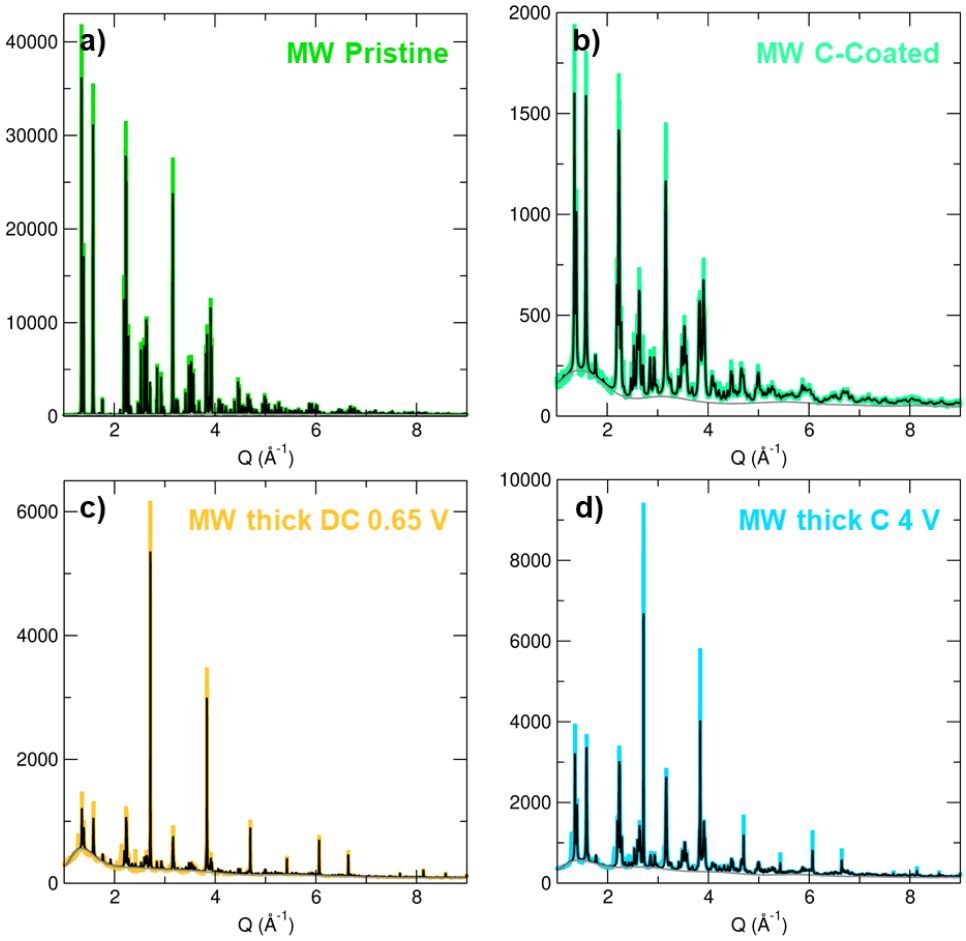

Figure 4.5 – Synchrotron XRD *ex situ* Characterization. Synchrotron XRD pattern (colored line) and the total Rietveld refinement (black) for MW pristine **(a)**, MW C-coated **(b)**, and MW thick discharge **(c)** and charge **(d)**. The grey line corresponds to the background used for each diffraction pattern which is predominantly attributed to the Kapton capillary used to hold each sample.

Ex situ ^{23}Na NMR is key in understanding the conversion behavior of Na_3FeF_6, as it enables us to identify and quantify both crystalline and amorphous Na-containing phases formed on (dis)charge. MW thick, BM thick and BM thin electrodes are examined here to investigate the impact of synthesis and electrode loading density on the degree of conversion during cycling. ^{23}Na spin echo spectra collected on *ex situ* samples stopped at the end of the initial discharge to 0.65 V, and upon subsequent charge to 4 V, for the

three electrode types, are shown in Figure 4.6. A more in-depth NMR analysis of a series of *ex situ* thick MW electrodes is shown in Figure 4.11. The three main resonances at ≈ 0 ppm (NaF), 1750 ppm (Na1), and 350 ppm (Na2), present in the spectra collected on the as-synthesized materials (Figure 4.2f) are also observed in the *ex situ* spectra, albeit with varying relative intensities as expected from the conversion process. Notably, no new ^{23}Na NMR signal appears on cycling. The evolution of the amount of diamagnetic Na-containing phase during cycling is obtained from the fitted ^{23}Na signal intensity at ≈ 0 ppm and shown in Figure 4.6b, with the remainder of the ^{23}Na NMR signal intensity attributed to Na_3FeF_6. Although most of the diamagnetic ^{23}Na signal can be attributed to NaF present in the pristine MW sample or formed on discharge, we cannot rule out a small contribution to the ≈ 0 ppm signal intensity from Na_2CO_3 formed upon decomposition of the carbonate electrolyte and reaction with Na during cycling. Overall, the NaF signal increases on discharge and decreases on charge, with at least 50% of the total ^{23}Na signal intensity arising from the Na_3FeF_6 phase even at the bottom of discharge. Thus, Na_3FeF_6 conversion is incomplete on discharge and only partially reversible on subsequent charge.

Complementary *ex situ* ^{19}F NMR experiments were performed to gain further insights into NaF formation during cycling. The ^{19}F NMR spectra are shown in Figure 4.7 and exhibit three main signals: the NaF resonance at −224 ppm, the PTFE binder resonance at −122 ppm, and a resonance at −74.5 ppm indicating adsorption of electrolyte salt (e.g. PF_6^-) at the surface of the particles.[163] Overall, the relative intensity of the NaF signal, as shown in Figure 4.7d, follows the same trend as that already

discussed for NaF through ^{23}Na NMR, confirming that Na_2CO_3 contributes minimally to the diamagnetic (≈ 0 ppm) resonance in the ^{23}Na NMR data.

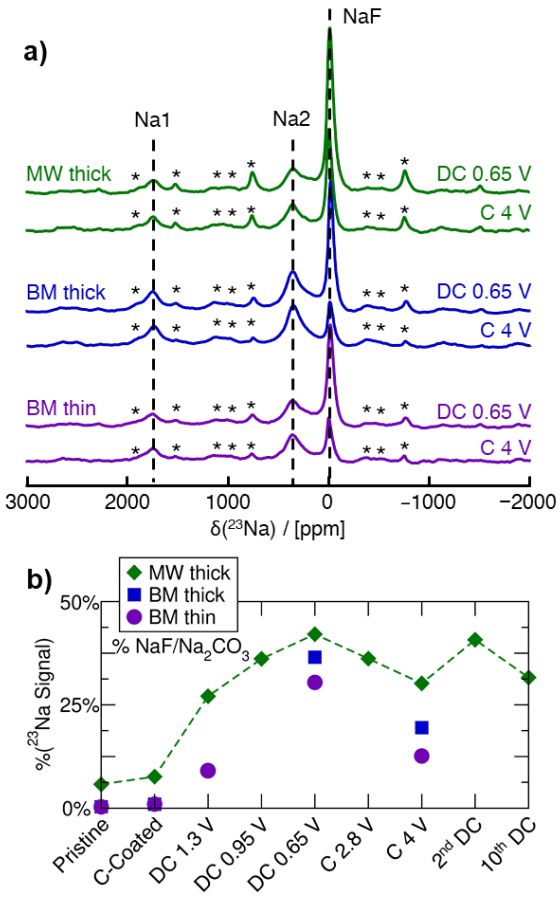

Figure 4.6 – ^{23}Na NMR of ex situ Na_3FeF_6. a) ^{23}Na spin echo NMR spectra of ex situ Na_3FeF_6 with each spectra scaled according to number of moles of material in the rotor and the number of scans used in the experiment. Spinning sidebands are indicated by an asterisk (*). **b)** Percent of the ^{23}Na signal (± 5%) after accounting for signal relaxation over the course of the NMR measurement (T2′ losses) corresponding to diamagnetic NaF at various states of charge.

After adjusting for the presence of NaF in the as-synthesized materials (see Table 4.2), ^{23}Na and ^{19}F NMR results indicate that high purity BM Na_3FeF_6 electrodes result in a higher degree of reconversion of NaF on charge (24 mol%) compared to MW Na_3FeF_6 (14 mol%), and therefore a higher degree of reversibility. Consistent with the electrochemical results presented earlier, the thinner BM electrode exhibits a low amount of conversion to NaF when discharged to 1.3 V (14 mol%) whereas the thicker

MW electrode shows much more conversion (40 mol%), indicating that a larger amount of the observed electrochemical capacity in the thin electrodes is attributable to the carbon additive rather than Na_3FeF_6 conversion. Thus, the higher reversibility of the thinner electrode is partially attributed to Na^+ intercalation into carbon[164,165] and/or capacitive storage at the surface of particles,[32,166] as these processes are fairly reversible.

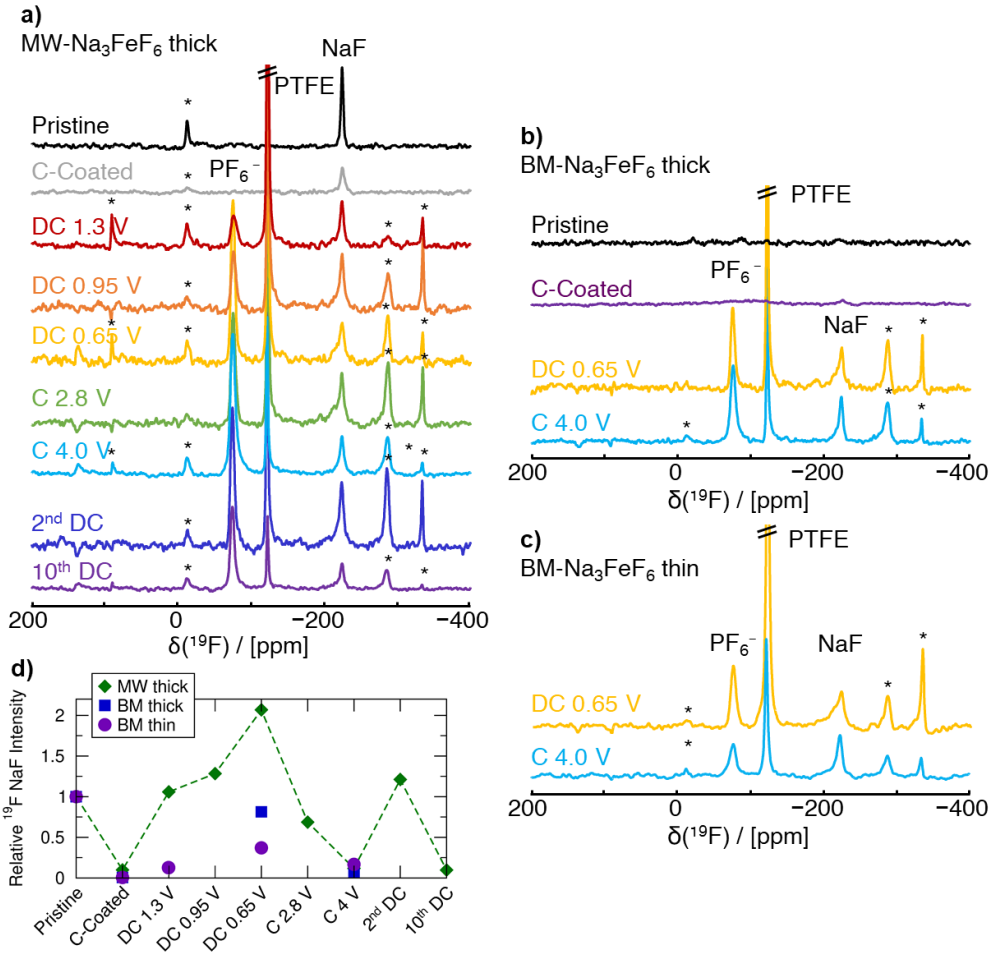

Figure 4.7 – ^{19}F NMR *ex situ* Characterization. ^{19}F spin echo NMR spectra collected on *ex situ* MW thick **(a)**, BM thick **(b)**, and BM thin **(c)** Na_3FeF_6. Each spectrum has been scaled according to the number of moles of material in the rotor and the number of scans collected during the NMR experiment. Spinning sidebands are indicated by an asterisk (*). **d)** Relative intensity of the ^{19}F NMR signal (± 0.1) corresponding to a diamagnetic NaF phase in *ex situ* samples stopped at various states of charge.

To monitor changes to the Fe redox state and local coordination environment on cycling, and to facilitate the identification of (a) new Fe-containing phase(s) formed

during electrochemical cycling, ^{57}Fe Mössbauer experiments were performed on *ex situ* MW thick, BM thick and BM thin electrode samples collected at the end of the initial discharge to 0.65 V, and upon subsequent charge to 4 V, with results shown in Figure 4.8 and values summarized in Appendix 4.5.3. All *ex situ* spectra exhibit a main (≥ 88%) resonance with similar δ and ΔE_Q values as the O_h-Fe^{3+} signal observed for the pristine Na_3FeF_6 powders. A minority (≤ 12%) doublet signal at $\delta \approx 1.16$ mm/s with $\Delta E_Q \approx 0.2$ mm/s is present in the spectra obtained on discharge and is attributed to a "reduced-Fe" species. Additional characterization of samples discharged to 0.65 V via XPS and magnetometry (details in Appendix 4.5.5) suggests the presence of an amorphous Fe^{2+}-containing phase that may also contain Fe^{3+} species. The evolution of the total ^{57}Fe Mössbauer signal throughout (dis)charge, as seen in Figure 4b, shows minimal change in this "reduced-Fe" signal. Clearly, the absence of a significant change to the main ^{57}Fe Mössbauer resonance upon cycling cannot simply be interpreted as a lack of electrochemical conversion, as ^{23}Na NMR indicated significant Na_3FeF_6 conversion to NaF upon cycling. Instead, part of the main O_h-Fe^{3+} signal may come from relaxation[161,167] and/or oxidation[168,169] of the newly formed metastable conversion products to (a) O_h-Fe^{3+} containing phase(s) upon removal from the cell for *ex situ* characterization, complicating the analysis of the Fe redox behavior by *ex situ* ^{57}Fe Mössbauer spectroscopy, XPS, and magnetometry.

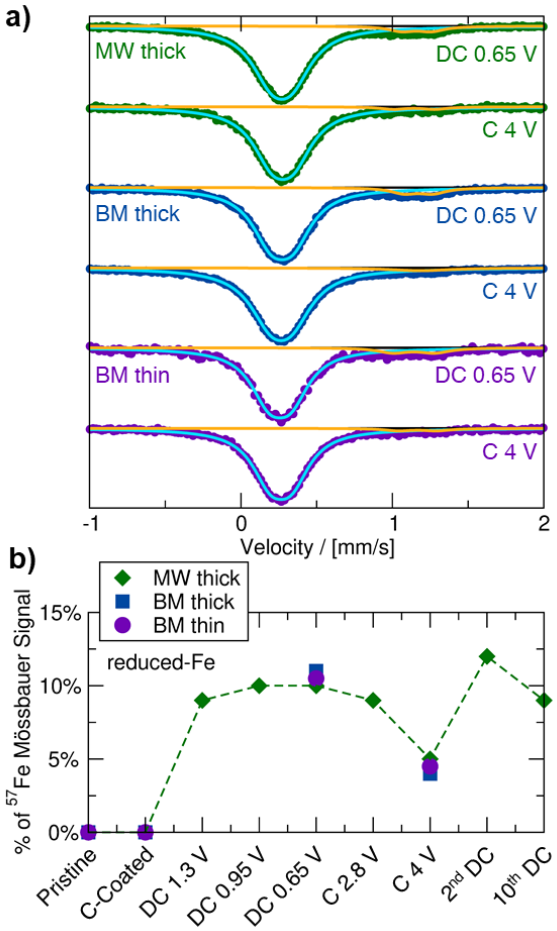

Figure 4.8 – ^{57}Fe Mössbauer of *ex situ* Na_3FeF_6.a) ^{57}Fe Mössbauer spectra of *ex situ* Na_3FeF_6 fit with two doublets for O_h-Fe^{3+} and reduced-Fe. **b)** Change in the amount of ^{57}Fe signal (± 2%) corresponding to the O_h-Fe^{3+} and reduced-Fe species at different states of charge.

4.3.4 Na_3FeF_6 Conversion Process & Insights into Performance Limitations

The reactive nature of the Fe-containing discharged products prevents the exploration of the electrochemical conversion mechanism using *ex situ* Fe probes, such as Mössbauer, XPS, and magnetometry. Thus, the way to obtain insights into the conversion mechanism is to carry out real-time *operando* measurements or focus on *ex*

situ experiments capable of identifying and quantifying stable conversion products (here, NaF). We employ the latter strategy here, and recall that ^{23}Na NMR is uniquely suited to quantitatively characterize all crystalline and amorphous Na-containing phases appearing upon (dis)charge. The only signals observed via ^{23}Na NMR (Figure 4.6) are NaF and Na_3FeF_6. Thus, NaF is the only Na-containing phase formed on discharge. Regarding Fe-containing phase(s) formed upon conversion, we consider two possible processes:

$$\text{Mechanism A: } Na_3FeF_6 + 3Na \rightleftarrows 6NaF + Fe \text{ and}$$

$$\text{Mechanism B: } Na_3FeF_6 + Na \rightleftarrows 4NaF + FeF_2.$$

Table 4.2 – Summary of Observed Conversion by ^{23}Na NMR Compared to the Electrochemical Capacity. Summary of ^{23}Na NMR *ex situ* characterization of conversion products and the expected capacity if conversion occurs through Reaction Path A (Fe^0) or B (Fe^{2+}). The observed capacity at each point for the different cells are shown in the last column.

	^{23}Na NMR Characterization						**Observed Capacity (mAh/g)**
	Phase mol % (± 5%)		**Phase mol % (± 5%) adjusted by initial NaF**		**Expected Capacity (mAh/g) for Each Reaction Path**		
	Na_3FeF_6	**NaF**	**Na_3FeF_6**	**NaF**	**A (Fe^0)**	**B (Fe^{2+})**	
MW thick							
Pristine	84%	16%	--	--	--	--	--
C-coated	80%	20%	--	--	--	--	--
DC 1.3 V	47%	53%	58%	42%	36	17	16
DC 0.65 V	31%	69%	39%	61%	70	32	100
C 4 V	44%	56%	53%	47%	43	20	29
BM thick							
Pristine	99%	1%	--	--	--	--	--
C-coated	97%	3%	--	--	--	--	--
DC 0.65 V	37%	63%	38%	62%	73	33	87
C 4 V	58%	42%	59%	41%	34	16	31
BM thin							
DC 1.3 V	77%	23%	91%	9%	3	6	17
DC 0.65 V	43%	57%	44%	56%	58	27	81
C 4 V	70%	30%	72%	28%	21	10	38

To distinguish between these two reaction pathways, ^{23}Na NMR can be used to compute the expected capacity based on Mechanisms A and B (with theoretical

capacities of 337 and 112 mAh/g, respectively) and on the observed mol % of NaF formed at various states of charge (SOCs), and compare the expected capacities to the observed capacity at these SOCs. We note here that the observed capacity is the actual Na_3FeF_6 active material capacity obtained after subtracting the capacity of the blank cell. Table 4.2 shows the details of this analysis at various SOCs for MW thick, BM thick, and BM thin electrodes. Clearly, the observed capacity at the end of discharge is much larger than what would be expected for mechanism B, whereas the expected capacity for Mechanism A is in much better agreement with what is observed experimentally, albeit still moderately lower. The good agreement between the expected capacity based on Mechanism A and the observed capacity leads us to conclude that $Na_3FeF_6 + 3Na \rightleftarrows 6NaF + Fe$ is the likely reaction pathway. The small discrepancies between the expected and observed capacities in this scenario can be explained by the intrinsic limitations of our fits of the NMR data (the mol % of NaF phase in the samples extracted from the fits is accurate to ± 5%), and how we have estimated the capacity solely attributable to Na_3FeF_6 conversion by subtracting out the blank cell capacity. Additionally, the presence of a small amount of electrochemically active FeF_3 in the MW Na_3FeF_6 electrode, which is unobservable in $^{23}Na/^{19}F$ NMR, also likely contributes additional experimental capacity that we have not accounted for in our calculations. Overall, our analysis suggests the incomplete conversion of Na_3FeF_6 (no more than 60%) to NaF and Fe on discharge through Mechanism A. As these Fe nanoparticles are likely less than a few nanometers in diameter,[41] they are metastable and oxidize upon *ex situ* analysis, even upon minimal exposure to ambient air (cells opened and electrodes handled in an inert atmosphere at all times). Additionally, ^{57}Fe Mössbauer analysis of a chemically reduced

BM Na_3FeF_6 powder sample (Figure 4.14) shows a clear Fe^0 singlet at δ = 0 mm/s, confirming that Fe^0 does in fact form on chemical reduction, with a small reduced-Fe signal similar to our previous Mössbauer results (Figure 4.8) also observed. We hypothesize that this Fe^0 phase is still present in the chemically reduced *ex situ* Mössbauer spectra as these Fe particles are much larger than those obtained electrochemically, and thus spontaneous Fe oxidation only occurs around the exterior of the particles.

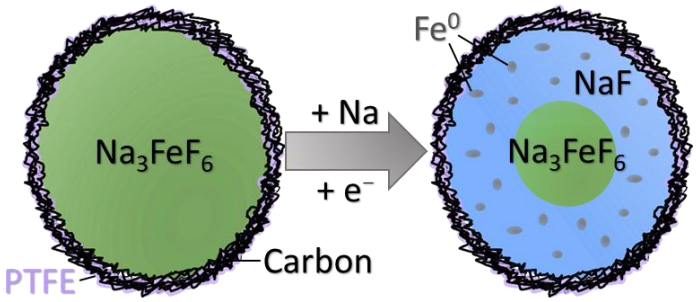

Figure 4.9 – Na_3FeF_6 Conversion Mechanism Schematic. Schematic diagram of conversion of Na_3FeF_6 particle from Na_3FeF_6 (green) in a PTFE (yellow) and carbon (black) electrode composite to a shell of NaF (blue) with interspersed Fe (silver) nanoparticles with an unreacted core of Na_3FeF_6.

The present work demonstrates that Na_3FeF_6 undergoes a conversion reaction to NaF and Fe on discharge, with the reverse transformation occurring on subsequent charge. While this process should provide a high capacity of 337 mAh/g, the electrochemical performance is limited by incomplete and poorly reversible phase transformations during cycling. Despite all particles in the C-coated starting materials being ≤ 100 nm in size, the sluggish conversion kinetics are exacerbated by the formation of NaF domains on the exterior of the Na_3FeF_6 particles. A schematic of the expected conversion process throughout a Na_3FeF_6 electrode particle is shown in Figure 4.9. The exterior of the particles is expected to undergo conversion through Mechanism

A, but the interior of the particles is unable to convert on the time-scale of the electrochemical experiments as this process hinges on both Na diffusion and electron tunneling through the poorly Na^+ conducting and insulating NaF. Indeed, NaF is a wide bandgap insulator, with a reported bandgap of 11.5 eV,[170,171] as well as a very poor Na^+ conductor, with large predicted Na^+ migration barriers (> 1 eV) at room temperature,[172] indicating that both transport processes are exceedingly kinetically limited.

To facilitate more facile Na^+ and electron transport, we have attempted to further decrease the Na_3FeF_6 particle size through an additional ball-milling step with a mixture of grinding ball sizes. SEM images of the resultant particles are shown in Figure 4.15a where the particles are now reduced to about 60 nm. The first charge-discharge cycle for this extended ball-milling compared to the BM thin electrodes is shown in Figure 4.15b with the capacity fade in Figure 4.15c. While the initial discharge capacity is not improved with these decreased particles, the reversibility is increased, albeit, still quickly fading with little to no capacity attributed to Na_3FeF_6 past cycle 15. Cycling this sample at faster rates (Figure 4.15d) results in comparable discharge capacities observed for C/20 and C/10 rates but with faster capacity fade observed for the higher rates. Thus, despite further reducing the particle sizes, Na_3FeF_6 is still intrinsically plagued by poor transport properties.

As the dominant kinetic limitation for Na_3FeF_6 prepared in this study is charge transport (Na^+ ions and electrons) into the interior of the particles, rather than through the bulk of the electrode film, the film thickness does not affect the kinetics nor the reversibility of the Na_3FeF_6 conversion process. In fact, lower loading densities lead to more facile Na intercalation into the carbon additive rather than more conversion of the

Na_3FeF_6 material. These results suggest that the energy density of Na_3FeF_6 and other fluoride-type Na-based conversion electrodes may be further increased through the preparation of thick electrodes utilizing nanosized particles of the active material embedded into a carbon matrix (*e.g.* carbon nanotubes), to further enhance the electronic conductivity of the composite. Ultimately, both the electronic conductivity and the Na^+ diffusion properties of the discharged products are key considerations for the design of higher rate and reversible conversion electrodes, and sulfide- and oxide-type conversion electrodes may compare more favorably than fluoride-based compounds.

4.3.5 Confirmation of Conversion Mechanism via *Operando* Magnetometry

As determined from the *ex situ* analysis presented in the previous subchapter, NaF and Fe form on discharge of Na_3FeF_6. However, this analysis is complicated by the oxidation of the Fe particles prior to *ex situ* characterization. While the novel analytical framework we developed is still able to identify the conversion mechanism, *operando* characterization is warranted for a more in-depth understanding of the thermodynamics and kinetics of the conversion processes. Thus, we attempted to use both *operando* magnetometry and *operando* XAS, and were successful using the former method, with the results presented in this section. Details on issues associated with the *operando* XAS measurement will be discussed in Appendix 4.5.8. We note that these results remain unpublished as they were completed following publication of the previously described Na_3FeF_6 paper.[38]

Operando magnetometry was performed on a BM thin Na_3FeF_6 electrode using the same electrochemical parameters as used for the galvanostatic data shown in Figure 4.4. The resulting electrochemical curve and change in the magnetization vs. time is shown in Figure 4.10. On first discharge, the magnetization decreases in magnitude down to 1.1 V, likely associated with Na intercalation into the carbon additive which increases the diamagnetic contribution to the magnetization. Below 1.1 V, the magnetization sharply increases through the end of discharge and into the following charge, reaching a maximum at 1.6 V on charge. As Fe^{2+} species are expected to have a lower magnetic response than Fe^{3+} species, conversion to ferromagnetic or superparamagnetic Fe^0 particles must be occurring upon Na insertion below 1.1 V. The onset potential for this conversion process is in good agreement with the plateaus observed in the electrochemical curve (Figure 4.4d). The increase in the magnetization into the following charge process indicates that the conversion processes in Na_3FeF_6 are sluggish, such that conversion continues even once the charge cycle begins.

Throughout the intermediate part of the charge process (1.6 to 2.5 V), a sharp decrease in the magnetization is observed consistent with reconversion of Fe^0 and NaF back to Na_3FeF_6. Notably, this process is irreversible as the magnetization is still higher than at the beginning of cycling. Once again, the onset potential for the reconversion process is in good agreement with the plateaus observed electrochemically (Figure 4.4d). At the end of charge (2.5 to 4 V), a moderate increase of the magnetization is observed, potentially associated with Na^+ removal from carbon, which continues into the following cycle down to 2.1 V. We note that capacity was observed for the blank cell in this voltage range, which we tentatively assign to Na^+ (de)intercalation but

acknowledge it could also be capacity generated by electrolyte degradation or other parasitic reactions. However, electrolyte degradation typically occurs predominantly on the first cycle and instead we see an increase in the change in magnetization on later cycles, complicating this conclusion. Further analysis and characterization are needed to definitively assign this region.

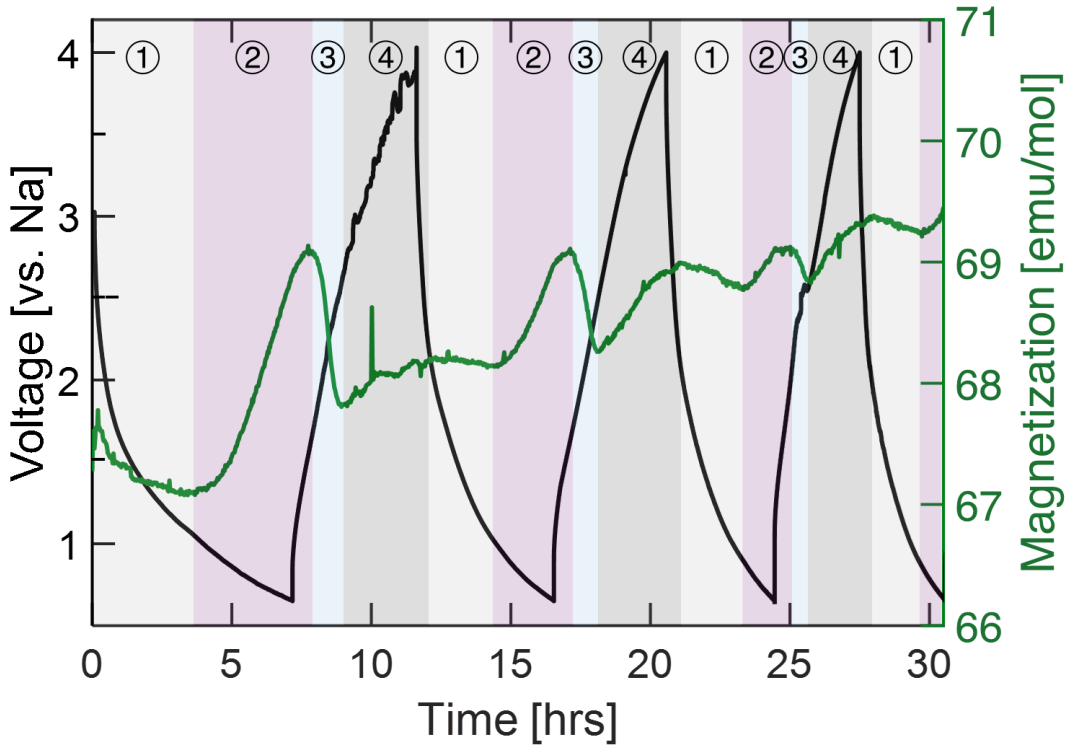

Figure 4.10 – *Operando* magnetometry. Galvanostatic charge-discharge curve (black) and change in magnetization (green) over the first 30 hours of cycling. The labeled regions are: **1)** Na intercalation into carbon, **2)** Na_3FeF_6 conversion to Fe^0 nanoparticles, **3)** reconversion to Na_3FeF_6, and **4)** Na deintercalation from carbon.

On following cycles, a similar trend is observed of: 1) slight decrease in magnetization due to Na intercalation into carbon from 2.1 to 1.1 V; 2) sharp increase in magnetization due to Na_3FeF_6 conversion to Fe^0 nanoparticles from 1.1 to 0.65 (bottom of discharge) to 1.6 V; 3) sharp decrease in magnetization due to reconversion to Na_3FeF_6 from 1.6 to 2.5 V; and 4) moderate increase in magnetization potentially due to

Na deintercalation out of carbon from 2.5 to 4 (top of charge) to 2.1 V and/or electrolyte degradation. These regions have been color-coded in Figure 4.10.

Note that the conversion onset voltage gradually decreases with cycle number from 1.1 to 0.9 V as well as the magnitude of magnetization change per cycle, consistent with a buildup of insulating phases that impede the conversion process on later cycles. Consistent with the electrochemical data, the magnetization never recovers its initial value due to significant capacity loss (e.g., the inability to reconvert Na_3FeF_6) following the first discharge. The coulombic efficiency (*CE*, ratio of the discharge capacity over the preceding charge capacity) for the following charge-discharge steps is shown in Table 4.3. The poor agreement of the magnetometry *CE* and magnetization ratios is likely related to Na (de)intercalation into carbon that still occurs in regions two and three, which has an inverse effect on the magnetization, as well as parasitic reactions that are magnetically silent. However, the standard electrochemical *CE* when the blank cell capacity is subtracted is in much better agreement with the magnetization ratios, with the deviation between the two related to parasitic reactions rather than Na_3FeF_6 (re)conversion. Overall, this data shows that Na_3FeF_6 conversion is even less reversible than the prior electrochemical data suggested.

Table 4.3 – Coulombic efficiencies for the standard (**Figure 4.4**) and operando magnetometry (**Figure 4.10**) electrochemical data and magnetization ratios of the Na_3FeF_6 discharge (region 2) over charge (region 3) magnetization changes. Na (de)intercalation into carbon has been accounted for in the standard electrochemical data as a similar blank cell was tested.

Cycle	Standard Less Blank CE	Magnetometry CE	$\Delta M_2/\Delta M_3$
1	98%	111%	76%
2	65%	97%	49%

Based on the present data, we are unable to assess whether the Fe particles forming upon conversion are contributing a ferromagnetic or superparamagnetic

response to the magnetization. Additional field-dependent measurements would be needed to determine this, and if superparamagnetic, the size of the Fe nanoparticles. However, based on prior magnetometry studies of conversion electrodes,[173–175] there is strong evidence that these Fe particles are superparamagnetic nanoparticles, especially considering the rapid oxidation of these particles upon cell disassembly. Regardless, based on these *operando* magnetometry results we can confirm the cycling mechanism of Na_3FeF_6, as previously identified using our analytical framework, as conversion to NaF and Fe^0, which is only partially reversible and sluggish. Overall, application of *operando* magnetometry to study conversion processes is an invaluable technique to isolate the bulk temporal magnetic, and thereby structural and redox state, changes occurring.

4.4 Conclusion

For the first time, Na_3FeF_6 was prepared through a rapid and sustainable assisted-MW preparation method. Electrochemical testing revealed that several distinct electrochemical processes occur in Na_3FeF_6 composite electrodes. Notably, carbon additives in the electrode film account for a large fraction of the observed capacity in this and other conversion-type fluoride electrodes, and thus should be accounted for in future studies of this class of materials. We identified that Na_3FeF_6 converts to NaF and Fe on discharge, as previously proposed. While this mechanism should yield a high theoretical capacity, conversion is incomplete and only moderately reversible due to sluggish conversion reaction kinetics that are exacerbated by the formation of insulating NaF domains with poor Na^+ diffusion properties on the exterior of the Na_3FeF_6 particles. Further, we found that *ex situ* characterization data on the metastable Fe-containing

phases formed on discharge are challenging to interpret due to spontaneous oxidation processes occurring during cell disassembly and/or sample handling, even in an inert environment. We devised a simple *ex situ* analytical method that relies on the quantification of stable conversion products using local structure probes (here, NaF characterized through ^{23}Na NMR) and a comparison with the observed capacity, to determine the conversion mechanism at play. This novel analytical framework holds promise for the study of a wide range of conversion processes that are often plagued by severe relaxation and oxidation processes during *ex situ* characterization. Ultimately, *in situ* and *operando* studies are better suited for the elucidation of conversion type processes and thus *operando* magnetometry was employed, which further confirmed the conversion mechanism and its sluggish kinetic behavior.

4.5 Appendix – Supplemental Material

4.5.1 Additional Diffraction & Refinement Results

Table 4.5 – Refined lattice parameters for Na_3FeF_6 and NaF phases in the pristine and ex situ cycled electrode samples.

	Na_3FeF_6					NaF	
	a (Å)	**b (Å)**	**c (Å)**	**beta**	**Vol. (Å³)**	**a (Å)**	**Vol.(Å³)**
Literature[157,176]	5.514	5.734	7.973	90.420	252.078	4.635	99.601
MW Pristine	5.512	5.727	7.962	90.396	251.334	4.633	99.460
MW C-Coated	5.514	5.728	7.964	90.420	251.542	4.632	99.389
BM Pristine	5.514	5.733	7.973	90.414	252.052	4.635	99.595
BM C-Coated	5.514	5.734	7.973	90.420	252.078	4.635	99.601
MW DC 0.65 V	5.514	5.734	7.973	90.420	252.078	4.635	99.601
MW C 4 V	5.513	5.726	7.969	90.430	251.557	4.632	99.390

Table 4.4 – Summary of attempted phases used to fit the unidentified reflections at Q ≈ 1.3, 1.9, 2.1, 2.4, 3.1, and 3.8 $Å^{-1}$ in the *ex situ* SXRD patterns. All the phases containing H_2O were also attempted dehydrated.

Formula	Space Group
Fe	*Fm*−3*m*, *Im*−3*m*
FeF_2	$P4_2/mnm$
$Fe_2F_5(OH)(H_2O)$	*Fd*−2*mZ*
$FeF_2(H_2O)_4$	*R*−3*mH*
FeF_3	*R*−3*c*, *Fd*−3*m*, *R*−3*c*, *P*321, *Cmcm*, *Pm*−3*m*
FeOF	$P4_2/mnm$
FeO	*Fm*−3*m*, *R*−3*m*
Fe_3O_4	*Cmcm*, *Cc*, *F*−43*m*, *Fd*−3*m*
Fe_2O_3	*Aea*2, *Cmcm*
Fe(OH)F	*Pnma*
$FeF_2(H_2O)_4$	*R*−3*m*
$Fe_3F_8(H_20)_2$	*C*2/*m*
$FeF_{2.5}(H_2O)_{0.5}$	*Fd*−3*m*
$Fe_2F_5(H_2O)_2$	*Imma*
$FeF_3(H_2O)_{0.33}$	*Cmcm*
$FeF_3(H_2O)3$	*P*4/*n*
$NaFeF_3$	*Cmcm*, *Pnma*
$Na_2Fe_2F_7$	*C*2/*c*
Na_3FeF_6	$P2_1$
$NaFeF_4$	$P2_1/c$
$Na_5Fe_3F_{14}$	$P2_1/c$, $P4_22_12$

4.5.2 Additional NMR Results and First-Principles Calculations

The computed hyperfine (paramagnetic) NMR properties are obtained at 0 K for Na_3FeF_6 supercells containing ferromagnetically-aligned open-shell Fe^{3+} ions. To compare CRYSTAL17 calculation results with experimental data acquired at room temperature, the computed shifts must be subsequently scaled to a value consistent with the paramagnetic state of the system at the temperature of the NMR experiments, using a magnetic scaling factor Φ of the form:

$$\boldsymbol{\Phi}\left(\boldsymbol{T_{exp}}\right) = \frac{\langle \boldsymbol{M}(\boldsymbol{T_{exp}})\rangle}{\boldsymbol{M_{sat}}} \quad 4.1$$

where M_{sat} is the saturated (ferromagnetic) Fe^{3+} magnetic moment at 0 K, and $\langle M(T_{exp})\rangle$ the bulk average magnetic moment measured at the sample experimental temperature, T_{exp}. Here, T_{exp} is set to 320 K to account for frictional heating caused by fast (60 kHz) sample rotation during NMR data acquisition.

The magnetic scaling factor in Eq. 4.1 be evaluated from the experimental magnetic properties of the material:

$$\boldsymbol{\Phi}(\mathbf{T}) = \frac{\boldsymbol{B_0}{\boldsymbol{\mu_{eff}}}^{\mathbf{2}}}{\mathbf{3}\boldsymbol{k_B}\boldsymbol{g_e}\boldsymbol{\mu_B}\boldsymbol{S}(\boldsymbol{T}-\boldsymbol{\Theta})} \quad 4.2$$

where B_0 is the external magnetic field, μ_{eff} is the effective magnetic moment per Fe site, k_B is Boltzmann's constant, g_e is the free electron g-value, μ_B is the Bohr magneton, S is the formal spin of Fe^{3+} ($3d^5$, $S = 5/2$), and Θ is the Weiss constant. A derivation of Eq. 4.2, starting from the Brillouin function in the low field, high temperature limit, can be found in a previous study by Kim et al.[60] Eq. 4.2 uses the "spin-only" expression for the magnetic moment and is only strictly valid when the orbital angular momentum is quenched.[64] Yet, for systems where spin-orbit coupling effects are negligible, such as

Na_3FeF_6, the spin-only expression is a good approximation to the true magnetic behavior of the system. The experimental inverse magnetic susceptibility vs. temperature curve obtained for Na_3FeF_6 is shown in Figure 4.3b. From the BM-Na_3FeF_6 data, an effective magnetic moment of 5.85 μ_B per Fe atom and a Weiss temperature of −10 K are obtained. A bulk magnetic scaling factor, Φ, of 0.0328 is obtained for T = 320 K and B_0 = 7.05 T. This value was used to scale the computed ^{23}Na and parameters listed in Table 4.1 and in Appendix 4.5.2. The ^{19}F NMR observed chemical shifts were computed to be between 19488 ppm (H20) and 20476 ppm (H35). However, we have previously shown that ^{19}F nuclei directly bonded to paramagnetic centers are too broad and too short lived to be observed[28] and so these signals were not observed.

Table 4.6 - First principles ^{23}Na NMR parameters computed on Na_3FeF_6 H20 and H35 optimized (OPT) structures using the CRYSTAL17 code. The predicted NMR properties have been scaled using a magnetic scaling factor $\boldsymbol{\Phi = 0.0328}$, and are comparable to the room temperature ^{23}Na solid-state NMR data obtained at an external magnetic field of B_0 = 7.05 T. There are two Na local environments in Na_3FeF_6, denoted Na1 and Na2, with multiplicities specified in parentheses in the table below. $\boldsymbol{\delta_{iso}}$ is the isotropic Fermi contact shift, $\Delta\boldsymbol{\delta}$ and $\boldsymbol{\eta}$ are the electron-nuclear dipolar anisotropy and asymmetry parameters, respectively, $\boldsymbol{C_Q}$ is the quadrupolar coupling constant, $\boldsymbol{\eta_Q}$ is the quadrupolar asymmetry, $\boldsymbol{\delta_Q}$ is the second-order quadrupolar shift, and $\boldsymbol{\delta_{obs} = \delta_{iso} + \delta_Q}$ is the observed chemical shift.

Environment	Parameter	OPT H20	OPT H35
Na1 (x1)	$\boldsymbol{\delta_{iso}}$/ppm	2564	1923
	$\Delta\boldsymbol{\delta}$/ppm	369	343
	$\boldsymbol{\eta}$	0.5	0.4
	$\boldsymbol{C_Q}$/MHz	−2.08	−2.13
	$\boldsymbol{\eta_Q}$	0.7	0.6
	$\boldsymbol{\delta_Q}$/ppm	−20	−20
	$\boldsymbol{\delta_{iso} + \delta_Q}$/ppm	2544	1903
Na2 (x2)	$\boldsymbol{\delta_{iso}}$/ppm	484	148
	$\Delta\boldsymbol{\delta}$/ppm	−1048	−1106
	$\boldsymbol{\eta}$	0.6	0.6
	$\boldsymbol{C_Q}$/MHz	−2.33	−2.38
	$\boldsymbol{\eta_Q}$	0.8	0.8
	$\boldsymbol{\delta_Q}$/ppm	−27	−28
	$\boldsymbol{\delta_{iso} + \delta_Q}$/ppm	457	120

Table 4.7 - Unit cell parameters for the experimental Na_3FeF_6 ($P2_1$) structure,[157] and for the structures optimized using the H20 and H35 functionals in this work.

Structure	*a* / Å	*b* / Å	*c* / Å	α / °	β / °	γ / °
EXP	11.028	11.468	15.946	90.0	90.42	90.0
OPT H20	10.972	11.452	15.875	90.0	90.9	90.0
OPT H35	10.905	11.381	15.777	90.0	90.9	90.0

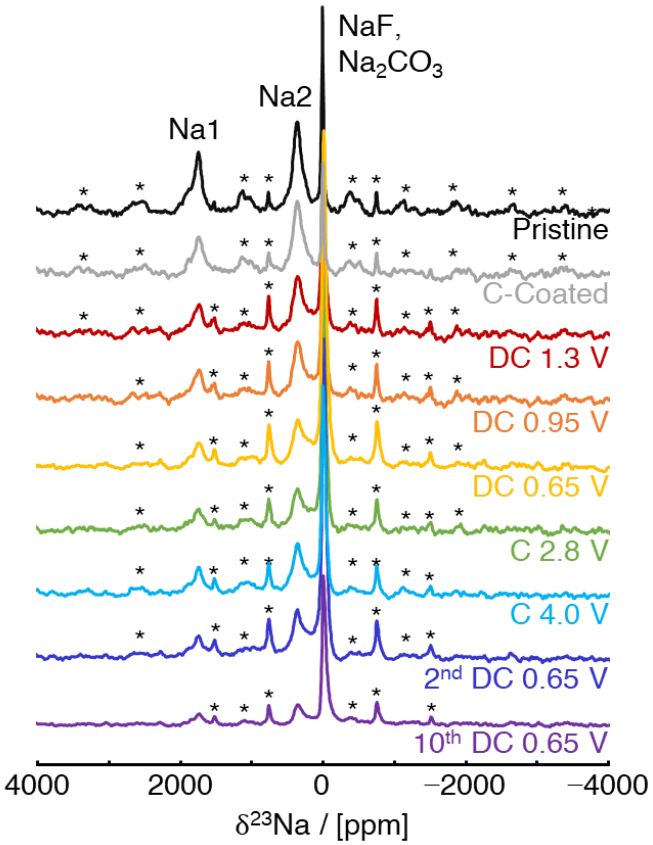

Figure 4.11 – Expanded ^{23}Na NMR *ex situ* Characterization. ^{23}Na spin echo NMR spectra obtained on MW thick Na_3FeF_6 at various stages of charge. Each spectrum has been scaled according to the number of moles of material in the rotor and the number of scans collected during the NMR experiment. Spinning sidebands are indicated by an asterisk (*).

4.5.3 Additional Mössbauer Results and Fit Parameters

Table 4.8 – Summary of ^{57}Fe Mössbauer parameters for this study and relevant reference materials. All values reported here are referenced to α-Fe at 290 K.

As-Synthesized		
	δ (mm/s)	**ΔE_Q (mm/s)**
MW Pristine	0.27	0.09
MW C-coated	0.27	0.11
BM Pristine	0.27	0.15
BM C-coated	0.27	0.15

Ex Situ		**Fe^{3+}**			**Reduced-Fe**		
		δ (mm/s)	**ΔE_Q (mm/s)**	**Signal %**	**δ (mm/s)**	**ΔE_Q (mm/s)**	**Signal %**
MW thick	**DC 1.3 V**	0.27	0.14	91%	1.16	0.19	9%
	DC 0.65 V	0.27	0.14	90%	1.16	0.2	10%
	C 4.0 V	0.28	0.14	95%	1.14	0.28	5%
	2nd DC 0.65 V	0.27	0.14	88%	1.15	0.20	12%
BM thick	**DC 0.65 V**	0.27	0.15	89%	1.17	0.19	11%
	C 4.0 V	0.26	0.14	96%	1.19	0.20	4%
BM thin	**DC 0.65 V**	0.26	0.15	90%	1.14	0.28	10%
	C 4.0 V	0.26	0.14	95%	1.17	0.25	5%

	δ (mm/s)	**ΔE_Q (mm/s)**	**Reference**
$Fe(II)F_2$	1.361	2.791	[177]
$Fe(III)F_3$	0.481	0.05	[178]
$NaFe(II)F_3$	1.25	1.25	[46]
$NaFe(III)F_4$	0.414	0.632	[179]
$Na_2Fe(II)Fe(III)F_7$	1.17	1.49	[179]
	0.402	0.566	
$Na_3Fe(III)F_6$	0.27	0.15	This work

4.5.4 Additional Electrochemical Results

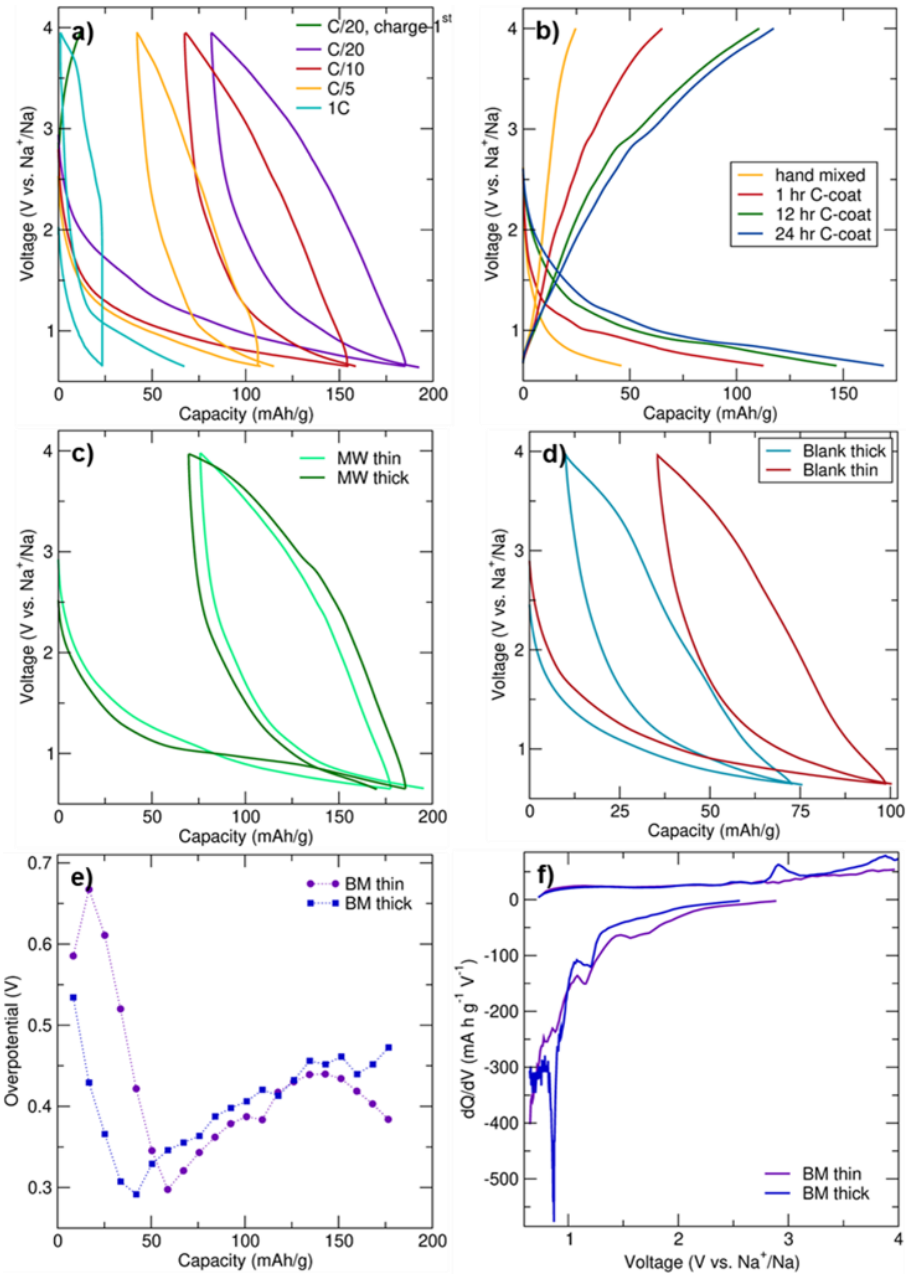

Figure 4.12 – Additional Electrochemical Characterization of Na_3FeF_6. a) Electrochemical profile obtained on BM thin cells when charged first and at various cycling rates. **b)** 1st discharge-charge electrochemical profiles obtained on BM thick cells hand ground with C for 15 min and C-coated for 1 h, 12 h, and 24 h. **c)** Electrochemical profiles corresponding to the 1st two discharge-charge cycles and obtained on MW thick and thin cells. **d)** Electrochemical profiles corresponding to the 1st discharge-charge cycle obtained on the thick and thin blank (NaF) cells. **e)** Overpotential measured by GITT at various points during the first discharge process. **f)** dQ/dV comparison for the 1st discharge-charge cycle for BM thin and thick cells.

4.5.5 XPS and Magnetometry Characterization of "Reduced-Fe" Species

The "reduced-Fe" species observed via ^{57}Fe Mössbauer may correspond to a surface-component of superparamagnetic Fe^0 nanoparticles,[174] as would be expected from the previously proposed reaction mechanism for Na_3FeF_6.[139] Alternatively, the "reduced-Fe" signal has an isomer shift similar to high spin Fe^{2+} species, such as in FeF_2 (δ = 1.36 mm/s, ΔE_Q = 2.79 mm/s),[180] but with a much smaller ΔE_Q. This small ΔE_Q indicates a more isotropic charge density around the Fe^{2+} species as compared to FeF_2, *e.g.*, due to fast electron hopping between Fe species on the timescale of the Mössbauer experiments, as in a mixed valent Fe^{2+}/Fe^{3+} phase.[87,181] To differentiate between the presence of Fe^{2+} species or Fe^0 nanoparticles, XPS and magnetometry measurements were carried out on *ex situ* BM thin samples.

XPS spectra shown in Figure 4.13a were fitted with one peak to the Fe^{3+} $2p_{3/2}$ state and one peak to the Fe^{2+} $2p_{3/2}$ state at 715 eV and 711 eV binding energy (BE), respectively, similarly to fits on Li_3FeF_6 reported elsewhere.[182] At higher BE within the Fe $2p_{3/2}$ envelope, another peak is ascribed to surface structures and/or a Fe^{2+} satellite peak.[183] The pristine XPS spectrum features both Fe^{3+} and Fe^{2+} due to the reduction of surface Fe^{2+} species induced by the high-energy milling synthesis technique. As the *ex situ* samples were carbon-coated and mixed with a polymeric binder, their overall intensity decreased compared to the pristine material. The *ex situ* sample obtained upon 0.65 V discharge exhibits an increased Fe^{2+} to Fe^{3+} signal ratio which decreases slightly in the sample obtained on subsequent charge to 4 V, suggesting the presence of Fe^{2+} species in the discharged sample, with minimal reversibility on charge. Fe^0 $2p_{3/2}$ (707

eV BE) and $2p_{1/2}$ (720 eV BE) signals are not observed but the overlapping of F 1*s* plasmon loss peaks near the Fe 2*p* envelope may obscure this signal if Fe^0 is present in small amounts. Thus, these results suggest that Fe^{2+} is present rather than Fe^0, at least at the surface of the particles.

Magnetic hysteresis curves at 2K (Figure 4.13b) for the BM thin pristine and 0.65 V discharged samples show characteristic paramagnetic behavior, reaching a saturation magnetization (M_s) at high fields proportional to the number of unpaired electrons on each magnetic ion (μ_B/Fe). The M_s decreases in the discharged sample (3.34 μ_B/Fe) compared to the pristine (4.61 μ_B/Fe) in line with the formation of Fe^{2+} on discharge from Fe^{3+} (5 μ_B/Fe^{3+}, 4 μ_B/Fe^{2+}), with slightly smaller M_s values obtained than theoretically predicted due to the weak antiferromagnetic interactions present in Na_3FeF_6 as discussed earlier. Magnetic susceptibility data are consistent with these results, and μ_{eff} values obtained from Curie-Weiss fits are equal to 5.80 μ_B and 5.05 μ_B per Fe atom for the pristine and 0.65 V discharged Na_3FeF_6 samples, respectively. Thus, these results along with our previous XPS and ^{57}Fe Mössbauer results, indicate that this "reduced-Fe" species is an amorphous Fe^{2+}-containing phase that may possibly also contain Fe^{3+} species.

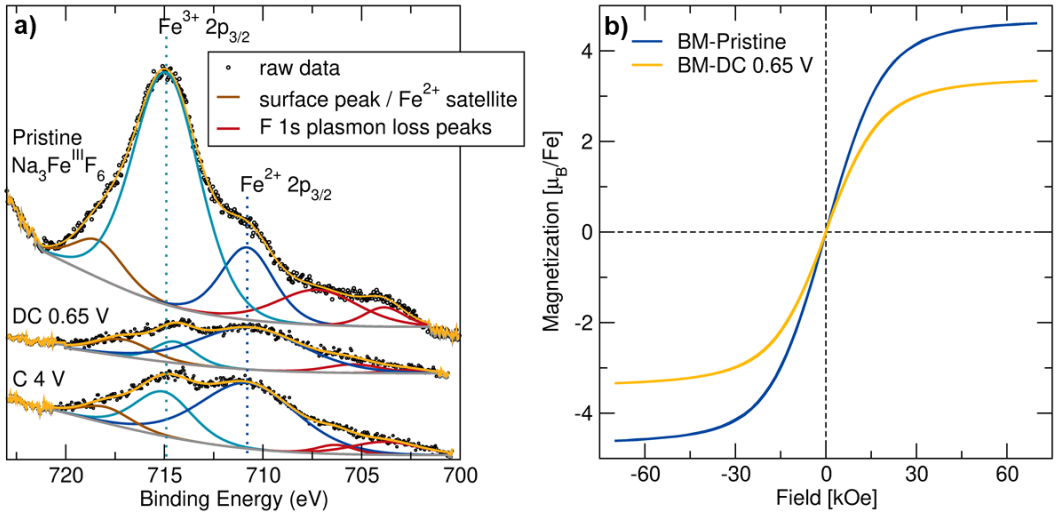

Figure 4.13 – XPS and Magnetometry of *ex situ* BM thin Na_3FeF_6. a) XPS spectra (black dots) with corresponding fits (yellow) for BM pristine Na_3FeF_6 and for thin discharged and charged *ex situ* electrodes show an increase in Fe^{2+} (dark blue) upon discharge compared to Fe^{3+} (cyan). **b)** Magnetization vs. field measurements for BM pristine Na_3FeF_6 and for thin *ex situ* discharged electrodes at 2 K showing an overall decrease of magnetization for the discharged sample.

4.5.6 ^{57}Fe Mössbauer of Chemically Reduced BM-Na_3FeF_6

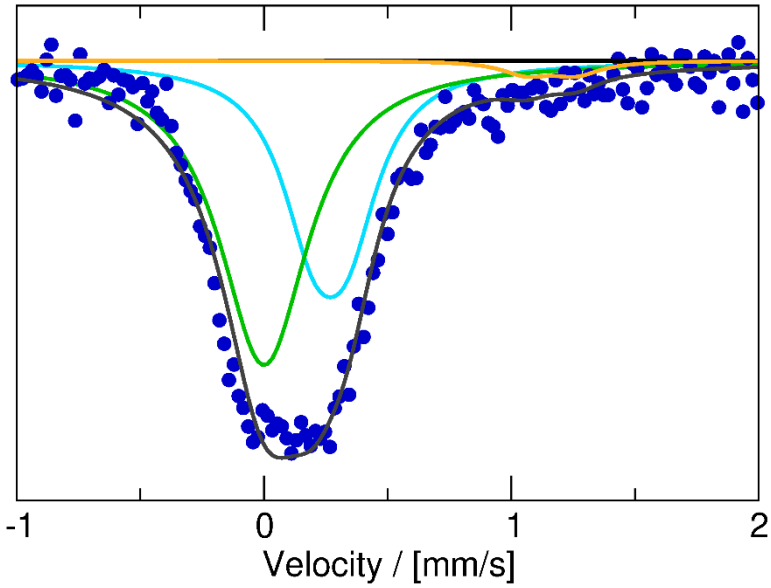

Figure 4.14 – ^{57}Fe Mössbauer of Chemically Reduced BM-Na_3FeF_6. ^{57}Fe Mössbauer spectra for chemically reduced BM-Na_3FeF_6 fitted with 58% bulk Fe^0 (δ = 0 mm/s, green), 39% O_h-Fe^{3+} in Na_3FeF_6 (δ = 0.27 mm/s, cyan), and 3% Fe^{2+} ($\delta \approx 1.16$ mm/s and $\Delta E_Q \approx 0.2$ mm/s, orange) like that seen in the *ex situ* samples.

4.5.7 SEM & Electrochemistry of Particle Size Reduction of BM-Na_3FeF_6

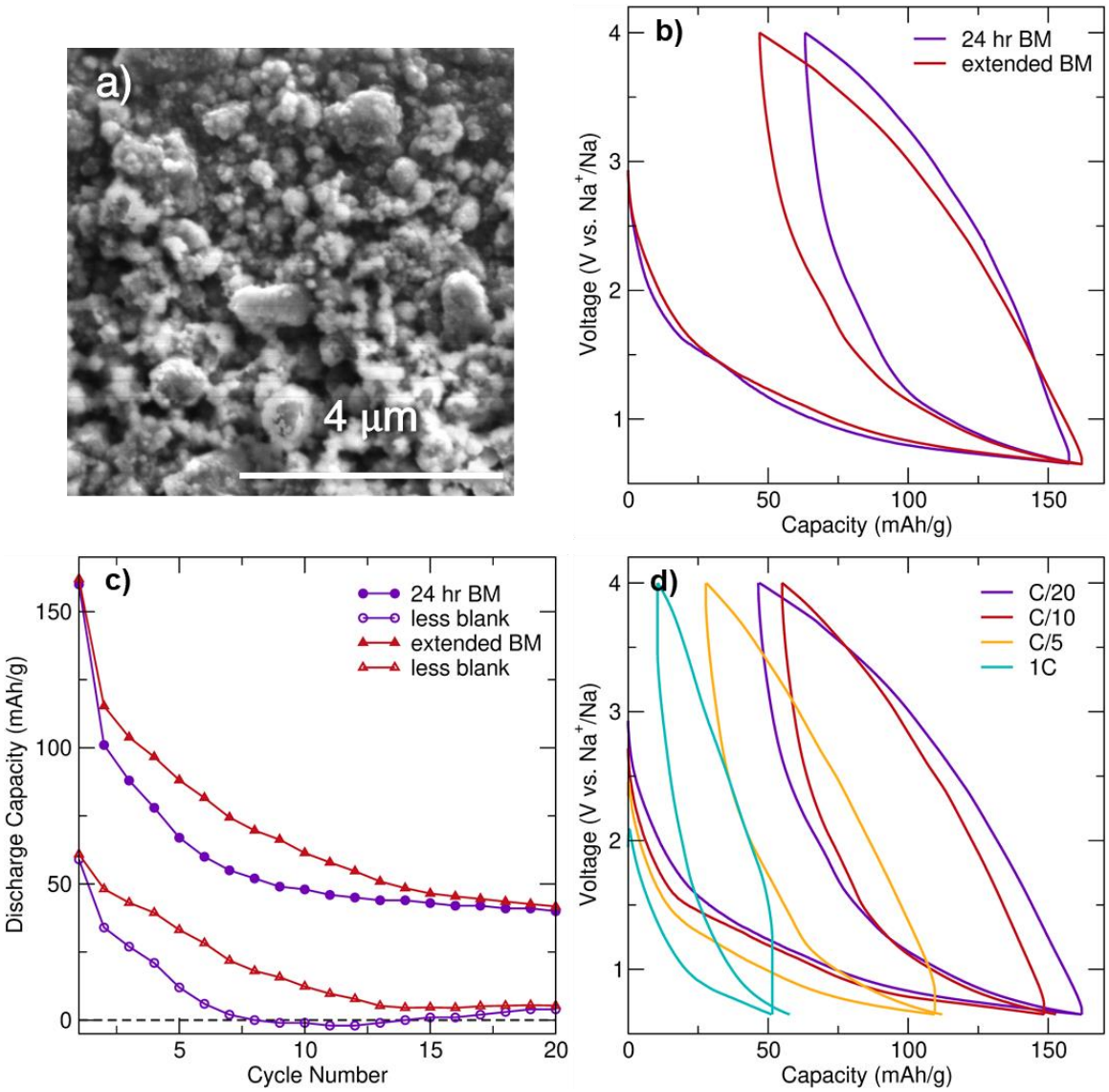

Figure 4.15 – SEM and Electrochemical Testing of Particle Size Reduction of BM-Na_3FeF_6. Particle size reduction of BM-Na_3FeF_6 was completed by adding an additional 12 h ball-milling step with five 10 mm and ten 5 mm ZrO_2 balls following the previous 24 h ball-milling step. **a)** SEM images of the extended BM-Na_3FeF_6 particles. 24 h BM C-Coating and extended C-coating BM-Na_3FeF_6 thin cells comparison of their **b)** first two charge and discharge cycles (C/20 rate) and **c)** discharge capacity retention for Na_3FeF_6 cells (filled symbols) and for Na_3FeF_6 cells with the corresponding blank cell capacity subtracted (unfilled symbols). **d)** First two charge and discharge cycles for the extended BM-Na_3FeF_6 thin cells at various rates.

4.5.8 *Operando* XAS on Na_3FeF_6

Operando XAS experiments were attempted to complement the *operando* magnetometry data collected in house. These experiments were conducted at the Stanford Synchrotron Radiation Lightsource (SSRL) at SLAC at beam line 4-3. As part of these experiments both iron references, pristine samples, *ex situ* samples, and pouch cells were measured. The iron references used were FeF_2 and FeF_3 with Fe^0 being an internal reference at most XAS beam lines when performing Fe K-edge experiments. The iron fluoride references were chosen as they had the most similar local environment as the materials of interest, which is important in correctly calculating the Fe oxidation state. XANES spectra of all but the *operando* samples are shown in Figure 4.16. Clearly, each sample closely corresponds to Fe^{3+}, with the *ex situ* samples exhibiting a slight shift towards lower energy, as expected from prior in-house characterization.

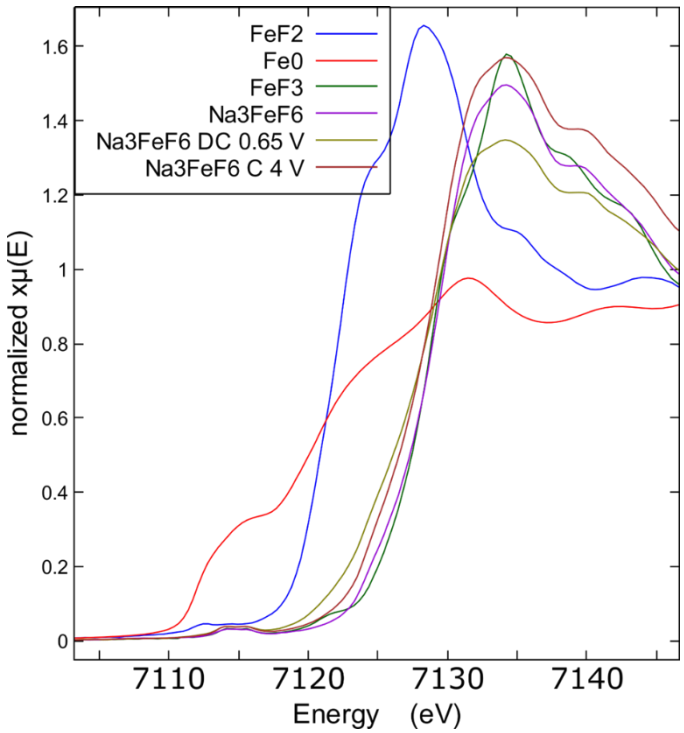

Figure 4.16 – XANES spectra of pristine Na_3FeF_6 powder and *ex situ* films stopped at DC 0.65 V and C 4 V. All materials of interest where prepared via ball-milling. FeF_2, FeF_3, and Fe^0 were used as references.

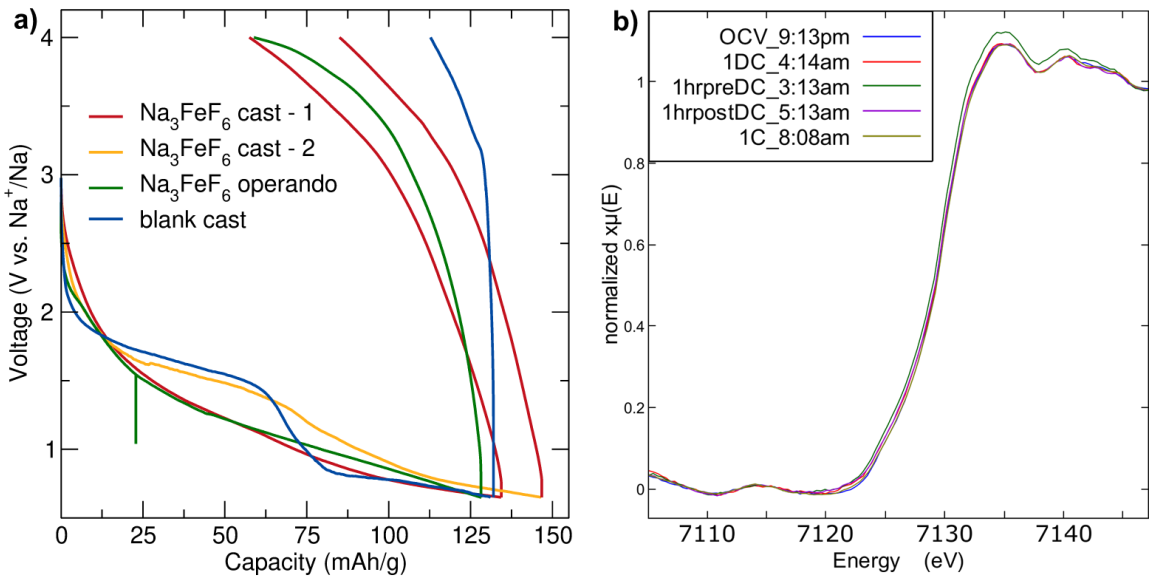

Figure 4.17 – a) Electrochemical profiles for cast Na_3FeF_6 electrodes tested in Swagelok cells (red, yellow), blank cast electrode in a Swagelok cell (blue), and the *operando* cast Na_3FeF_6 electrode in a pouch cell (green). **b)** Corresponding XANES spectra for the *operando* Na_3FeF_6 cell at various points throughout cycling.

The operando XANES data and corresponding electrochemical profile is shown below in Figure 4.17. Unfortunately, this experiment was unable to successfully monitor the evolution of Fe valence state upon cycling as all XANES spectra exhibit little to no change despite being from different parts of the electrochemical curve. There are several hypotheses for why this might be, including electrode preparation, cell design, *operando* setup. First, the electrodes had to be cast on aluminum foil (rather than made into free-standing films) to be incorporated into a pouch cell and improper casting may have contributed to a conversion reaction no longer occurring. Notably, there are no noticeable features on the electrochemical profile. Second, very large voltage hysteresis suggests there may have been very poor contact within the cell (e.g. too little pressure applied to the cell stack, misalignment of electrodes, etc.). Third, beam line 4-3 contains an incredibly small hutch that complicates proper *operando* setup and as such may have presented difficulties in appropriate beam alignment. Additionally, the lack of *operando*

cell setups at SSRL impeded the experiment design and as such should be more carefully considered in the future. And finally, this experiment was complicated by it being run during the first days of SSRL being back open to users (at the time, only California users) due to prior COVID-19 lockdowns, and only one researcher being able to travel for the experiment.

Overall, while the present *operando* XAS experiment was unsuccessful, there are many lessons to be learned from it to enable the success of future *operando* beam line experiments.

Chapter 5 – Polymorphism in Weberite $Na_2Fe_2F_7$ & its Effects on Electrochemical Properties

[ff]Weberite-type sodium transition metal fluorides ($Na_2M^{2+}M'^{3+}F_7$) have emerged as potential high performance sodium intercalation cathodes, with predicted energy densities in the 600-800 Wh/kg range and fast Na-ion transport. One of the few weberites that has been electrochemically tested is $Na_2Fe_2F_7$, yet inconsistencies in its reported structure and electrochemical properties have hampered the establishment of clear structure-property relationships. In this study, we reconcile structural characteristics and electrochemical behavior using a combined experimental-computational approach. First principles calculations reveal the inherent metastability of weberite-type phases, the close energetics of several $Na_2Fe_2F_7$ weberite polymorphs,

[ff] The contents of this chapter have substantially appeared in reference [13]: **E. E. Foley**, V. C. Wu, W. Jin, W. Cui, E. Yoshida, A. Manche, and R. J. Clément. Polymorphism in Weberite $Na_2Fe_2F_7$ and its Effects on Electrochemical Properties as a Na-ion Cathode. *Chem. Mater.* **35** (2023) 3614-3627. doi:10.1021/acs.chemmater.3c00233

as well as their predicted (de)intercalation behavior. We find that as-prepared $Na_2Fe_2F_7$ samples inevitably contain a mixture of polymorphs, with local probes such as solid-state nuclear magnetic resonance and Mössbauer spectroscopy providing unique insights into the distribution of Na and Fe local environments. Polymorphic $Na_2Fe_2F_7$ exhibits a respectable initial capacity yet steady capacity fade, a consequence of the transformation of the $Na_2Fe_2F_7$ weberite phases to the more stable perovskite-type $NaFeF_3$ phase upon cycling, as revealed by *ex situ* synchrotron X-ray diffraction and solid-state NMR. Overall, these findings highlight the need for greater control over weberite polymorphism and phase stability through compositional tuning and synthesis optimization.

5.1 Introduction

Weberite-type sodium transition metal fluorides have been studied for their magnetic properties since the 1970s[184,185], but have only been explored as Na-ion battery electrode materials over the past few years.[47–49,179,186] In 2019, Euchner *et al.* predicted, using first principles calculations, that this material class should lead to good Na-ion diffusion properties, high Na insertion potentials, and high capacities, resulting in energy densities competitive with common Li-ion cathode materials.[186] A recent experimental report by Park *et al.* demonstrated exceptional performance for the $Na_2Fe_2F_7$ weberite cathode, including an initial capacity of 184 mAh/g at C/20, and an outstanding full cell capacity retention of 88.3% at 2C (initial capacity of 118 mAh/g) after 1000 cycles.[47] While $Na_2Fe_2F_7$ remains the best performing weberite cathode to

date,[47] other chemistries such as Na_2TiFeF_7[48] and Na_2MVF_7 (*M* = Mn, Fe, Co)[49] have been shown to result in capacities in excess of 185 and 147 mAh/g, respectively.

While Park *et al.* reported a trigonal $Na_2Fe_2F_7$ weberite,[47] two other variants of the weberite structure (orthorhombic and monoclinic) have been reported for this compound,[20,28] indicating a complex phase stability landscape for $Na_2Fe_2F_7$, with direct impacts on its applicability as an intercalation electrode. Here, we report an in-depth computational-experimental investigation of the structure, phase stability, and electrochemistry of $Na_2Fe_2F_7$, aiming to establish clear links between local and long-range structural features and Na intercalation properties. We find that $Na_2Fe_2F_7$ is prone to polymorphism, with all three weberite forms present in our samples despite extensive synthesis optimization, as evidenced by synchrotron X-ray diffraction (SXRD), and supported by ^{57}Fe Mössbauer and ^{23}Na solid-state nuclear magnetic resonance (ss-NMR) spectroscopy. Notably, this is the first NMR investigation of a weberite material (supplemented with first principles calculations of NMR parameters) and provides key insights into the Na local environments. From an electrochemical performance standpoint, we highlight both the promise presented and difficulties faced by weberite cathodes such as $Na_2Fe_2F_7$. While density functional theory (DFT) calculations reveal that all three $Na_2Fe_2F_7$ polymorphs can exchange 2 Na-ions per formula unit (compositions between $NaFe_2F_7$ and $Na_3Fe_2F_7$) through a solid solution mechanism on charge and discharge, kinetic limitations on deep discharge limit the practical capacity, which may be related to the large, predicted volume expansion at high Na contents. We further identify a phase transformation upon cycling, revealed by *ex situ* SXRD and ^{23}Na ss-NMR. While this study confirms the suitability of weberites as potential high energy

cathode materials for SIBs, it also highlights a need for controlled synthesis routes to obtain single-phase weberite samples, for the optimization of electrode preparation methods to achieve the full redox capacity of $Na_2Fe_2F_7$ and related systems, and for a better understanding of the metastability issues facing this class of cathode materials.

The work presented in this chapter was lead and designed by me with a team of collaborators within Prof. Raphaële Clément's group aiding with characterization. Vincent Wu collected the SEM data. Wei Cui and Alexis Manche performed first-principles calculations of NMR parameters. Eric Yoshida acquired and analyzed the inductively coupled plasma mass spectrometry (ICP) results. Wen Jin aided in material synthesis, diffraction, and electrochemical cell testing. All other work in this chapter (including material synthesis; running of DFT calculations and analysis; acquisition and analysis of the electrochemical, diffraction, Mössbauer, and NMR results) was completed by me and I did most of the writing of the submitted manuscript.

5.2 Experimental

5.2.1 Materials Synthesis

Mechanochemical-assisted solid state $Na_2Fe_2F_7$ was prepared using a stoichiometric mixture of dried binary fluoride precursors: NaF (Sigma-Aldrich, 99.99%), FeF_2 (Sigma-Aldrich, 99%), and FeF_3 (Sigma-Aldrich, 99.5%). All precursors and prepared materials were handled in an argon glovebox or else always sealed under argon as fluorides react readily with water to form hydrofluoric acid which is highly corrosive. The precursors were hand-mixed and then 1 g of the powder was sealed in a

50 mL ZrO_2 ball mill jar with five 10 mm and ten 5 mm ZrO_2 balls and ball-milled at 400 rpm for 36 h to ensure homogenous mixing. The resultant powder was pelletized, annealed at 500°C for 30 min under an argon flow, and then immediately quenched. To prevent air and water exposure, the quench was performed by using an extra-long alumina tube that was shifted horizontally in a tube furnace following the anneal such that the pellet was no longer within the heating element. Subsequently the alumina tube surrounding the pellet was flushed with room temperature nitrogen gas for 10 min. The resultant pellet was then hand ground and used for all further characterization.

5.2.2 Electrochemical Characterization

The as-synthesized $Na_2Fe_2F_7$ materials were carbon-coated prior to electrochemical testing to form an electronically conductive carbon nanocomposite. The pristine materials were combined with carbon black (Super C65, MTI Corporation) in a 7:2 ratio along with three 10 mm and three 5 mm ZrO_2 balls, in a 50 mL ZrO_2 ball mill jar and ball-milled at 300 rpm for 24 h. The resultant carbon-coated materials were hand ground for 30 min with 10 wt.% polytetrafluoroethylene (PTFE, Sigma-Aldrich), rolled into free-standing film electrodes, and punched into 6 mm disks with a loading density of 10 mg cm^{-2}. All electrochemical testing occurred in Swagelok-type cells against Na metal (Sigma) with a glass fiber separator (Whatman GF/D) using 200 µL of an in-house prepared electrolyte (< 20 ppm water content) of 1 M $NaPF_6$ (Strem Chemicals, 99%) in propylene carbonate (PC, Sigma, 99.7%) with 2 vol% fluoroethylene carbonate (FEC, Sigma-Aldrich, ≥ 99%).

5.2.3 Structural Characterization

X-ray Diffraction – High-resolution synchrotron powder diffraction patterns were collected on Beamline 11-BM at the Advanced Photon Source (APS), Argonne National Laboratory using an average wavelength of 0.458940 Å. Room temperature data were collected between 2θ of 0.5° and 50°. Resulting patterns were refined using first the Pawley method, to determine accurate peak shape fitting parameters, and then using the Rietveld method in TOPAS v7.[188] Crystal structures were depicted using VESTA 3.[189]

Scanning Electron Microscopy – SEM images were obtained using a Thermo Fisher Apreo C LoVac SEM instrument with an accelerating voltage of 5 keV and current of 0.4 nA.

^{57}Fe Mössbauer Spectroscopy – Room temperature ^{57}Fe Mössbauer spectroscopy was performed using a SEECo Model W304 resonant gamma-ray spectrometer (activity = 60 mCi +/- 10%, ^{57}Co/Rh source) equipped with a Janis Research Model SVT-400 cryostat system. The source linewidth was < 0.12 mm s^{-1} for the innermost lines of a 25 μm α-Fe foil standard. Isomer shifts were referred to α-Fe foil at room temperature. All samples consisted of 15 to 20 mg of material loaded into a plastic holder in an Ar glovebox, coated with oil, capped, and then measured under a positive flow of N_2 at 305 K. The data were fit using MossA.[144]

Inductively Coupled Plasma Mass Spectrometry – Bulk chemical compositions were determined via ICP (Agilent 5800 ICP-OES). Samples were dissolved in a solution consisting of a 10:1 (v:v) ratio of 70% HNO_3 (Sigma-Aldrich) and concentrated HCl (Sigma-Aldrich).

^{23}Na Solid-State Nuclear Magnetic Resonance Spectroscopy (ssNMR) – ^{23}Na ssNMR data were collected on the $Na_2Fe_2F_7$ as-prepared and *ex situ* samples using a Bruker Avance 100 MHz (2.35 T) wide-bore NMR spectrometer with Larmor frequencies of 26.48 MHz at room temperature. The data were obtained at 60 kHz magic-angle spinning (MAS) using a 1.3 mm double-resonance HX probe. ^{23}Na NMR data were referenced against 1 M aqueous solutions of sodium chloride (NaCl, $\delta(^{23}Na) = 0$ ppm) and these samples were also used for pulse calibration. ^{23}Na spin echo spectra were acquired on all samples using π/2-π-π/2 and π/6-π/3-π/6 pulse sequences to selectively excite less quadrupolar environments and equally excite all environments, respectively. The radiofrequency (RF) pulse lengths were 0.125 μs for π/6, 0.25 μs for π/3, 0.375 μs for π/2, and 0.75 μs for π at a power of 62.5 W. A recycle delay between 30 ms to 80 ms was used to with the exact value optimized for each sample to ensure the full ^{23}Na signal was fully relaxed between pulses.

^{19}F Solid-State Nuclear Magnetic Resonance Spectroscopy (ssNMR) – ^{19}F ssNMR data were collected on the $Na_2Fe_2F_7$ *ex situ* samples using a Bruker Avance 100 MHz (2.35 T) wide-bore NMR spectrometer with Larmor frequencies of 94.08 MHz at room temperature. The data were obtained at 60 kHz magic-angle spinning (MAS) using a 1.3 mm double-resonance HX probe. ^{19}F NMR data were referenced against 1 M aqueous solutions of sodium fluoride (NaF, $\delta(^{19}F) = -118.14$ ppm) and these samples were also used for pulse calibration. The radiofrequency (RF) pulse lengths were 0.35 μs for π/2, and 0.7 μs for π. A recycle delay of 60 s was used for each sample to ensure the full ^{19}F signal was fully relaxed between pulses.

5.2.4 First Principles Calculations

Phase Stability & Energetics – Density functional theory (DFT) calculations were performed using the Vienna *ab initio* Simulation Package (VASP).[106,107,190,191] All VASP calculations used projector augmented wave (PAW) pseudopotentials (Na pv, Fe, and F),[192,193] a plane-wave energy cutoff of 520 eV, and the Perdew-Burke-Ernzerhof (PBE) generalized-gradient approximation (GGA)[194] functional with the Hubbard *U* correction.[195] A *U* value of 4 eV was used for Fe based on previous reports that have shown it to be broadly reliable for ionic solids.[196,197]

All calculations were performed on a 1x1x1 cell of the $Na_xFe_2F_7$ 2*O*, 3*T*, and 4*M* structures. For structures containing partial occupation of Na sites, symmetrically unique Na-vacancy orderings were enumerated and ranked according to their Ewald sum energy as implemented in Pymatgen[198] and only the three lowest energy structures considered. The structures were fully optimized (atomic positions and cell parameters), and the theoretical lattice parameters are compared to experimental values[47,179,187] in Table 5.11. To obtain accurate final energies, all relaxations were followed by a final static calculation. The convergence criteria were set as 10^{-5} eV for total energy and 0.01 eV/Å for the interatomic forces. Gaussian smearing with a width of 0.05 eV was used. All calculations were spin polarized with ferromagnetic ordering assumed. For the 2*O* and 3*T* structures, the Brillouin zone was sampled with a 4x3x4 and 6x6x3 k-point grid while the 4*M* structure used a reciprocal space discretization of 25 $Å^{-1}$.

Calculation of NMR Parameters – Spin-unrestricted hybrid density functional theory (DFT) / Hartree Fock (HF) calculations were performed using the CRYSTAL17 all-electron linear combination of atomic orbital code[146,147] to determine ^{23}Na NMR

parameters for the $Na_2Fe_2F_7$ 2*O*, 3*T*, and 4*M* structures optimized in VASP, as described above, which were further relaxed in CRYSTAL. Two spin-polarized exchange-correlation functionals based upon the B3LYP form,[104,148–150] and with Fock exchange weights of F_0 = 20% (B3LYP or H20) and 35% (H35), were chosen for their good performance regarding the prediction of the electronic structure and band gaps of transition metal compounds (B3LYP or H20),[151,152] and for their accurate description of the magnetic properties of related compounds (H35).[153–155] All-electron atom-centered basis sets comprising fixed contractions of Gaussian primitive functions were employed throughout. Two types of basis sets were used: a smaller basis set (BS-I) was employed for structural optimizations, and a larger basis set (BS-II) was used for computing ^{23}Na NMR parameters which require an accurate description of the occupation of core-like electronic states. For BS-I, individual atomic sets are of the form (15*s*7*p*)/[1*s*3*sp*] for Na, (20*s*12*p*5*d*)/[1*s*4*sp*2*d*] for Fe, and (10*s*6*p*1*d*)/[4*s*3*p*1*d*] for F, where the values in parentheses denote the number of Gaussian primitives and the values in square brackets the contraction scheme. All BS-I sets were obtained from the CRYSTAL online repository and were unmodified from their previous use in a broad range of compounds.[146] For BS-II, a flexible and extended TSDP-derived (11*s*7*p*)/[7*s*3*p*] set for Na, an Ahlrichs DZP-derived[156] (13*s*9*p*5*d*)/[7*s*5*p*3*d*] set for Fe^{3+}, and a modified IGLO-III and (10*s*6*p*2*d*)/[6*s*5*p*2*d*] set for F.

NMR parameters were computed on the fully optimized (atomic positions and cell parameters) $Na_2Fe_2F_7$ structures. All first principles structural optimizations were carried out in the ferromagnetic state on 1x1x1 cells (containing 44, 66, and 176 atoms for 2*O*, 3*T*, and 4*M* $Na_2Fe_2F_7$, respectively), after removal of all symmetry constraints and

using the H20 and H35 hybrid functionals. Structural optimizations were pursued using the quasi-Newton algorithm with root-mean-square (RMS) convergence tolerances of 10^{-7}, 0.0003, and 0.0012 a.u. for total energy, RMS force, and RMS displacement, respectively. Tolerances for maximum force and displacement components were set to 1.5 times the respective RMS values. Sufficient convergence in total energies and spin densities was obtained by application of integral series truncation thresholds of 10^{-7}, 10^{-7}, 10^{-7}, 10^{-7}, and 10^{-14} for Coulomb overlap and penetration, exchange overlap, and g- and n-series exchange penetration, respectively as defined in the CRYSTAL17 documentation.[146] The final total energies and spin and charge distributions were obtained in the absence of any spin and eigenvalue constraints. NMR parameters were obtained on ferromagnetically aligned 2x1x2, 1x1x1, and 1x1x1 cells for 2*O*, 3*T*, and 4*M* $Na_2Fe_2F_7$, respectively, and on cells where one Fe spin was flipped using BS-II sets and a method described by Middlemiss *et al*.[63] Anisotropic Monkhorst-Pack reciprocal space meshes[158] with shrinking factors of 9 6 9 for 2*O*, 9 9 4 for 3*T*, and 9 6 3 for 4*M* were used throughout.

5.3 Results & Discussion

5.3.1 Weberite Structure and its Variants

The weberite structure is a fluorine-deficient superstructure of fluorite (CaF_2) with general formula $A_2B_2X_7$, where *A* and *B* are cations and *X* is an anion. The high symmetry variant (*Imma* space group) and *A* site local environments are shown in Figure 5.1a-c for the weberite mineral, Na_2MgAlF_7. Weberites retain the same cationic face-centered cubic stacking sequence as fluorite, but as they are anion-deficient the *B*

cations are now only 6-fold coordinated, while the *A* cations retain the 8-fold coordination typical of the fluorite structure. The mixed-valence *B* cations, *B*1 and *B*2 (typically divalent M^{2+} and trivalent M^{3+} metals, respectively), form a network of three-dimensional corner-connected octahedra composed of one-dimensional chains of *B*1 octahedra that are connected to each other by *B*2 octahedra. The *A* cations occupy distorted cubic sites (*A*1, Figure 5.1b) and bihexagonal pyramidal sites (*A*2, Figure 5.1c). The *A*1 polyhedra form edge-sharing chains that also share edges with the *A*2 corner-connected polyhedral chains, creating a three-dimensionally connected *A* cation network. Additionally, the weberite structure can be viewed as alternating close-packed cation layers of A_3B and AB_3, as shown in Figure 5.2. In each layer, the majority cation species (e.g. *A* in A_3B) forms a Kagomé-type network, and the minority cation species occupies the center of the Kagomé rings.

Several weberite variants have been reported that differ in their stacking sequence of the Kagomé-like layers. A nomenclature system has been proposed by Grey et al.[199] based on the crystal system and number of close-packed cation slabs (*e.g.*, a pair of A_3B and AB_3 layers) within the unit cell. For example, the high symmetry weberite variant (shown in Figure 5.1a) is denoted 2*O* as it is based on the orthorhombic crystal system and the smallest repeating unit contains two cation slabs. Na-*M*-F weberites reported to date form the 2*O* (*Imma*), 2*M* (monoclinic *C*2/*c*), 3*T* (trigonal $P3_121$), and/or 4*M* (monoclinic *C*2/*c*) structures, where the different slab stackings can be summarized as *AA* for 2*O*, *ABAB* for 2*M*, *AABBAABB* for 4*M*, and *ABCABC* for 3*T*. Structural diagrams that illustrate those differences are shown in Figure 5.3. We note that the 2*M* variant has

only been reported for Na_2CuGaF_7 and we do not consider this variant further in this work.

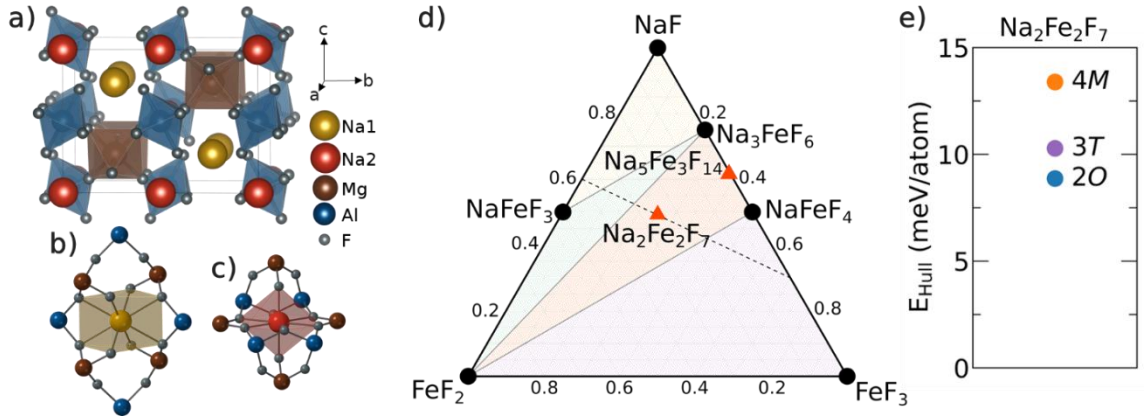

Figure 5.1 – Weberite structure, stability, and polymorphism. Crystal structure of the Na_2MgAlF_7 weberite mineral, highlighting the MF_6 (where M = Mg, Al) polyhedral network in **a)**, and the local Na coordination environments: Na1 in distorted cubic sites in **b)**, and Na2 in bihexagonal pyramidal sites in **c)**. **d)** DFT-predicted NaF-FeF_2-FeF_3 ternary phase diagram, where stable compounds are shown as black circles, metastable compounds as orange triangles, and regions of phase coexistence are shaded. The black, dotted tie-line represents the compositional evolution of the weberite at various stages of charge. **e)** Energy above the hull for the three $Na_2Fe_2F_7$ weberite variants.

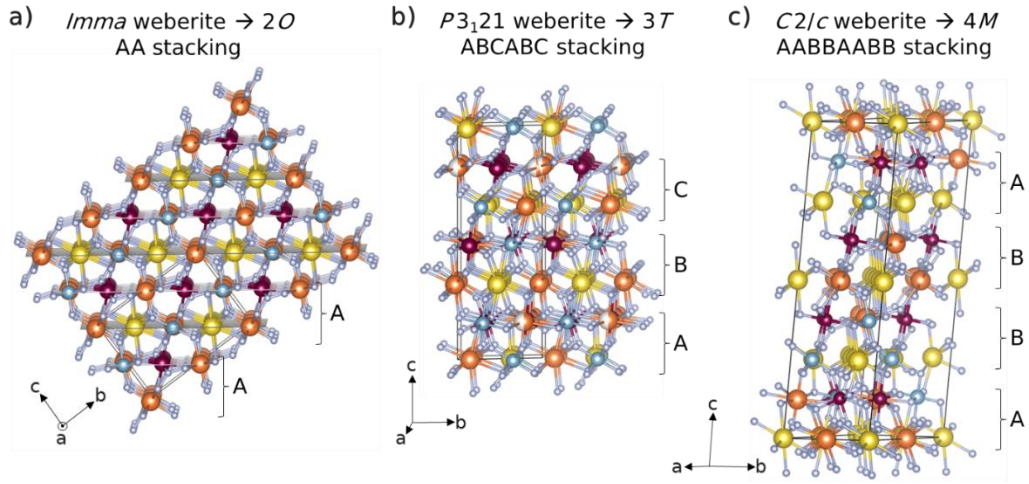

Figure 5.2 – Crystal structure diagrams for the three weberite polymorphs: a) 2*O*, orthorhombic where all *B*1 chains are parallel to [100]; **b)** 3*T*, trigonal where *B*1 chains are parallel to [010], [$\bar{1}$10], and [100] for the *A*, *B*, *C* layers, respectively; **c)** and 4*M*, monoclinic where *B*1 chains are parallel to [$\bar{1}$10] and [110] for the *A* and *B* layers, respectively. Each slab (denoted by *A*, *B*, or *C*) corresponds to one AB_3 and one A_3B Kagomé-like layer. Note that within each *AA* and *BB* pair of the 4*M* structure, the A_3B layers differ slightly while the AB_3 layers remain identical.

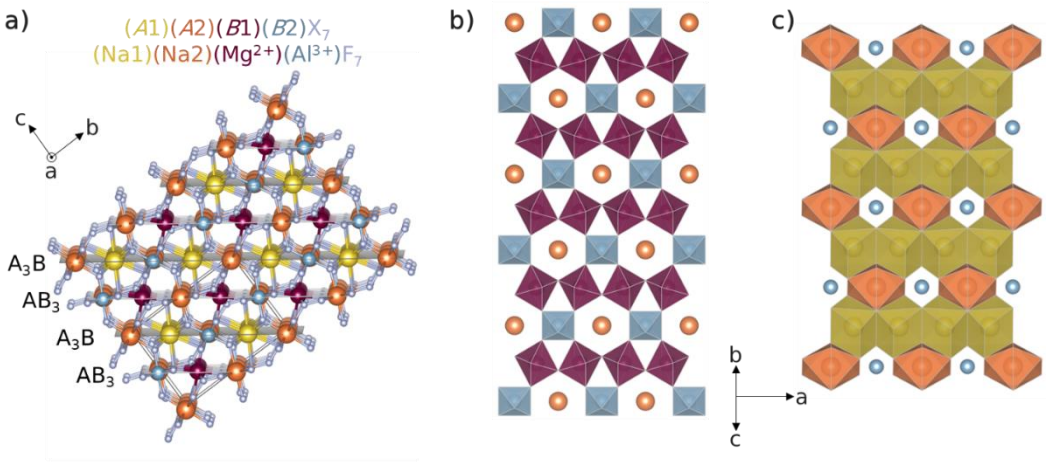

Figure 5.3 – a) Stacking of the Kagomé-like (011) planes as viewed along the [100] direction in Na_2MgAlF_7. The unique Kagomé-like layers AB_3 and A_3B are shown in **b)** and **c)**, respectively, as viewed along the [011] direction.

5.3.2 $Na_2Fe_2F_7$ Polymorphism and Energetics

Given the structural diversity of weberites, a detailed investigation of possible $Na_2Fe_2F_7$ polymorphism and its impact on electrochemical properties is warranted if this material is to be considered for SIB applications. In 1993, a single crystal XRD study by Yakubovich *et al.* suggested that $Na_2Fe_2F_7$ crystallizes in the 4*M* weberite variant,[187] in line with prior reports of the 4*M* structure for other Fe^{2+}-based weberites.[184,200,201] Yet, more recently, Dey *et al.*[179] and Park *et al.*[47] reported the synthesis of the 2*O* and 3*T* variants of $Na_2Fe_2F_7$, respectively, as well as their electrochemical properties in Na-ion cells. Those contrasting reports are difficult to reconcile, especially since they either do not include any diffraction data,[187] or they include patterns with significantly broadened reflections[47,179] and that lack both the sensitivity and resolution to distinguish between the very similar diffraction patterns of the 4*M*, 2*O*, and 3*T* polymorphs (see simulated patterns in Figure 5.4). The main differences between those patterns lie in the splitting

of select peaks, and a few low intensity peaks characteristic of the 3*T* and 4*M* structures. Thus, to identify the weberite structural variant(s) present in each sample using XRD, high quality data on highly crystalline materials – if not single crystals – is necessary.

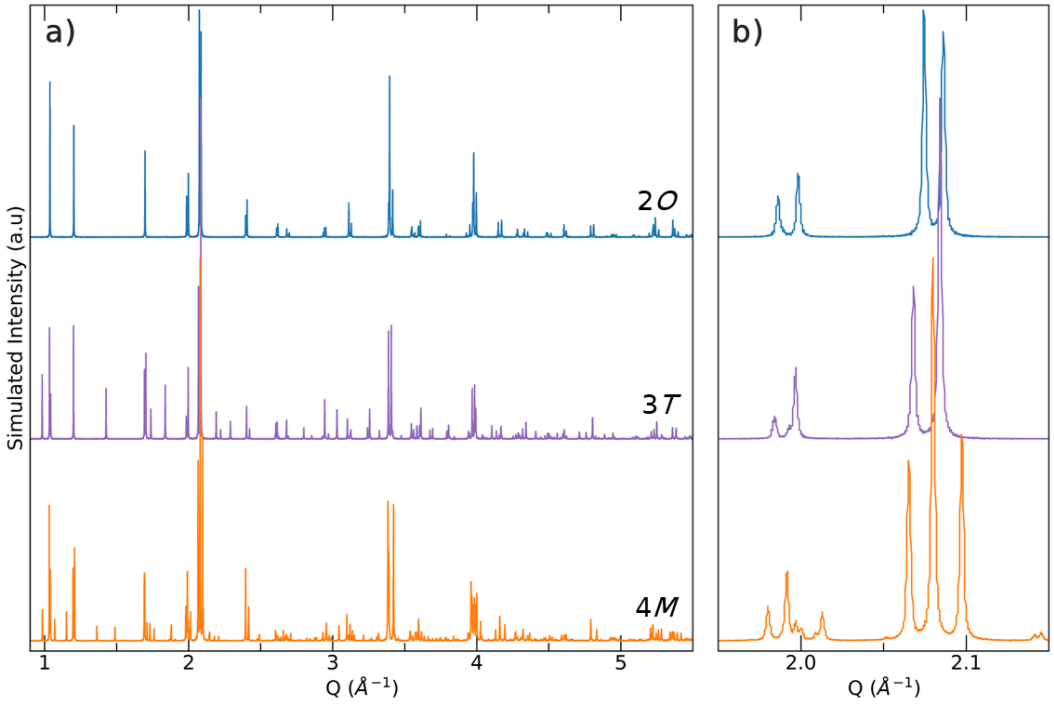

Figure 5.4 – Simulated diffraction patterns for the three reported $Na_2Fe_2F_7$ weberite polymorphs: 2*O* (top), 3*T* (middle), and 4*M* (bottom). The full patterns are shown in **a)**, with an enlarged view of the highest intensity diffraction peaks shown in **b)**. Simulated diffraction patterns were obtained using GSAS-II and a step size of 0.001°.

To gain insight into the likelihood of obtaining the various weberite structural variants of $Na_2Fe_2F_7$, the phase stability of Na-Fe-Fe compounds was investigated. The formation energy of each polymorph, as well as competing phases, was calculated using DFT, with the resultant NaF-FeF_2-FeF_3 ternary diagram shown in Figure 5.1d (values in Table 5.4). Within this space, the weberite polymorphs and $Na_5Fe_3F_{14}$ are metastable, lying 5 to 15 meV/atom above the hull, while the most stable phase is Na_3FeF_6, lying on the hull. As illustrated in Figure 5.1e, the energy above the hull for each weberite polymorph is within 5 meV/atom of each other, suggesting that all three of the

polymorphs may be stabilized at room temperature. These DFT results, as well as the multiple polymorphs previously reported for $Na_2Fe_2F_7$, suggest that X-ray diffraction patterns for $Na_2Fe_2F_7$ weberites should be analyzed with care and complemented with local structure characterization to identify the polymorph(s) present in each sample.

5.3.3 Synthesis and Long-range Structural Characterization of $Na_2Fe_2F_7$

$Na_2Fe_2F_7$ was prepared using a mechanochemically assisted solid-state synthesis procedure adapted from Park *et al*.[47] Several annealing temperatures were tested, and the laboratory powder diffraction patterns obtained on the as-prepared samples are shown in Figure 5.5**.** While Park *et al*. utilized an annealing temperature of 650°C, we found that this temperature resulted in a large amount of impurities (namely, Na_3FeF_6 and FeF_2). In contrast, an annealing temperature of 500°C minimized the amount of impurity phases and was used for the remainder of this study. The SXRD pattern collected on the 500°C annealed sample and its corresponding Rietveld refinement are shown in Figure 5.6a. Despite careful optimization of the synthesis conditions, impurity phases were still observed (9.5 wt.% Na_3FeF_6 and 0.9 wt.% FeF_2). The presence of a significant amount of Na_3FeF_6 in our sample can be explained by its very negative formation energy (Figure 5.1d) compared to those of the weberite $Na_2Fe_2F_7$ variants.

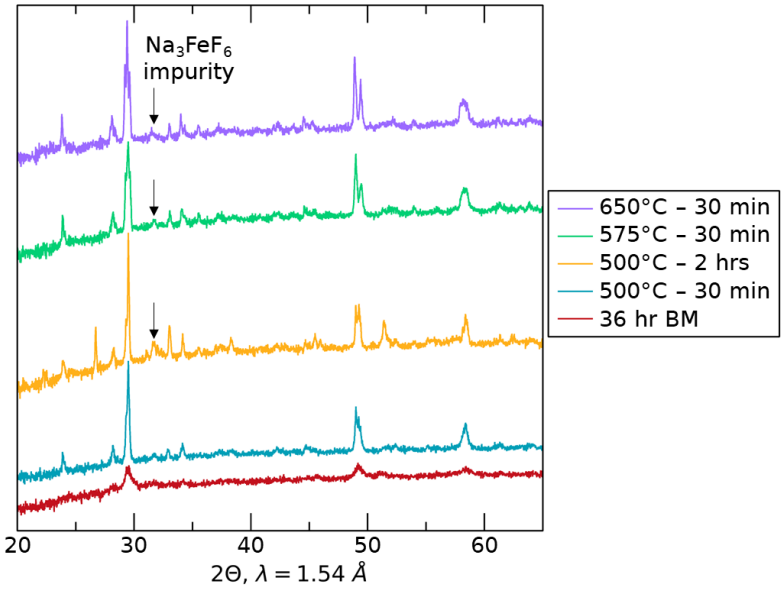

Figure 5.5 – Laboratory XRD patterns of various synthesis conditions used to obtain $Na_2Fe_2F_7$. All syntheses began with a 36 h ball-milling (BM) step (resulting XRD pattern shown in red) that was then followed by an anneal at the temperature and time specified in the figure. Na_3FeF_6 impurities were identified in all patterns besides the one obtained after a 500°C 30 min anneal, which was selected for the remainder of this work.

The SXRD data collected on $Na_2Fe_2F_7$ was analyzed using a combination of Pawley and Rietveld refinements. Refinements involving a single weberite polymorph resulted in poor fits ($\chi^2 > 3.5$, $R_{WP} > 17\%$) due to the complexity of the experimental peak shapes (Figure 5.6a inset), clearly suggesting the presence of many overlapping diffraction peaks and a mixture of phases. Refinement models using all three weberite polymorphs resulted in much improved refinements, with the best refinement ($\chi^2 = 2.12$, $R_{WP} = 9.75\%$)-indicating a sample composition of 4.4 wt.% of the 2*O*, 42.4 wt.% of the 3*T*, and 42.8 wt.% of the 4*M* polymorph. To prevent overfitting the diffraction pattern, site occupancies were not refined and thermal factors were constrained to be equal for each atom type, with detailed Rietveld refinement parameters listed in Table 5.5 and Table 5.7. An additional refinement was performed without the 2*O* polymorph (Figure 5.15), which resulted in a moderately worse fit ($\chi^2 = 2.16$, $R_{WP} = 9.94\%$) indicating that the 2*O*

polymorph is in fact present. Given that a multi-phasic $Na_2Fe_2F_7$ sample was obtained in this work, consistent with the similar energetics of the various $Na_2Fe_2F_7$ polymorphs obtained from first principles (Figure 5.1c), it is possible that previous studies of this material overlooked the presence of multiple phases in their samples.

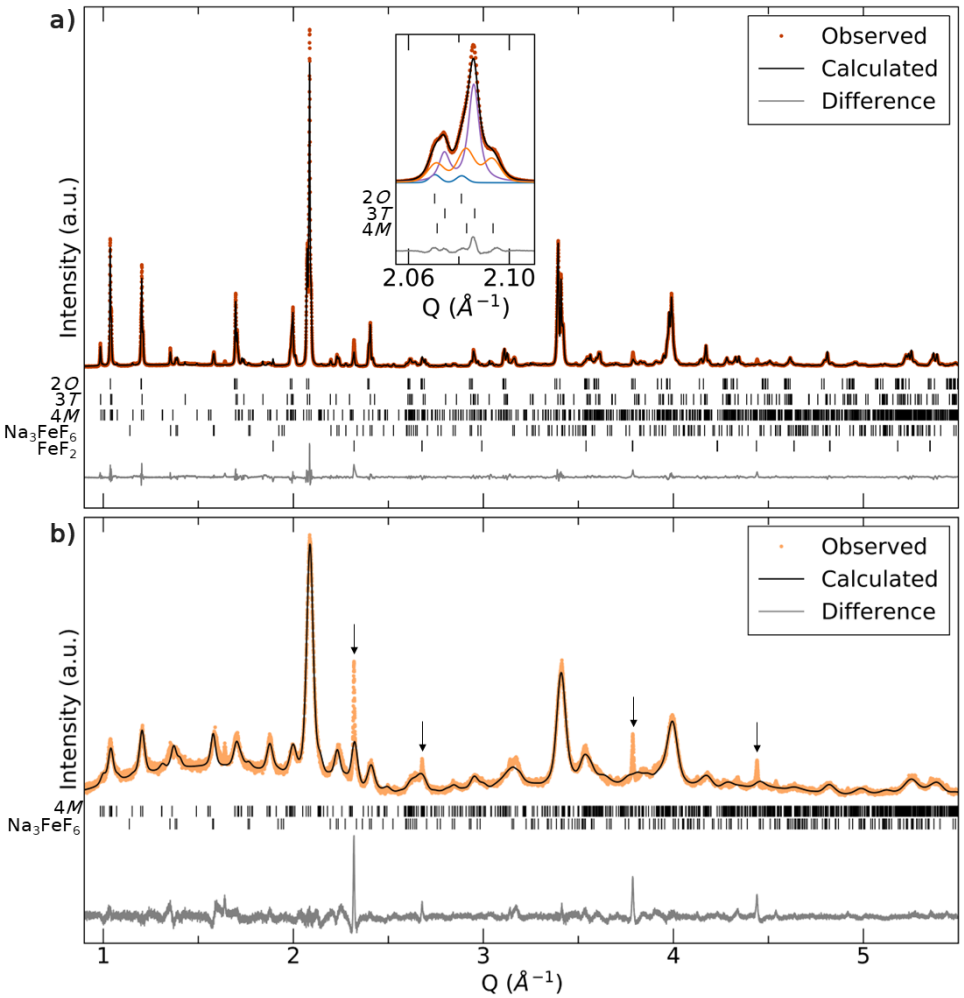

Figure 5.6 – *Synchrotron* XRD characterization of $Na_2Fe_2F_7$ weberite samples. Synchrotron XRD pattern collected on **a)** pristine and **b)** carbon-coated $Na_2Fe_2F_7$ with their corresponding Rietveld refinements. The inset in **a)** shows an enlarged version of the main weberite peaks with the individual profiles shown for the 2O (blue), 3T (purple), and 4M (orange) polymorphs. The arrows in **b)** indicate reflections associated with an unidentified impurity phase.

In preparation for electrochemical testing, the pristine material was ball-milled with carbon to improve its electronic conductivity through both particle size reduction and carbon-coating.[36,202,203] Scanning electron microscopy (SEM) images are shown in

Figure 5.7a,b inset for pristine and carbon-coated $Na_2Fe_2F_7$. The pristine $Na_2Fe_2F_7$ sample contains ≈ 1-2 μm particles, while the carbon-coated $Na_2Fe_2F_7$ sample contains ≈ 100 nm particles, indicating successful particle downsizing. The SXRD pattern collected on carbon-coated $Na_2Fe_2F_7$, shown in Figure 5.6b, exhibits significant peak broadening and a poor signal-to-noise ratio, a likely consequence of the small average particle size and the buildup of strain in the material during the ball-milling process. Thus, the sole purpose of the Rietveld refinement was to identify the amount of impurity phases present: this was done using a single weberite phase, 4*M*, with detailed Rietveld refinement parameters listed in Table 5.6. The amount of impurity phases in the carbon-coated sample is similar to that prior to carbon-coating, but with 11.4 wt.% of Na_3FeF_6 and no FeF_2 present. Carbon-coated $Na_2Fe_2F_7$ also exhibits a minor crystalline impurity (that we are unable to assign to any phase containing Na, Fe, F, C, Zr, and/or O, or fit using an anisotropic strain model)[204] indicated with an arrow in Figure 5.6b and associated with relatively sharp, low intensity diffraction peaks.

5.3.4 Insights into Fe & Na local environments from Mössbauer and solid-state NMR spectroscopy

^{57}Fe Mössbauer spectroscopy was used to characterize the Fe local environments in the pristine and carbon-coated $Na_2Fe_2F_7$ samples. The spectrum collected on pristine $Na_2Fe_2F_7$ is shown in Figure 5.7a. A good fit (χ^2 = 1.12) of this spectrum was obtained using five components (fitting parameters are provided in Table 5.1): two doublets at isomer shifts (δ) of 1.45 and 1.25 mm/s, with quadrupolar splittings (ΔE_Q) of 1.38 and 1.42 mm/s, respectively, assigned to $Fe^{2+}F_6$ in the weberite phases; two doublets at δ =

0.43 and 0.45 mm/s, with ΔE_Q = 0.72 and 0.49 mm/s, respectively, assigned to $Fe^{3+}F_6$ in the weberite phases; and a doublet assigned to Na_3FeF_6 using previously-reported Mössbauer parameters (δ = 0.27 mm/s, ΔE_Q = 0.15 mm/s).[38] The $Fe^{2+}F_6$ and $Fe^{3+}F_6$ signals closely match values obtained for other Fe-containing weberite phases.[179,205–207] The multiple doublets assigned to $Fe^{2+}F_6$ and to $Fe^{3+}F_6$ species indicates a distribution of Fe local environments in the distinct weberite polymorphs. Notably, the $Fe^{2+}F_6$ local environment changes more than the $Fe^{3+}F_6$ local environment in the various forms of $Na_2Fe_2F_7$, which may account for the larger variation in the isomer shift of $Fe^{2+}F_6$ signals. Integration of the Mössbauer signals leads to an average Fe oxidation state of 2.55+ for the weberite phases resulting in a stoichiometry of $Na_{1.90}Fe^{2.55+}{}_2F_7$ (assuming full F occupation)[208] indicating a slight Na deficiency, in line with the ICP results (Table 5.10).

The ^{57}Fe Mössbauer spectrum collected on the carbon-coated $Na_2Fe_2F_7$ sample (Figure 5.7b) suggests moderate Fe oxidation upon carbon-coating (average Fe oxidation state of 2.67+). Notably, this spectrum could be fitted with one broad signal for $Fe^{2+}F_6$ and one broad signal for $Fe^{3+}F_6$ (fitting parameters are provided in Table 5.1), indicating greater disorder within the weberite phase(s) upon ball-milling. Overall ^{57}Fe Mössbauer spectroscopy confirms that the weberite material is slightly Na deficient, with this deficiency increasing upon carbon-coating, resulting in a stoichiometry of about $Na_{1.68}Fe^{2.7+}{}_2F_7$ prior to electrochemical cycling.

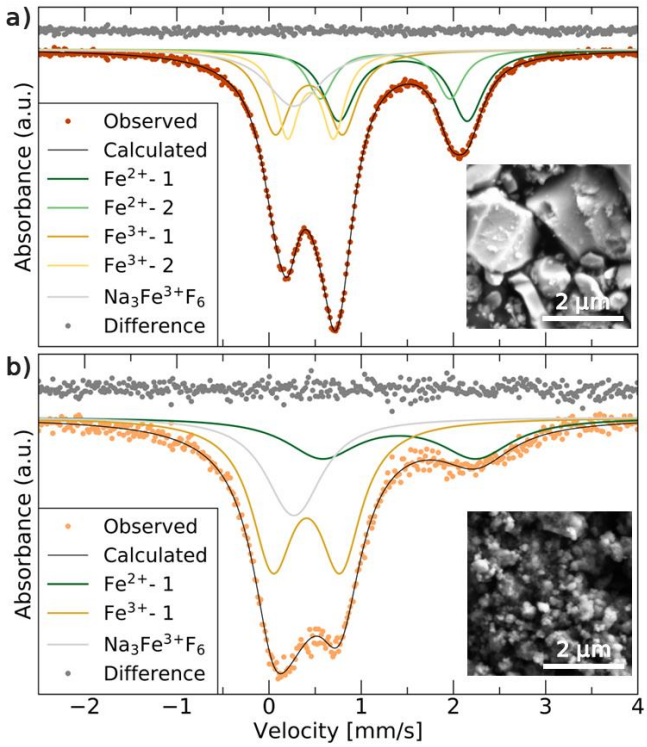

Figure 5.7 – ^{57}Fe Mössbauer spectroscopy and SEM characterization of $Na_2Fe_2F_7$ weberite samples. a) ^{57}Fe Mössbauer spectrum and fit collected on **a)** pristine and **b)** carbon-coated $Na_2Fe_2F_7$. The insets show the corresponding SEM micrographs for each material.

Table 5.1 – Fitting parameters for ^{57}Fe Mössbauer spectra collected on the pristine and carbon-coated $Na_2Fe_2F_7$ samples and resulting average iron oxidation state and sodium stoichiometry in the weberite phase.

	Signal	Isomer Shift (δ, mm/s)	Quad. Splitting (ΔE_Q, mm/s)	FWHM (mm/s)	Integrated Intensity	χ^2	Avg. Fe Ox. State		Weberite Na Stoich.
							Weberite	Total	
Pristine	Fe^{2+}- 1	1.45(6)	1.38(12)	0.43(3)	25(6)%	1.1	2.55(16)	2.62(15)	1.90(33)
	Fe^{2+}- 2	1.25(2)	1.42(3)	0.34(5)	13(5)%				
	Fe^{3+}- 1	0.43(4)	0.72(9)	0.39(4)	27(9)%				
	Fe^{3+}- 2	0.45(1)	0.49(4)	0.29(4)	20(8)%				
	$Na_3Fe^{3+}F_6$	0.27	0.15	0.68(9)	15(4)%				
Carbon-Coated	Fe^{2+}	1.41(9)	1.67(9)	0.94(8)	28(8)%	1.2	2.66(15)	2.70(16)	1.68(30)
	Fe^{3+}	0.41(1)	0.73(3)	0.55(8)	54(9)%				
	$Na_3Fe^{3+}F_6$	0.27	0.15	0.68(9)	18(9)%				

The Na local environments in $Na_2Fe_2F_7$ were examined using ^{23}Na ss-NMR. As $Na_2Fe_2F_7$ contains unpaired electrons from the Fe^{2+}/Fe^{3+} species and ^{23}Na is a quadrupolar nucleus (I = 3/2), both paramagnetic and quadrupolar effects are present. These interactions result in significant NMR line broadening and large chemical shifts,

leading to significant signal overlap and complicating the attribution of spectral features to specific local environments in the material. Here, the assignment of the complex NMR spectra was assisted by first principles hybrid density functional theory (DFT)/Hartree Fock (HF) calculations of ^{23}Na NMR parameters using the CRYSTAL17 code on the different $Na_2Fe_2F_7$ weberite structural variants (see Appendix 5.5.4 for computational parameters and methodology), with results shown in Table 5.2. The ^{23}Na isotropic chemical shift (δ_{iso}) is dominated by the paramagnetic (Fermi contact) shift resulting from delocalization of unpaired electron spin density from nearby Fe 3*d* orbitals to the ^{23}Na *s* orbital. These paramagnetic interactions also lead to significant spectral broadening. The interaction between the ^{23}Na nuclear quadrupole moment and the electric field gradient (EFG) present at the Na nucleus leads to a further broadening of the spectrum and to a shift of the ^{23}Na resonant frequency due to second-order effects (denoted δ_Q). The observed chemical shift (δ_{obs}) is then the sum of the isotropic Fermi contact shift and of the second-order quadrupolar shift: $\delta_{obs} = \delta_{iso} + \delta_Q$.

Obtaining high resolution spectra of quadrupolar nuclei in paramagnetic materials is complicated by the opposing magnetic field (B_0) dependence of quadrupolar and paramagnetic interactions. While second-order quadrupolar effects (e.g., δ_Q and associated line broadening) are inversely related to B_0, such that NMR spectra of quadrupolar nuclei are typically obtained at high fields, high field strengths exacerbate paramagnetic broadening and lower fields are preferred for strongly paramagnetic samples. Here, the optimal field strength that maximizes spectral resolution was determined by plotting the predicted δ_{obs} at various magnetic field strengths for cubic and bihexagonal pyramidal Na sites in each weberite polymorph, as shown in Figure

5.8a. The highly asymmetrical bihexagonal pyramidal Na environments exhibit a greater field-dependence of their δ_{obs} due to their larger quadrupolar coupling constants ($C_Q \geq 5$ MHz) compared to cubic Na sites ($C_Q \leq 3.5$ MHz). Our first principles calculations suggest: 1) significant overlap between the ^{23}Na ss-NMR signals associated with cubic Na sites in the 3*T* and 4*M* weberite variants, and similarly for the bihexagonal pyramidal Na signals in those two phases. For the 2*O* polymorph, the resonance associated with the cubic Na environment likely overlaps with those of the bihexagonal pyramidal Na signals from the 3*T* and 4*M* weberite variants, while the signal arising from 2*O* bihexagonal pyramidal Na sites is expected at very negative shifts and should be discernable. 2) At low fields (2.35 T), ^{23}Na signals corresponding to cubic and bihexagonal pyramidal Na sites within a single weberite phase are expected to be separated by nearly 1000 ppm owing to their different second-order quadrupolar shifts (δ_Q), while at higher fields δ_Q becomes negligible and the signals overlap. Thus, to maximally resolve ^{23}Na signals from the different local environments present in the samples of interest, all ^{23}Na ss-NMR spectra were obtained at our lowest field of 2.35 T.

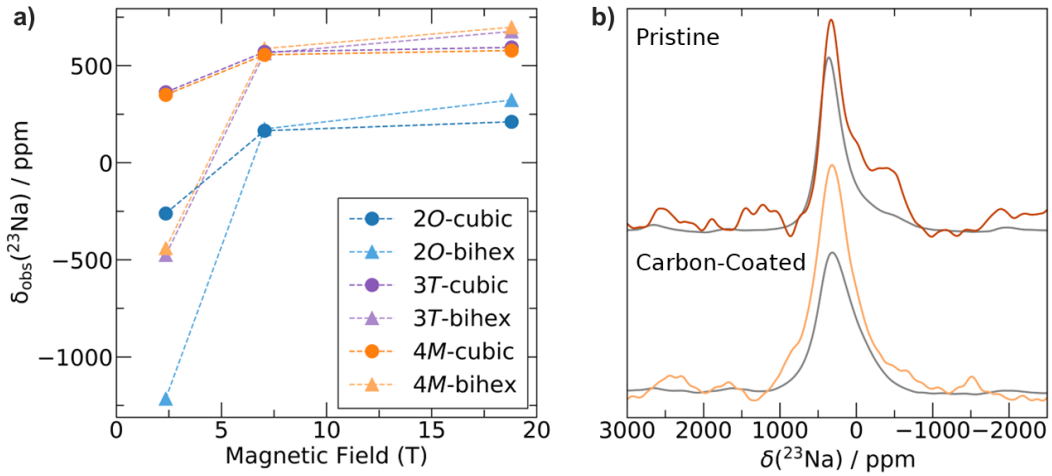

Figure 5.8 – ^{23}Na ss-NMR Predictions & Spectra a) Field-dependence of the calculated chemical shifts for the average cubic and bihexagonal pyramidal sites in $Na_2Fe_2F_7$ weberite polymorphs. **b)** ^{23}Na ss-NMR spin echo spectra collected on pristine and carbon-coated $Na_2Fe_2F_7$ using $\pi/2$ (grey) and $\pi/6$ (orange) excitation pulses.

Table 5.2 – First principles ^{23}Na NMR parameters computed using the CRYSTAL17 code on 2O, 3T, and 4M $Na_2Fe_2F_7$ structures optimized with VASP. The predicted NMR properties were scaled using a scaling factor $\Phi = 0.008066$ to compare them to room temperature ^{23}Na solid-state NMR data obtained at an external magnetic field of $B_0 = 2.35$ T. There are two unique Na local environments in 2*O*, three in 3*T*, and six in 4*M* $Na_2Fe_2F_7$, with multiplicities specified in parentheses in the table below. δ_{iso} is the isotropic Fermi contact shift, $\Delta\delta$ and η are the electron-nuclear dipolar anisotropy and asymmetry parameters, respectively, C_Q is the quadrupolar coupling constant, η_Q is the quadrupolar asymmetry, δ_Q is the second-order quadrupolar shift, and $\delta_{obs} = \delta_{iso} + \delta_Q$ is the observed chemical shift.

Phase	Site	Coord. Type	δ_{iso} (ppm)	$\Delta\delta$ (ppm)	η	$\lvert QCC \rvert$ (MHz)	η_Q	δ_Q (ppm)	$\delta_{iso} - \delta_Q$ (ppm)
2O	**Na1 (x1)**	cubic	218	207300	0.87	3.53	0.48	479	-261
2O	**Na2 (x1)**	bihex.	347	-246700	0.65	6.24	0.61	1562	-1215
3T	**Na1 (x2)**	cubic	650	-2191	0.48	2.73	0.65	314	336
3T	**Na2 (x1)**	cubic	494	-2028	0.17	1.31	0.89	78	416
3T	**Na3 (x1)**	bihex.	694	-2133	0.50	5.62	0.34	1169	-475
4M	**Na1 (x1)**	cubic	505	-2124	0.78	2.61	0.67	280	224
4M	**Na2 (x1)**	bihex.	801	-2243	0.45	5.00	0.37	934	-133
4M	**Na3 (x1)**	cubic	516	-2028	0.83	2.62	0.36	256	260
4M	**Na4 (x1)**	cubic	529	-1974	0.09	0.89	0.66	33	497
4M	**Na5 (x2)**	cubic	680	-2238	0.47	2.80	0.40	296	384
4M	**Na6 (x2)**	bihex.	673	-2181	0.44	5.77	0.45	1267	-593

^{23}Na ss-NMR spin echo spectra collected on pristine and carbon-coated $Na_2Fe_2F_7$ samples are shown in Figure 5.8b. For each sample, the two overlaid spectra were obtained using a typical π/2 excitation pulse and a small flip angle (π/6) excitation pulse, respectively. Despite the decrease in sensitivity caused by the small flip angle, the π/6 spectra exhibit at least one additional signal at ≈ −400 ppm compared to the π/2 spectra, that is more prevalent for pristine $Na_2Fe_2F_7$. This additional signal is attributed to bihexagonal pyramidal Na sites, whose larger quadrupolar interactions result in broader, lower intensity signals that are poorly excited by a π/2 pulse.[72] Thus, the π/2 spectra are dominated by signals arising from Na in cubic sites, while the π/6 spectra reflect all Na environments present in the samples. The spectra also contain low intensity signals arising from the Na_3FeF_6 impurity phase, as revealed by the ^{23}Na ss-NMR spin echo spectrum obtained on a Na_3FeF_6 sample overlaid in Figure 5.16 with the π/2 spectra shown in Figure 5.8b. While the 200 ppm Na_3FeF_6 signal is difficult to discern from the $Na_2Fe_2F_7$ phase, the Na_3FeF_6 signal at 1800 ppm is distinguishable but very low in intensity. Finally, while the π/6 spectra shown in Figure 5.8b could in theory provide some information on the relative population of cubic and bihexagonal pyramidal Na sites, the strong quadrupolar and paramagnetic interactions present in $Na_2Fe_2F_7$ result in short ^{23}Na ss-NMR signal lifetimes and signal loss over the course of the experiments. Hence, the relative signal intensities in these spectra are not quantitative; besides, measurements of transverse relaxation times (T_2') to account for signal loss are impractical due to their extremely low sensitivity (*e.g.,* the π/6 spectrum collected on pristine $Na_2Fe_2F_7$ took over 48 h to acquire).

Nearly all the ^{23}Na ss-NMR signals from the weberite variants are predicted to lie within the −500 ppm to 500 ppm range, save from the bihexagonal pyramidal Na resonance and the Na signals arising from the 2*O* variant at more negative shifts (see Figure 5.8a). Clearly, all the main resonances observed in the spectra in Figure 5.8b lie within the expected range for $Na_2Fe_2F_7$ weberites. Yet, the π/6 spectra show clear differences in the distribution of Na local environments in the pristine and carbon-coated $Na_2Fe_2F_7$ samples. The spectrum collected on the pristine sample exhibits signals at negative shifts (centered around −400 ppm) consistent with the presence of Na in bihexagonal pyramidal sites in the 3*T* and 4*M* phases. Notably, this spectrum appears to contain several overlapping signals, including distinct cubic and bihexagonal pyramidal signals, suggestive of multiple polymorphs present. The carbon-coated sample, however, shows noticeably fewer signals at negative shifts, suggesting that the C-coating process may be reducing the intensity of the quadrupolar interactions and/or reducing the occupation of bihexagonal pyramidal Na sites by introducing more overall disorder into the system.

These results, combined with the previously discussed SXRD and ^{57}Fe Mössbauer data, suggest the preparation of a multi-phasic (predominantly 3*T* and 4*M*) $Na_2Fe_2F_7$ weberite material containing Na_3FeF_6 impurities that partially disorders upon carbon-coating while still retaining the long-range weberite structure.

5.3.5 Electrochemical properties of $Na_2Fe_2F_7$

As the 24 h carbon-coating process affects the weberite structure, several shorter mechanochemical milling times and an *in situ* carbon-coating method were investigated

to reduce structural disordering, with results presented in Appendix 5.5.5.1. Briefly, none of the alternative carbon-coating methods tested here led to an electrochemical performance on par with that obtained after a 24 h milling step, which was therefore adopted for the remainder of this work.

Results from electrochemical tests on the $Na_2Fe_2F_7$ cathode are presented in Figure 5.9. The voltage profiles for $Na_2Fe_2F_7$ are shown in Figure 5.9a through cycle 50. Unless indicated otherwise, $Na_2Fe_2F_7$ was cycled at a rate of C/20 (full (dis)charge in 20 h assuming the transfer of 2 Na per formula unit) by first charging to 4.3 V vs. Na^+/Na and subsequent cycling between 4.3 V and 1.5 V. Upon first charge, a capacity of 70 mAh/g is achieved with the following discharge providing a reversible capacity of 125 mAh/g. We note that all capacities reported here are calculated assuming that the entire active material is composed of $Na_2Fe_2F_7$, which leads to an underestimation of the capacity attributable to the electrochemically active phase as SXRD suggests the presence of about 10 wt.% Na_3FeF_6 prior to cycling. This was done as the carbon-coated material likely contains an unknown component of amorphous domains, which SXRD is unable to detect. While more Na may be able to intercalate upon discharging the cell to a lower potential, the discharge cutoff voltage was maintained at 1.5 V to prevent the Na_3FeF_6 impurity phase from becoming electrochemically active at lower potentials[38] and interfering with the analysis of the electrochemical behavior of $Na_2Fe_2F_7$. Beyond the first cycle, the capacity fades steadily (Figure 5.18a). Differential capacity (dQ/dV) plots recorded over the first 50 cycles are shown in Figure 5.9b. During the first few cycles, several broad features are observed on charge and discharge, which gradually evolve into two sharp features centered around 3.3/3.6 and 2.8/3.1 V on

discharge/charge. The average discharge voltage (Figure 5.18b) begins at about 2.8 V but gradually fades to 2.7 V, and the charge-discharge voltage hysteresis increases from 0.5 V to 0.75 V after 50 cycles. The rate performance is shown in Figure 5.9c. A respectable capacity of 85 mAh/g is achieved at a rate of C/5, but the capacity quickly drops off as the rate is increased to 1C, suggesting that Na (de)intercalation from/into the weberite cathode is kinetically limited. Galvanostatic intermittent titration technique (GITT) tests were performed to understand the extent of charge-transfer and Na-ion conduction limitations which additively contribute to the observed overpotential,[3] with results shown in Figure 5.9d. At high and low voltage, large overpotentials (approaching 0.5 V) are observed, while overpotentials are minimal throughout the rest of the electrochemical profile. This suggests that the processes between 2.5 to 4 V, approximately corresponding to Na (de)intercalation and Fe redox between the compositional bounds of $Na_2Fe^{2+}Fe^{3+}F_7$ and $Na_1Fe^{3+}{}_2F_7$, are kinetically facile, while Na (de)intercalation and Fe redox beyond those bounds is hindered. Even after a 2-hour equilibration period after each current pulse, a significant voltage hysteresis remains throughout the electrochemical profile, suggesting some asymmetry associated with the charge-discharge processes, which will be revisited in the following sections.

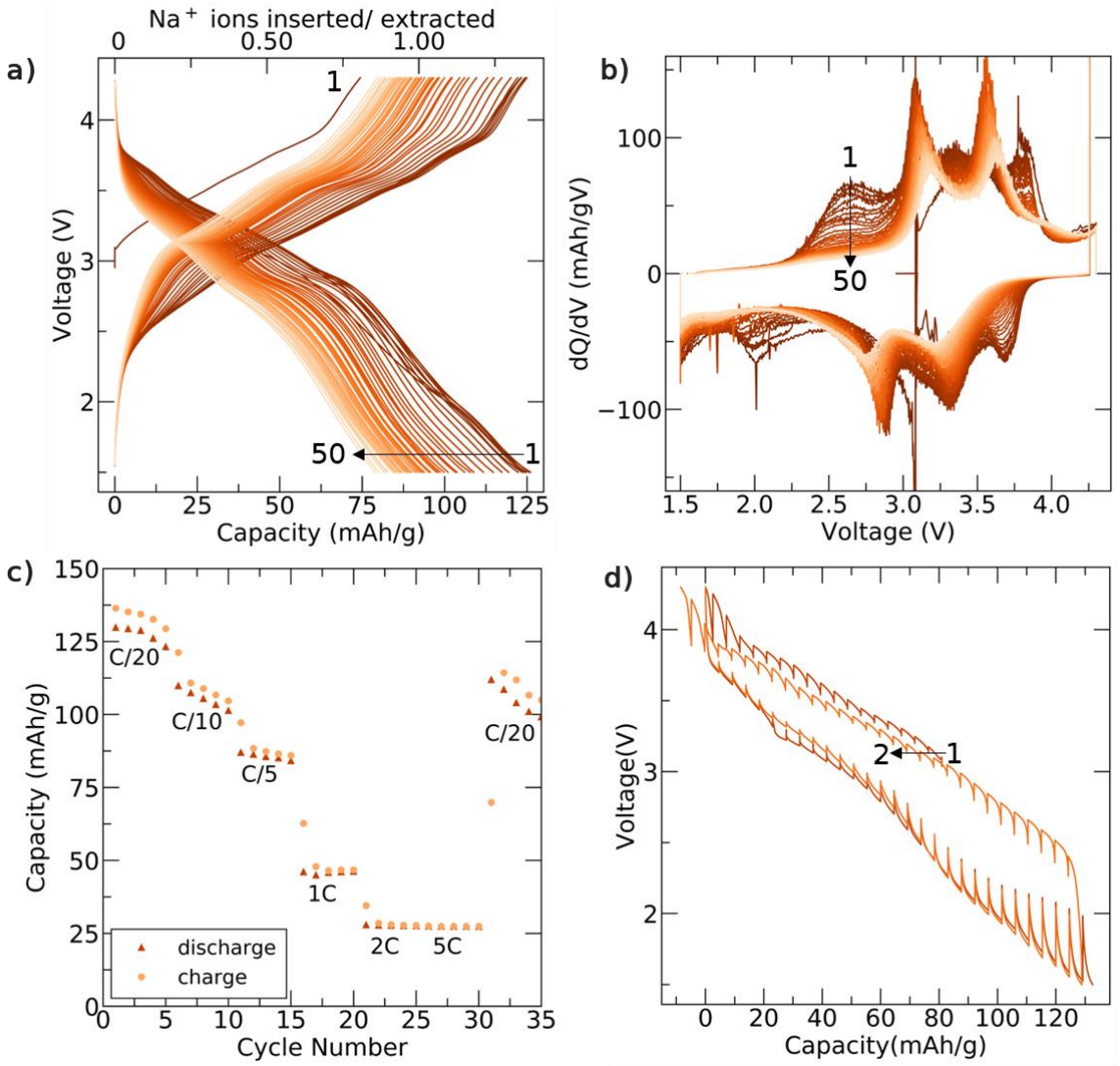

Figure 5.9 – Electrochemical characterization of $Na_2Fe_2F_7$. a) Galvanostatic charge-discharge curves recorded at C/20 over the first 50 cycles, and **b**) corresponding differential capacity plots. **c)** Charge and discharge capacity obtained at various cycling rates and recorded over 35 cycles. The first charge step was omitted from the plot for clarity. **d)** Galvanostatic intermittent titration technique (GITT) data obtained over the first 2 cycles, where a 30-minute C/20 current pulse was applied followed by a 2-hour rest period. All the electrochemical results shown here were obtained using voltage cutoffs of 4.3 V and 1.5 V on charge and discharge, respectively.

Overall, the present $Na_2Fe_2F_7$ cathode exhibits respectable capacities over the first few cycles, but steady capacity fade upon extended cycling. These results differ from prior reports: Dey *et al.* reported a much lower initial reversible capacity of 58 mAh/g for a $Na_2Fe_2F_7$ cathode synthesized via a topochemical route,[179] while Park *et al.* obtained a higher initial capacity and higher cycling stability for a cathode prepared

using a very similar synthesis route to the one adopted here.[47] While those discrepancies may stem from a different ratio of weberite variants in their samples, the electrochemical performance is likely also strongly dependent on the specific cathode preparation method used in each study. Such a strong dependence on electrode formulation and processing has been reported in poor electron conducting materials, such as transition metal fluoride electrodes for sodium-[202,209–212] and lithium-based[34,36,202] batteries, but also lithium iron phosphate.[203,213,214]

To better understand the origin of the capacity fade observed here, and the differences in the electrochemical performance reported in the three studies of $Na_2Fe_2F_7$, *ex situ* characterization of cathode samples and a computational investigation of the dependence of the electrochemical properties of weberite $Na_2Fe_2F_7$ on the structural variant are presented in the next sections.

5.3.6 *Ex Situ* Characterization of the Charge-Discharge Mechanism

The evolution of the dQ/dV features (Figure 5.9b) suggests a change in the bulk structure and redox mechanism of the $Na_2Fe_2F_7$ cathode upon extended cycling. To monitor those structural changes, *ex situ* SXRD and ^{23}Na ss-NMR characterization was performed on samples collected at the end of the 1st and 10th discharge, with results shown in Figure 5.10. Prior to cycling, weberite-type $Na_xFe_2F_7$ is the main active component of the cathode, with about 10 wt.% of Na_3FeF_6 present. However, *ex situ* SXRD data indicate a partial phase transformation of the $Na_xFe_2F_7$ weberite phase during cycling. Rietveld refinements of the SXRD patterns collected after the 1st and 10th cycle (see Rietveld refinement parameters listed in Table 5.8 and Table 5.9) suggest that the

newly formed phase is perovskite-like $NaFeF_3$ (*Pnma*), which accounts for 40 wt.% of the sample after the 1st discharge and 53 wt.% of the sample after the 10th discharge. A constant weight fraction of Na_3FeF_6 remains in the sample upon cycling, suggesting that the Na_yFeF_3 phase evolves at the expense of $Na_xFe_2F_7$ weberite phases only. Note that the unassigned impurity peaks are still present and do not evolve throughout cycling suggesting they are an electrochemically-inactive component.

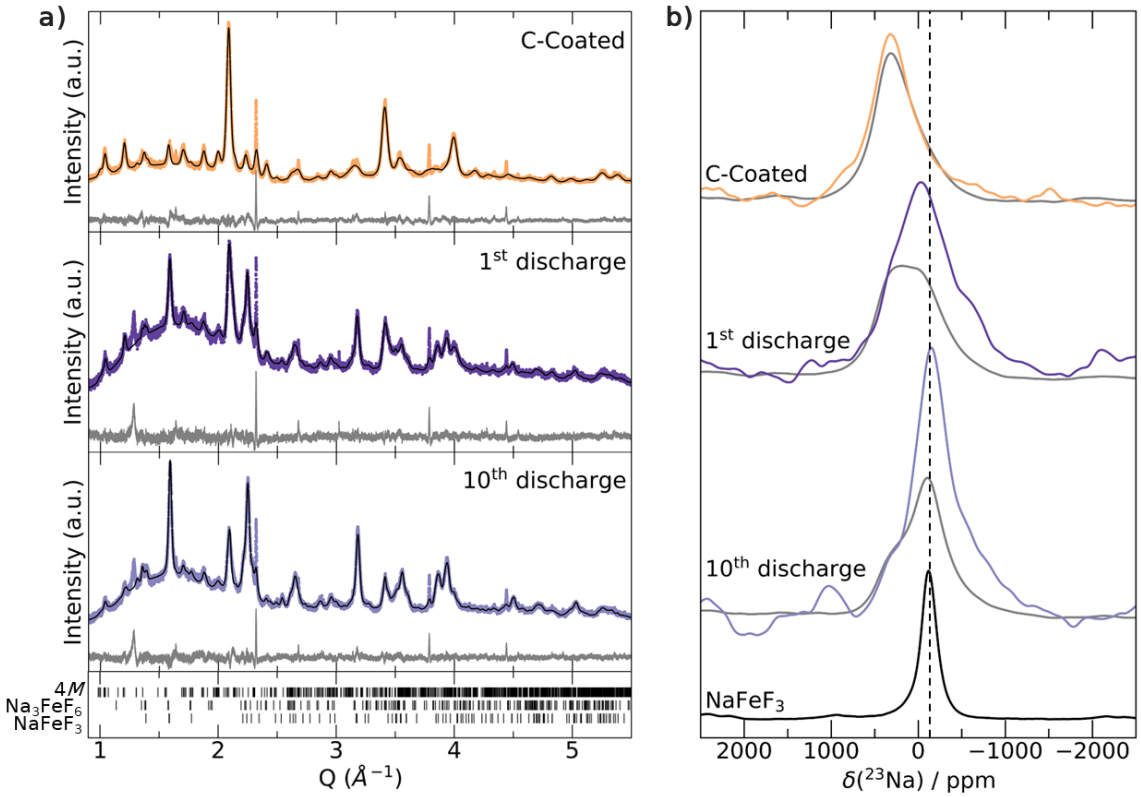

Figure 5.10 – Characterization of ex situ $Na_xFe_2F_7$ cathode samples. a) SXRD patterns with corresponding Rietveld refinements (black, difference pattern in grey) and **b)** ^{23}Na ss-NMR spin echo spectra obtained on carbon-coated $Na_2Fe_2F_7$ (top), and on *ex situ* $Na_xFe_2F_7$ samples collected after the 1st (middle) and 10th (bottom) discharge. Spectra obtained with a π/2 excitation pulse are shown in grey, and those obtained with a π/6 excitation pulse are colored. The bottom ^{23}Na ss-NMR spectrum was obtained on $NaFeF_3$ using a π/2 pulse. The dashed line indicates the position of the $NaFeF_3$ resonance.

As SXRD is only sensitive to crystalline domains, ^{23}Na ss-NMR spectra were also collected on the *ex situ* samples, as shown in Figure 5.10b. For comparison, $NaFeF_3$ was synthesized – its crystal structure, laboratory XRD pattern, and corresponding refinement are shown in Figure 5.11 – and its ^{23}Na ss-NMR spectrum is also shown in Figure 5.10b. The single, broad ^{23}Na signal at –118 ppm in the spectrum collected on $NaFeF_3$ presumably corresponds to the single, relatively symmetric Na environment in the perovskite-like structure. The NMR spectra collected on $Na_xFe_2F_7$ cathode samples reveal significant structural changes upon cycling, with the appearance of a signal at –118 ppm consistent with the formation of $NaFeF_3$. In line with the SXRD results, the fraction of $NaFeF_3$ increases with cycling, as indicated by the gradual growth of the –118 ppm peak. The broader and low intensity signals in the *ex situ* spectra likely correspond to cubic and bihexagonal pyramidal Na environments in residual $Na_xFe_2F_7$ domains, which can be differentiated using π/2 and π/6 flip angle spin echo experiments as discussed previously. Additionally, ^{19}F NMR data, shown in **Figure S10**, indicates a very minor NaF component in the *ex situ* samples. Integration of this signal suggests the presence of < 0.05 wt.% of NaF in the total sample and thus this component is likely resulting from electrolyte decomposition[215,216] rather than from the phase transformation process.

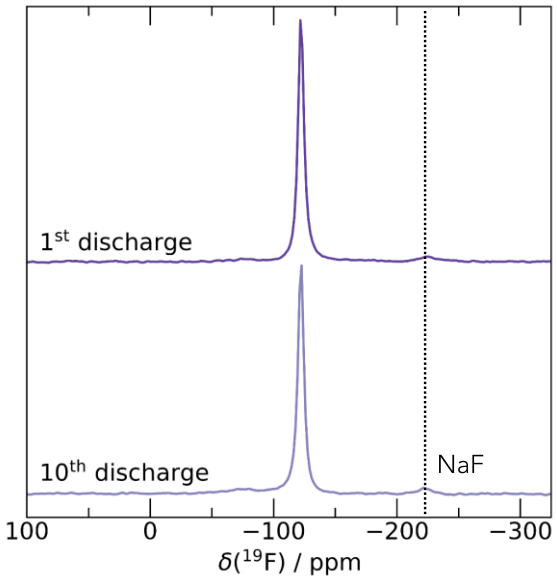

Figure 5.12 – Quantitative ^{19}F ss-NMR spin echo spectra obtained on *ex situ* $Na_xFe_2F_7$ samples collected after the 1st and 10th discharge using a long interpulse delay of 60 s. Both spectra show a prominent signal at −120 ppm assigned to the PTFE binder, and very minor signals at −74.5 ppm and −224 ppm, which we attribute to decomposed electrolyte species containing PF_6^-,[163] and NaF, respectively. The NaF signal is indicated with a dashed line. By taking the ratio of NaF to PTFE integrated signal intensity (assuming the presence of 10 wt.% PTFE in the sample, as used to prepare the cathode films), we find that the NaF content in the two *ex situ* samples is < 0.05 wt.%. Thus, NaF is not related to the phase transformation process occurring in the bulk of the cathode and most likely arises from electrolyte decomposition during cycling. We note that NMR signals from ^{19}F nuclei directly bonded to paramagnetic Fe species (as is the case for all F environments in $Na_xFe_2F_7$ and Na_yFeF_3) in the cathode materials are too broad (and short-lived) to be observed experimentally.

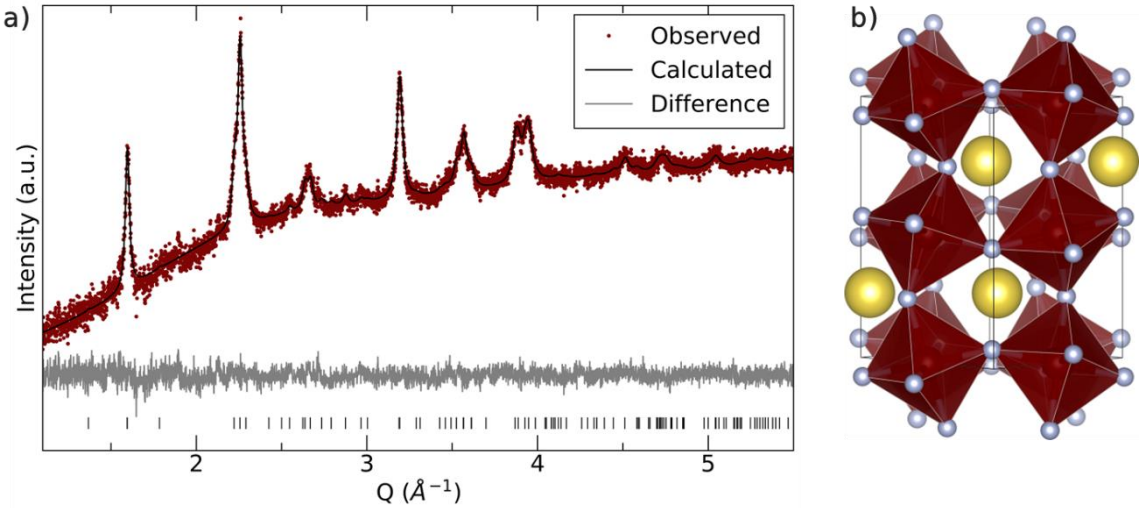

Figure 5.11 – a) Laboratory XRD pattern collected on $NaFeF_3$ prepared via 12 hrs of ball-milling at 600 rpm and corresponding Rietveld refinement. Refined lattice parameters are a = 5.48782, b = 7.88543, c = 5.65752, with a χ^2 = 1.54. **b)** Perovskite $NaFeF_3$ (*Pnma*) structure viewed along the [101] direction.

Thus, our *ex situ* results show that our weberite cathode undergoes a phase transformation to Na_yFeF_3 upon cycling. Those findings agree well with the electrochemical results, as Na_yFeF_3 is electrochemically active with very similar dQ/dV features and comparable experimental capacities (≈ 105 mAh/g) as those observed on later cycles in Figure 5.9b.[217,218] Further, the several kinks observed in the galvanostatic data during the first discharge process may indicate the beginning of this phase transformation, as shown with select single cycle dQ/dV plots in Figure 5.18c-f. As the dQ/dV curve evolves at least to the 20th cycle, the $Na_xFe_2F_7$ to Na_yFeF_3 phase transformation continues up to this point. The electrochemical behavior on later cycles suggests that little to no weberite phase is left after 20 cycles, and the capacity observed is mostly due to Na (de)intercalation from/into Na_yFeF_3.

Based on the ternary phase diagram presented in **Figure 1d**, one would anticipate the as-synthesized $Na_2Fe_2F_7$ weberite cathode to decompose into FeF_2, $NaFeF_4$, and Na_3FeF_6. However, the black, dotted tie-line in the phase diagram represents the compositional evolution of the weberite at various stages of charge, clearly indicating that, on charge and discharge, thermodynamically-stable, perovskite-like Na_yFeF_3 phases (including FeF_3 and $NaFeF_3$) become possible decomposition phases of the metastable weberite cathode, providing a potential explanation for the observed phase transformation. While thermodynamics is important to rationalize phase transformations, kinetics must also be considered. Kinetic considerations may provide further insights into the mechanism of the phase transformation. Here, the perovskite-type Na_yFeF_3 and weberite $Na_xFe_2F_7$ structures contain similar building blocks, likely facilitating the structural rearrangements. As previously mentioned, weberite $Na_xFe_2F_7$

contains a 3D network of corner-sharing FeF_6 octahedra, and 1D $Fe^{2+}F_6$ octahedral chains. Na_yFeF_3 similarly contains corner-sharing $Fe^{2+}F_6$ octahedral chains, now connected in 3D, as it forms a perovskite-like structure with Na occupying lattice sites in-between the chains (Figure S9b). Thus, upon Na (de)intercalation from/into the weberite structure, rearrangement of the FeF_6 octahedra may enable the weberite to perovskite phase transformation. Notably, Fe^{3+} possesses a high spin d^5 electron configuration, hence no octahedral vs. tetrahedral site preference, and can easily migrate to nearby sites as has been observed in other Fe-containing cathode materials.[219–222] Hence, the phase transformation is expected to be both kinetically facile and thermodynamically favored. Additional clues as to the onset and mechanism of the phase transformation come from the electrochemical, and *ex situ* SXRD and NMR analysis. First, the sharp and prominent dQ/dV feature observed at ~3.1 V during the first discharge process (Figure 5b) is tentatively attributed to the onset of the phase transformation, suggesting that this phase transformation initiates at a Na content $x < 2$ in the weberite phase. Given that the only two Na-containing phases observed by ^{23}Na NMR and SXRD in the discharged samples are the weberite and perovskite phases, and ^{19}F NMR data further confirms a negligible amount of NaF in these samples, the Na content in the perovskite phase formed on discharge is presumably equal to that in the initial weberite phase. Hence, a possible reaction mechanism is $Na_xFe_2F_7 \rightarrow 2\ Na_{x/2}FeF_3 + ½\ F_{2(g)}$, where $F_{2(g)}$ likely reacts with the electrolyte to form HF. In turn, HF formation during cycling could contribute to the rapid capacity decay. In fact, we have seen evidence of residues on the stainless steel plungers used in the Swagelok cells that are suggestive of corrosion.

The phase transformation observed here appears to be dependent on the specific weberite variant composition and/or the electrode preparation method, as Park *et al.* observed only the weberite phase via *ex situ* XRD after the 1000th cycle.[47] Regardless, the metastability and polymorphism of weberite compounds, exemplified here for $Na_2Fe_2F_7$, are important considerations for the development and accurate evaluation of this class of cathode materials.

5.3.7 Computational Investigation of the Electrochemical Properties of $Na_2Fe_2F_7$ Weberite Variants

To elucidate the influence of the weberite polymorph identity on the electrochemical performance of $Na_2Fe_2F_7$, the thermodynamic stability of a series of $Na_xFe_2F_7$ ($0 \leq x \leq 3$) compositions was evaluated from first principles for the 2*O*, 3*T*, and 4*M* variants. The three resulting convex hulls are overlaid in Figure 5.13a, which include various Na-vacancy orderings at intermediate $Na_xFe_2F_7$ compositions, and polymorph-specific Fe_2F_7 and $Na_3Fe_2F_7$ end-member phases (additional computational details are provided in Appendix 5.5.1.1). To achieve compositions with $x > 2$, additional Na intercalation sites were identified within the 2*O* and 4*M* $Na_2Fe_2F_7$ structures using bond valence sum mapping in the SoftBV software program,[223–225] as these polymorphs do not contain any intrinsic Na vacancies. The coordinates of possible intercalation sites are listed in Table 5.3**.** For the 3*T* structure with two half-filled Na sites at $x = 2$, no additional intercalation sites needed to be considered. The three variants have very similar energetics within the $0 \leq x \leq 3$ compositional range (differing by no more than 30 meV/atom), with the 3*T* structure being most stable overall, followed by the 4*M* variant.

Notably, the presence of many intermediate $Na_xFe_2F_7$ compositions on the convex hulls (dashed lines), each with many Na-vacancy orderings within 10-20 meV/atom, suggests that all three weberite variants should undergo a solid solution mechanism leading to a sloped voltage profile (if the weberite structure does not transform during cycling).

From those results, equilibrium voltage curves were generated for the three variants using the Nernst equation below,[8] where μ_{Na} is the chemical potential of Na in $Na_xFe_2F_7$, μ_{Na}^{o} is the Na chemical potential in the reference anode, and *e* is the elementary charge:

$$V = -\frac{\mu_{Na}-\mu_{Na}^{o}}{e} \quad 5.1$$

Those equilibrium voltage curves are shown in Figure 5.13b along with the experimental $Na_2Fe_2F_7$ GITT data reproduced from Figure 5.9d. The computed curves are only an approximation to the true voltage curves as they are obtained from the 0 K DFT energies of intermediate $Na_xFe_2F_7$ phases, and as such neglect any temperature effects and assume that all intermediate phases have been correctly identified.[8] Here, the step-like voltage profiles obtained from first principles result from sampling over a small subset of intermediate $Na_xFe_2F_7$ compositions and Na/vacancy orderings on the hull, whereas the smoother, finite-temperature experimental profile is the result of entropic effects that create disorder on the Na sublattice. Overall, the predicted voltage profiles of the three polymorphs are very similar, with average voltages of 3.46, 3.49, and 3.43 V between *x* = 1 to 2 and of 2.75, 2.63, and 2.7 V between *x* = 1 to 3 for the 2*O*, 3*T*, and 4*M* polymorphs. In addition, the predicted profiles align well with experimental results. Below *x* = 1, large overpotentials are observed in the GITT data, which our DFT results suggest is due to the high potentials (> 5.75 V) required for further Na extraction,

well outside the electrochemical stability window of conventional carbonate electrolytes.[6,226,227] The high predicted potentials at the top of charge arise from a rather unstable fully deintercalated structure, which is likely partly due to the difficulty of oxidizing Fe past Fe^{3+}.[228,229] In fact, Fe^{4+} has never been observed in fluoride materials. Large overpotentials are also observed in the GITT data at the end of discharge (x > 2), although our calculations suggest that Na should be able to intercalate up to x = 3 within the potential range used in our experiments. Thus, Na intercalation past x = 2 appears to be kinetically hindered in our experiments, which may in part be due to the large volume expansion (upwards of 10%) predicted past x = 2 (as shown in Figure 5.14), or by the phase transformation to $NaFeF_3$.

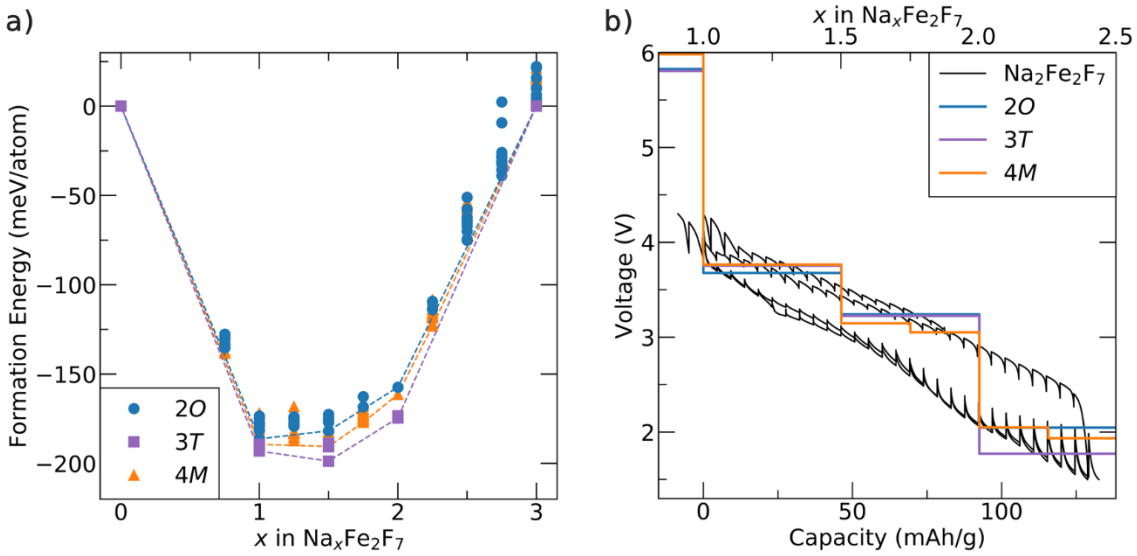

Figure 5.13 – First principles investigation of the Na (de)intercalation behavior of $Na_2Fe_2F_7$ polymorphs. a) Calculated formation energies for 2*O*, 3*T*, and 4*M* $Na_xFe_2F_7$ structures. The convex hull for each polymorph is shown as a dashed line. **b)** Predicted voltage curves for the three weberite polymorphs derived from the 0 K $Na_xFe_2F_7$ formation energies shown in **a)**. The GITT data from Figure 5.9d has been reproduced in black for comparison.

Table 5.3 – Possible Na-ion intercalation sites in 2O, 3T, and 4M $Na_xFe_2F_7$. Crystallographic information for sites that may be able to accommodate Na-ions in the various polymorphs, including sites occupied in the $Na_2Fe_2F_7$ crystal structures and those predicted by SoftBV.[223–225] The occupancy (occ.) is given at x = 2. The relative site energy is calculated using bond valence sum mapping within SoftBV. The coordination environment for each site is also provided, including the number of nearest neighbors (NN) and coordination environment.

Phase	Site	Occ.	Wyckoff Position	Coordinates			Relative Site Energy (eV/atom)	Coordination	
				x	y	z		NN	Polyhedron-Type
2*O*	**Na1**	1	4*a*	0	0	0	0	8	Bihexagonal Pyramidal
2*O*	**Na2**	1	4*d*	0.25	0.25	0.75	0.085	8	Cubic
2*O*	***i*1**	0	4*e*	0.5	0.25	0.917	0.491	6	Prismatic
2*O*	***i*2**	0	8*g*	0.75	0.542	0.25	0.562	6	Prismatic
2*O*	***i*3**	0	16*j*	0.24	0.558	0.208	0.569	6	Prismatic
3*T*	**Na1**	1	6*c*	0.523	0.849	0.665	0	8	Cubic
3*T*	**Na2**	0.5	6*c*	0.949	0.186	0.336	0.019	8	Cubic
3*T*	**Na3**	0.5	6*c*	0.902	0.169	0.863	0.014	8	Bihexagonal Pyramidal
4*M*	**Na1**	1	4*a*	0	0	0.5	0	8	Cubic
4*M*	**Na2**	1	4*b*	0.5	0	0	0.019	8	Bihexagonal Pyramidal
4*M*	**Na5**	1	4*d*	0.736	0.042	0.25	0.014	8	Cubic
4*M*	**Na3**	1	4*e*	0.25	0.25	0.5	0.043	8	Cubic
4*M*	**Na4**	1	8*f*	0.5	0.729	0.75	0.048	8	Cubic
4*M*	**Na6**	1	8*f*	0.861	0.979	0.125	0.112	8	Bihexagonal Pyramidal
4*M*	***i*1**	0	8*f*	0.333	0.458	0.458	0.578	6	Prismatic
4*M*	***i*2**	0	8*f*	0.208	0.438	0.556	0.611	6	Prismatic
4*M*	***i*3**	0	8*f*	0.458	0.667	0.563	0.699	6	Prismatic
4*M*	***i*4**	0	8*f*	0.306	0.271	0.701	0.725	6	Prismatic
4*M*	***i*5**	0	8*f*	0.056	0.979	0.194	0.736	6	Prismatic

Overall, our DFT calculations predict a very similar electrochemical behavior for the three weberite structural variants, suggesting that the different layer stackings do not have a significant influence on the range of stoichiometries accessible via Na (de)intercalation. While we did not investigate the Na-ion conduction behavior within each polymorph, the slight structural variations between 2*O*, 3*T*, and 4*M* $Na_xFe_2F_7$ likely do not affect Na-ion transport drastically, especially considering that the Na polyhedral connectivity is largely retained in each structural variant and the slow cycling rate used

here (C/20). However, a more detailed study of the Na-ion transport properties of the three weberite variants is warranted.

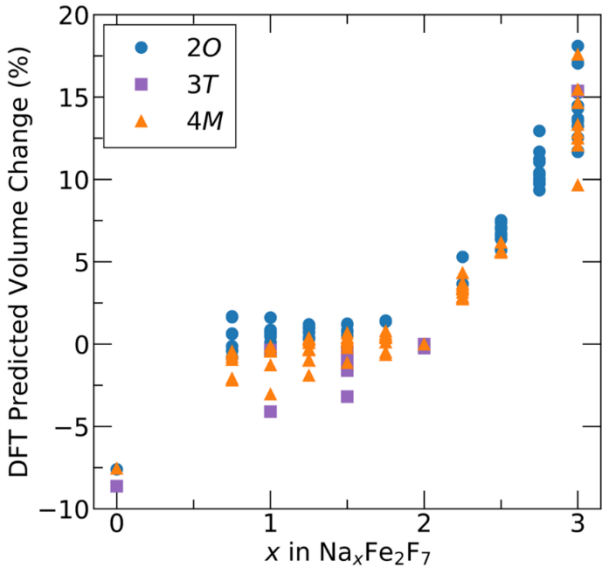

Figure 5.14 – Predicted Volume Change for $Na_{2-x}Fe_2F_7$ Polymorphs. The volume expansion is plotted with respect to the $Na_2Fe_2F_7$ structure for each Na-vacancy ordering within 10 meV/atom of the lowest energy ordering at a given $Na_xFe_2F_7$ composition.

While the origin of the very different electrochemical behaviors reported here and in Park *et al.*'s work[47] is difficult to ascertain, particularly since we are unable to compare the $Na_2Fe_2F_7$ polymorph ratios present in the starting cathodes due to the significant broadening of the diffraction patterns, we suspect that the different electrode preparation methods employed in the two studies play a large role, and kinetic limitations in our electrode films encourage a phase transformation to perovskite Na_yFeF_3 to occur, rather than topotactic Na intercalation. Thus, to prevent transformation of the weberite phase, these kinetic limitations must be overcome and/or the weberite phase must be stabilized with respect to competing phases.

5.4 Conclusion

This work comprises an in-depth examination of the structure, phase stability, and electrochemical performance of the $Na_2Fe_2F_7$ weberite cathode, using a combined experimental-computational approach. First principles calculations reveal that $Na_2Fe_2F_7$ is metastable and highly prone to polymorphism, as confirmed by Rietveld analysis of the synchrotron XRD data collected on the pristine $Na_2Fe_2F_7$ sample, indicating a mixture of the orthorhombic (2*O*), trigonal (3*T*), and monoclinic (4*M*) weberite polymorphs. Those results are consistent with the multiple Fe environments observed by ^{57}Fe Mössbauer spectroscopy, as well as the cubic and bihexagonal pyramidal Na environments identified by ^{23}Na solid-state NMR and first principles calculations of NMR parameters. The $Na_2Fe_2F_7$ cathode exhibits an initial reversible capacity of 125 mAh/g, and a 60% capacity retention after 50 cycles. Contributing to the capacity fade is a transformation of the $Na_2Fe_2F_7$ weberite phases to the Na_yFeF_3 perovskite, as revealed via *ex situ* synchrotron XRD and ^{23}Na solid-state NMR. A first principles investigation of the impact of polymorphism on the electrochemical performance reveals that the orthorhombic (2*O*), trigonal (3*T*), and monoclinic (4*M*) $Na_2Fe_2F_7$ polymorphs should behave similarly, transferring up to 2 Na between $Na_1Fe_2F_7$ to $Na_3Fe_2F_7$ at an average voltage of 2.7 V. Thus, from a thermodynamic standpoint, the polymorphic makeup of the $Na_2Fe_2F_7$ weberite cathode does not have a strong impact on the electrochemical behavior, although future investigations of the Na-ion transport properties of the weberite variants are warranted. We suspect that the poorer electrochemical performance of our $Na_2Fe_2F_7$ cathode compared to that reported in a previous study by Park *et al.* is largely due to differences in cathode film formulation and preparation

methods. In this work, poorer overall kinetics hinder topotactic Na-ion (de)intercalation and favor a phase transformation reaction. Therefore, detailed reports regarding composite electrode preparation protocols and a careful analysis of the structure of weberite compounds are needed to assist the further development of this new class of Na-ion cathodes.

5.5 Appendix – Supplemental Material

5.5.1 Additional DFT Details and Results

Table 5.4 – DFT-computed energy, formation energy (E_F), and energy above the hull (E_{Hull}) for all compounds within the NaF-FeF_2-FeF_3 phase space. Binary fluorides were used to compute the formation energies of the ternary phases.

	Energy (meV/atom)	Energy (eV/f.u.)	E_F (meV/atom)	E_F (eV/f.u.)	E_{Hull} (meV/atom)
NaF	−4324.62	−8.65	--	--	0.00
FeF_2	−5685.78	−17.06	--	--	0.00
FeF_3	−5317.44	−21.27	--	--	0.00
$NaFeF_3$	−5159.27	−25.80	−17.96	−0.09	0.00
Na_3FeF_6	−4809.44	−48.09	−87.69	−0.88	0.00
$NaFeF_4$	−4935.05	−108.57	−68.89	−1.52	7.68
$Na_5Fe_3F_{14}$	−5051.95	−30.31	−65.45	−0.39	0.00
2*O*-$Na_2Fe_2F_7$	−5108.21	−56.19	−51.34	−0.56	8.87
3*T*-$Na_2Fe_2F_7$	−5106.8	−56.17	−49.93	−0.55	10.28
4*M*-$Na_2Fe_2F_7$	−5105.58	−56.16	−48.71	−0.54	11.50

5.5.1.1 Selection of Na-vacancy enumerated structures

All calculations were performed on 1x1x1 cells of the different weberite variants, leading to cells containing 44, 66, and 176 atoms for 2*O*, 3*T*, and 4*M* $Na_2Fe_2F_7$, respectively. As each weberite polymorph contains many individual Na sites, it is impractical to consider all possible Na-vacancy orderings. For example, there are 17,000 Na-vacancy orderings between x = 1 and 2 for the 4*M* polymorph. Thus, select configurations were considered for each polymorph at x = 0, 0.75, 1, 1.25, 1.5, 1.75, 2, 2.25, 2.5, and 3, and for the 4*M* polymorph only full or zero occupation of each of the Wyckoff sites was considered. Symmetrically-unique Na-vacancy orderings were enumerated and ranked according to their Ewald Sum Energy using Pymatgen (Python Materials Genomics)[198] and the five lowest energy orderings were considered. In total, 71 $Na_xFe_2F_7$ structures were calculated for the 2*O* polymorph, 12 for the 3*T* polymorph,

and 85 for the 4*M* polymorph. Only a small number of structures were calculated for the 3T $Na_xFe_2F_7$ polymorph as a convex hull has already been reported for this variant, although only down to $x = 0.5$.[47]

As the 2*O* and 4*M* polymorphs contain no intrinsic Na vacancies, bond valence sum mapping using the SoftBV[223–225] software program was used to identify possible intercalation sites. This resulted in three and five possible intercalation sites for the 2*O* and 4*M* polymorphs, respectively. The coordinates for these possible intercalation sites are listed in Table 5.3. As the 3*T* structure contains two half-filled Na sites at $x = 2$, no additional intercalation sites were investigated. Below $x = 2$, only the Na sites that are occupied at $x = 2$ were considered.

5.5.2 Additional SXRD Details and Refinement Results

Table 5.5 – Refined lattice constants and weight percentages for all phases used to fit the SXRD data collected on pristine $Na_2Fe_2F_7$. The fit residuals are: $\chi^2 = 2.12$ and $R_{WP} = 9.75\%$.

Phase	**2*O***	**3*T***	**4*M***	**Na_3FeF_6**	**FeF_2**
Space Group	*Imma*	$P3_121$	$C2/c$	$P2_1$	$P4_2/mnm$
a (Å)	7.3811(4)	7.3726(1)	12.6985(3)	5.5195(2)	4.6932(1)
b (Å)	10.5049(6)	7.3726(1)	7.4094(2)	5.7166(2)	4.6932(1)
c (Å)	7.4377(3)	18.1752(4)	24.6541(6)	7.9621(3)	3.3162(1)
alpha (°)	90	90	90	90	90
beta (°)	90	90	100.132(1)	90.351(3)	90
gamma (°)	90	120	90	90	90
wt.%	**3.0(2)%**	**41.2(4)%**	**45.6(4)%**	**9.4(1)%**	**0.90(2)%**

Table 5.6 – Refined lattice constants and weight percentages for all phases used to fit the SXRD data for carbon-coated $Na_2Fe_2F_7$. The fit residuals are: $\chi^2 = 1.31$ and $R_{WP} = 7.01\%$. Note that the 4*M* weberite polymorph was used to fit the low crystallinity, carbon-coated data as it was the majority weberite variant in the pristine material.

	4*M*	**Na_3FeF_6**
Space Group	$C2/c$	$P2_1$
a (Å)	12.749(2)	5.413(1)
b (Å)	7.381(1)	5.808(1)
c (Å)	24.452(6)	7.964(2)
alpha (°)	90	90
beta (°)	99.39(1)	90.646(6)
gamma (°)	90	90
wt.%	**88.3(2)%**	**11.4(5)%**

Table 5.7 – Refined site parameters for all three weberite phases present in the pristine $Na_2Fe_2F_7$ sample.

Phase	Atom	Wyckoff Position	x	y	z	Occ.	Beq
2*O*	Na1	4*a*	0.000	0.000	0.000	1	1.16(8)
2*O*	Na2	4*d*	0.250	0.250	0.750	1	1.16(8)
2*O*	Fe1	4*c*	0.250	0.250	0.250	1	1.08(1)
2*O*	Fe2	4*b*	0.000	0.000	0.500	1	1.08(1)
2*O*	F1	4*e*	0.000	0.250	0.231(6)	1	1.20(6)
2*O*	F2	8*h*	0.000	0.401(3)	0.762(4)	1	1.20(6)
2*O*	F3	16*j*	0.187(3)	0.373(2)	0.404(3)	1	1.20(6)
3*T*	Na1	6*c*	0.5307(1)	0.873(1)	0.6713(6)	1	1.16(8)
3*T*	Na2	6*c*	0.82(3)	0.010(4)	0.3462(8)	0.5	1.16(8)
3*T*	Na3	6*c*	0.841(2)	0.014(3)	0.8381(9)	0.5	1.16(8)
3*T*	Fe1	3*a*	0.3364(9)	0.000	0.333	1	1.08(1)
3*T*	Fe2	3*b*	0.3263(7)	0.000	0.833	1	1.08(1)
3*T*	Fe3	6*c*	0.5037(6)	0.8368(7)	0.1688(2)	1	1.08(1)
3*T*	F1	6*c*	0.7456(1)	0.211(2)	0.6087(5)	1	1.20(6)
3*T*	F2	6*c*	0.748(1)	0.910(1)	0.9468(6)	1	1.20(6)
3*T*	F3	6*c*	0.544(2)	0.421(1)	0.0596(5)	1	1.20(6)
3*T*	F4	6*c*	0.832(2)	0.447(2)	0.1931(6)	1	1.20(6)
3*T*	F5	6*c*	0.026(2)	0.347(2)	0.2692(4)	1	1.20(6)
3*T*	F6	6*c*	0.203(2)	0.251(1)	0.1416(6)	1	1.20(6)
3*T*	F7	6*c*	0.069(2)	0.436(1)	0.8538(4)	1	1.20(6)
4*M*	Na1	4*a*	0.000	0.000	0.000	1	1.16(8)
4*M*	Na2	4*b*	0.000	0.500	0.000	1	1.16(8)
4*M*	Na3	4*d*	0.250	0.250	0.500	1	1.16(8)
4*M*	Na4	4*e*	0.000	0.758(2)	0.250	1	1.16(8)
4*M*	Na5	8*f*	0.2458(9)	0.0582(1)	0.2462(4)	1	1.16(8)
4*M*	Na6	8*f*	0.365(1)	0.501(2)	0.1245(4)	1	1.16(8)
4*M*	Fe1	4*c*	0.250	0.250	0.000	1	1.08(1)
4*M*	Fe2	4*e*	0.000	0.246	0.250	1	1.08(1)
4*M*	Fe3	8*f*	0.1299(4)	0.7578(6)	0.1291(2)	1	1.08(1)
4*M*	Fe4	8*f*	0.3775(5)	0.0132(8)	0.1306(2)	1	1.08(1)
4*M*	Fe5	8*f*	0.1236(5)	0.2613(6)	0.1244(3)	1	1.08(1)
4*M*	F1	8*f*	0.334(1)	0.054(1)	0.041(5)	1	1.20(6)
4*M*	F2	8*f*	0.422(1)	-0.044(2)	0.207(5)	1	1.20(6)
4*M*	F3	8*f*	0.464(1)	0.268(2)	0.125(5)	1	1.20(6)
4*M*	F4	8*f*	0.266(1)	-0.176(2)	0.100(5)	1	1.20(6)
4*M*	F5	8*f*	0.151(1)	0.3010(2)	0.047(6)	1	1.20(6)
4*M*	F6	8*f*	0.131(1)	0.305(2)	0.212(7)	1	1.20(6)
4*M*	F7	8*f*	0.055(1)	-0.002(2)	0.105(5)	1	1.20(6)
4*M*	F8	8*f*	0.163(1)	0.509(2)	0.141(5)	1	1.20(6)
4*M*	F9	8*f*	0.299(1)	0.212(2)	0.159(5)	1	1.20(6)
4*M*	F10	8*f*	-0.020(1)	0.334(2)	0.103(5)	1	1.20(6)
4*M*	F11	8*f*	0.321(1)	0.484(2)	0.032(5)	1	1.20(6)
4*M*	F12	8*f*	0.064(1)	0.065(2)	0.297(5)	1	1.20(6)
4*M*	F13	8*f*	0.155(1)	0.80(2)	0.202(7)	1	1.20(6)
4*M*	F14	8*f*	0.076(1)	0.703(2)	0.053(6)	1	1.20(6)

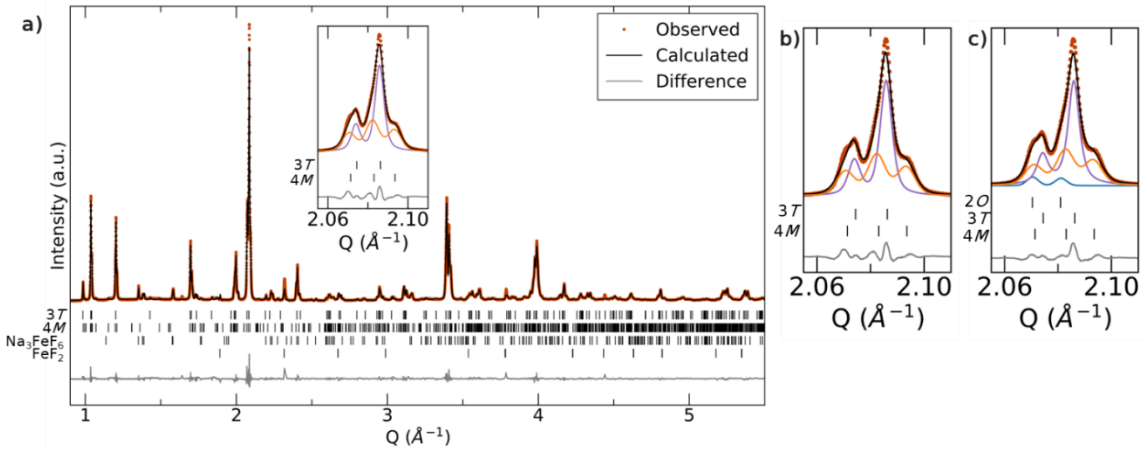

Figure 5.15 – a) SXRD pattern for pristine $Na_2Fe_2F_7$ as shown in Figure 5.6a fitted analogously with the Rietveld method but without inclusion of the 2*O* weberite polymorph. The inset shows an enlarged version of the main weberite peaks which is duplicated in **b)**. The inset from Figure 5.6a where the 2*O* polymorph is included in the refinement is shown again in **c)**.

Table 5.8 – Refined lattice constants and weight percentages for all phases used to fit the SXRD data collected on *ex situ* 1st discharge $Na_2Fe_2F_7$. The fit residuals are: χ^2 = 1.18 and R_{WP} =4.84%.

4*M*	**Na_3FeF_6**	**$NaFeF_3$**
*C*2/*c*	*P*2$_1$	*Pnma*
12.533(3)	5.508(2)	5.679(2)
7.390(2)	5.702(2	7.917(2)
24.497(6)	8.003(2)	5.499(1)
90	90	90
99.94(1)	90.646(6)	90
90	90	90
54.4(3)%	**4.9(4)%**	**40.8(3)%**

Table 5.9 – Refined lattice constants and weight percentages for all phases used to fit the SXRD data collected on *ex situ* 10th discharge $Na_2Fe_2F_7$. The fit residuals are: χ^2 = 1.19 and R_{WP} = 4.98%.

4*M*	**Na_3FeF_6**	**$NaFeF_3$**
*C*2/*c*	*P*2$_1$	*Pnma*
12.624(2)	5.493(2)	5.6725(9)
7.377(1)	5.697(1)	7.899(1)
24.577(4)	7.980(2)	5.4917(9)
90	90	90
100.506(6)	90.53(2)	90
90	90	90
37.6(3)%	**9.2(4)%**	**53.2(4)%**

5.5.3 Additional Characterization

Table 5.10 – ICP results for $Na_2Fe_2F_7$. All data have been normalized to the Fe content. The errors listed here only account for uncertainties in the calibration curves and do not include other experimental errors, such as trace ions in the deionized water used for dilution and in the sample containers.

	Na	Fe
Pristine	1.94(1)	2
Carbon-Coated	1.95(1)	2

5.5.4 Additional NMR Results and First-Principles Calculations

The computed hyperfine (paramagnetic) NMR properties were obtained at 0 K for the $Na_2Fe_2F_7$ 2*O*, 3*T*, and 4*M* weberite polymorphs using a 2x1x2 supercell for the 2*O* variant, and a 1x1x1 cell for the 3*T* and 4*M* variants. All computations were carried out on ferromagnetically-aligned cells. To compare CRYSTAL17 calculation results with experimental data acquired at room temperature, the computed shifts were subsequently scaled to a value consistent with the paramagnetic state of the system at the temperature of the NMR experiments, using a magnetic scaling factor Φ of the form:

$$\Phi\left(T_{exp}\right) = \frac{\langle M(T_{exp})\rangle}{M_{sat}} \qquad 5.2$$

where M_{sat} is the saturated (ferromagnetic) $Fe^{2.5+}$ magnetic moment at 0 K, and $\langle M(T_{exp})\rangle$ the bulk average magnetic moment measured at the sample experimental temperature, T_{exp}. Here, T_{exp} is set to 320 K to account for frictional heating caused by fast (60 kHz) sample rotation during NMR data acquisition.

The magnetic scaling factor in Eq. 5.2 can be evaluated from the experimental magnetic properties of the material:

$$\Phi(\mathrm{T}) = \frac{B_0 {\mu_{eff}}^2}{3k_B g_e \mu_B S(T-\Theta)} \qquad 5.3$$

where B_0 is the external magnetic field, μ_{eff} is the effective magnetic moment per Fe site, k_B is Boltzmann's constant, g_e is the free electron *g*-value, μ_B is the Bohr magneton, *S* is the formal spin of $Fe^{2.5+}$ ($S = 4.5/2$), and Θ is the Weiss constant. A derivation of Eq. 5.3, starting from the Brillouin function in the low field, high temperature limit, can be found in a previous study by Kim et al.[60] Eq. 5.3 uses the "spin-only" expression for the magnetic moment and is only strictly valid when the orbital angular momentum is

quenched.[64] Yet, for systems where spin-orbit coupling effects are negligible, such as $Na_2Fe_2F_7$, the spin-only expression is a good approximation of the magnetic behavior of the system.

Given the multi-phasic nature of $Na_2Fe_2F_7$ samples, we are unable to obtain the magnetic properties (μ_{eff} and Θ) of individual $Na_2Fe_2F_7$ polymorphs experimentally. However, similar magnetic properties may be expected for the different polymorphs as they all retain a similar transition metal network, solely differentiated by variations in layer stacking.[184] Thus, we approximated μ_{eff} by the theoretical, "spin-only" magnetic moment ($\mu_{SO} = 5.41\ \mu_B/Fe^{2.5+}$), and used a previously-reported value[184] of $\Theta = -104$ K for $Na_2Fe_2F_7$ to compute the magnetic scaling factor. A bulk magnetic scaling factor, Φ, of 0.008066 was obtained at T = 320 K and B_0 = 2.35 T using Eq. 5.3 which was used to scale the computed ^{23}Na and parameters listed in Table 5.2.

Table 5.11 – Unit cell parameters for the reported experimental $Na_2Fe_2F_7$ structures[47,179,187] and for the structures optimized using the H20 and H35 functionals in this work.

	2O			***3T***			***4M***		
	Exp.	**Opt. H20**	**Opt. H35**	**Exp.**	**Opt. H20**	**Opt. H35**	**Exp.**	**Opt. H20**	**Opt. H35**
a (Å)	7.357	7.449	7.475	7.377	7.374	7.359	12.767	12.646	12.604
b (Å)	10.492	10.266	10.275	7.377	7.366	7.358	7.422	7.423	7.381
c (Å)	7.418	7.479	7.336	18.229	18.202	18.075	24.710	24.740	24.645
alpha (°)	90	90	90	90	90.054	90	90	90	90
beta (°)	90	90	90	90	90.149	90	99.970	99.710	99.815
gamma (°)	90	90	90	120	119.675	120	90	90	90
Vol. (Å^3)	572.569	571.939	563.484	859.202	859.051	847.570	2341.437	2289.023	2259.164

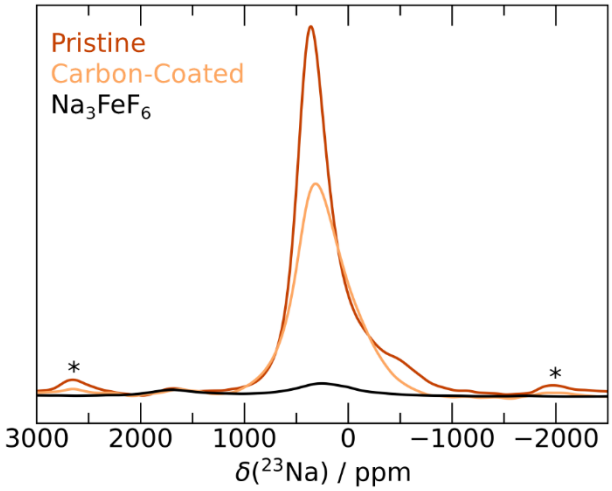

Figure 5.16 – Comparison of ^{23}Na solid-state NMR spin echo spectra collected with a $\pi/2$ excitation pulse on Na_3FeF_6, and on pristine and carbon-coated $Na_2Fe_2F_7$. All spectra are scaled according to the intensity of the 1800 ppm Na_3FeF_6 signal. Asterisks indicate spinning sidebands.

5.5.5 Additional Electrochemical Results

5.5.5.1 Carbon-coating optimization for the preparation of $Na_2Fe_2F_7$ cathode films

As the 24 h carbon-coating process affects the weberite structure (based on the SXRD and Mössbauer results in Figure 5.6 and Figure 5.7, and ^{23}Na ss-NMR results presented in Figure 5.8 in the main text), several shorter mechanochemical milling times and an in situ carbon-coating method were investigated to reduce structural disordering. The in situ carbon-coating method involved mixing the $Na_2Fe_2F_7$ material with sugar prior to the annealing step and then heating the mixture to 650°C for 30 min. The laboratory XRD patterns collected on the various cathode films are shown in Figure 5.17a. These cathode films were galvanostatically cycled at a rate of C/20 (full (dis)charge in 20 hrs assuming the transfer of 2 Na per formula unit) by first charging to 4.3 V vs. Na^+/Na and subsequent cycling between 4.3 V and 1.5 V. The resulting electrochemical profiles are shown in Figure 5.17b. While the *in situ* carbon-coating method led to a highly crystalline cathode, it also resulted in significant decomposition of the weberite phases. Further, the shorter milling procedures all resulted in reduced crystallinity and worse electrochemistry than the 24 h ball-milled carbon-coated $Na_2Fe_2F_7$ cathode considered thus far. Hence, carbon-coating using a 24 h ball-milling step was deemed optimal and used for the remainder of this study.

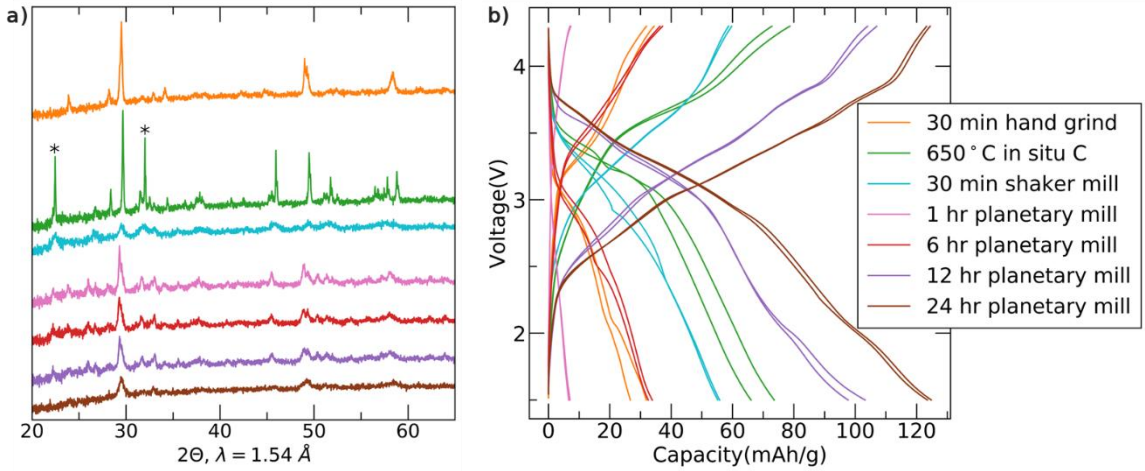

Figure 5.17 – a) Laboratory XRD patterns, and **b)** galvanostatic charge-discharge curves obtained for $Na_2Fe_2F_7$ after different carbon-coating methods. Asterisks denote impurity/decomposition phases formed during the carbon-coating step.

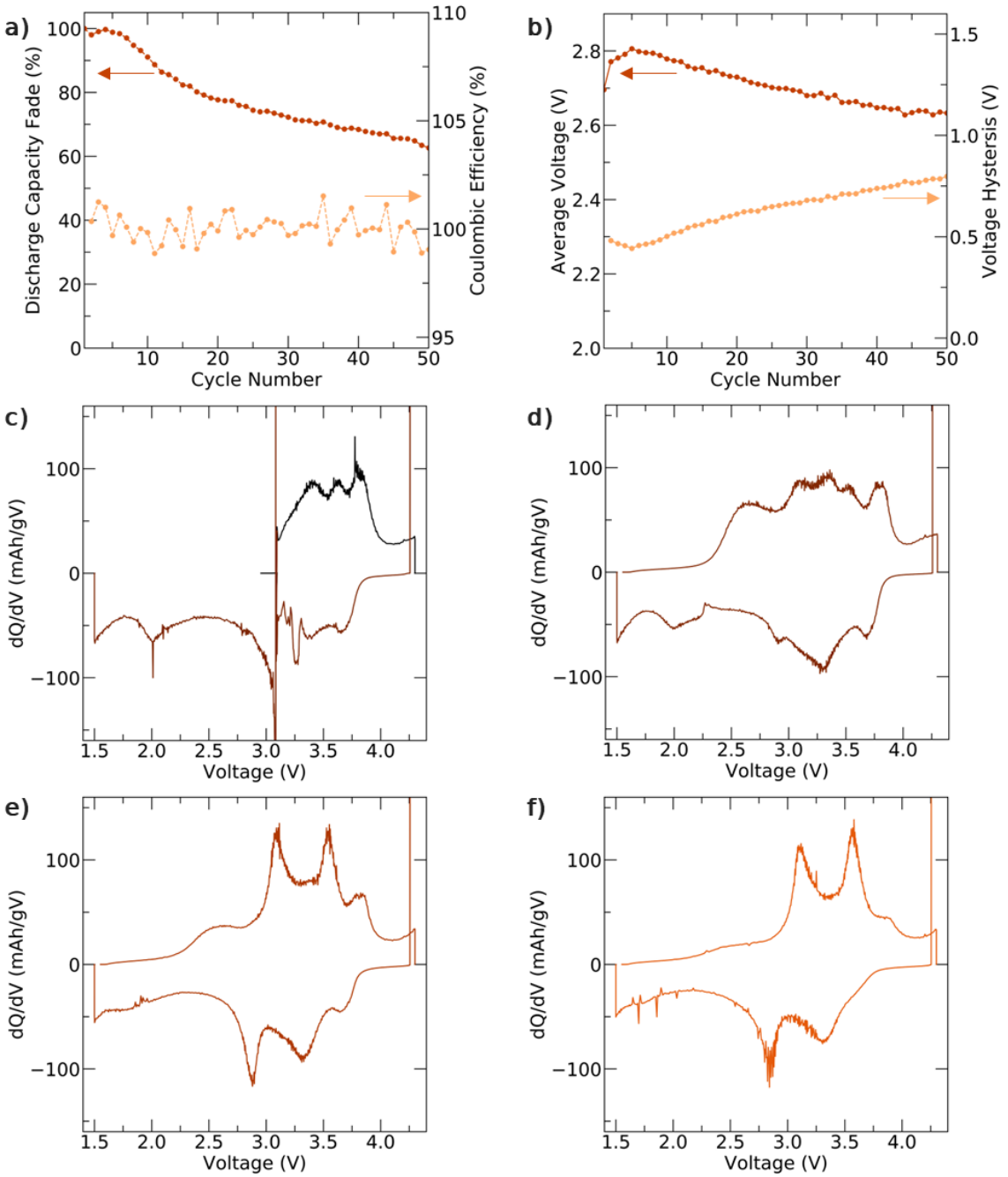

Figure 5.18 – a) Plots of discharge capacity retention and coulombic efficiency **and b)** average discharge voltage and voltage hysteresis vs. cycle number for the galvanostatic data shown in Figure 5.9. dQ/dV plots for cycles 1 **(c)**, 2 **(d)**, 10 **(e)**, and 20 **(f)** from the galvanostatic data shown in Figure 5.9b. The cycle 1 charge data is shown in black with the remaining data coloring analogous to that in Figure 5.9b.

Chapter 6 – Exploration of Weberite Compositions Beyond $Na_2Fe_2F_7$

As demonstrated in Chapter 5 for $Na_2Fe_2F_7$, weberite materials tend to be metastable which affect their synthesis and electrochemical performance. Thus, we have explored several solid solutions aimed at improving material stability, energy density, and synthesizability. These compositions are $Na_2M_xFe_{2-x}F_7$ with x = Mn^{2+}, Mg^{2+}, and Al^{3+} and x between 0 and 1. The motivation, work, and results for each substituting element will be discussed separately in this chapter and a final summary and outlook informed by both experimental and computational results is provided at the end aimed to improve weberite material design. These results are yet to be published and, where appropriate, the additional work necessary to complete the study will be noted. Additionally, we outline in Appendix 6.6 the synthetic strategies used to prepare weberite materials in the literature and in this dissertation.

The work presented in this chapter was led and designed by myself with a team of undergraduate researchers aiding in materials synthesis, diffraction measurements, and electrochemical cell testing: Wen Jin (UCSB) was involved in the Mn- and Mg-substituted weberite project and refined some of the XRD pattern refinements, Lanette

Espinosa (California State University, Fullerton) was involved in the Al-substituted project, and Allyson Ee (UCSB) attempted an alternative PTFE-assisted synthesis route. All other work in this chapter (including remaining materials synthesis; running of DFT calculations and analysis; acquisition and analysis of the electrochemical and diffraction results; and analysis of the XAS results) was completed by me.

6.1 Mn^{2+}-substitution in $Na_2Mn_xFe_{2-x}F_7$

As a strategy to increase the operating voltage, and thereby the energy density of the $Na_2Fe_2F_7$ weberite cathode, Mn^{2+} substitution for Fe^{2+} to form $Na_2Mn_xFe_{2-x}F_7$ ($0 < x \leq 1$) was investigated. This substitution could enable both a higher voltage Mn^{2+}/Mn^{3+} redox couple compared to Fe^{2+}/Fe^{3+},[gg] but also cycling over a wider Na compositional range spanning from $Mn^{4+}Fe^{3+}F_7$ all the way to $Na_3Mn^{2+}Fe^{2+}F_7$ (transfer of $3Na^+$ per f.u.) as Mn can more readily access its 4+ redox state compared to Fe. Thus, from an electrochemical standpoint, Mn incorporation in weberites is very promising for developing high energy density NIB cathodes.

We synthesized a series of Mn^{2+} substituted $Na_2Mn_xFe_{2-x}F_7$ compositions with x = 0, 0.25, 0.5, 0.75, and 1 (hereafter referred to as Mn0, Mn0.25, Mn0.5, Mn0.75, and Mn1) using a similar synthesis protocol as $Na_2Fe_2F_7$ as described in Chapter 5.[hh] Their

[gg] Despite Mn being to the left of Fe on the periodic table, the Mn^{2+}/Mn^{3+} redox couple operates at a higher voltage than the Fe^{2+}/Fe^{3+}, redox couple due to the increased stabilization of a d^5 electron configuration, which Mn^{2+} and Fe^{3+} have.

[hh] Chronologically, this was the first study we pursued after developing mechanochemically-assisted solid-state synthesis protocols for weberite materials, and we were yet to understand the extent of polymorphism (i.e. having multiple weberite variants present at once) in weberite compounds.

optimized synthesis conditions and final refined weberite contents are summarized in Table 6.2. The lab XRD patterns obtained after ball milling and SXRD patterns obtained after annealing are shown in Figure 6.1. All Rietveld refinements were performed assuming the presence of a single 4*M* weberite variant, as this variant was found to best fit the experimental data. Future refinements will also consider the possibility of polymorphism in annealed samples. Most of the Mn-substituted samples showed significant weberite formation with minor Na_3FeF_6 and $NaMnF_3$ impurities after the initial ball milling step. The subsequent anneal increased the fraction of weberite phase and improved the overall crystallinity of the sample. Interestingly, the lab XRD pattern for Mn0.75 after ball milling showed no weberite formation, but the subsequent anneal led to a comparable weberite fraction as in the lower Mn-content samples. Mn1 still showed significant impurities following the anneal.

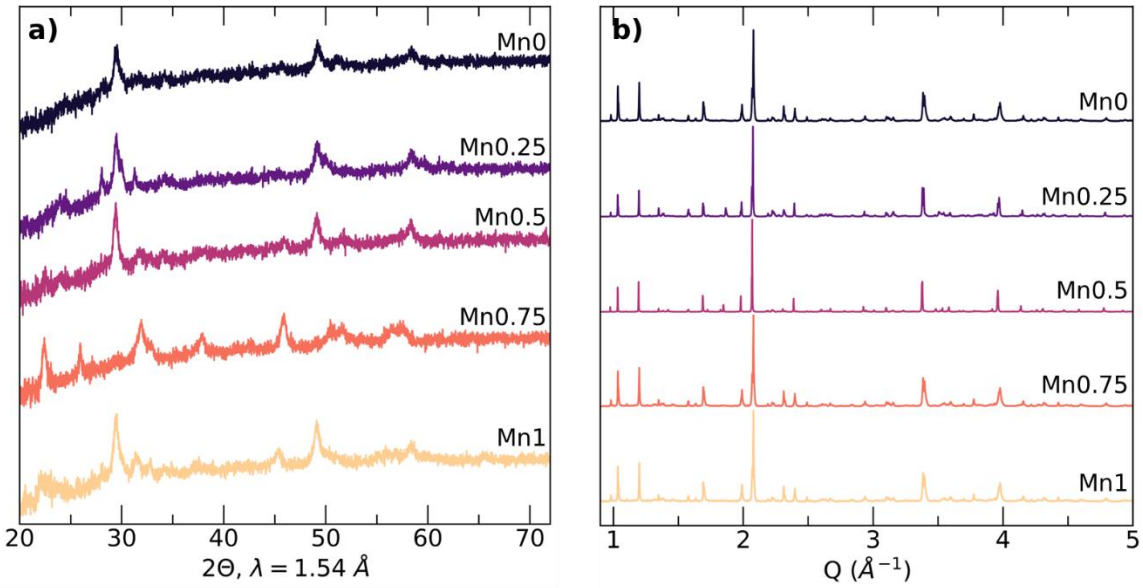

Figure 6.1 – a) Lab XRD and **b)** SXRD patterns for $Na_2Mn_xFe_{2-x}F_7$ samples after ball milling and after a subsequent anneal, respectively.

Table 6.2 – Optimized synthesis parameters for $Na_2Mn_xFe_{2-x}F_7$ samples and corresponding weberite wt. % refined based on the SXRD pattern.

	BM time (h)	Anneal Temperature (°C)	Anneal Time (min)	wt. % weberite phase
Mn0	36	500	30	92%
Mn0.25	48	500	30	90%
Mn0.5	84	575	30	90%
Mn0.75	104	500	30	85%
Mn1	164	650	30	65%

Mn and Fe K-edge X-ray absorption near-edge spectroscopy (XANES) experiments were performed to determine their average oxidation state. These results are summarized in Figure 6.2 and Table 6.1. The Mn K-edge XANES spectra clearly indicates that Mn is present as Mn^{2+}, as anticipated. The Fe K-edge spectra shows a general trend of increasing Fe oxidation state upon Mn substitution, in agreement with expectation. However, a much lower Fe oxidation state is observed for Na_2MnFeF_7 (Mn1) than its expected value of 3+, likely due to the significant impurity content in this sample identified via SXRD. Overall, the results presented here indicate that the previously-unreported Mn-substituted $Na_2Mn_xFe_{2-x}F_7$ compositions targeted here were successfully prepared with respectable purity when $x \leq 0.75$.

Table 6.1 – Expected and observed average Fe and Mn oxidation states based on the Mn-substitution level and K-edge XANES spectra, respectively, fit using a linear combination fit of the MF_2 and MF_3 standards.

	Fe Oxidation State		Mn Oxidation State	
	Expected	**Observed**	**Expected**	**Observed**
Mn0	2.50	2.550(7)	---	---
Mn0.25	2.57	2.54(1)	2	2.000(6)
Mn0.5	2.67	2.66(2)	2	2.030(4)
Mn0.75	2.80	2.88(3)	2	2.053(4)
Mn1	3.00	2.77(3)	2	2.026(4)

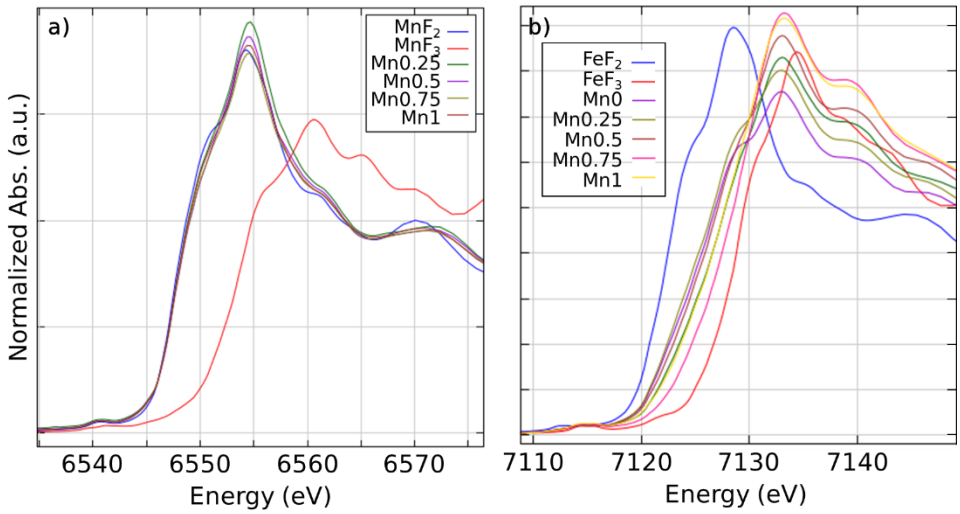

Figure 6.2 – XANES **a)** Mn K-edge and **b)** Fe K-edge spectra for a series of $Na_2Mn_xFe_{2-x}F_7$ samples.

To rationalize the dependence of the weberite sample purity on the Mn content and assess the propensity of this family of compounds to polymorphism, we investigated the thermodynamic stability of a representative series of $Na_2Mn_xFe_{2-x}F_7$ compositions through first-principles calculations. The formation energy *vs*. composition for this compositional range is shown in Figure 6.3a. In agreement with the decreased weberite purity as more Mn is incorporated (Figure 6.1, Table 6.2), the structure is predicted to be less stable, showing a general trend of less negative formation energy (with respect to the binary fluoride precursors MnF_2, FeF_3, and NaF) as the Mn content is increased across the series. Regarding polymorphism, all the structural variants are metastable and within 5 to 10 meV/atom of each other across the entire composition range. Thus, at relevant experimental temperatures, any of the variants can likely be stabilized and various polymorphs may be present in our samples. Interestingly, in agreement with a prior structural study of Na_2MnFeF_7, the 3*T* ($P3_121$, trigonal) structure is predicted to be the most stable across the entire compositional range, except at $x = 0$ (previously discussed in Chapter 5). However, the structural refinements performed on the SXRD

data did not consider the possibility of a mixed-polymorph material but will be considered in future refinements.

Due to the insulating nature of weberite fluorides, before proceeding with electrochemical testing, each weberite sample was mixed with a carbon additive to provide an electronically conductive framework amenable to Na (de)intercalation. This process had previously been carried out for $Na_2Fe_2F_7$ (Chapter 5) and Na_3FeF_6 (Chapter 4) by mixing the sample for 24 h with an appropriate amount of Carbon Super C65 via planetary ball milling at 300 rpm. Thus, a similar procedure was adopted here (using a 7:2 weberite:carbon ratio). Unfortunately, all attempts to carbon-coat the Mn-substituted weberite materials resulted in significant phase decomposition (shown in Figure 6.3b). We rationalize this to be due to the reduced phase stability of the weberite material as Mn is incorporated, as identified in Figure 6.3a.

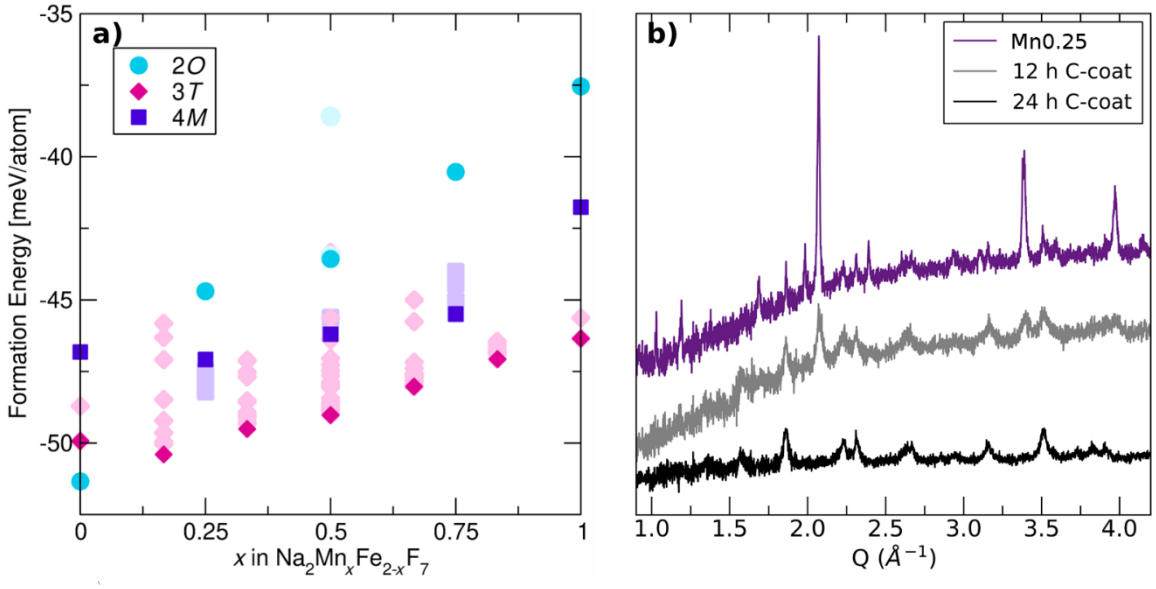

Figure 6.3 – a) Formation energy *vs.* Mn-content (x) in $Na_2Mn_xFe_{2-x}F_7$ weberite 2*O* (blue circles), 3*T* (pink diamonds), and 4*M* (purple squares) polymorphs referenced to their binary fluoride precursors. The dark symbols indicate the ground state structure for each polymorph at a given composition while the lighter symbols represent higher energy orderings. **b)** Lab XRD pattern for Mn0.25 after annealing (black) and then after a subsequent 12 h (purple) or 24 h (blue) carbon-coating process showing significant decomposition of the weberite phase (highest intensity peak at ≈ 2°).

Thus, as electrochemical testing of $Na_2Mn_xFe_{2-x}F_7$ cannot proceed until an effective, low energy carbon-coating method is developed, we have paused the study of these doped compositions. Regardless, this study has further highlighted the importance of material stability in the development of weberite cathodes and confirmed the effectiveness for first-principles calculations for establishing stability trends across weberite compositions.

Next, we decided to investigate the effect of diamagnetic substituents on the structural stability of the cathode in the as-synthesized state and upon electrochemical cycling. We hypothesized that Mg^{2+} and Al^{3+} substituents could lead to a more stable weberite structure, given that both of those cations are present in the weberite mineral, Na_2MgAlF_7. We first investigated the stability of Mg^{2+} and Al^{3+}-substituted $Na_2M_xFe_{2-x}F_7$ ($0 < x \leq 1$) compounds from first principles (Figure 6.4). Due to the computational complexity of investigating *M* substitution in all three weberite structure variants, we focused on the higher symmetry variant, the 2*O* polymorph, with the smallest unit cell. While the formation energies of the different series of compounds obtained using Mg, Al, and Mn substituents are not directly comparable due to the different binary fluoride precursors used experimentally and, in the calculations, the general trends of increasing or decreasing stability upon *M* substitution can be qualitatively compared. Based on Figure 6.4 and as already discussed for Figure 6.3a, Mn-substituted $Na_2Mn_xFe_{2-x}F_7$ shows a continuously decreasing phase stability as more Mn is incorporated. Conversely, upon Al-substitution, $Na_2Fe_{2-x}Al_xF_7$[ii] shows an initial decrease in stability that is partially

[ii] The metal order in $Na_2Fe_{2-x}Al_xF_7$ is switched compared to $Na_2Mg_xFe_{2-x}F_7$ or $Na_2Mn_xFe_{2-x}F_7$ to indicate Al^{3+} occupies the M^{3+} site.

mitigated at higher Al contents with a minimum observed at x = 0.5. $Na_2Mg_xFe_{2-x}F_7$ shows an overall increase in stability across the entire compositional range. Thus, motivated by these results, we continued with an investigation of the synthesis, structure, and electrochemical performance of the Mg^{2+} and Al^{3+}-substituted weberites.

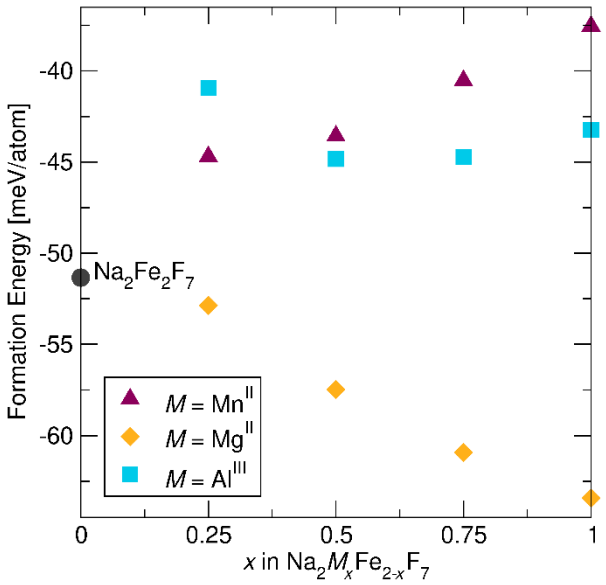

Figure 6.4 – Formation energy *vs.* *M* content in $Na_2M_xFe_{2-x}F_7$ with *M* = Mn^{2+}(magenta triangles), Mg^{2+} (yellow diamonds), and Al^{3+} (blue squares). Each $Na_2M_xFe_{2-x}F_7$ series uses the comprising binary fluorides as reference states (e.g. NaF, MnF_2, FeF_2, and FeF_3 for $Na_2Mn_xFe_{2-x}F_7$).

6.2 Al^{3+}-substitution in $Na_2Fe_{2-x}Al_xF_7$

Al substitution was investigated for x = 0.125 and 0.25 in $Na_2Fe_{2-x}Al_xF_7$; those two compounds are hereafter referred to as Al0.125 and Al0.25.[jj] While incorporation of a diamagnetic dopant lowers the available redox reservoir, substitution on the M^{3+} site

[jj] x = 0.5 and 1 compositions were also prepared by a summer intern but their precursor stoichiometries were incorrectly calculated so they are not discussed in much detail here. The best estimate for the composition of the "x = 0.5" sample is $Na_{1.82}Fe^{2+}_{0.55}Fe^{3+}_{0.34}Al_{1.02}F_7$. Further testing is necessary to fully understand the effect of Al substitution on the weberite phase stability.

still enables cycling between $Na_1Fe_{2-x}M_xF_7$ and $Na_{3-x}Fe_{2-x}M_xF_7$. Thus, M^{3+} substitution by Al^{3+} only limits the accessible low voltage capacity, which already faces significant kinetic limitations in $Na_yFe_2F_7$ beyond the as-synthesized Na stoichiometry of y = 2. Additionally, ^{27}Al is an NMR-active nuclei, and can be used as an additional probe of the local structure of weberite compounds.

Al0.125 and Al0.25 were prepared once again through a mechanochemically-assisted solid-state synthesis method, where they were first ball milled for 48 h, resulting in the formation of a weberite phase (Figure 6.5a). Each composition was then annealed at 500°C and 575°C with the resulting lab XRD patterns shown in Figure 6.5b,c. A similar trend of increasing crystallinity was observed with increasing anneal temperature. Pawley refinements of the lab XRD data were best fit using the 4*M* polymorph, which was then used as the only weberite polymorph in the Rietveld refinement due to the low signal to noise in the XRD data and desire to not overfit the data. Weberite-type Al0.125 accounted for 84 wt.% and 88 wt.% of the sample when annealed at 500°C and 575°C, respectively (4.6% and 5.4% R_{WP}). Weberite-type Al0.25 accounted for 87 wt.% and 73 wt.% of the sample when annealed at 500°C and 575°C, respectively (6.5% and 5.9% R_{WP}). All samples contained Na_3FeF_6, Na_3AlF_6, and FeF_2 impurity phases. Multi-polymorph refinements were not attempted as no SXRD data was obtained on these samples.

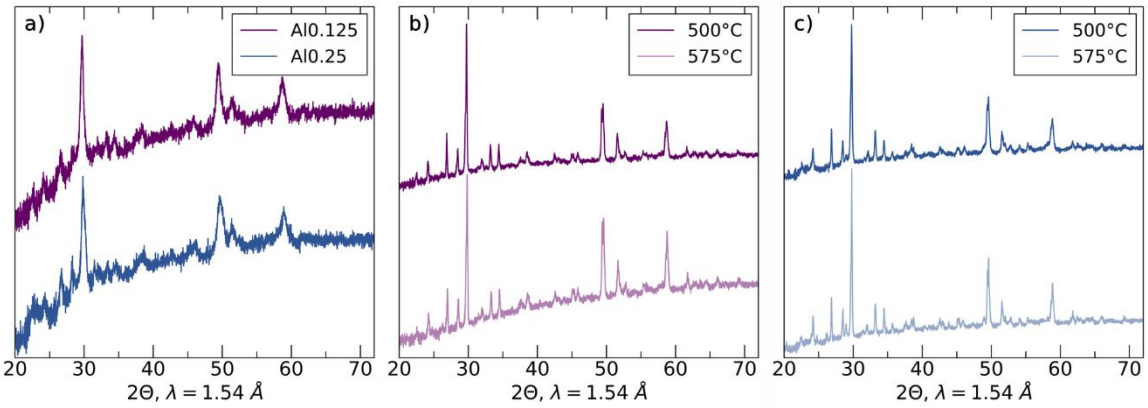

Figure 6.5 – Lab XRD of **a)** Al0.125 and Al0.25 after ball milling and **b,c)** after annealing, respectively.

We then assessed whether the Al-substituted weberites decomposed during carbon-coating. A gentler carbon-coating procedure was used, and Al0.125 575°C and Al0.25 500°C were mixed with carbon in a planetary ball mill for 12 and 6 h, respectively.[kk] The resulting lab XRD patterns are shown in Figure 6.6a. Unfortunately, the weberite phase began to decompose for both materials with more significant decomposition appearing for Al0.125. Whether more pronounced phase decomposition was due to the lower Al content, or the longer ball-milling time used for Al0.125 was unclear based on those results alone. And we therefore tested a weberite compound containing a greater amount of Al (targeted for x = 0.5 but likely closer to $x \approx 1$[jj]) processed using the same carbon-coating conditions as Al0.25, which showed even less decomposition suggesting that Al may more effectively stabilize the weberite structure at higher dopant concentrations (beyond x = 0.5), consistent with the first principles predictions presented in Figure 6.4. Notably, Al0.25 showed moderate capacity (calculated assuming that the active material was entirely $Na_2Fe_{1.75}Al_{0.25}F_7$), even after

[kk] Al0.125 was carbon-coated first, hence the longer milling time.

only 6 h of carbon-coating (Figure 6.6b) and despite the presence of many impurity phases that are electrochemically inactive in this voltage range.

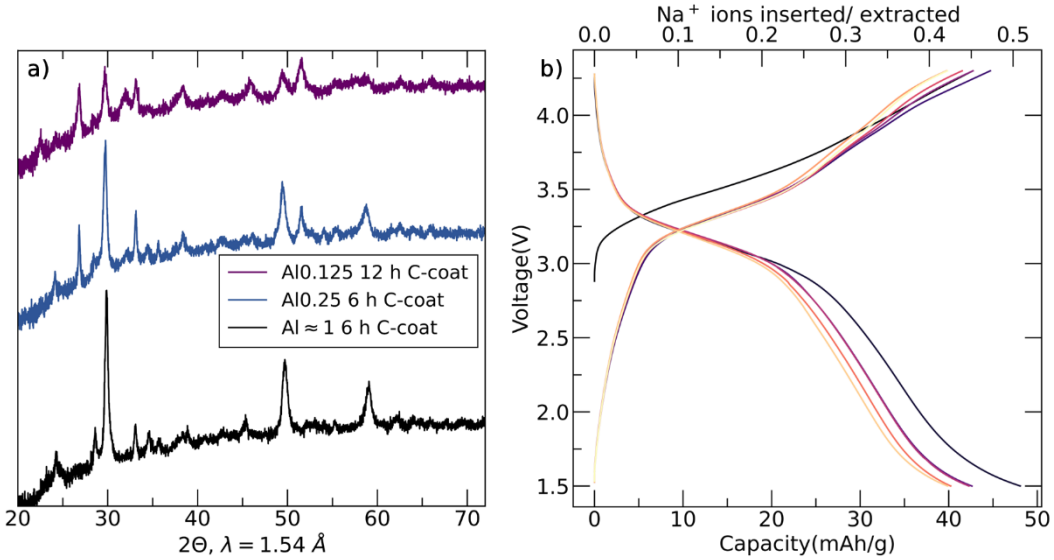

Figure 6.6 – a) Lab XRD of carbon-coated Al0.125, Al0.25 and Al≈1 showing different extents of weberite phase decomposition (highest intensity peak at ≈ 29°). Al≈1 is only shown in **(a)** as the precursors used in its synthesis were incorrectly measured, so that its actual composition is unknown. It is nevertheless a useful comparison to assess the impact of an increased amount of Al on weberite decomposition upon carbon-coating. **b)** Charge-discharge curve for Al0.25 cycled between 1.5 and 4.3 V at a C/20 rate. The electrode film and cell were prepared analogously to $Na_2Fe_2F_7$ in Chapter 5. The capacity is calculated assuming that the active material is entirely $Na_2Fe_{1.75}Al_{0.25}F_7$ and thus underestimates the capacity attributable to the weberite phase.

Thus, similarly to the Mn-substituted $Na_2Mn_xFe_{2-x}F_7$ compounds, if decomposition on carbon-coating can be prevented, these materials may perform well as cathodes.

6.3 Mg^{2+}-substitution in $Na_2Mg_xFe_{2-x}F_7$

As substitution of Fe by Mn or Al in $Na_2M_xFe_{2-x}F_7$ is complicated by their poor phase stability, Mg^{2+} substitution in $Na_2Mg_xFe_{2-x}F_7$ may be a promising direction due to the predicted increase in stability of the weberite structure with increasing Mg content (Figure 6.4). However, by substituting a diamagnetic element onto the M^{2+} site of $Na_2M_xFe_{2-x}F_7$ the electrochemical capacity will be limited to between $Na_{1+x}M_xFe_{2-x}F_7$ and

$Na_3Fe_{2-x}M_xF_7$, thereby reducing the higher voltage and less kinetically-limited capacity. Thus, the amount of diamagnetic M^{2+} substitution should be limited to enable higher electrochemical performance while still improving the material's thermodynamic stability. From an NMR point of view, while ^{25}Mg is an NMR active nucleus, its high quadrupolar moment and low sensitivity prevents its ready use. However, diamagnetic substitution for paramagnetic transition metals does enable some of the ^{19}F atoms to become visible as select nuclei are no longer directly bonded to a paramagnetic transition metal enabling broader NMR characterization.

A series of $Na_2Mg_xFe_{2-x}F_7$ compounds were investigated with x = 0.125, 0.25, 0.5, and 1 (hereafter referred to as Mg0.125, Mg0.25, Mg0.5, and Mg1). As poor electrochemical properties are expected for high Mg contents, we will focus here on Mg0.125—see Appendix 6.7 for high-Mg content electrochemical data. As for the other weberite compounds, Mg0.125 was prepared by mechanochemically-assisted solid-state synthesis where stoichiometric amounts of binary fluoride precursors were ball milled at 400 rpm for 48 h. The resulting powder, now predominantly the weberite phase, was then pelletized and annealed at 425°C, 500°C, and 575°C and their corresponding lab XRD patterns are shown in Figure 6.7a, each being well fit by the 4*M* polymorph with minor impurities of Na_3FeF_6, FeF_2, and $NaMgF_3$. These materials were then carbon-coated for 12 to 24 h with corresponding lab XRD patterns shown in Figure 6.7b. Consistent with our DFT predictions, none of the Mg0.125 samples showed signs of decomposition upon carbon-coating, indicating that Mg-substitution leads to a more stable weberite structure than Mn^{2+}- or Al^{3+}-substitution. Electrochemical characterization of the Mg0.125 samples show an interesting trend as the anneal

temperature is increased with the cycling becoming significantly more reversible and the signatures in the dQ/dV data that suggested a phase transformation in $Na_2Fe_2F_7$, fading away as the anneal temperature is increased.

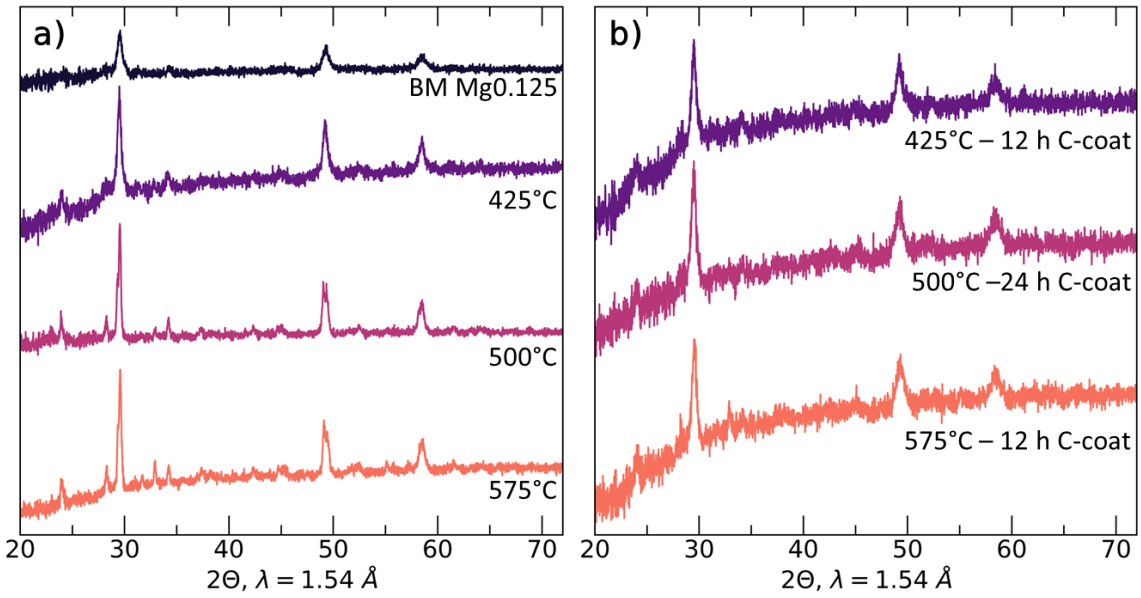

Figure 6.7 – a) Lab XRD of annealed and **b)** carbon-coated Mg0.125 showing retainment of the weberite phase (highest intensity peak at ≈ 29°).

Motivated by these results, we proceeded to study the effect of the anneal temperature on the structure and resulting electrochemistry of Mg0.125 as well as of $Na_2Fe_2F_7$ (now abbreviated as Fe2). Both compositions were prepared using a 48 h or 36 h ball mill step, respectively, and then the resulting powders were pelletized and annealed at 425°C, 500°C, 575°C, and 650°C with corresponding SXRD patterns shown in Figure 6.9 and Figure 6.10. As expected, each material shows an increase in crystallinity as the anneal temperature is increased, although both 575°C anneal samples deviate largely from the general trend and exhibit broad peaks, and their syntheses should be repeated before drawing any final conclusions from those samples. The patterns obtained on the samples annealed at 425°C, 500°C and 650°C were fit using

a combination of Pawley and Rietveld refinements to determine the polymorphic makeup of the samples (the results summarized in Table 6.3, and the full refinement of Mg0.125 annealed at 650°C is shown in Figure 6.11). For Mg0.125, the lower temperature anneals (425°C and 500°C) show a mixture of weberite polymorphs. This may be related to the ball-mill induced disorder that is unable to be resolved by these anneal temperatures, as the SXRD data collected on the sample annealed at the highest temperature (650°C) indicates a single, 4*M* weberite phase. Similarly, the Fe2 425°C and 500°C samples are also composed of a mixture of weberite polymorphs, consistent with our prior study (Chapter 5) that focused on the Fe2 sample annealed at 500°C.

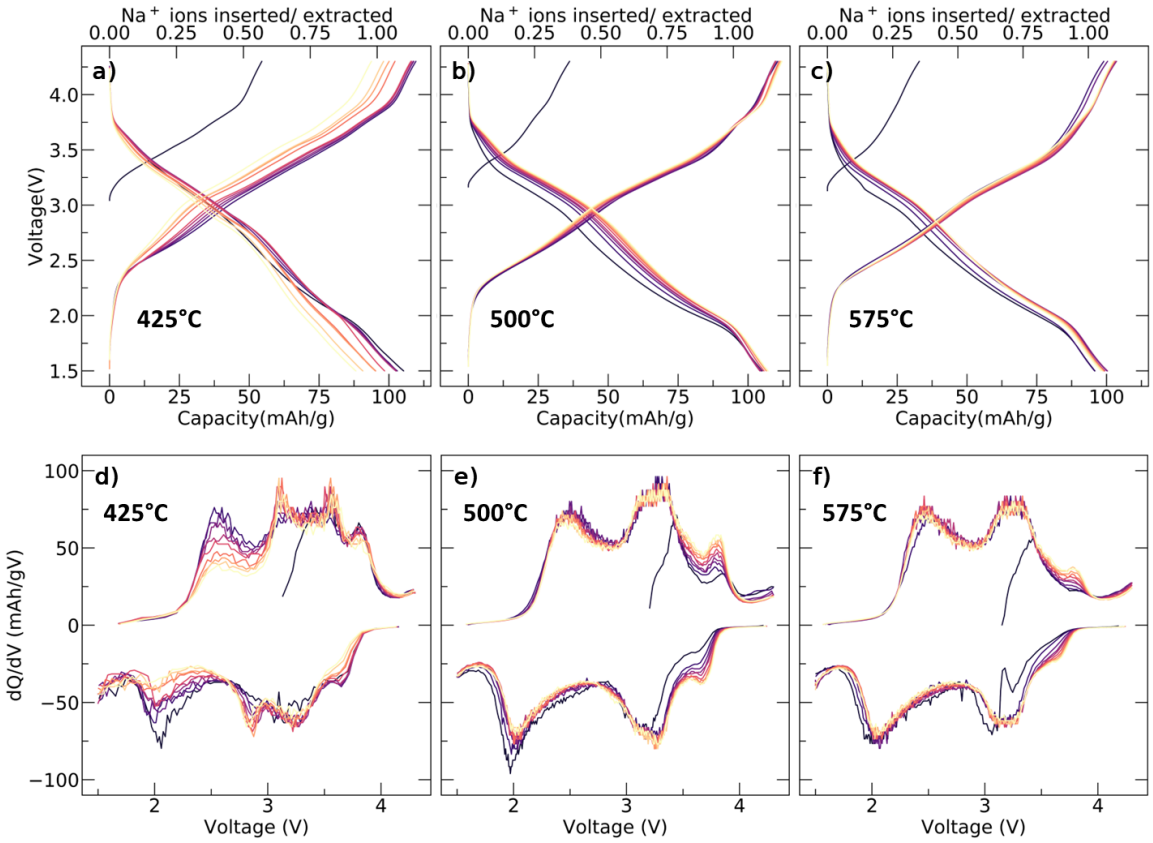

Figure 6.8 – a-c) Charge-discharge curve for Mg0.125 annealed at 425°C (left), 500°C (center), and 575°C (right) cycled between 1.5 and 4.3 V at a C/20 rate. The electrode and cell are prepared analogously as $Na_2Fe_2F_7$ in Chapter 5. Their corresponding dQ/dV plots are shown in **d-f)**.

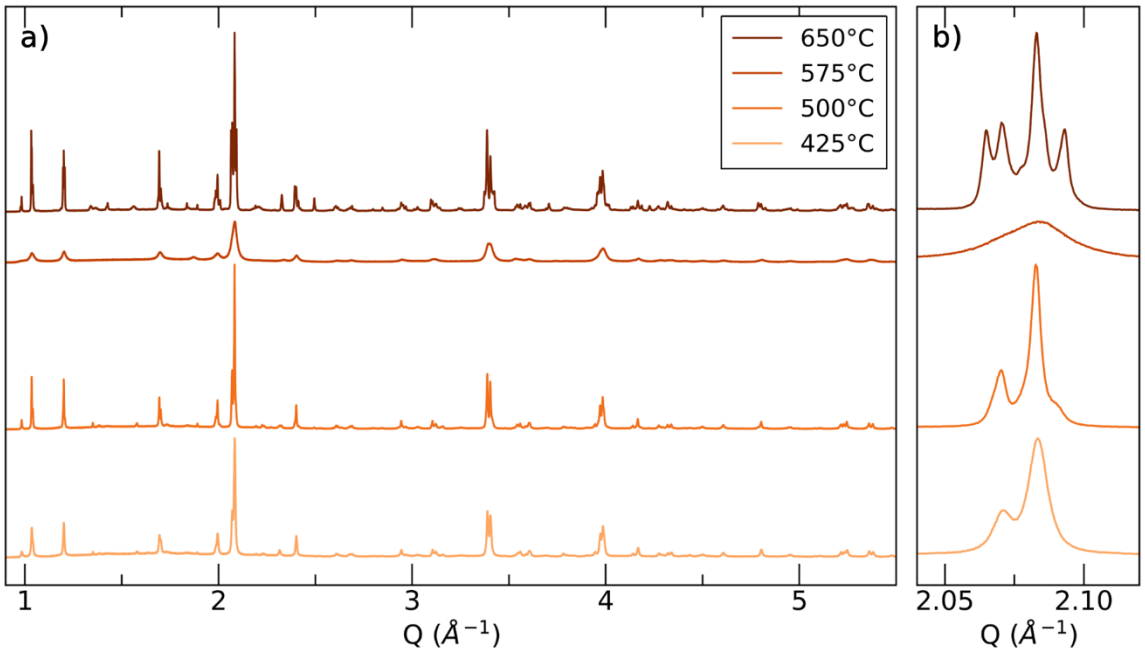

Figure 6.9 – a) Full SXRD pattern obtained on $Na_2Fe_2F_7$ (Fe2) samples prepared at four different anneal temperatures, and **b)** enlarged views of the highest intensity weberite peak.

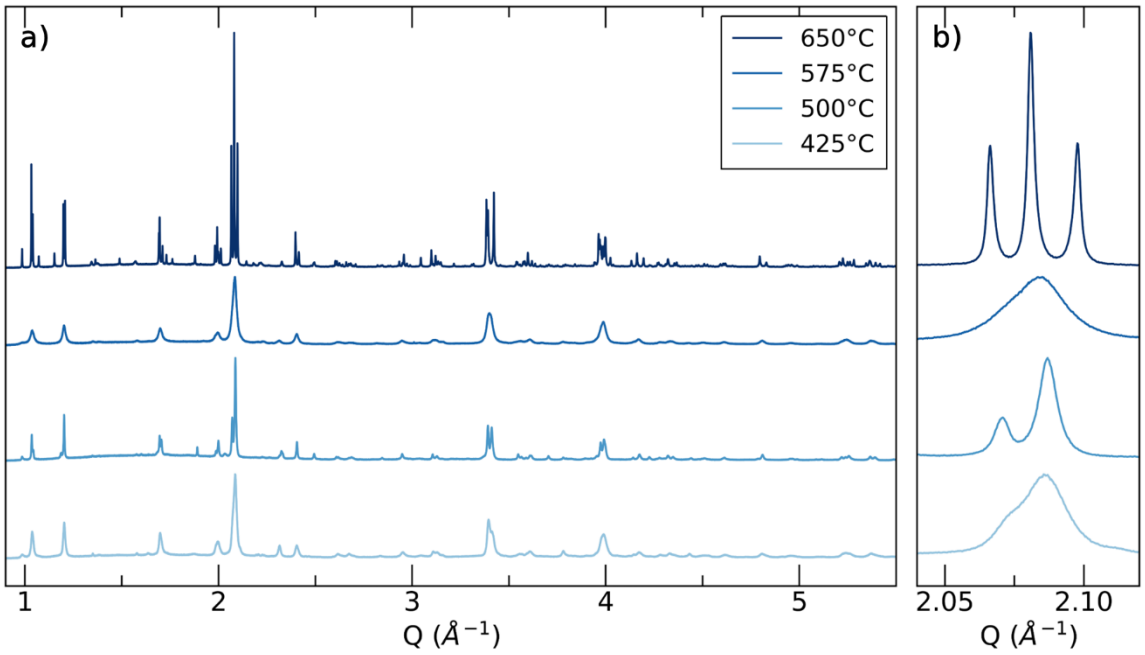

Figure 6.10 – a) Full SXRD pattern obtained on $Na_2Mg_{0.125}Fe_{1.875}F_7$ (Mg0.125) samples prepared at four different anneal temperatures, and **b)** enlarged view of the highest intensity weberite peak.

Table 6.3 – Refined phase wt.% for select SXRD patterns shown in **Figure 6.9**. The 575°C data was not refined as the synthesis should be repeated before drawing any conclusions due to the presence of significantly broadened peaks.

	2*O*	**3*T***	**4*M***	**Na_3FeF_6**	**FeF_2**	**$NaMgF_3$**	**R_{WP}**
Fe2 425°C	12.7(3)%	34.1(4)%	49.7(6)%	2.8(1)%	0.81(3)%	--	7.66%
Fe2 500°C	14.8(4)%	59.0(4)%	20.9(3)%	4.1(1)%	1.22(6)%	--	8.85%
Mg0.125 425°C	7.6(1)%	13.1(2)%	74.2(1)%	1.9(3)%	0.81(5)%	2.1(4)%	6.84%
Mg0.125 500°C	15.5(3)%	24.4(5)%	56.9(1)%	0.46(4)%	1.9(4)%	0.81(3)%	7.13%
Mg0.125 650°C	0%	0%	94.8(2)%	4.8(1)%	0.13(4)%	0.32(9)%	7.48%

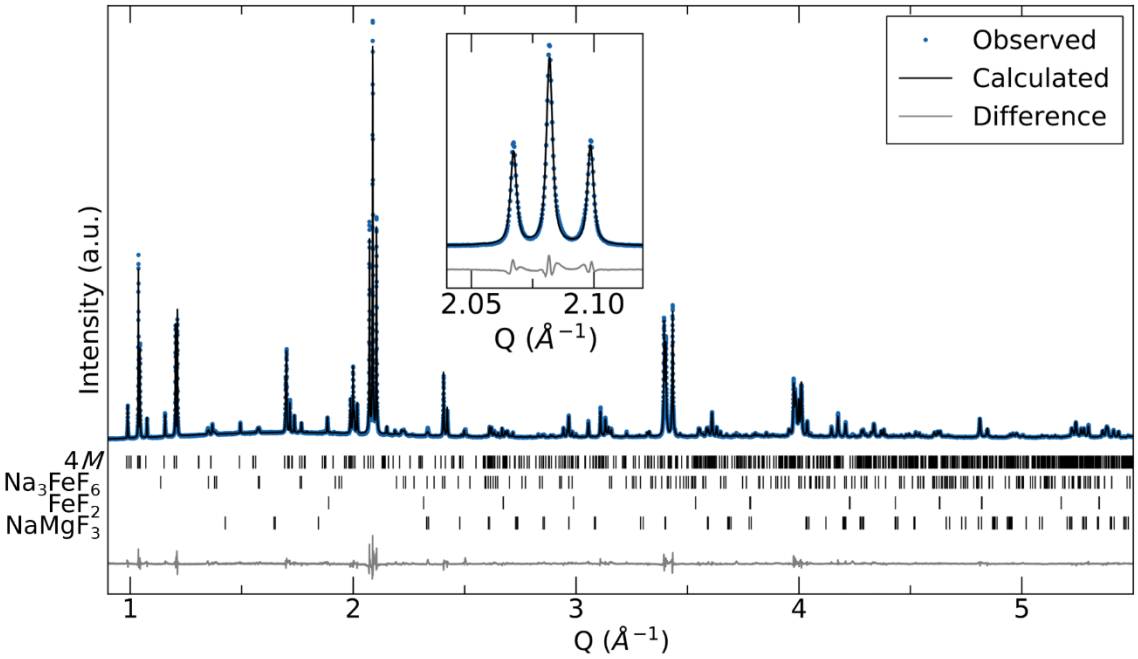

Figure 6.11 – SXRD pattern and corresponding Rietveld refinement for $Na_2Mg_{0.125}Fe_{1.875}F_7$ (Mg0.125) annealed at 650°C. The inset shows an enlarged view of the main weberite peak that was able to be well fit using only the 4*M* polymorph.

Further structural characterization of these materials, and especially of the single-phase Mg0.125 at 650°C, using ^{57}Fe Mössbauer and ^{23}Na/^{19}F NMR spectroscopy is warranted and will be pursued to understand the evolution of the weberite structure

as a function of anneal temperature. An assessment of the thermodynamic weberite polymorph stability as a function of Mg-content is also underway to aid the analysis.

Carbon-coating of all materials has been completed (SXRD patterns in Figure 6.12), confirming the trend of increased phase stability as Mg is incorporated as predicted by DFT. Electrochemical characterization will be carried out soon. One question to be answered is whether the phase transformation in $Na_2Fe_2F_7$ can be effectively suppressed by a higher annealing temperature and/or by Mg-incorporation. Additionally, *ex situ* and *operando* SXRD will be pursued for both Mg0.125 and Fe2 samples, with exact samples of interest to be determined based on their observed electrochemical behavior.

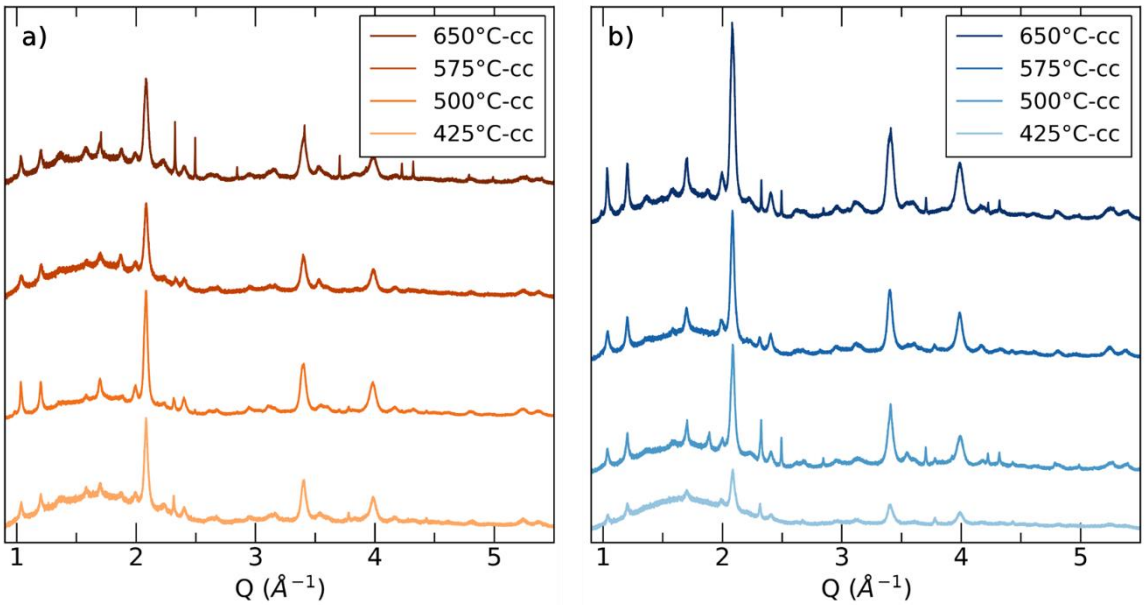

Figure 6.12 – SXRD patterns for 12 h C-coated **a)** Fe2 and **b)** Mg0.125 annealed samples. Full refinements of this data are yet to be completed but we note that Fe2-650°C, Mg0.125-650°C, and Mg0.125-500°C all exhibit the same sharp signals likely associated with an impurity phase.

6.4 Weberite Material Design Rules

While weberites show promise as next generation Na-ion cathode materials, there are several problems that currently limit their successful implementation. As shown in Chapter 5, $Na_2Fe_2F_7$ shows a tendency towards polymorphism during synthesis as well as a tendency to transform on electrochemical cycling. Both issues are directly tied to the stability of the weberite polymorphs to each other and competing phases. Additionally, throughout Chapter 6, we presented Mn- and Al-substituted weberite materials that while synthesizable, decomposed upon carbon-coating.

Based on these conclusions, we present a set of material design rules to enable successful weberite cathode materials. These materials design rules are tentatively listed below in order of increasing importance:

1. Stabilization of a single weberite polymorph
2. Thermodynamic resistance to phase decomposition
3. Incorporation of redox couples that enable at minimum cycling from $NaM^{3+}M^{3+}F_7$ to $Na_2M^{2+}M^{3+}F_7$ (de)intercalation, and preferably from $M^{3+}M^{4+}F_7$ to $Na_3M^{2+}M^{2+}F_7$

The following sections outline a preliminary computational assessment of a range of weberite compositions based on the above design rules. These and future results will comprise an upcoming computational study to enable targeted weberite material design.

6.4.1 Methodology

The weberite compositions, $Na_2M^{2+}M^{3+}F_7$, explored in this study were composed of M = Mg^{2+}, Al^{3+}, Ti^{3+}, V^{3+}, Mn^{2+}, Mn^{3+}, Fe^{2+}, and Fe^{3+} where only a single atom type occupied the M^{2+} and M^{3+} sites due to the compositional complexity involved in investigating site disorder. All binary and ternary phases within the Na-M-F phase space (M = Mg^{2+}, Al^{3+}, Ti^{3+}, V^{3+}, Mn^{2+}, Mn^{3+}, Fe^{2+}, and Fe^{3+}) were additionally calculated to determine a given weberite's decomposition energy.

Density functional theory (DFT) calculations were performed using the Vienna *ab initio* Simulation Package (VASP).[106,107,190,191] All VASP calculations used projector augmented wave (PAW) pseudopotentials (Na pv, F, Mg, Al, Ti sv, V sv, Cr pv, Mn pv, and Fe),[192,193] a plane-wave energy cutoff of 520 eV, and the Perdew-Burke-Ernzerhof (PBE) generalized-gradient approximation (GGA)[194] functional with the Hubbard U correction.[195] U values of 3.1, 3.5, 3.9, and 4 eV were used for V, Cr, Mn, and Fe, respectively, based on previous reports that have shown them be broadly reliable for ionic solids.[196,197]

All calculations were performed on a 1x1x1 cell of the $Na_2Fe_2F_7$ 2O (44 atoms), 3T (66 atoms), and 4M (176 atoms) structures. As the 3T structure contains partial occupation of Na sites, symmetrically unique Na-vacancy orderings were enumerated and ranked according to their Ewald sum energy as implemented in Pymatgen,[198] resulting in two unique structures where only the lowest energy structure is included in the analysis. All structures were fully optimized (atomic positions and cell parameters). To obtain accurate final energies, all relaxations were followed by a final static calculation. The convergence criteria were set as 10^{-5} eV for total energy and 0.01 eV/Å

for the interatomic forces. Gaussian smearing with a width of 0.05 eV was used. All calculations were spin polarized with ferromagnetic ordering assumed. All structures used a reciprocal space discretization of 25 $Å^{-1}$.

6.4.2 Weberite Polymorphism

To evaluate the tendency for a given weberite composition to exhibit polymorphism, the formation energy of the 2*O*, 3*T*, and 4*M* polymorph is shown in Figure 6.13a for a variety of compositions. The polymorph energetics for Na_2MgTiF_7, Na_2MgVF_7, Na_2MgMnF_7, Na_2MnAlF_7, Na_2MnTiF_7, Na_2MnVF_7, and $Na_2Mn_2F_7$ will additionally be calculated and added in for an upcoming study. Based on the present results, polymorphism still appears to be very likely for nearly all the compositions with no more than 5 meV/atom separating the three polymorphs. The only compositions considered that show sizeable differences in polymorph energetics are Na_2MnFeF_7, Na_2FeVF_7, and Na_2FeTiF_7, although they are all still within 30 meV/atom and mixed-polymorph materials will likely continue to be synthesized. However, as shown in Figure 6.11 a single phase (4*M*) weberite was prepared for $Na_2Mg_{0.125}Fe_{1.875}F_7$ annealed at 650°C suggests that it is still possible to synthesize a single phase material.

Thus, as polymorphism may likely continue to be present in weberite compounds, we aim to understand whether one polymorph may enable better electrochemical performance. In Chapter 5, we showed that for $Na_2Fe_2F_7$ each polymorph variant can transfer 2 Na^+ ions at similar voltages and inducing similar volume changes (Figure 5.13 and Figure 5.14). However, the kinetics of Na diffusion in each polymorph was not investigated and will be addressed in this upcoming study to

evaluate whether one polymorph can provide more desirable electrochemical properties. Hanna Porter will investigate the Na diffusion behavior in each of the $Na_2Fe_2F_7$ polymorphs using nudged elastic band theory.[230,231] These results, paired with the polymorph energetics in Figure 6.13a, which will be expanded on, will aid in understanding whether a certain polymorph should be targeted and, if so, the compositions best equipped to do so.

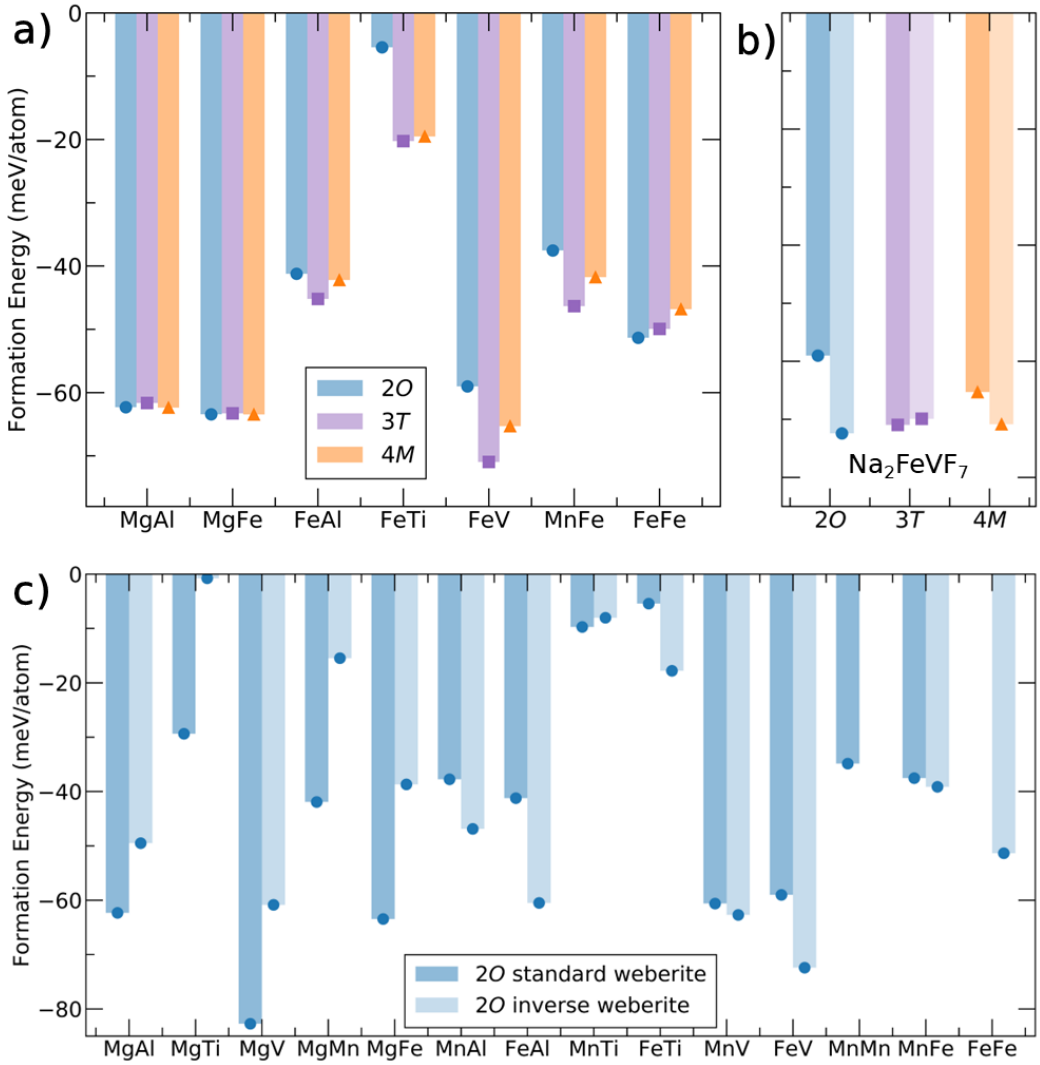

Figure 6.13 – a) Formation energy for various weberite 2*O*, 3*T*, and 4*M* polymorph compositions. **b)** Formation energy for the 2*O*, 3*T*, and 4*M* Na_2FeVF_7 standard and inverse weberites. **c)** Formation energy for various 2*O* compositions comparing the propensity for a given composition to exhibit a "standard" or an "inverse" (i.e. where the M^{2+} and M^{3+} sites are inverted) weberite structure.

Additionally, we have identified that in select weberite compositions it is energetically favorable for the M^{2+} and M^{3+} sites to exchange places (Figure 6.13b,c), referred to here as the "inverse" weberite structure. Inverse weberites have been reported before, but only in compounds with chemical formula $M^{2+}M^{3+}F_5 \bullet 2H_2O$, which retain the same *M* octahedral network as the standard weberite, but two H_2O molecules take the place of two F^- anions to maintain charge neutrality. This structure has been reported for $Fe_2F_5(H_2O)_2$, $ZnFeF_5(H_2O)_2$, $MnFeF_5(H_2O)_2$, $MnAlF_5(H_2O)_2$, $MgAlF_5(H_2O)_2$, and $MnVF_5(H_2O)_2$.[232–237] However, an inverse weberite structure that retains a $A_2M^{2+}M^{3+}F_7$ composition has not been reported before but is computationally predicted to be favorable for weberites containing Al^{3+}, V^{3+}, and to a lesser extent Ti^{3+}, as well as $Na_2Fe_2F_7$. This computational analysis has been largely limited to the 2*O* variant so far, but the 3*T* and 4*M* variants for Na_2FeVF_7 (Figure 6.13b) indicate that the inverse weberite structure is nearly equal in energy or favored compared to the standard weberite. Further study is warranted to assess whether there is a polymorph-dependence for this behavior. Future experimental investigations of weberite materials should endeavor to understand whether an inverse $Na_2M^{2+}M^{3+}F_7$ structure can occur. Notably, we have not investigated disordering on the M^{2+} and M^{3+} sites yet but considering the close energetics of the standard and inverse weberite structures it may be possible and will be considered in the upcoming study as disorder on the metal octahedral network could have significant implications on the propensity for Na^+/vacancy ordering and therefore on the electrochemical profile.

6.4.3 Weberite Metastability

We have assessed the stability of a given weberite composition by determining its decomposition energy[238] as shown in Figure 6.14 for the 2*O* polymorph. Based on Figure 6.14, it is clear that nearly all weberite compositions are metastable with only Mg-containing weberites (besides $Na_2MgMnFeF_7$) and Na_2MnVF_7 being thermodynamically stable. Interestingly, Al-containing weberites, besides the Na_2MgAlF_7 mineral, are among the most unstable compounds, which may be due to the significant difference in M^{2+}-M^{3+} ionic sizes. A dashed line at the decomposition energy for $Na_2Fe_2F_7$ is also shown in Figure 6.14 as an empirical estimate of the minimum decomposition energy that still enables successful carbon-coating. While this estimate is based on only a few compositions investigated in this dissertation (namely, Na_2MgFeF_7, Na_2FeAlF_7, Na_2MnFeF_7, and $Na_2Fe_2F_7$) it can still be used to assess whether a given composition may be worth investigating. Based on this estimate, materials are resistant to decomposition upon carbon-coating if their decomposition energies are $\gtrsim$ −20 meV/atom. Notably, all of the compositions considered here that have been previously demonstrated as Na-ion cathodes—Na_2FeVF_7, Na_2MnVF_7, and Na_2FeTiF_7[48,49]—lie above this −20 meV/atom empirical estimate, supporting these computational results. While we have only included compositions with no substitution on the M^{2+} or M^{3+} site, these results suggest that Al^{3+} and $Mn^{2+/3+}$ incorporation may lead to a decrease in material stability while Mg^{2+} and V^{3+} may improve material stability. For new material design, phases that are resistant to phase decomposition should be targeted to improve phase purity, electrochemical testing, and cycling reversibility.

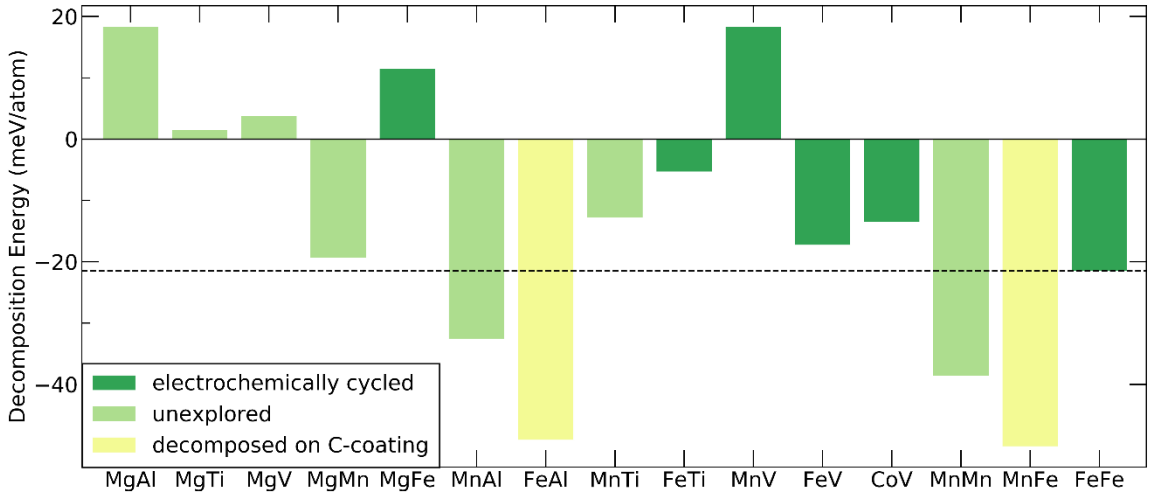

Figure 6.14 – Decomposition energy of all considered weberite compositions where a negative value indicates it is thermodynamically favorable for the given phase to decompose into competing phases. The decomposition energy was calculated using the most stable weberite polymorph for a given composition and all possible decomposition pathways were considered that obeyed conservation of mass. The specific decomposition pathway is shown in Table 6.4. The dashed line highlights the decomposition energy for $Na_2Fe_2F_7$.

Table 6.4 – Decomposition pathways for considered weberite compositions shown in Figure 6.14. We note that the observed decomposition pathway may differ from that proposed here, as phase transformations rely on both thermodynamic and kinetic factors, of which the latter is not considered here.

	Weberite Decomposition Pathway
MgAl	$Na_2MgAlF_7 \rightarrow NaMgF_3 + NaAlF_4$
MgTi	$Na_2MgTiF_7 \rightarrow NaMgF_3 + NaTiF_4$
MgV	$Na_2MgAlF_7 \rightarrow MgF_2 + Na_2VF_5$
MgMn	$Na_2MgMnF_7 \rightarrow MgF_2 + Na_2MnF_5$
MgFe	$2Na_2MgFeF_7 \rightarrow 2MgF_2 + NaFeF_4 + Na_3FeF_6$
MnAl	$4Na_2MnAlF_7 \rightarrow 4MnF_2 + Na_3AlF_6 + Na_5Al_3F_{14}$
FeAl	$4Na_2FeAlF_7 \rightarrow 4FeF_2 + Na_3AlF_6 + Na_5Al_3F_{14}$
MnTi	$3Na_2MnTiF_7 \rightarrow 3MnF_2 + 2Na_3TiF_6 + TiF_3$
FeTi	$3Na_2FeTiF_7 \rightarrow 3FeF_2 + 2Na_3TiF_6 + TiF_3$
MnV	$Na_2MnVF_7 \rightarrow MnF_2 + Na_2VF_5$
FeV	$Na_2FeVF_7 \rightarrow FeF_2 + Na_2VF_5$
MnMn	$Na_2Mn_2F_7 \rightarrow MnF_2 + Na_2MnF_5$
MnFe	$2Na_2MnFeF_7 \rightarrow 2MnF_2 + Na_3FeF_6 + NaFeF_4$
FeFe	$2Na_2Fe_2F_7 \rightarrow 2FeF_2 + NaFeF_4 + Na_3FeF_6$

6.4.4 Weberite Redox Behavior

To further aid weberite compositional design, I intend to calculate theoretical voltages for Na (de)intercalation for the weberite compositions investigated in Figure 6.14. A similar dataset was provided in the first study to propose weberites as battery

materials,[186] but the predicted operating voltages were calculating using only GGA and assumed only Na (de)intercalation between $M^{3+}M^{4+}F_7$ and $Na_2M^{2+}M^{3+}F_7$. Thus, by updating this data using an appropriate level of theory (GGA+*U*) and the newly understood Na (de)intercalation ranges identified in this dissertation, and in since published literature, enables a more accurate assessment of promising weberite cathode materials.

As we demonstrated in Chapter 5 that predicted weberite voltages are largely polymorph-independent, I will only consider the 2*O* weberite polymorph. Due to the computational complexity of calculating full voltage curves for each composition, this analysis will be limited to Na (de)intercalation of $x = 0$, 1, 2, and 3 in Na_xMMF_7 and makes the following assumptions regarding possible redox couples:

- Mg^{2+} and Al^{3+} are redox-inactive
- Ti can operate on the $Ti^{3+/4+}$ redox couple
- V can operate on the $V^{2+/3+}$, $V^{3+/4+}$, and $V^{4+/5+}$ redox couples
- Mn can operate on the $Mn^{2+/3+}$ and $Mn^{3+/4+}$ redox couples
- Fe can operate on the $Fe^{2+/3+}$ and $Fe^{3+/4+}$ redox couple

This work is still ongoing but is a key part to targeting high energy density weberite compositions, potentially enabling the design of a material that can transfer three Na^+ ions per formula unit. This data will be further used to predict the volume change expected for Na (de)intercalation to assess material reversibility.

6.5 Conclusion

We have demonstrated the first reported synthesis of substituted weberite compounds based on M = Mn^{2+}, Al^{3+}, and Mg^{2+} substitution in $Na_2M_xFe_{2-x}F_7$ with x between 0 and 1. However, despite successful synthesis, the Mn- and Al-substituted materials are prone to decomposition upon carbon-coating preventing their implementation as Na-ion cathode materials. Mg-substituted materials, however, can be carbon-coated and preliminary results show that through incorporation of a small amount of Mg (x = 0.125) and optimized synthetic conditions, the electrochemically-induced phase transformation observed in Chapter 5 for $Na_2Fe_2F_7$ can be suppressed. Further assessment of this behavior will comprise a forthcoming study.

The metastability issues exemplified by the Mg- and Al-substituted materials further confirm the necessity of first-principles calculations to enable informed materials prediction. Thus we have proposed a set of preliminary design rules based on polymorph energetics, thermodynamic stability, voltage predictions, and volume changes upon cycling. Assessment of a series of weberite compounds based on these design rules is in progress and will be published in a future study.

6.6 Appendix – Weberite Material Synthesis

The weberite materials studied in this dissertation are currently limited by metastability issues exemplified in Chapter 5 for $Na_2Fe_2F_7$. This complicates their synthesis and prevents preparation of phase pure materials. Weberites have been synthesized through the following methods:

- Traditional solid-state synthesis – reported for weberites in 1978[239]
- Topochemical synthesis – reported for weberites January 2019[240]
- Mechanochemically-assisted solid-state synthesis – reported for weberites January 2021[47]
- PTFE-assisted fluorination synthesis – reported for weberites October 2021[49]

Here, we will briefly summarize each of these synthetic strategies – and additionally microwave synthesis – and describe the implementation and result of each method throughout this PhD. Overall, we found mechanochemically-assisted solid-state synthesis to be the most effective at preparing a broad range of compositions, while PTFE-assisted fluorination synthesis presents promise for improved electrochemical behavior through *in situ* carbon-coating.

6.6.1 Traditional Solid-State Synthesis

The vast majority of weberite materials have been prepared using traditional solid-state synthesis methods as implemented beginning in the 1970s.[187,200,201,205,207,239,241–244] These syntheses typically began with preparation of the relevant binary fluoride precursors via fluorination using either fluorine gas ($F_{2(g)}$) and

hydrofluoric acid (HF) of the binary chlorides except for FeF_2 and ZnF_3 which were prepared from hydrated iron oxalate (which was first dehydrated) and zinc carbonate, respectively. The binary fluoride precursors were then dried and hand ground in stoichiometric ratios. The resulting mixture was then sealed inside platinum or gold ampoules under vacuum or Ar and heated to temperatures around 500-900°C for several days with slow heating and cooling rates. The resulting products were either polycrystalline powders – which were occasionally used to grow single crystals – or single crystals. Several of these studies do suggest the presence of various impurities that the authors were unable to get rid of. For Fe-containing weberites, these impurities are often Na_3FeF_6 and FeF_2, which were observed in Chapter 5 for $Na_2Fe_2F_7$. This method was shown to be successful at preparing a broad range of compounds of $Na_2MM'F_7$ where M = Mg^{2+}, Al^{3+}, Sc^{2+}, Ti^{3+}, V^{3+}, Cr^{3+}, $Mn^{2+/3+}$, $Fe^{2+/3+}$, $Co^{2+/3+}$, Ni^{2+}, Cu^{2+}, Zn^{2+}, and Ga^{3+}.[187,200,201,205,207,239,241–244] For a review of the materials prepared via these methods and their corresponding identified space groups, we direct the reader to the work of Cai and Nino.[208] However, this synthesis method is time intensive due to the multi-day high-temperature reactions, costly due to the platinum and gold ampoules, and presents safety concerns due to the use of $F_{2(g)}$ and/or hydrofluoric acid.

To circumvent the cost and safety issues, we endeavored to use fluoride-resistant nickel superalloy[ll] or silver[mm] ampoules and used commercially-available binary

[ll] At high-temperatures, fluorides readily corrode most materials. Nickel superalloys (specifically, Monel, Inconel, and Hastelloy) show superior resistance to stainless steel, which is only moderately fluoride resistant. However, they do still undergo phase transformations at high temperatures so the Swagelok tube caps will "seize" up and become impossible to remove after a couple of heat treatments.

[mm] Silver is also resistant to fluorides but above 700°C $O_{2(g)}$ can readily diffuse through it. Thus, they need to be sealed inside a quartz ampoule.

fluoride precursors to synthesize Na_2MgAlF_7, Na_2FeAlF_7, Na_2MgAlF_7, Na_2MgFeF_7, $Na_2Fe_2F_7$, and Na_2MnFeF_7. A schematic of the nickel superalloy tube design is shown in Figure 6.15. The remainder of the synthesis was the same as previously reported, along with an Ar gas flow being used to prevent oxygen contamination and, in some cases, using 5% Na excess. The synthesis results were overall mixed with most syntheses producing little of the targeted weberite phase. The best synthesis result was for Na_2MgAlF_7 heat treated in a nickel superalloy tube at 750°C for 100 h, although this synthesis was still only 70% pure. This may have been due to impure precursors[nn], unoptimized heat treatments, and/or oxygen contamination. These long, high temperature syntheses are likely thermodynamically controlled and thus even a slight deviation from the correct stoichiometry may result in decomposition of the metastable weberite phase. Thus, for future syntheses following this method, we recommend using high quality binary fluoride precursors (preferably obtained through direct fluorination) and platinum or gold tubes sealed using an arc melter under inert environment.

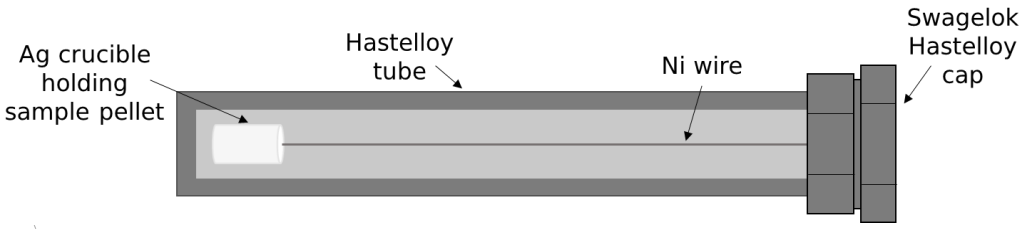

Figure 6.15 – Reaction vessel used for weberite solid-state syntheses. A nickel superalloy (here, Hastelloy) tube and Swagelok cap were used to contain a silver crucible containing the sample pellet that was attached to a nickel wire to position the sample.

[nn] It is very difficult to obtain high quality fluoride precursors even when bought. Always dry precursors and check their purity using XRD.

6.6.1.1 Microwave Synthesis

While microwave synthesis has never been reported for synthesizing weberite materials, we did attempt to use it here as the rapid reactions and fast cooling rates can enable stabilization of metastable phases.[120,142] Similar to solid-state synthesis, the binary fluoride precursors were stoichiometrically combined (in some cases using 5% Na excess), hand ground, and pelletized. To maintain an air-free environment, each pellet was placed in a boron nitride crucible and sealed inside a quartz tube under vacuum or 0.25 atm of Ar. The sealed tube was then placed inside a crucible surrounded by activated carbon and placed inside a conventional microwave. The microwaves were then used to heat the carbon susceptor material until the sample pellet also coupled to the microwaves and both materials began to rapidly heat from the inside-out allowing for rapid interdiffusion.[oo] As fluorides (and potentially halides in general as this has been observed for chloride materials as well) melt and more strongly couple with the microwaves at lower temperatures, the reaction times and microwave power must be significantly reduced. For example, a lithium disordered rocksalt material is readily synthesized at a microwave power of 720 W for 20 minutes whereas the fluoride materials tested in this dissertation melt above 10 minutes at 360 W. Regardless, synthesis of weberite materials via microwave synthesis was moderately effective, achieving similar purity levels as solid-state synthesis within only a few minutes – XRD patterns for representative syntheses are shown in Figure 6.16 However, as fluorides readily corrode glass, silica contamination was identified via XRD and thus this synthesis

[oo] This contrasts with solid-state furnace synthesis where reactions occur through an outside-in conductive heating mechanism, which involves heat transfer from the surface to the core of the particles. This leads to much shorter reaction times for microwave synthesis.

method was abandoned despite the promising results after only a few attempts. Thus, if an air- and glass-free microwave setup can be designed, weberites may be able to be prepared via microwave synthesis.

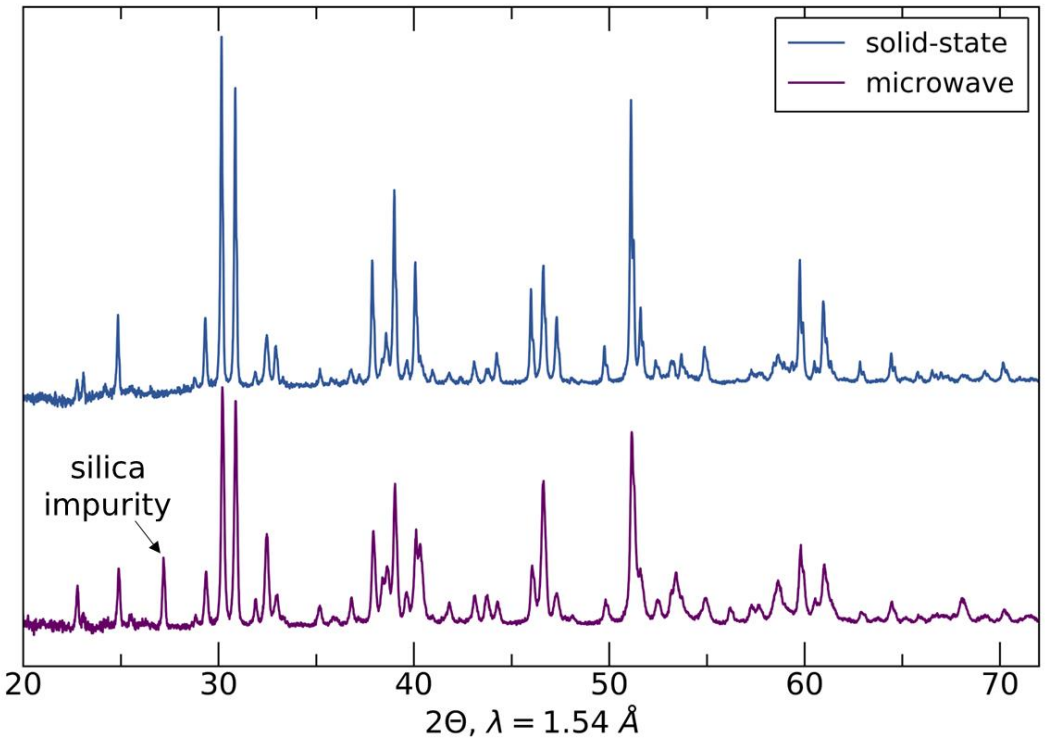

Figure 6.16 – Lab XRD patterns for solid-state (blue, top) and microwave (purple, bottom) prepared Na_2MgAlF_7 where a purity of 70 wt.% and 65 wt.% were achieved, respectively. Note that a silica impurity was identified in the microwave prepared sample.

6.6.2 Topochemical/Hydrothermal Synthesis

Topochemical synthesis was used to prepare $Na_2Fe_2F_7$ by Dey et al.[240] This synthesis involved NaF and $FeF_3 \bullet 3H_2O$ in a 1:1 (Na:Fe) ratio in tetraethylene glycol (TEG), which was then sealed in a PTFE-lined autoclave, placed on an oil bath, and the temperature gradually increased to 225°C for 24 hrs under constant stirring. The hypothesized reaction process is dissolution of NaF, and removal of H_2O from the Fe-F structure induced by TEG, rearrangement of the Fe-F framework to first form layered

$NaFeF_4$, and then further rearrangement to form $Na_2Fe_2F_7$. Unfortunately, this synthesis requires very fine heat rate, temperature, and stirring control which is not readily achieved without an automated setup and is thus difficult to implement and reliably produce phase pure materials[pp]. Additionally, as the synthesis is reliant on the Fe-F structure rearrangement, it is not readily extended to other compositions. We only ever achieved 60% $Na_2Fe_2F_7$ purity using this method. Further, while Dey et al. reported their $Na_2Fe_2F_7$ material in the 2*O* structure, we note that polymorphism is still likely present as discussed in Chapter 5. SXRD data we acquired on $Na_2Fe_2F_7$ produced by their group showed strong evidence that there were multiple weberite phases present. Similarly to the $Na_2Fe_2F_7$ pristine material discussed in Chapter 5, we performed a combination of Pawley and Rietveld refinements (χ^2 = 1.18, R_{WP} = 7.7%) indicating on the topochemically-prepared $Na_2Fe_2F_7$ as shown in Figure 6.17. We identified that there was 16% 2*O*, 25% 3*T*, and 40% 4*M* weberite polymorphs present with 18.2% of Na_3FeF_6 and 0.3% FeF_2 with additional refinement data shown in Table 6.5. While this was a new batch of material – which may be the origin of the large Na_3FeF_6 impurity –, it is regardless very likely that even topochemically-prepared $Na_2Fe_2F_7$ is polymorphic.

Overall, topochemical synthesis of weberite materials is a compositionally-limited and difficult to optimize synthesis route.

[pp] This comment comes from both my experience with trying this synthesis method and conversations with the group that authored this study.

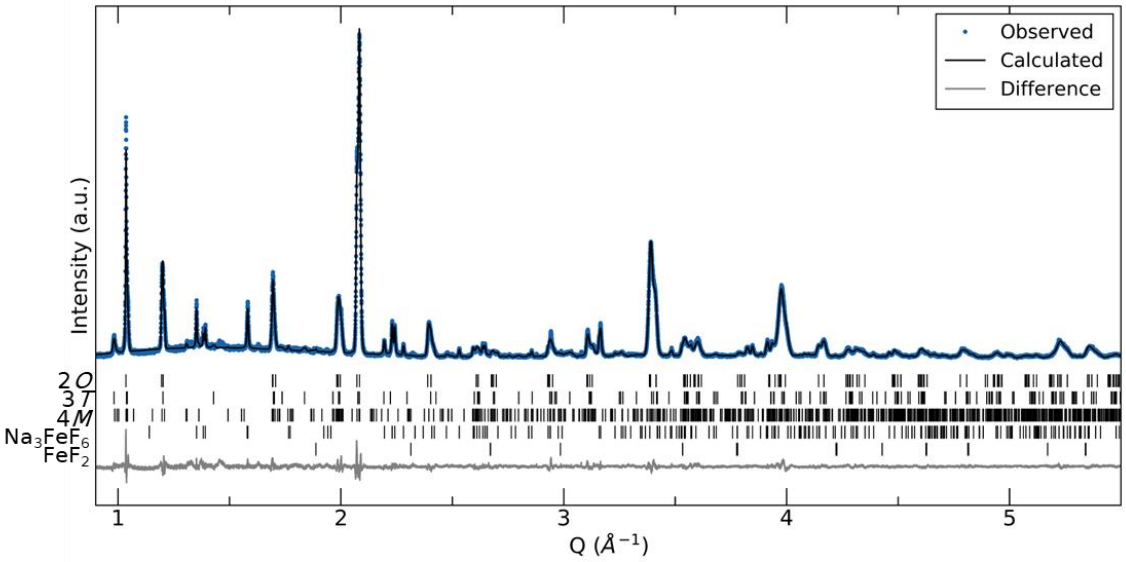

Figure 6.17 – SXRD pattern and corresponding Rietveld refinement for topochemically-prepared $Na_2Fe_2F_7$ (material prepared by collaborators). The data was analyzed using an analogous method as done for the pristine $Na_2Fe_2F_7$ material prepared in Chapter 5.

Table 6.5 – Refined lattice constants and weight percentages for all phases used to fit the SXRD data collected on topochemically-prepared $Na_2Fe_2F_7$. The fit residuals are: χ^2 = 1.18 and R_{WP} = 7.7%.

Phase	**2*O***	**3*T***	**4*M***	**Na_3FeF_6**	**FeF_2**
Space Group	*Imma*	$P3_121$	$C2/c$	$P2_1$	$P4_2/mnm$
a (Å)	7.3481(3)	7.3740(5)	12.7224(5)	5.5004(2)	4.6979(7)
b (Å)	10.5003(5)	7.3740(5)	7.3994(3)	5.7153(2)	4.6979(7)
c (Å)	7.4126(4)	18.130(2)	24.613(1)	7.9429(3)	3.319(1)
alpha (°)	90	90	90	90	90
beta (°)	90	90	100.358(3)	90.413(1)	90
gamma (°)	90	120	90	90	90
wt.%	**16.0(4)%**	**25.4(3)%**	**40.1(3)%**	**18.2(1)%**	**0.29(2)%**

6.6.3 Mechanochemically-Assisted Solid-State Synthesis

Mechanochemically-assisted solid-state synthesis is the method employed throughout this dissertation for the synthesis of weberite materials and was first introduced by Park et al. for $Na_2Fe_2F_7$[47] and has also been reported for Na_2FeTiF_7.[48] In this method dried, stoichiometry binary fluoride precursors are combined and mixed in a planetary ball mill at 400 rpm for 12 to 48 h to first form the weberite phase. Following

ball milling, the resulting powder is pelletized and annealed at an intermediate temperature (between 500 and 650°C)[qq] for 30 min under an Ar flow. This method leverages mechanochemical synthesis' ability to readily form metastable phases and solid-state synthesis' ability to produce highly crystalline materials, to develop a relatively low energy synthesis method that we have found to be robust for numerous compositions ($Na_2M_xFe_{2-x}F_7$ with M = Mg^{2+}, Al^{3+}, Mn^{2+} from x = 0 to 1). Additionally, as fluorine is commonly used as a sintering agent due to its small ionic size and charge and ability to quickly diffuse through a structure,[245–247] high crystallinity can be obtained even after a 30 min anneal. Notably, to prevent significant impurity formation, we have found that the pelletized sample should be placed in a tube furnace already at 500°C, rather than going through the heating ramp, to minimize time at high temperature as the material will start to decompose. Similarly, the sample must be quenched from high temperature – this has been done by using an extra-long alumina tube where the sample region is physically moved out of the tube furnace and a nitrogen flow is passed over it until the tube is cool to the touch.

6.6.4 PTFE-Assisted Fluorination Synthesis

A PTFE-assisted fluorination synthesis method was used by Liao et al. to prepare Na_2MnVF_7, Na_2FeVF_7,and Na_2CoVF_7.[49] In this method, precursors of NaF, $MC_2O_4 \bullet 2H_2O$ (M = Mn^{2+}, Fe^{2+}, and Co^{2+}), NH_4VO_4, and PTFE were first mixed by planetary ball milling in ethanol in a 2:1:1.05:2 molar ratio. The resultant mixture was then dried to remove

[qq] As fluorides do not attack alumina until around 700°C, alumina boats and tubes can still be used.

ethanol, pelletized and fired at 550°C for 1 h under Ar flow, ground, and repelletized and fired at 650°C for 1 h under Ar flow. This method enabled the preparation of weberite materials without expensive transition metal binary fluorides making it the most environmentally-friendly and scalable method used to prepare weberite materials. Additionally, upon decomposition of PTFE, a thin carbon layer is deposited on the surface of the resulting particles, which likely improves the electrochemical behavior by improving the electronic conductivity of the final electrode.

Implementation of this method in our lab showed slight promise as shown in Figure 6.18 as the weberite phase was forming but oxide phases were consistently present, likely due to insufficient fluorination. We concluded that the synthesis was highly dependent on the Ar flow rate and starting PTFE particle size, both of which will impact the fluorination reaction occurring at high temperatures. In our syntheses, the PTFE particles were about five times larger than those reported by Liao et al.[49] so implementation of more appropriately sized PTFE will likely have a significant positive impact on weberite formation. Overall, this method seems quite promising for more facile weberite synthesis, but the accessible compositional range is yet to be determined. While the M^{2+} site can be varied by changing the transition metal acetate, it is unclear whether the M^{3+} site can be occupied by any element besides V^{3+} using this synthesis method. This has not been extensively tested yet and should be investigated in the future to examine the versatility of this method.

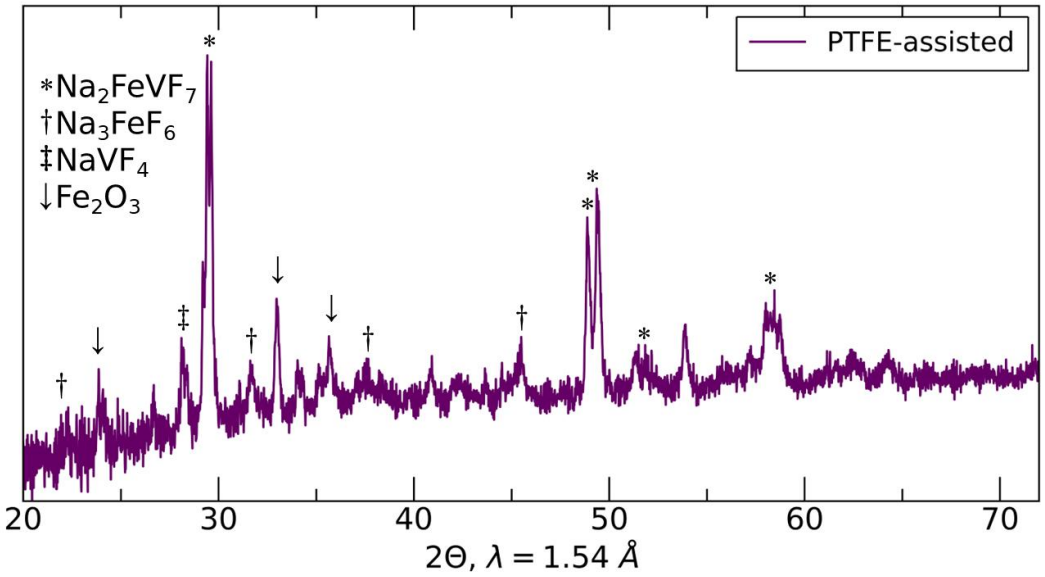

Figure 6.18 – Lab XRD pattern for PTFE-assisted prepared Na_2FeVF_7 with individual phases marked by the corresponding symbols: * Na_2FeVF_7, † Na_3FeF_6, ‡ $NaVF_4$, and ↓ Fe_2O_3.

6.7 Appendix – High Mg-content $Na_2Mg_xFe_{2-x}F_7$ Electrochemistry

As expected for increasing Mg^{2+}-substituents, less electrochemical capacity is observed due to the reduction of the Fe^{2+}/Fe^{3+} redox reservoir. Interestingly, the poorest reversibility is Mg0.25 even though Mg0.125 is transferring a higher amount of Na^+ ions.

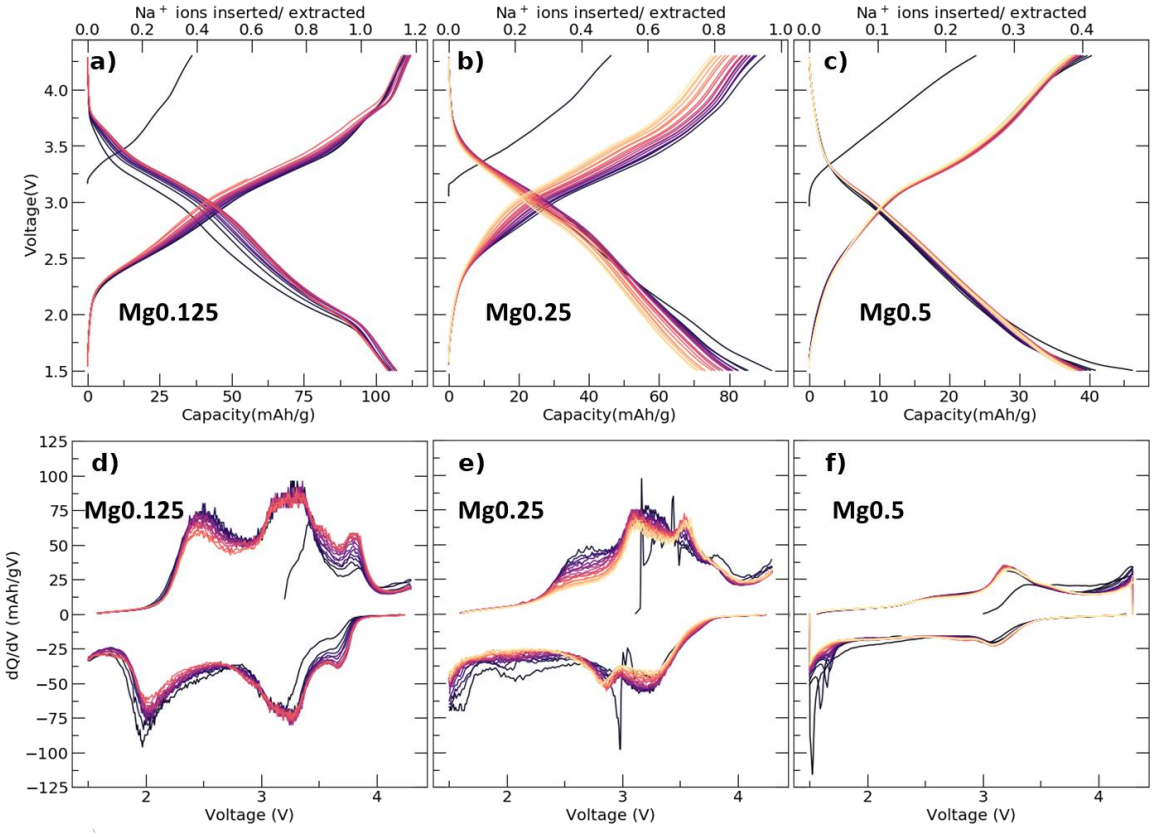

Figure 6.19 – a-c) Charge-discharge curve for Mg0.125 (left), Mg0.25 (center), and Mg0.5 (right) annealed at 500°C cycled between 1.5 and 4.3 V at a C/20 rate. The electrode and cell are prepared analogously as $Na_2Fe_2F_7$ in Chapter 5. Their corresponding dQ/dV plots are shown in **d-f)**.

Chapter 7 – Conclusions

Continuing to rely on a select few battery cathodes is untenable with the increasing demand for batteries, especially as these select battery cathodes rely on expensive, insecure, and ethically-complex elements. Thus, in this dissertation I have explored three classes of battery cathodes using both experimental—including complementary long-range and short-range structural techniques—and computational techniques to characterize the behaviour of these materials.

The first class investigated are Li-ion disordered rocksalt (DRX) oxyfluorides (Chapter 3), where I used ^{7}Li and ^{19}F NMR to better understand the nuanced effect of short-range ordering in DRX materials. Beyond, assessing the incorporation of Li and F in diamagnetic- vs. paramagnetic-like environments, which is especially relevant for these metastable DRX materials, we have shown that both decreasing short-range order and increasing short-range order can have positive effects on the electrochemical behavior, yet the nature of this order is only somewhat understood. Thus, careful tuning, design, and characterization of the short-range order is necessary to realize the potential of Li-excess DRX oxyfluoride cathode materials and future investigations carefully tuning the degree of short-range ordering is warranted.

The second and third structure classes investigated are both sodium metal fluorides but their differing structures lead to significantly different Na transfer mechanisms—conversion in perovskite-like Na_3FeF_6 due to its dense structure, and intercalation in weberite $Na_2Fe_2F_7$ due to its more open framework structure.

The former material, Na_3FeF_6 (Chapter 4), we identified to form NaF and Fe on discharge, which is only moderately reversible due to sluggish conversion reaction kinetics. Despite the rapid oxidation of the metastable Fe particles formed on discharge, we were able to use a simple *ex situ* analytical method that relies on the quantification of stable conversion products using local structure probes (here, NaF characterized through ^{23}Na NMR) and a comparison with the observed capacity, to determine the conversion mechanism at play. This novel analytical framework holds promise for the study of a wide range of conversion processes that are often plagued by severe relaxation and oxidation processes during *ex situ* characterization. Ultimately, *in situ* and *operando* studies are better suited for the elucidation of conversion type processes and thus *operando* magnetometry was employed, which further confirmed the conversion mechanism and its sluggish kinetics.

The latter material, $Na_2Fe_2F_7$ (Chapter 5), showed markedly improved electrochemical performance as it operates *via* an intercalation mechanism. However, the metastability and processing of the weberite $Na_xFe_2F_7$ phase leads to an electrochemically induced phase transformation to the Na_yFeF_3 perovskite phase that has not been reported in prior studies. We suspect that, here, poorer overall kinetics hinders topotactic Na-ion (de)intercalation and favors a phase transformation reaction. Additionally, using a combined experimental-computational approach, we identified

that $Na_2Fe_2F_7$ is prone to and exhibits polymorphism, which has been frequently overlooked throughout literature. From a thermodynamic standpoint, the polymorphic makeup of the $Na_2Fe_2F_7$ weberite cathode does not have a strong impact on the electrochemical behavior, although future investigations of the Na-ion transport properties of the weberite variants is warranted.

Motivated by the improved performance of weberite $Na_2Fe_2F_7$ we explored a variety of Mn^{2}-, Al^{3+}-, and Mg^{2+}-substituted $Na_2M_xFe_{2-x}F_7$ compositions with x between 0 and 1 to tune its performance. However, thermodynamic differences between these substituents leads to markedly different behaviors—the reduced stability of Mn- and Al-substituted $Na_2M_xFe_{2-x}F_7$ leads to phase decomposition prior to electrochemical cycling, while the improved stability of Mg-substituted $Na_2M_xFe_{2-x}F_7$, along with optimized synthetic conditions, leads to suppression of the phase transformation. A full study of the cycling behavior and factors influencing phase transformation suppression is underway. Additionally, to aid in material design, a computational assessment of the vast weberite compositional space is underway to assess structural polymorphism, metastability, operating voltages, and volume changes upon cycling. These forthcoming studies will contribute significant knowledge towards the improved electrochemical performance of weberite Na-ion cathodes.

References

(1) IPCC. *Climate Change 2022 Impacts, Adaptation and Vulnerability ,Sixth Assessment Report*; 2022. https://doi.org/10.1017/9781009325844.Front.

(2) Mizushima, K.; Jones, P. C.; Wiseman, P. J.; Goodenough, J. B. LixCoO2 (0<X<-1): A New Cathode Material for Batteries of High Energy Density. *Mater. Res. Bull.* **1980**, *15* (6), 783–789. https://doi.org/10.1016/0025-5408(80)90012-4.

(3) Bard, A. J.; Faulkner, L. R. *Electrochemical Methods*; Wiley, New York, 2001.

(4) Van Der Ven, A.; See, K. A.; Pilon, | Laurent; Pilon, L. Hysteresis in Electrochemical Systems. *Batter. Energy* **2022**, *1* (2), 20210017. https://doi.org/10.1002/bte2.20210017.

(5) Dugas, R.; Forero-Saboya, J. D.; Ponrouch, A. Methods and Protocols for Reliable Electrochemical Testing in Post-Li Batteries (Na, K, Mg, and Ca). *Chem. Mater.* **2019**. https://doi.org/10.1021/acs.chemmater.9b02776.

(6) Yan, G.; Alves-Dalla-Corte, D.; Yin, W.; Madern, N.; Gachot, G.; Tarascon, J.-M. Assessment of the Electrochemical Stability of Carbonate-Based Electrolytes in Na-Ion Batteries. *J. Electrochem. Soc.* **2018**, *165* (7), A1222–A1230. https://doi.org/10.1149/2.0311807jes.

(7) Kim, J.; Park, S.; Hwang, S.; Yoon, W. S. Principles and Applications of Galvanostatic Intermittent Titration Technique for Lithium-Ion Batteries. *J. Electrochem. Sci. Technol.* **2022**, *13* (1), 19–31. https://doi.org/10.33961/jecst.2021.00836.

(8) Van Der Ven, A.; Deng, Z.; Banerjee, S.; Ong, S. P. Rechargeable Alkali-Ion Battery Materials: Theory and Computation. *Chem. Rev.* **2020**, *120* (14), 6977–7019. https://doi.org/10.1021/acs.chemrev.9b00601.

(9) Wu, F.; Yushin, G. Conversion Cathodes for Rechargeable Lithium and Lithium-Ion Batteries. *Energy and Environmental Science*. Royal Society of Chemistry February 1, 2017, pp 435–459. https://doi.org/10.1039/c6ee02326f.

(10) Kim, J.; Kim, H.; Kang, K. Conversion-Based Cathode Materials for Rechargeable Sodium Batteries. *Adv. Energy Mater.* **2018**, *8* (17), 1702646. https://doi.org/10.1002/aenm.201702646.

(11) Hua, X.; Eggeman, A. S.; Castillo-Martínez, E.; Robert, R.; Geddes, H. S.; Lu, Z.; Pickard, C. J.; Meng, W.; Wiaderek, K. M.; Pereira, N.; Amatucci, G. G.; Midgley, P. A.; Chapman, K. W.; Steiner, U.; Goodwin, A. L.; Grey, C. P. Revisiting Metal Fluorides as Lithium-Ion Battery Cathodes. *Nat. Mater.* **2021**, *20*, 841–850.

https://doi.org/10.1038/s41563-020-00893-1.

(12) Kwon, D. H.; Lee, J.; Artrith, N.; Kim, H.; Wu, L.; Lun, Z.; Tian, Y.; Zhu, Y.; Ceder, G. The Impact of Surface Structure Transformations on the Performance of Li-Excess Cation-Disordered Rocksalt Cathodes. *Cell Reports Phys. Sci.* **2020**, *1* (9), 100187. https://doi.org/10.1016/J.XCRP.2020.100187.

(13) Foley, E. E.; Wu, V. C.; Jin, W.; Cui, W.; Yoshida, E.; Manche, A.; Clément, R. J. Polymorphism in Weberite Na2Fe2F7 and Its Effects on Electrochemical Properties as a Na-Ion Cathode. *Chem. Mater.* **2023**, *35* (9), 3614–3627. https://doi.org/10.1021/ACS.CHEMMATER.3C00233.

(14) Ahn, J.; Giovine, R.; Wu, V. C.; Koirala, K. P.; Wang, C.; Clément, R. J.; Chen, G. Ultrahigh-Capacity Rocksalt Cathodes Enabled by Cycling-Activated Structural Changes. *Adv. Energy Mater.* **2023**. https://doi.org/10.1002/AENM.202300221.

(15) Clément, R. J.; Bruce, P. G.; Grey, C. P. Review-Manganese-Based P2-Type Transition Metal Oxides as Sodium-Ion Battery Cathode Materials. *Journal of the Electrochemical Society*. Electrochemical Society Inc. 2015, pp A2589–A2604. https://doi.org/10.1149/2.0201514jes.

(16) Rudola, A.; Rennie, A. J. R.; Heap, R.; Meysami, S. S.; Lowbridge, A.; Mazzali, F.; Sayers, R.; Wright, C. J.; Barker, J. Commercialisation of High Energy Density Sodium-Ion Batteries: Faradion's Journey and Outlook. *J. Mater. Chem. A* **2021**, *9* (13), 8279–8302. https://doi.org/10.1039/d1ta00376c.

(17) Yabuuchi, N.; Kajiyama, M.; Iwatate, J.; Nishikawa, H.; Hitomi, S.; Okuyama, R.; Usui, R.; Yamada, Y.; Komaba, S. P2-Type Nax[Fe1/2Mn1/2]O2 Made from Earth-Abundant Elements for Rechargeable Na Batteries. *Nat. Mater. 2012 116* **2012**, *11* (6), 512–517. https://doi.org/10.1038/nmat3309.

(18) Goodenough, J. B.; Hong, H. Y. P.; Kafalas, J. A. Fast Na+-Ion Transport in Skeleton Structures. *Mater. Res. Bull.* **1976**, *11* (2), 203–220. https://doi.org/10.1016/0025-5408(76)90077-5.

(19) Wu, V. C.; Giovine, R.; Foley, E. E.; Finzel, J.; Balasubramanian, M.; Sebti, E.; Mozur, E. M.; Kwon, A. H.; Clément, R. J. Unlocking New Redox Activity in Alluaudite Cathodes through Compositional Design. *Chem. Mater.* **2022**, *2022*, 50.

(20) Masquelier, C.; Croguennec, L. Polyanionic (Phosphates, Silicates, Sulfates) Frameworks as Electrode Materials for Rechargeable Li (or Na) Batteries. *Chem. Rev.* **2013**. https://doi.org/10.1021/cr3001862.

(21) Lu, Y.; Wang, L.; Cheng, J.; Goodenough, J. B. Prussian Blue: A New Framework of Electrode Materials for Sodium Batteries. *Chem. Commun.* **2012**, *48* (52), 6544–6546. https://doi.org/10.1039/c2cc31777j.

(22) Lim, C. Q. X.; Tan, Z. K. Prussian White with Near-Maximum Specific Capacity in Sodium-Ion Batteries. *ACS Appl. Energy Mater.* **2021**, *4* (6), 6214–6220. https://doi.org/10.1021/acsaem.1c00987.

(23) Tapia-Ruiz, N.; Armstrong, A. R.; Alptekin, H.; Amores, M. A.; Au, H.; Barker, J.; Boston, R.; Brant, W. R.; Brittain, J. M.; Chen, Y.; Chhowalla, M.; Choi, Y. S.; Costa, S. I. R.; Ribadeneyra, M. C.; Cussen, S. A.; Cussen, E. J.; David, W. I. F.; Desai, A. V.; Dickson, S. A. M.; Eweka, E. I.; Forero-Saboya, J. D.; Grey, C. P.; Griffin, J. M.; Gross, P.; Hua, X.; Irvine, J. T. S.; Johansson, P.; Jones, M. O.; Karlsmo, M.; Kendrick, E.; Kim, E.; Kolosov, O. V.; Li, Z.; Mertens, S. F. L.; Mogensen, R.; Monconduit, L.; Morris, R. E.; Naylor, A. J.; Nikman, S.; O'Keefe, C. A.; Ould, D. M. C.; Palgrave, R. G.; Poizot, P.; Ponrouch, A.; Renault, S.; Reynolds, E. M.; Rudola, A.; Sayers, R.; Scanlon, D. O.; Sen, S.; Seymour, V. R.; Silván, B.; Sougrati, M. T.; Stievano, L.; Stone, G. S.; Thomas, C. I.; Titirici, M. M.; Tong, J.; Wood, T. J.; Wright, D. S.; Younesi, R. 2021 Roadmap for Sodium-Ion Batteries. *J. Phys. Energy* **2021**, *3* (3), 031503. https://doi.org/10.1088/2515-7655/AC01EF.

(24) Barpanda, P.; Oyama, G.; Nishimura, S. I.; Chung, S. C.; Yamada, A. A 3.8-V Earth-Abundant Sodium Battery Electrode. *Nat. Commun. 2014 51* **2014**, *5* (1), 1–8. https://doi.org/10.1038/ncomms5358.

(25) Whittingham, M. S. Chemistry of Intercalation Compounds: Metal Guests in Chalcogenide Hosts. *Prog. Solid State Chem.* **1978**, *12* (1), 41–99. https://doi.org/10.1016/0079-6786(78)90003-1.

(26) U.S. Geological Survey. *Mineral Commodity Summaries 2023: U.S. Geological Survey*; 2023. https://doi.org/https://doi.org/10.3133/mcs2023.

(27) Lee, J.; Papp, J. K.; Clément, R. J.; Sallis, S.; Kwon, D.-H.; Shi, T.; Yang, W.; McCloskey, B. D.; Ceder, G. Mitigating Oxygen Loss to Improve the Cycling Performance of High Capacity Cation-Disordered Cathode Materials. *Nat. Commun.* **2017**, *8* (1), 981. https://doi.org/10.1038/s41467-017-01115-0.

(28) Clément, R. J.; Kitchaev, D.; Lee, J.; Gerbrand Ceder. Short-Range Order and Unusual Modes of Nickel Redox in a Fluorine-Substituted Disordered Rocksalt Oxide Lithium-Ion Cathode. *Chem. Mater.* **2018**, *30* (19), 6945–6956. https://doi.org/10.1021/acs.chemmater.8b03794.

(29) Huang, H.; Faulkner, T.; Barker, J.; Saidi, M. Y. Lithium Metal Phosphates, Power and Automotive Applications. *J. Power Sources* **2009**, *189* (1), 748–751. https://doi.org/10.1016/J.JPOWSOUR.2008.08.024.

(30) Recham, N.; Chotard, J.-N.; Dupont, L.; Delacourt, C.; Walker, W.; Armand, M.; Tarascon, J.-M. A 3.6 V Lithium-Based Fluorosulphate Insertion Positive Electrode for Lithium-Ion Batteries. *Nat. Mater.* **2010**, *9* (1), 68–74. https://doi.org/10.1038/nmat2590.

(31) Nishijima, M.; Gocheva, I. D.; Okada, S.; Doi, T.; Yamaki, J. ichi; Nishida, T. Cathode Properties of Metal Trifluorides in Li and Na Secondary Batteries. *J. Power Sources* **2009**, *190* (2), 558–562. https://doi.org/10.1016/j.jpowsour.2009.01.051.

(32) Dimov, N.; Nishimura, A.; Chihara, K.; Kitajou, A.; Gocheva, I. D.; Okada, S. Transition Metal NaMF3 Compounds as Model Systems for Studying the Feasibility of Ternary Li-M-F and Na-M-F Single Phases as Cathodes for Lithium-Ion and Sodium-Ion Batteries. *Electrochim. Acta* **2013**, *110*, 214–220. https://doi.org/10.1016/j.electacta.2013.05.103.

(33) Amatucci, G. G.; Pereira, N. Fluoride Based Electrode Materials for Advanced Energy Storage Devices. *J. Fluor. Chem.* **2007**, *128* (4), 243–262. https://doi.org/10.1016/j.jfluchem.2006.11.016.

(34) Lemoine, K.; Hémon-Ribaud, A.; Leblanc, M.; Lhoste, J.; Tarascon, J. M.; Maisonneuve, V. Fluorinated Materials as Positive Electrodes for Li- and Na-Ion Batteries. *Chem. Rev.* **2022**, *122* (18), 14405–14439. https://doi.org/10.1021/acs.chemrev.2c00247.

(35) Li, H.; Zhou, H. Enhancing the Performances of Li-Ion Batteries by Carbon-Coating: Present and Future. *Chem. Commun.* **2012**, *48* (9), 1201–1217. https://doi.org/10.1039/C1CC14764A.

(36) Badway, F.; Pereira, N.; Cosandey, F.; Amatucci, G. G. Carbon-Metal Fluoride Nanocomposites: Structure and Electrochemistry of FeF3:C. *J. Electrochem. Soc.* **2003**, *150* (9), A1209. https://doi.org/10.1149/1.1596162.

(37) Li, C.; Gu, L.; Tong, J.; Maier, J. Carbon Nanotube Wiring of Electrodes for High-Rate Lithium Batteries Using an Imidazolium-Based Ionic Liquid Precursor as Dispersant and Binder: A Case Study on Iron Fluoride Nanoparticles. *ACS Nano* **2011**, *5* (4), 2930–2938. https://doi.org/10.1021/nn1035608.

(38) Foley, E. E.; Wong, A.; Vincent, R. C.; Manche, A.; Zaveri, A.; Gonzalez-Correa, E.; Ménard, G.; Clément, R. J. Probing Reaction Processes and Reversibility in Earth-Abundant Na3FeF6 for Na-Ion Batteries. *Phys. Chem. Chem. Phys.* **2021**, *23* (36), 20052–20064. https://doi.org/10.1039/d1cp02763h.

(39) Ponrouch, A.; Cabana, J.; Dugas, R.; Slack, J. L.; Palacín, M. R. Electroanalytical Study of the Viability of Conversion Reactions as Energy Storage Mechanisms. *RSC Adv.* **2014**, *4* (68), 35988–35996. https://doi.org/10.1039/C4RA05189K.

(40) Wang, F.; Robert, R.; Chernova, N. A.; Pereira, N.; Omenya, F.; Badway, F.; Hua, X.; Ruotolo, M.; Zhang, R.; Wu, L.; Volkov, V.; Su, D.; Key, B.; Stanley Whittingham, M.; Grey, C. P.; Amatucci, G. G.; Zhu, Y.; Graetz, J. Conversion Reaction Mechanisms in Lithium Ion Batteries: Study of the Binary Metal Fluoride Electrodes. *J. Am. Chem. Soc.* **2011**, *133* (46), 18828–18836. https://doi.org/10.1021/ja206268a.

(41) He, K.; Zhou, Y.; Gao, P.; Wang, L.; Pereira, N.; Amatucci, G. G.; Nam, K. W.; Yang, X. Q.; Zhu, Y.; Wang, F.; Su, D. Sodiation via Heterogeneous Disproportionation in FeF2 Electrodes for Sodium-Ion Batteries. *ACS Nano* **2014**, *8* (7), 7251–7259. https://doi.org/10.1021/nn502284y.

(42) Ni, D.; Fang, L.; Sun, W.; Shi, B.; Chen, X.; Li, H.; Wang, Z.; Sun, K. FeF2@MHCS Cathodes with High Capacity and Fast Sodium Storage Based on Nanostructure Construction. *ACS Appl. Energy Mater.* **2020**, *3* (11), 10340–10348. https://doi.org/10.1021/acsaem.0c00876.

(43) Zheng, Y.; Hwang, J.; Matsumoto, K.; Hagiwara, R. Electrochemical and Structural Behavior of Trirutile-Derived FeF3 during Sodiation and Desodiation. *ACS Appl. Energy Mater.* **2022**, *5* (3), 3137–3145. https://doi.org/10.1021/ACSAEM.1C03756/ASSET/IMAGES/LARGE/AE1C03756_0007.JPEG.

(44) Arai, H.; Okada, S.; Sakurai, Y.; Yamaki, J. I. Cathode Performance and Voltage Estimation of Metal Trihalides. *J. Power Sources* **1997**, *68* (2), 716–719. https://doi.org/10.1016/S0378-7753(96)02580-3.

(45) Kitajou, A.; Ishado, Y.; Yamashita, T.; Momida, H.; Oguchi, T.; Okada, S. Cathode Properties of Perovskite-Type NaMF3 (M = Fe, Mn, and Co) Prepared by Mechanical Ball Milling for Sodium-Ion Battery. *Electrochim. Acta* **2017**, *245*, 424–429. https://doi.org/10.1016/J.ELECTACTA.2017.05.153.

(46) Gocheva, I. D.; Nishijima, M.; Doi, T.; Okada, S.; Yamaki, J. ichi; Nishida, T. Mechanochemical Synthesis of NaMF3 (M = Fe, Mn, Ni) and Their Electrochemical Properties as Positive Electrode Materials for Sodium Batteries. *J. Power Sources* **2009**, *187* (1), 247–252. https://doi.org/10.1016/j.jpowsour.2008.10.110.

(47) Park, H.; Lee, Y.; Cho, M.-K.; Kang, J.; Ko, W.; Jung, Y. H.; Jeon, T.-Y.; Hong, J.; Kim, H.; Myung, S.-T.; Kim, J. Na2Fe2F7: A Fluoride-Based Cathode for High Power and Long Life Na-Ion Batteries. *Energy Environ. Sci* **2021**, *14*, 1469–1479. https://doi.org/10.1039/d0ee02803g.

(48) Kang, J.; Ahn, J.; Park, H.; Ko, W.; Lee, Y.; Lee, S.; Lee, S.; Jung, S.-K.; Kim, J.; Kang, J.; Ahn, J.; Park, H.; Ko, W.; Lee, Y.; Lee, S.; Kim, J.; Jung, S.-K. Highly Stable Fe2+/Ti3+-Based Fluoride Cathode Enabling Low-Cost and High-Performance Na-Ion Batteries. *Adv. Funct. Mater.* **2022**, *32* (29), 2201816. https://doi.org/10.1002/ADFM.202201816.

(49) Liao, J.; Han, J.; Xu, J.; Du, Y.; Sun, Y.; Duan, L.; Zhou, X. Scalable Synthesis of Na2MVF7 (M = Mn, Fe, and Co) as High- Performance Cathode Materials for Sodium-Ion Batteries. *Chem. Commun.* **2021**, *57*, 11497–11500. https://doi.org/10.1039/D1CC04449D.

(50) Pawley, G. S.; IUCr. Unit-Cell Refinement from Powder Diffraction Scans.

urn:issn:0021-8898 **1981**, *14* (6), 357–361. https://doi.org/10.1107/S0021889881009618.

(51) Rietveld, H. M.; IUCr. A Profile Refinement Method for Nuclear and Magnetic Structures. *urn:issn:0021-8898* **1969**, *2* (2), 65–71. https://doi.org/10.1107/S0021889869006558.

(52) Toby, B. H. R Factors in Rietveld Analysis: How Good Is Good Enough? . *Powder Diffr.* **2006**, *21* (1), 67–70. https://doi.org/10.1154/1.2179804.

(53) Keeler, J. *Understanding NMR Spectroscopy, 2nd Edition*; Wiley, 2002.

(54) Duer, M. J. *Solid-State NMR Spectroscopy Principles and Applications*; Blackwell Science Ltd, 2002.

(55) Harris, R. K.; Becker, E. D.; Cabral de Menezes, S. M.; Goodfellow, R.; Granger, P. NMR Nomenclacture. Nuclear Spin Properties and Convetions for Chemical Shifts. *Pure Appl. Chem.* **2001**, *73* (11), 1795–1818.

(56) Watts, A. Solid-State NMR in Drug Design and Discovery for Membrane-Embedded Targets. *Nat. Rev. Drug Discov.* **2005**, *4* (7), 555–568. https://doi.org/10.1038/nrd1773.

(57) Bertini, I.; Luchinat, C. Chapter 3 Relaxation. *Coord. Chem. Rev.* **1996**, *150*, 77–110.

(58) Peng, L.; Clément, R. J.; Lin, M.; Yang, Y. Chapter 1: NMR Principles of Paramagnetic Materials. In *NMR and MRI of Electrochemical Energy Storage Materials and Devices*; Yang, Y., Fu, R., Huo, H., Eds.; Royal Society of Chemistry, 2021. https://doi.org/10.1039/9781839160097-00001.

(59) Pell, A. J.; Pintacuda, G.; Grey, C. P. Paramagnetic NMR in Solution and the Solid State. *Prog. Nucl. Magn. Reson. Spectrosc.* **2019**, *111*, 1–271. https://doi.org/10.1016/J.PNMRS.2018.05.001.

(60) Kim, J.; Middlemiss, D. S.; Chernova, N. A.; Zhu, B. Y. X.; Masquelier, C.; Grey, C. P. Linking Local Environments and Hyperfine Shifts: A Combined Experimental and Theoretical 31P and 7Li Solid-State NMR Study of Paramagnetic Fe(III) Phosphates. *J. Am. Chem. Soc.* **2010**, *132* (47), 16825–16840. https://doi.org/10.1021/ja102678r.

(61) Clément, R. J.; Pell, A. J.; Middlemiss, D. S.; Strobridge, F. C.; Miller, J. K.; Whittingham, M. S.; Emsley, L.; Grey, C. P.; Pintacuda, G. Spin-Transfer Pathways in Paramagnetic Lithium Transition-Metal Phosphates from Combined Broadband Isotropic Solid-State MAS NMR Spectroscopy and DFT Calculations. *J. Am. Chem. Soc.* **2012**, *134* (41), 17178–17185. https://doi.org/10.1021/ja306876u.

(62) Bertini, I.; Luchinat, C.; Parigi, G. Magnetic Susceptibility in Paramagnetic NMR. *Prog. Nucl. Magn. Reson. Spectrosc.* **2002**, *40* (3), 249–273. https://doi.org/10.1016/S0079-6565(02)00002-X.

(63) Middlemiss, D. S.; Ilott, A. J.; Clément, R. J.; Strobridge, F. C.; Grey, C. P. Density Functional Theory-Based Bond Pathway Decompositions of Hyperfine Shifts: Equipping Solid-State NMR to Characterize Atomic Environments in Paramagnetic Materials. *Chem. Mater.* **2013**, *25* (9), 1723–1734. https://doi.org/10.1021/cm400201t.

(64) Delmas, C.; Carlier, D.; Ceder, G.; Ménétrier, M.; Grey, C. P. Understanding the NMR Shifts in Paramagnetic Transition Metal Oxides Using Density Functional Theory Calculations. *Phys. Rev. B* **2003**, *67* (17), 174103. https://doi.org/10.1103/PhysRevB.67.174103.

(65) Goodenough, J. Jahn-Teller Phenomena. *Phys. Rev.* **1955**, *100*, 564.

(66) Goodenough, J. B. An Interpretation of the Magnetic Properties of the Perovskite-Type Mixed Crystals La1−xSrxCoO3−λ. *J. Phys. Chem. Solids* **1958**, *6* (2–3), 287–297. https://doi.org/10.1016/0022-3697(58)90107-0.

(67) Kanamori, J. Theory of the Magnetic Properties of Ferrous and Cobaltous Oxides, I. *Prog. Theor. Phys.* **1957**, *17* (2), 177–196. https://doi.org/10.1143/PTP.17.177.

(68) Pell, A. J.; Pintacuda, G. Broadband Solid-State MAS NMR of Paramagnetic Systems. *Prog. Nucl. Magn. Reson. Spectrosc.* **2015**, *84–85*, 33–72. https://doi.org/10.1016/j.pnmrs.2014.12.002.

(69) Pigliapochi, R.; Pell, A. J.; Seymour, I. D.; Grey, C. P.; Ceresoli, D.; Kaupp, M. DFT Investigation of the Effect of Spin-Orbit Coupling on the NMR Shifts in Paramagnetic Solids. *Phys. Rev. B* **2017**, *95*, 54412. https://doi.org/10.1103/PhysRevB.95.054412.

(70) Kentgens, A. P. M. A Practical Guide to Solid-State NMR of Half-Integer Quadrupolar Nuclei with Some Applications to Disordered Systems. *Geoderma* **1997**, *80* (3–4), 271–306. https://doi.org/10.1016/S0016-7061(97)00056-6.

(71) Koller, H.; Engelhardt, G.; Kentgens, A. P. M.; Sauer, J. 23Na NMR Spectroscopy of Solids: Interpretation of Quadrupole Interaction Parameters and Chemical Shifts. *J. Physial Chem.* **1994**, *98* (6), 1544–1551. https://doi.org/10.1021/j100057a004.

(72) Wasylishen, R. E.; Ashbrook, S. E.; Wimperis, S. *NMR of Quadrupolar Nuclei in Solid Materials*; 2012.

(73) Grey, C. P.; Dupré, N. NMR Studies of Cathode Materials for Lithium-Ion Rechargeable Batteries. **2004**. https://doi.org/10.1021/cr020734p.

(74) Freude, D.; Haase, J.; Klinowski, J.; Carpenter, T. A.; Ronikier, G. NMR Line Shifts Caused by the Second-Order Quadrupolar Interaction. *Chem. Phys. Lett.* **1985**, *119* (4), 365–367. https://doi.org/10.1016/0009-2614(85)80434-6.

(75) O'Dell, L. A.; Rossini, A. J.; Schurko, R. W. Acquisition of Ultra-Wideline NMR Spectra from Quadrupolar Nuclei by Frequency Stepped WURST-QCPMG. *Chem. Phys. Lett.* **2009**, *468* (4–6), 330–335. https://doi.org/10.1016/j.cplett.2008.12.044.

(76) Pell, A. J.; Clément, R. J.; Grey, C. P.; Emsley, L.; Pintacuda, G. Frequency-Stepped Acquisition in Nuclear Magnetic Resonance Spectroscopy under Magic Angle Spinning. *J. Chem. Phys.* **2013**, *138* (11), 114201. https://doi.org/10.1063/1.4795001.

(77) Sananes, M. T.; Tuel, A.; Hutchings, G. J.; Volta, J. C. Characterization of Different Precursors and Activated Vanadium Phosphate Catalysis by 31P NMR Spin Echo Mapping. *J. Catal.* **1994**, *148* (1), 395–398. https://doi.org/10.1006/jcat.1994.1221.

(78) Massiot, D.; Farnan, I.; Gautier, N.; Trumeau, D.; Trokiner, A.; Coutures, J. P. 71Ga and 69Ga Nuclear Magnetic Resonance Study of β-Ga2O3: Resolution of Four- and Six-Fold Coordinated Ga Sites in Static Conditions. *Solid State Nucl. Magn. Reson.* **1995**, *4* (4), 241–248. https://doi.org/10.1016/0926-2040(95)00002-8.

(79) Hung, I.; Zhou, L.; Pourpoint, F.; Grey, C. P.; Gan, Z. Isotropic High Field NMR Spectra of Li-Ion Battery Materials with Anisotropy > 1 MHz. *J. Am. Chem. Soc.* **2012**, *134* (4), 1898–1901. https://doi.org/10.1021/ja209600m.

(80) Frydman, L.; Harwood, J. S. Isotropic Spectra of Half-Integer Quadrupolar Spins from Bidimensional Magic-Angle Spinning NMR. *J. Am. Chem. Soc.* **1995**, *117* (19), 5367–5368. https://doi.org/10.1021/JA00124A023/SUPPL_FILE/JA5367.PDF.

(81) Medek, A.; Harwood, J. S.; Frydman, L. Multiple-Quantum Magic-Angle Spinning NMR: A New Method for the Study of Quadrupolar Nuclei in Solids. *J. Am. Chem. Soc* **1995**, *117*, 12779–12787.

(82) Hahn, E. L. Spin Echoes. *Phys. Rev* **1950**, *80* (4), 580–594.

(83) Zhou, L.; Leskes, M.; Liu, T.; Grey, C. P. Probing Dynamic Processes in Lithium-Ion Batteries by in Situ NMR Spectroscopy: Application to Li1.08Mn1.92O4 Electrodes. *Angew. Chemie - Int. Ed.* **2015**, *54* (49), 14782–14786. https://doi.org/10.1002/anie.201507632.

(84) Dixon, W. T. Spinning-sideband-free and Spinning-sideband-only NMR Spectra in Spinning Samples. *J. Chem. Phys.* **1998**, *77* (4), 1800. https://doi.org/10.1063/1.444076.

(85) Antzutkin, O. N. Sideband Manipulation in Magic-Angle-Spinning Nuclear Magnetic Resonance. *Prog. Nucl. Magn. Reson. Spectrosc.* **1999**, *35* (3), 203–266. https://doi.org/10.1016/S0079-6565(99)00010-2.

(86) Mössbauer, R. L. Kernresonanzabsorption von Gammastrahlung in Ir191. *Naturwissenschaften* **1958**, *45* (22), 538–539. https://doi.org/10.1007/BF00632050/METRICS.

(87) Gütlich, P. Fifty Years of Mössbauer Spectroscopy in Solid State Research - Remarkable Achievements, Future Perspectives. *Z. Anorg. Allg. Chem.* **2012**, *638* (1), 15–43. https://doi.org/10.1002/zaac.201100416.

(88) Drago, R. S. *Physical Methods in Inorganic Chemistry*; 1992; Vol. 2nd. https://doi.org/10.1016/S0070-4571(08)70018-9.

(89) Lamb, W. E. Capture of Neutrons by Atoms in a Crystal. *Phys. Rev.* **1939**, *55* (2), 190. https://doi.org/10.1103/PhysRev.55.190.

(90) Tzara, C. Diffusion Des Photons Sur Les Atomes et Les Noyaux Dans Les Cristaux. *J. Phys. le Radium* **1961**, *22* (5), 303–307. https://doi.org/10.1051/JPHYSRAD:01961002205030300.

(91) Mugiraneza, S.; Hallas, A. M. Tutorial: A Beginner's Guide to Interpreting Magnetic Susceptibility Data with the Curie-Weiss Law. *Commun. Phys. 2022 51* **2022**, *5* (1), 1–12. https://doi.org/10.1038/s42005-022-00853-y.

(92) Mozur, E. M.; Seshadri, R. Methods and Protocols: Practical Magnetic Measurement. *Chem. Mater.* **2023**. https://doi.org/10.1021/ACS.CHEMMATER.3C00297.

(93) Bain, G. A.; Berry, J. F. Diamagnetic Corrections and Pascal's Constants. *J. Chem. Educ.* **2008**, *85* (4), 532–536. https://doi.org/10.1021/ED085P532.

(94) Schrödinger, E. An Undulatory Theory of the Mechanics of Atoms and Molecules. *Phys. Rev.* **1926**, *28* (6), 1049–1070. https://doi.org/10.1103/PhysRev.28.1049.

(95) Born, M.; Oppenheimer, R. Zur Quantentheorie Der Molekeln,. *Ann. Phys.* **1927**, *389* (20), 457–484.

(96) Hohenberg, P.; Kohn, W. Inhomogeneous Electron Gas. *Phys. Rev.* **1964**, *136* (3B), B864. https://doi.org/10.1103/PHYSREV.136.B864/FIGURE/1/THUMB.

(97) Kohn, W.; Sham, L. J. Self-Consistent Equations Including Exchange and Correlation Effects. *Phys. Rev.* **1965**, *140* (4A), A1133. https://doi.org/10.1103/PHYSREV.140.A1133/FIGURE/1/THUMB.

(98) Payne, M. C.; Teter, M. P.; Allan, D. C.; Arias, T. A.; Joannopoulos, J. D. Iterative

Minimization Techniques for Ab Initio Total-Energy Calculations: Molecular Dynamics and Conjugate Gradients. *Rev. Mod. Phys.* **1992**, *64* (4), 1045–1097. https://doi.org/10.1103/RevModPhys.64.1045.

(99) Anisimov, V. I.; Zaanen, J.; Andersen, O. K. Band Theory and Mott Insulators: Hubbard U Instead of Stoner I. *Phys. Rev. 8*, 15–1991.

(100) Anisimov, V. I.; Solovyev, I. V; Korotin, M. A.; Czyzyk, M. T.; Sawatzky, G. A. Density-Functional Theory and Nio Photoemission Spectra E =ELDER +-g U(Ll Np)(Tl ' Lip). *Phys. Rev. B* **1993**, *48* (23).

(101) Liechtenstein, A. I.; Anisimov, V. I.; Zaanen, J. Density-Functional Theory and Strong Interactions: Orbital Ordering in Mott-Hubbard Insulators. *Phys. Rev. B* **1995**, *52*, 15.

(102) Zhou, F.; Cococcioni, M.; Marianetti, C. A.; Morgan, D.; Ceder, G. First-Principles Prediction of Redox Potentials in Transition-Metal Compounds with LDA + U. *Phys. Rev. B - Condens. Matter Mater. Phys.* **2004**, *70* (23), 1–8. https://doi.org/10.1103/PHYSREVB.70.235121/FIGURES/6/MEDIUM.

(103) Franchini, C.; Podloucky, R.; Paier, J.; Marsman, M.; Kresse, G. Ground-State Properties of Multivalent Manganese Oxides: Density Functional and Hybrid Density Functional Calculations. *Phys. Rev. B - Condens. Matter Mater. Phys.* **2007**, *75* (19), 195128. https://doi.org/10.1103/PHYSREVB.75.195128/FIGURES/5/MEDIUM.

(104) Becke, A. D. A New Mixing of Hartree-Fock and Local Density-Functional Theories. *J. Chem. Phys.* **1993**, *98* (2), 1372–1377. https://doi.org/10.1063/1.464304.

(105) Becke, A. D. Density-functional Thermochemistry. III. The Role of Exact Exchange. *J. Chem. Phys.* **1993**, *98* (7), 5648–5652. https://doi.org/10.1063/1.464913.

(106) Kresse, G.; Furthmüller, J. Efficient Iterative Schemes for *Ab Initio* Total-Energy Calculations Using a Plane-Wave Basis Set. *Phys. Rev. B* **1996**, *54* (16), 11169. https://doi.org/10.1103/PhysRevB.54.11169.

(107) Kresse, G.; Furthmüller, J. Efficiency of Ab-Initio Total Energy Calculations for Metals and Semiconductors Using a Plane-Wave Basis Set. *Comput. Mater. Sci.* **1996**, *6* (1), 15–50. https://doi.org/10.1016/0927-0256(96)00008-0.

(108) Lun, Z.; Ouyang, B.; Kwon, D. H. D.-H.; Ha, Y.; Foley, E. E. E. E.; Huang, T. Y. T.-Y.; Cai, Z.; Kim, H. H.; Balasubramanian, M.; Sun, Y.; Huang, J.; Tian, Y.; Kim, H. H.; McCloskey, B. D. B. D.; Yang, W.; Clément, R. J. R. J.; Ji, H.; Ceder, G. Cation-Disordered Rocksalt-Type High-Entropy Cathodes for Li-Ion Batteries. *Nat. Mater.* **2020**, *20*, 1–8. https://doi.org/10.1038/s41563-020-00816-0.

(109) Ji, H.; Kitchaev, D. A. D. A.; Lun, Z.; Kim, H.; Foley, E.; Kwon, D.-H. D.-H.; Tian, Y.;

Balasubramanian, M.; Bianchini, M.; Cai, Z.; Le, R.; Clément, J. C.; Kim, J. C. J. C.; Ceder, G.; Clément, R. J.; Kim, J. C. J. C.; Ceder, G. Computational Investigation and Experimental Realization of Disordered High-Capacity Li-Ion Cathodes Based on Ni Redox. *Chem. Mater* **2019**, *31* (7), 2431–2442. https://doi.org/10.1021/acs.chemmater.8b05096.

(110) Yue, Y.; Li, N.; Li, L.; Foley, E. E.; Fu, Y.; Battaglia, V. S.; Le, R.; Clément, J. C.; Wang, C.; Tong, W. Redox Behaviors in a Li-Excess Cation-Disordered Mn–Nb–O–F Rocksalt Cathode. *Chem. Mater* **2020**, *32*, 4490–4498. https://doi.org/10.1021/acs.chemmater.9b05221.

(111) Ji, H.; Wu, J.; Cai, Z.; Liu, J.; Kwon, D.-H.; Kim, H.; Urban, A.; Papp, J. K.; Foley, E.; Tian, Y.; Balasubramanian, M.; Kim, H.; Clément, R. J.; McCloskey, B. D.; Yang, W.; Ceder, G. Ultrahigh Power and Energy Density in Partially Ordered Lithium-Ion Cathode Materials. *Nat. Energy* **2020**, *5* (3), 1–9. https://doi.org/10.1038/s41560-020-0573-1.

(112) Cai, Z.; Ji, H.; Ha, Y.; Liu, J.; Kwon, D. H.; Zhang, Y.; Urban, A.; Foley, E. E.; Giovine, R.; Kim, H.; Lun, Z.; Huang, T. Y.; Zeng, G.; Chen, Y.; Wang, J.; McCloskey, B. D.; Balasubramanian, M.; Clément, R. J.; Yang, W.; Ceder, G. Realizing Continuous Cation Order-to-Disorder Tuning in a Class of High-Energy Spinel-Type Li-Ion Cathodes. *Matter* **2021**, *4* (12), 3897–3916. https://doi.org/10.1016/J.MATT.2021.10.013.

(113) Clément, R. J.; Lun, Z.; Ceder, G. Cation-Disordered Rocksalt Transition Metal Oxides for High Energy Lithium-Ion Cathodes. *Energy Environ. Sci.* **2020**, *13* (2), 1–46. https://doi.org/10.1039/c9ee02803j.

(114) Urban, A.; Abdellahi, A.; Dacek, S.; Artrith, N.; Ceder, G. Electronic-Structure Origin of Cation Disorder in Transition-Metal Oxides. *Phys. Rev. Lett.* **2017**, *119* (17), 176402. https://doi.org/10.1103/PhysRevLett.119.176402.

(115) Lee, J.; Kitchaev, D. A.; Kwon, D.-H.; Lee, C.-W.; Papp, J. K.; Liu, Y.-S.; Lun, Z.; Clément, R. J.; Shi, T.; McCloskey, B. D.; Guo, J.; Balasubramanian, M.; Ceder, G. Reversible Mn2+/Mn4+ Double Redox in Lithium-Excess Cathode Materials. *Nature* **2018**, *556* (7700), 185–190. https://doi.org/10.1038/s41586-018-0015-4.

(116) Lee, J.; Urban, A.; Li, X.; Su, D.; Hautier, G.; Ceder, G. Unlocking the Potential of Cation-Disordered Oxides for Rechargeable Lithium Batteries. *Science* **2014**, *343*, 519–521. https://doi.org/10.1126/science.1122152.

(117) Hoshino, S.; Glushenkov, A. M.; Ichikawa, S.; Ozaki, T.; Inamasu, T.; Yabuuchi, N. Reversible Three-Electron Redox Reaction of Mo3+/Mo6+ for Rechargeable Lithium Batteries. *ACS Energy Lett.* **2017**, *2* (4), 733–738. https://doi.org/10.1021/ACSENERGYLETT.7B00037/ASSET/IMAGES/LARGE/NZ-2017-00037E_0003.JPEG.

(118) Yabuuchi, N.; Takeuchi, M.; Nakayama, M.; Shiiba, H.; Ogawa, M.; Nakayama, K.; Ohta, T.; Endo, D.; Ozaki, T.; Inamasu, T.; Sato, K.; Komaba, S. High-Capacity Electrode Materials for Rechargeable Lithium Batteries: Li3NbO4-Based System with Cation-Disordered Rocksalt Structure. *Proc. Natl. Acad. Sci. U. S. A.* **2015**, *112* (25), 7650–7655. https://doi.org/10.1073/PNAS.1504901112/SUPPL_FILE/PNAS.1504901112.SAPP.PDF.

(119) Ji, H.; Urban, A.; Kitchaev, D. A.; Kwon, D.-H.; Artrith, N.; Ophus, C.; Huang, W.; Cai, Z.; Shi, T.; Kim, J. C.; Kim, H.; Ceder, G. Hidden Structural and Chemical Order Controls Lithium Transport in Cation-Disordered Oxides for Rechargeable Batteries. *Nat. Commun.* **2019**, *10* (1), 592. https://doi.org/10.1038/s41467-019-08490-w.

(120) Wu, V. C.; Evans, H. A.; Giovine, R.; Preefer, M. B.; Ong, J.; Yoshida, E.; Cabelguen, P.-E. P.-E.; Clément, R. J.; Wu, V. C.; Giovine, R.; Ong, J.; Yoshida, E.; Clément, R. J.; Evans, H. A.; Preefer, M. B.; Cabelguen, P.-E. P.-E. Rapid and Energy-Efficient Synthesis of Disordered Rocksalt Cathodes.Pdf. *Adv. Energy Mater.* **2023**, *13* (10), 2203860. https://doi.org/10.1002/AENM.202203860.

(121) Van der Ven, A.; Ceder, G. Lithium Diffusion Mechanisms in Layered Intercalation Compounds. *J. Power Sources* **2001**, *97–98*, 529–531. https://doi.org/10.1016/S0378-7753(01)00638-3.

(122) Urban, A.; Lee, J.; Ceder, G.; Urban, A.; Lee, J.; Ceder, G. The Configurational Space of Rocksalt-Type Oxides for High-Capacity Lithium Battery Electrodes. *Adv. Energy Mater.* **2014**, *4* (13), 1400478. https://doi.org/10.1002/aenm.201400478.

(123) Richards, W. D.; Dacek, S. T.; Kitchaev, D. A.; Ceder, G. Fluorination of Lithium-Excess Transition Metal Oxide Cathode Materials. *Adv. Energy Mater.* **2018**, *8* (5), 1701533. https://doi.org/10.1002/aenm.201701533.

(124) Seo, D. H.; Lee, J.; Urban, A.; Malik, R.; Kang, S.; Ceder, G. The Structural and Chemical Origin of the Oxygen Redox Activity in Layered and Cation-Disordered Li-Excess Cathode Materials. *Nat. Chem. 2016 87* **2016**, *8* (7), 692–697. https://doi.org/10.1038/nchem.2524.

(125) Yeh, J. W.; Chen, S. K.; Lin, S. J.; Gan, J. Y.; Chin, T. S.; Shun, T. T.; Tsau, C. H.; Chang, S. Y. Nanostructured High-Entropy Alloys with Multiple Principal Elements: Novel Alloy Design Concepts and Outcomes. *Adv. Eng. Mater.* **2004**, *6* (5), 299–303. https://doi.org/10.1002/ADEM.200300567.

(126) Oses, C.; Toher, C.; Curtarolo, S. High-Entropy Ceramics. *Nat. Rev. Mater. 2020 54* **2020**, *5* (4), 295–309. https://doi.org/10.1038/s41578-019-0170-8.

(127) Kan, W. H.; Deng, B.; Xu, Y.; Shukla, A. K.; Bo, T.; Zhang, S.; Liu, J.; Pianetta, P.; Wang,

B. T.; Liu, Y.; Chen, G. Understanding the Effect of Local Short-Range Ordering on Lithium Diffusion in Li1.3Nb0.3Mn0.4O2 Single-Crystal Cathode. *Chem* **2018**, *4* (9), 2108–2123. https://doi.org/10.1016/j.chempr.2018.05.008.

(128) Ouyang, B.; Artrith, N.; Lun, Z.; Jadidi, Z.; Kitchaev, D. A.; Ji, H.; Urban, A.; Ceder, G. Effect of Fluorination on Lithium Transport and Short-Range Order in Disordered-Rocksalt-Type Lithium-Ion Battery Cathodes. *Adv. Energy Mater.* **2020**, *10* (10), 1903240. https://doi.org/10.1002/AENM.201903240.

(129) Lun, Z.; Ouyang, B.; Kitchaev, D. A.; Clément, R. J.; Papp, J. K.; Balasubramanian, M.; Tian, Y.; Lei, T.; Shi, T.; McCloskey, B. D.; Lee, J.; Ceder, G. Improved Cycling Performance of Li-Excess Cation-Disordered Cathode Materials upon Fluorine Substitution. *Adv. Energy Mater.* **2019**, *9* (2), 1802959. https://doi.org/10.1002/aenm.201802959.

(130) Kitchaev, D. A.; Lun, Z.; Richards, W. D.; Ji, H.; Clément, R. J.; Balasubramanian, M.; Kwon, D.-H. H.; Dai, K.; Papp, J. K.; Lei, T.; McCloskey, B. D.; Yang, W.; Lee, J.; Ceder, G.; Le, R.; Clé, J.; Balasubramanian, M.; Kwon, D.-H. H.; Dai, K.; Papp, J. K.; Lei, T.; McCloskey, B. D.; Yang, W.; Lee, J.; Ceder, G. Design Principles for High Transition Metal Capacity in Disordered Rocksalt Li-Ion Cathodes †. *Energy Environ. Sci.* **2018**, *11* (8), 2159–2171. https://doi.org/10.1039/c8ee00816g.

(131) Chen, D.; Kan, W. H.; Chen, G. Understanding Performance Degradation in Cation-Disordered Rock-Salt Oxide.Pdf. *Adv. Energy Mater.* **2019**, *9*, 1901255.

(132) Lun, Z.; Ouyang, B.; Cai, Z.; Clément, R. J.; Kwon, D. H.; Huang, J.; Papp, J. K.; Balasubramanian, M.; Tian, Y.; McCloskey, B. D.; Ji, H.; Kim, H.; Kitchaev, D. A.; Ceder, G. Design Principles for High-Capacity Mn-Based Cation-Disordered Rocksalt Cathodes. *Chem* **2020**, *6* (1), 153–168. https://doi.org/10.1016/j.chempr.2019.10.001.

(133) Manthiram, A.; Chemelewski, K.; Lee, E. S. A Perspective on the High-Voltage LiMn 1.5 Ni 0.5 O 4 Spinel Cathode for Lithium-Ion Batteries. *Energy Environ. Sci.* **2014**, *7* (4), 1339–1350. https://doi.org/10.1039/C3EE42981D.

(134) Gummow, R. J.; de Kock, A.; Thackeray, M. M. Improved Capacity Retention in Rechargeable 4 V Lithium/Lithium-Manganese Oxide (Spinel) Cells. *Solid State Ionics* **1994**, *69* (1), 59–67. https://doi.org/10.1016/0167-2738(94)90450-2.

(135) Lee, Y. J.; Wang, F.; Grey, C. P. 6Li and 7Li MAS NMR Studies of Lithium Manganate Cathode Materials. *J. Am. Chem. Soc.* **1998**, *120* (48), 12601–12613. https://doi.org/10.1021/ja9817794.

(136) Reddy, M. A.; Fichtner, M. Fluoride Cathodes for Secondary Batteries. In *Advanced Fluoride-Based Materials for Energy Conversion*; Elsevier Inc., 2015; pp 51–76. https://doi.org/10.1016/B978-0-12-800679-5.00003-8.

(137) Doe, R. E.; Persson, K. A.; Meng, Y. S.; Ceder, G. First-Principles Investigation of the Li-Fe-F Phase Diagram and Equilibrium and Nonequilibrium Conversion Reactions of Iron Fluorides with Lithium. *Chem. Mater.* **2008**, *20* (16), 5274–5283. https://doi.org/10.1021/cm801105p.

(138) Chevrier, V. L.; Hautier, G.; Shyue, †; Ong, P.; Doe, R. E.; Ceder, G. First-Principles Study of Iron Oxyfluorides and Lithiation of FeOF. *Phys. Rev. B* **2013**, *87*, 94118. https://doi.org/10.1103/PhysRevB.87.094118.

(139) Shakoor, R. A.; Lim, S. Y.; Kim, H.; Nam, K. W.; Kang, J. K.; Kang, K.; Choi, J. W. Mechanochemical Synthesis and Electrochemical Behavior of Na3FeF6 in Sodium and Lithium Batteries. *Solid State Ionics* **2012**, *218*, 35–40. https://doi.org/10.1016/j.ssi.2012.05.002.

(140) Guo, H.; Liu, W.; Qin, M.; Tang, J.; Cheng, J.; Ling, Y. Room-Temperature Liquid-Phase Synthesis of Na3FeF6 and Its Lithium/Sodium Storage Properties. *Mater. Res. Express* **2019**, *6*, 085507. https://doi.org/10.1088/2053-1591/ab1c0f.

(141) Liu, W.; Wang, W.; Qin, M.; Shen, B. Successive Synthesis and Electrochemical Properties of Na3FeF6 and NaFeF3/C Cathode Materials for Lithium-Ion and Sodium-Ion Batteries. *Ceram. Int.* **2020**, *46* (8), 11436–11440. https://doi.org/10.1016/j.ceramint.2020.01.059.

(142) Levin, E. E.; Grebenkemper, J. H.; Pollock, T. M.; Seshadri, R. Protocols for High Temperature Assisted-Microwave Preparation of Inorganic Compounds. *Chem. Mater.* **2019**, *31* (18), 7151–7159. https://doi.org/10.1021/acs.chemmater.9b02594.

(143) Toby, B. H.; Von Dreele, R. B. GSAS-II: The Genesis of a Modern Open-Source All Purpose Crystallography Software Package. *J. Appl. Crystallogr.* **2013**, *46* (2), 544–549. https://doi.org/10.1107/S0021889813003531.

(144) Prescher, C.; McCammon, C.; Dubrovinsky, L. MossA: A Program for Analyzing Energy-Domain Mössbauer Spectra from Conventional and Synchrotron Sources. *J. Appl. Crystallogr.* **2012**, *45* (2), 329–331. https://doi.org/10.1107/S0021889812004979.

(145) Van Attekum, P. M. T. M.; Wertheim, G. K. Excitonic Effects in Core-Hole Screening. *Phys. Rev. Lett.* **1979**, *43* (25), 1896–1898. https://doi.org/10.1103/PhysRevLett.43.1896.

(146) Dovesi, R.; Erba, A.; Orlando, R.; Zicovich-Wilson, C. M.; Civalleri, B.; Maschio, L.; Rérat, M.; Casassa, S.; Baima, J.; Salustro, S.; Kirtman, B. CRYSTAL17 User's Manual. *WIREs Comput. Mol. Sci.* **2018**, *e1360*.

(147) Dovesi, R.; Erba, A.; Orlando, R.; Zicovich-Wilson, C. M.; Civalleri, B.; Maschio, L.; Rérat, M.; Casassa, S.; Baima, J.; Salustro, S.; Kirtman, B. Quantum-Mechanical

Condensed Matter Simulations with CRYSTAL. *Wiley Interdiscip. Rev. Comput. Mol. Sci.* **2018**, *8* (4), e1360. https://doi.org/10.1002/wcms.1360.

(148) Lee, C.; Yang, W.; Parr, R. G. Development of the Colle-Salvetti Correlation-Energy Formula into a Functional of the Electron Density. *Phys. Rev. B* **1988**, *37* (2), 785–789. https://doi.org/10.1103/PhysRevB.37.785.

(149) Vosko, S. H.; Wilk, L.; Nusair, M. Accurate Spin-Dependent Electron Liquid Correlation Energies for Local Spin Density Calculations: A Critical Analysis. *Can. J. Phys.* **1980**, *58* (8), 1200–1211. https://doi.org/10.1139/p80-159.

(150) Stephens, P. J.; Devlin, F. J.; Chabalowski, C. F.; Frisch, M. J. Ab Initio Calculation of Vibrational Absorption and Circular Dichroism Spectra Using Density Functional Force Fields. *J. Phys. Chem.* **1994**, *98* (45), 11623–11627.

(151) Corà, F.; Alfredsson, M.; Mallia, G.; Middlemiss, D. S.; Mackrodt, W. C.; Dovesi, R.; Orlando, R. The Performance of Hybrid Density Functionals in Solid State Chemistry. In *Structure and Bonding*; Springer, Berlin, Heidelberg, 2012; Vol. 113, pp 171–232. https://doi.org/10.1007/b97944.

(152) Muscat, J.; Wander, A.; Harrison, N. M. On the Prediction of Band Gaps from Hybrid Functional Theory. *Chem. Phys. Lett.* **2001**, *342* (3–4), 397–401. https://doi.org/10.1016/S0009-2614(01)00616-9.

(153) Feng, X.; Harrison, N. M. Magnetic Coupling Constants from a Hybrid Density Functional with 35% Hartree-Fock Exchange. *Phys. Rev. B - Condens. Matter Mater. Phys.* **2004**, *70* (9), 092402. https://doi.org/10.1103/PhysRevB.70.092402.

(154) Middlemiss, D. S.; Lawton, L. M.; Wilson, C. C. A Solid-State Hybrid Density Functional Theory Study of Prussian Blue Analogues and Related Chlorides at Pressure. *J. Phys. Condens. Matter* **2008**, *20* (33), 335231. https://doi.org/10.1088/0953-8984/20/33/335231.

(155) de P. R. Moreira, I.; Illas, F.; Martin, R. L. Effect of Fock Exchange on the Electronic Structure and Magnetic Coupling in NiO. *Phys. Rev. B - Condens. Matter Mater. Phys.* **2002**, *65* (15), 1551021–15510214. https://doi.org/10.1103/PhysRevB.65.155102.

(156) Schäfer, A.; Horn, H.; Ahlrichs, R. Fully Optimized Contracted Gaussian Basis Sets for Atoms Li to Kr. *J. Chem. Phys.* **1992**, *97* (4), 2571–2577. https://doi.org/10.1063/1.463096.

(157) Matvienko, E. N.; Yakubovich, O. V.; Simonov, M. A.; Ivashchenko, A. N.; Mel'nikov, O. K.; Belov, N. V. The Crystal Structure of the Synthetic Fe-Cryolite Na3FeF6. *Dokl. Akad. Nauk SSSR* **1981**, *257*, 105–108.

(158) Monkhorst, H. J.; Pack, J. D. Special Points for Brillouin-Zone Integrations. *Phys.*

Rev. B **1976**, *13* (12), 5188–5192. https://doi.org/10.1103/PhysRevB.13.5188.

(159) Tressaud, A.; Portier, J.; Shearer-Turrell, S.; Dupin, J. L.; Hagenmuller, P. Les Hexafluoferrites M3FeF6 (M = Li, Na, K, Rb, Cs, Ag, Tl, NH4): Etude Radiocristallographique, Spectroscopique et Magnetique. *J. Inorg. Nucl. Chem.* **1970**, *32*, 2179–2186. https://doi.org/10.1016/0022-1902(70)80495-X.

(160) Guntlin, C. P.; Tanja, ab Z.; Kostiantyn Kravchyk, ab V; Michael, ab W.; Bodnarchuk ab, M. I.; Kovalenko, M. V. Nanocrystalline FeF3 and MF2 (M = Fe, Co, and Mn) from Metal Trifluoroacetates and Their Li(Na)-Ion Storage Properties. *J. Mater. Chem. A* **2017**, *5*, 7383–7393. https://doi.org/10.1039/c7ta00862g.

(161) Gershinsky, G.; Bar, E.; Monconduit, L.; Zitoun, D. Operando Electron Magnetic Measurements of Li-Ion Batteries. *Energy Environ. Sci.* **2014**, *7* (6), 2012–2016. https://doi.org/10.1039/c4ee00490f.

(162) Wiaderek, K. M.; Borkiewicz, O. J.; Castillo-Martínez, E.; Robert, R.; Pereira, N.; Amatucci, G. G.; Grey, C. P.; Chupas, P. J.; Chapman, K. W. Comprehensive Insights into the Structural and Chemical Changes in Mixed-Anion FeOF Electrodes by Using Operando Pdf and NMR Spectroscopy. *J. Am. Chem. Soc.* **2013**, *135* (10), 4070–4078. https://doi.org/10.1021/ja400229v.

(163) Dupre, N.; Cuisinier, M.; Guyomard, D. Electrode/Electrolyte Interface Studies in Lithium Batteries Using NMR. *Interface Mag.* **2011**, *20* (3), 61–67. https://doi.org/10.1149/2.F06113if.

(164) See, K. A.; Lumley, M. A.; Stucky, G. D.; Grey, C. P.; Seshadri, R. Reversible Capacity of Conductive Carbon Additives at Low Potentials: Caveats for Testing Alternative Anode Materials for Li-Ion Batteries. *J. Electrochem. Soc.* **2017**, *164* (2), 327–333. https://doi.org/10.1149/2.0971702jes.

(165) Stratford, J. M.; Allan, P. K.; Pecher, O.; Chater, P. A.; Grey, C. P. Mechanistic Insights into Sodium Storage in Hard Carbon Anodes Using Local Structure Probes. *Chem. Commun.* **2016**, *52* (84), 12430–12433.

(166) Nava-Avendaño, J.; Arroyo-De Dompablo, M. E.; Frontera, C.; Ayllón, J. A.; Palacín, M. R. Study of Sodium Manganese Fluorides as Positive Electrodes for Na-Ion Batteries. *Solid State Ionics* **2015**, *278*, 106–113. https://doi.org/10.1016/j.ssi.2015.05.023.

(167) Johnston, K. E.; Sougrati, M. T.; Stievano, L.; Darwiche, A.; Dupré, N.; Grey, C. P.; Monconduit, L. Effects of Relaxation on Conversion Negative Electrode Materials for Li-Ion Batteries: A Study of TiSnSb Using 119Sn Mössbauer and 7Li MAS NMR Spectroscopies. *Chem. Mater.* **2016**, *28* (11), 4032–4041. https://doi.org/10.1021/acs.chemmater.6b01502.

(168) Haneda, K.; Zhou, X. Z.; Morrish, A. H.; Pollard, R. J. Mössbauer Study of Ultrafine

FeF2 Particles. *Hyperfine Interact.* **1990**, *54*, 551–556.

(169) Ramasamy, S.; Jiang, J.; Gleiter, H.; Birringer, R.; Gonser, U. Investigation of Nanocrystalline FeF2 by Mössbauer Spectroscopy. *Solid State Commun.* **1990**, *74* (8), 851–855. https://doi.org/10.1016/0038-1098(90)90949-C.

(170) Brown, F. C.; Gähwiller, C.; Fujita, H.; Kunz, A. B.; Scheifley, W.; Carrera, N. Extreme-Ultraviolet Spectra of Ionic Crystals. *Phys. Rev. B* **1970**, *2* (6), 2126–2138. https://doi.org/10.1103/PhysRevB.2.2126.

(171) Roy, G.; Singh, G.; Gallon, T. E. The Electron Energy Loss Spectra of Some Alkali Halides in the Band Gap Region. *Surf. Sci.* **1985**, *152–153* (PART 2), 1042–1050. https://doi.org/10.1016/0039-6028(85)90519-9.

(172) Yildirim, H.; Kinaci, A.; Chan, M. K. Y.; Greeley, J. P. First-Principles Analysis of Defect Thermodynamics and Ion Transport in Inorganic SEI Compounds: LiF and NaF. *ACS Appl. Mater. Interfaces* **2015**, *7* (34), 18985–18996. https://doi.org/10.1021/acsami.5b02904.

(173) Li, Q.; Li, H.; Xia, Q.; Hu, Z.; Zhu, Y.; Yan, S.; Ge, C.; Zhang, Q.; Wang, X.; Shang, X.; Fan, S.; Long, Y.; Gu, L.; Miao, G. X.; Yu, G.; Moodera, J. S. Extra Storage Capacity in Transition Metal Oxide Lithium-Ion Batteries Revealed by in Situ Magnetometry. *Nat. Mater.* **2021**, *20* (1), 76–83. https://doi.org/10.1038/s41563-020-0756-y.

(174) Liao, P.; MacDonald, B. L.; Dunlap, R. A.; Dahn, J. R. Combinatorially Prepared [LiF]1-XFex Nanocomposites for Positive Electrode Materials in Li-Ion Batteries. *Chem. Mater.* **2008**, *20* (2), 454–461. https://doi.org/10.1021/cm702656k.

(175) Yamakawa, N.; Jiang, M.; Key, B.; Grey, C. P. Identifying the Local Structures Formed during Lithiation of the Conversion Material, Iron Fluoride, in a Li Ion Battery: A Solid-State NMR, X-Ray Diffraction, and Pair Distribution Function Analysis Study. *J. Am. Chem. Soc.* **2009**, *131* (30), 10525–10536. https://doi.org/10.1021/ja902639w.

(176) Shirako, Y.; Shi, Y. G.; Aimi, A.; Mori, D.; Kojitani, H.; Yamaura, K.; Inaguma, Y.; Akaogi, M. High-Pressure Stability Relations, Crystal Structures, and Physical Properties of Perovskite and Post-Perovskite of NaNiF3. *J. Solid State Chem.* **2012**, *191*, 167–174. https://doi.org/10.1016/j.jssc.2012.03.004.

(177) Walker, L. R.; Wertheim, G. K.; Jaccarino, V. Interpretation of the 57Fe Isomer Shift. *Phys. Rev. Lett.* **1961**, *6* (3), 98–101.

(178) Wertheim, G. K.; Guggenheim, H. J.; Buchanan, D. N. E. Sublattice Magnetization in FeF3 near the Critical Point. *Phys. Rev.* **1968**, *169* (2), 465–470. https://doi.org/10.1103/PhysRev.169.465.

(179) Dey, U. K.; Barman, N.; Ghosh, S.; Sarkar, S.; Peter, S. C.; Senguttuvan, P.

SI:Topochemical Bottom-Up Synthesis of 2D- and 3D-Sodium Iron Fluoride Frameworks. *Chem. Mater.* **2019**, *31* (2), 295–299. https://doi.org/10.1021/acs.chemmater.8b04010.

(180) Wertheim, G. K.; Buchanan, D. N. E. Temperature Dependence of the Fe57 Hfs in FeF2 below the Néel Temperature. *Phys. Rev.* **1967**, *161* (2), 478–482. https://doi.org/10.1103/PhysRev.161.478.

(181) Panda, R. N.; Gajbhiye, N. S.; Balaji, G. Magnetic Properties of Interacting Single Domain Fe3O4 Particles. *J. Alloys Compd.* **2001**, *326* (1–2), 50–53. https://doi.org/10.1016/S0925-8388(01)01225-7.

(182) Basa, A.; Wojtulewski, S.; Kalska-Szostko, B.; Perkowski, M.; Gonzalo, E.; Chernyayeva, O.; Kuhn, A.; García-Alvarado, F. Carbon Coating of Air-Sensitive Insulating Transition Metal Fluorides: An Example Study on α-Li3FeF6 High-Performance Cathode for Lithium Ion Batteries. *J. Mater. Sci. Technol.* **2020**, *55*, 107–115. https://doi.org/10.1016/j.jmst.2019.10.002.

(183) Grosvenor, A. P.; Kobe, B. A.; Biesinger, M. C.; McIntyre, N. S. Investigation of Multiplet Splitting of Fe 2p XPS Spectra and Bonding in Iron Compounds. *Surf. Interface Anal.* **2004**, *36* (12), 1564–1574. https://doi.org/10.1002/sia.1984.

(184) Tressaud, A.; Dance, J. M.; Portier, J.; Hagenmuller, P. Interactions Magnetiques Dans Les Fluorures de Type Weberite. *Mat. Res. Bull* **1974**, *9* (9), 1219–1226.

(185) Cosier, R.; Wise, A.; Tressaud, A.; Grannec, J.; Olazcuaga, R.; Portier, J. Sur de Nouveaux Composés Fluorés Ferrimagnétiques à Structure Wébérite. *C. R. Hebd. Seances Acad. Sci. C* **1970**, *271*, 142–145.

(186) Euchner, H.; Clemens, O.; Reddy, M. A. Unlocking the Potential of Weberite-Type Metal Fluorides in Electrochemical Energy Storage. *npj Comput. Mater.* **2019**, *5* (1), 31. https://doi.org/10.1038/s41524-019-0166-3.

(187) Yakubovich, O.; Urusov, V.; Massa, W.; Frenzen, G.; Babel, D. Structure of Na2Fe2F7 and Structural Relations in the Family of Weberites Na2MIIMIIIF7. *Zeitschrift für Anorg. und Allg. Chemie* **1993**, *619* (11), 1909–1919. https://doi.org/10.1002/zaac.19936191115.

(188) Coelho, A. A. TOPAS and TOPAS-Academic: An Optimization Program Integrating Computer Algebra and Crystallographic Objects Written in C++. *J. Appl. Crystallogr.* **2018**, *51* (1), 210–218. https://doi.org/10.1107/S1600576718000183.

(189) Momma, K.; Izumi, F. VESTA 3 for Three-Dimensional Visualization of Crystal, Volumetric and Morphology Data. *J. Appl. Crystallogr.* **2011**, *44* (6), 1272–1276. https://doi.org/10.1107/S0021889811038970.

(190) Kresse, G.; Hafner, J. *Ab Initio* Molecular Dynamics for Liquid Metals. *Phys. Rev. B*

1993, *47* (1), 558. https://doi.org/10.1103/PhysRevB.47.558.

(191) Kresse, G.; Hafner, J. *Ab Initio* Molecular-Dynamics Simulation of the Liquid-Metal–Amorphous-Semiconductor Transition in Germanium. *Phys. Rev. B* **1994**, *49* (20), 14251. https://doi.org/10.1103/PhysRevB.49.14251.

(192) Blöchl, P. E. Projector Augmented-Wave Method. *Phys. Rev. B* **1994**, *50* (24), 17953. https://doi.org/10.1103/PhysRevB.50.17953.

(193) Kresse, G.; Joubert, D. From Ultrasoft Pseudopotentials to the Projector Augmented-Wave Method. *Phys. Rev. B* **1999**, *59* (3), 1758. https://doi.org/10.1103/PhysRevB.59.1758.

(194) Perdew, J. P.; Burke, K.; Ernzerhof, M. Generalized Gradient Approximation Made Simple. *Phys. Rev. Lett.* **1996**, *77* (18), 3865–3868. https://doi.org/10.1103/PhysRevLett.77.3865.

(195) Anisimov, V. I.; Aryasetiawan, F.; Lichtenstein, A. I. First-Principles Calculations of the Electronic Structure and Spectra of Strongly Correlated Systems: The LDA+ U Method. *J. Phys. Condens. Matter* **1997**, *9* (4), 767. https://doi.org/10.1088/0953-8984/9/4/002.

(196) Jain, A.; Hautier, G.; Ong, S. P.; Moore, C. J.; Fischer, C. C.; Persson, K. A.; Ceder, G. Formation Enthalpies by Mixing GGA and GGA + U Calculations. *Phys. Rev. B - Condens. Matter Mater. Phys.* **2011**, *84* (4), 045115. https://doi.org/10.1103/PhysRevB.84.045115.

(197) Wang, L.; Maxisch, T.; Ceder, G. Oxidation Energies of Transition Metal Oxides within the GGA+ U Framework. *Phys. Rev. B* **2006**, *73*, 195107. https://doi.org/10.1103/PhysRevB.73.195107.

(198) Ong, S. P.; Richards, W. D.; Jain, A.; Hautier, G.; Kocher, M.; Cholia, S.; Gunter, D.; Chevrier, V. L.; Persson, K. A.; Ceder, G. Python Materials Genomics (Pymatgen): A Robust, Open-Source Python Library for Materials Analysis. *Comput. Mater. Sci.* **2013**, *68*, 314–319. https://doi.org/10.1016/J.COMMATSCI.2012.10.028.

(199) Grey, I. E.; Mumme, W. G.; Ness, T. J.; Roth, R. S.; Smith, K. L. Structural Relations between Weberite and Zirconolite Polytypes—Refinements of Doped 3T and 4M Ca2Ta2O7 and 3T CaZrTi2O7. *J. Solid State Chem.* **2003**, *174* (2), 285–295. https://doi.org/10.1016/S0022-4596(03)00222-6.

(200) Peschel, B.; Molinier, M.; Babel, D. Kristallstrukturbestimmungen an Vier Monoklinen Weberiten Na2MIIMIIIF7 (MII = Fe, Co; MIII = V, Cr). *Zeitschrift für Anorg. und Allg. Chemie* **1995**, *621* (9), 1573–1581. https://doi.org/10.1002/zaac.19956210923.

(201) Dahlke, P.; Peschel, B.; Babel, D. Über Röntgenographische

Einkristalluntersuchungen an Na2FeAlF7, Na2MIIGaF7 (MII = Ni, Zn) Und Na2ZnFeF7 Und Die Strukturchemie Der Weberite. *Zeitschrift für Anorg. und Allg. Chemie* **1998**, *624* (6), 1003–1010. https://doi.org/10.1002/(sici)1521-3749(199806)624:6<1003::aid-zaac1003>3.0.co;2-c.

(202) Badway, F.; Cosandey, F.; Pereira, N.; Amatucci, G. G. Carbon Metal Fluoride Nanocomposites: High-Capacity Reversible Metal Fluoride Conversion Materials as Rechargeable Positive Electrodes for Li Batteries. *J. Electrochem. Soc.* **2003**, *150* (10), A1318. https://doi.org/10.1149/1.1602454.

(203) Wang, J.; Sun, X. Understanding and Recent Development of Carbon Coating on LiFePO4 Cathode Materials for Lithium-Ion Batteries. *Energy Environ. Sci.* **2012**, *5* (1), 5163–5185. https://doi.org/10.1039/C1EE01263K.

(204) Stephens, P. W. Phenomenological Model of Anisotropic Peak Broadening in Powder Diffraction. *J. Appl. Crystallogr.* **1999**, *32* (2), 281–289. https://doi.org/10.1107/S0021889898006001.

(205) Laligant, Y.; Calage, Y.; Heger, G.; Pannetier, J.; Ferey, G. Ordered Magnetic Frustration. VII. Na2NiFeF7: Reexamination of Its Crystal Structure in the True Space Group after Corrections from Renninger Effect and Refinement of Its Frustrated Magnetic Structure at 4.2 and 55 K. *J. Solid State Chem.* **1989**, *78* (1), 66–77. https://doi.org/10.1016/0022-4596(89)90128-X.

(206) Pebler, J.; Schmidt, K.; Babel, D.; Verscharen, W. Mössbauer-Spektroskopische Untersuchungen an Na2MnFeF7 / Mössbauer Spectroscopic Investigation of Na2MnFeF7. *Zeitschrift für Naturforsch. B* **2015**, *32* (4), 369–372. https://doi.org/10.1515/znb-1977-0403.

(207) Pankhurst, Q. A.; Johnson, C. E.; Wanklyn, B. M. A Mössbauer Study of Paramagnetic Na2MgFeF7. *J. Magn. Magn. Mater.* **1991**, *97* (1–3), 126–130. https://doi.org/10.1016/0304-8853(91)90170-F.

(208) Cai, L.; Nino, J. C. Complex Ceramic Structures. I. Weberites. *Acta Crystallogr. Sect. B Struct. Sci.* **2009**, *65* (3), 269–290. https://doi.org/10.1107/S0108768109011355.

(209) Brennhagen, A.; Cavallo, C.; Wragg, D. S.; Vajeeston, P.; Sjåstad, A. O.; Koposov, A. Y.; Fjellvåg, H. Operando XRD Studies on Bi2MoO6 as Anode Material for Na-Ion Batteries. *Nanotechnology* **2022**, *33* (18). https://doi.org/10.1088/1361-6528/ac4eb5.

(210) Yabuuchi, N.; Kubota, K.; Aoki, Y.; Komaba, S. Understanding Particle-Size-Dependent Electrochemical Properties of Li2MnO3-Based Positive Electrode Materials for Rechargeable Lithium Batteries. *J. Phys. Chem. C* **2016**, *120* (2), 875–885. https://doi.org/10.1021/acs.jpcc.5b10517.

(211) Jiang, C.; Wei, M.; Qi, Z.; Kudo, T.; Honma, I.; Zhou, H. Particle Size Dependence of the Lithium Storage Capability and High Rate Performance of Nanocrystalline Anatase TiO2 Electrode. *J. Power Sources* **2007**, *166* (1), 239–243. https://doi.org/10.1016/J.JPOWSOUR.2007.01.004.

(212) Li, C.; Gu, L.; Tong, J.; Maier, J. Carbon Nanotube Wiring of Electrodes for High-Rate Lithium Batteries Using an Imidazolium-Based Ionic Liquid Precursor as Dispersant and Binder: A Case Study on Iron Fluoride Nanoparticles. *ACS Nano* **2011**, *5* (4), 2930–2938. https://doi.org/10.1021/nn1035608.

(213) Belharouak, I.; Johnson, C.; Amine, K. Synthesis and Electrochemical Analysis of Vapor-Deposited Carbon-Coated LiFePO4. *Electrochem. commun.* **2005**, *7* (10), 983–988. https://doi.org/10.1016/j.elecom.2005.06.019.

(214) Lepage, D.; Sobh, F.; Kuss, C.; Liang, G.; Schougaard, S. B. Delithiation Kinetics Study of Carbon Coated and Carbon Free LiFePO4. *J. Power Sources* **2014**, *256*, 61–65. https://doi.org/10.1016/J.JPOWSOUR.2013.12.054.

(215) Komaba, S.; Ishikawa, T.; Yabuuchi, N.; Murata, W.; Ito, A.; Ohsawa, Y. Fluorinated Ethylene Carbonate as Electrolyte Additive for Rechargeable Na Batteries. *ACS Appl. Mater. Interfaces* **2011**, *3* (11), 4165–4168. https://doi.org/10.1021/AM200973K/SUPPL_FILE/AM200973K_SI_001.PDF.

(216) Chen, L.; Kishore, B.; Walker, M.; Dancer, C. E. J.; Kendrick, E. Nanozeolite ZSM-5 Electrolyte Additive for Long Life Sodium-Ion Batteries. *Chem. Commun.* **2020**, *56* (78), 11609–11612. https://doi.org/10.1039/D0CC03976D.

(217) Martin, A.; Doublet, M.-L.; Kemnitz, E.; Pinna, N.; Martin, A.; Kemnitz, E.; Pinna, N.; Doublet, M. Reversible Sodium and Lithium Insertion in Iron Fluoride Perovskites. *Adv. Funct. Mater.* **2018**, *28* (29), 1802057. https://doi.org/10.1002/ADFM.201802057.

(218) Zheng, Y.; Jitto, S.; Hwang, J.; Matsumoto, K.; Hagiwara, R. Multiphase Transformation of NaFeF3 During Desodiation and Sodiation. *ACS Appl. Energy Mater.* **2022**. https://doi.org/10.1021/ACSAEM.2C02904.

(219) Lim, S. G.; Kwon, M. S.; Kim, T.; Kim, H.; Lee, S.; Lim, J.; Kim, H.; Lee, K. T. Correlation between the Cation Disorders of Fe3+ and Li+ in P3-Type Na0.67[Li0.1(Fe0.5Mn0.5)0.9]O2 for Sodium Ion Batteries. *ACS Appl. Mater. Interfaces* **2022**, *14*, 33129. https://doi.org/10.1021/ACSAMI.2C05784/ASSET/IMAGES/LARGE/AM2C05784_0009.JPEG.

(220) Yabuuchi, N.; Yoshida, H.; Komaba, S. Crystal Structures and Electrode Performance of Alpha-NaFeO2 for Rechargeable Sodium Batteries. *Electrochemistry* **2012**, *80* (10), 716–719. https://doi.org/10.5796/electrochemistry.80.716.

(221) Li, Y.; Gao, Y.; Wang, X.; Shen, X.; Kong, Q.; Yu, R.; Lu, G.; Wang, Z.; Chen, L. Iron Migration and Oxygen Oxidation during Sodium Extraction from NaFeO2. *Nano Energy* **2018**, *47*, 519–526. https://doi.org/10.1016/J.NANOEN.2018.03.007.

(222) Ye, T.; Barpanda, P.; Nishimura, S. I.; Furuta, N.; Chung, S. C.; Yamada, A. General Observation of Fe3+/Fe2+ Redox Couple Close to 4 v in Partially Substituted Li2FeP2O7 Pyrophosphate Solid-Solution Cathodes. *Chem. Mater.* **2013**, *25* (18), 3623–3629. https://doi.org/10.1021/CM401547Z/SUPPL_FILE/CM401547Z_SI_001.PDF.

(223) Chen, H.; Adams, S. Bond Softness Sensitive Bond-Valence Parameters for Crystal Structure Plausibility Tests. *IUCrJ* **2017**, *4* (5), 614–625. https://doi.org/10.1107/S2052252517010211/YC5011SUP1.PDF.

(224) Chen, H.; Wong, L. L.; Adams, S. SoftBV – a Software Tool for Screening the Materials Genome of Inorganic Fast Ion Conductors. *Acta Crystallogr. Sect. B Struct. Sci.* **2019**, *75* (1), 18–33. https://doi.org/10.1107/S2052520618015718.

(225) Wong, L. L.; Phuah, K. C.; Dai, R.; Chen, H.; Chew, W. S.; Adams, S. Bond Valence Pathway Analyzer-An Automatic Rapid Screening Tool for Fast Ion Conductors within SoftBV. *Chem. Mater.* **2021**, *33* (2), 625–641. https://doi.org/10.1021/ACS.CHEMMATER.0C03893/ASSET/IMAGES/LARGE/CM0C03893_0019.JPEG.

(226) Ponrouch, A.; Marchante, E.; Courty, M.; Tarascon, J.-M. M.; Palacín, M. R. In Search of an Optimized Electrolyte for Na-Ion Batteries. *Energy Environ. Sci.* **2012**, *5* (9), 8572. https://doi.org/10.1039/c2ee22258b.

(227) Liang, H. J.; Gu, Z. Y.; Zhao, X. X.; Guo, J. Z.; Yang, J. L.; Li, W. H.; Li, B.; Liu, Z. M.; Li, W. L.; Wu, X. L. Ether-Based Electrolyte Chemistry Towards High-Voltage and Long-Life Na-Ion Full Batteries. *Angew. Chemie Int. Ed.* **2021**, *60* (51), 26837–26846. https://doi.org/10.1002/ANIE.202112550.

(228) Li, B.; Sougrati, M. T.; Rousse, G.; Morozov, A. V.; Dedryvère, R.; Iadecola, A.; Senyshyn, A.; Zhang, L.; Abakumov, A. M.; Doublet, M. L.; Tarascon, J. M. Correlating Ligand-to-Metal Charge Transfer with Voltage Hysteresis in a Li-Rich Rock-Salt Compound Exhibiting Anionic Redox. *Nat. Chem.* **2021**, *13* (11), 1070–1080. https://doi.org/10.1038/s41557-021-00775-2.

(229) Fehse, M.; Bessas, D.; Mahmoud, A.; Diatta, A.; Hermann, R. P.; Stievano, L.; Sougrati, M. T. The Fe4+/3+ Redox Mechanism in NaFeO2: A Simultaneous Operando Nuclear Resonance and X-Ray Scattering Study. *Batter. Supercaps* **2020**, *3* (12), 1341–1349. https://doi.org/10.1002/BATT.202000157.

(230) Henkelman, G.; Uberuaga, B. P.; Jónsson, H. A Climbing Image Nudged Elastic Band Method for Finding Saddle Points and Minimum Energy Paths. *J. Chem. Phys.* **2000**, *113*, 9901–9904. https://doi.org/https://doi.org/10.1063/1.1329672.

(231) Jónsson, H.; Mills, G.; Jacobsen, K. W. Nudged Elastic Band Method for Finding Minimum Energy Paths of Transitions. In *Classical and Quantum Dynamics in Condensed Phase Simulations*; World Scientific, Singapore, 1998; p 385.

(232) Laligant, Y.; Pannetier, J.; Labbe, P.; Ferey, G. A New Refinement of the Crystal Structure of the Inverse Weberite Fe2F5(H2O)2. *J. Solid State Chem.* **1986**, *62* (2), 274–277. https://doi.org/10.1016/0022-4596(86)90240-9.

(233) Subramanian, M. A.; Marshall, W. J.; Hoffmann, R. D.; Sleight, A. W. Synthesis and Structure of Some MII/MIII Mixed Fluorides with Pyrochlore and Weberite Related Structures. *Zeitschrift fur Naturforsch. - Sect. B J. Chem. Sci.* **2006**, *61* (7), 808–812. https://doi.org/10.1515/znb-2006-0706.

(234) Greneche, J. M.; Linares, J.; Varret, F.; Laligant, Y. MoSSBAUER SPECTROSCOPY SPECTROSCOPY OF THE MAGNETIC BEHAVIOUR OF THE FRUSTRATED SERIES AFeF ,(H , O),: A = Mn , Fe , Co , Ni. *J. Magn. Magn. Mater.* **1988**, *73*, 115–122.

(235) Weil, M.; Werner, F. The Thermal Dehydration of Magnesium Aluminum Pentafluoride Dihydrate: Crystal Structures of MgAlF5(H2O)2 and MgAlF5. *Monatshefte fur Chemie* **2001**, *132* (7), 769–777. https://doi.org/10.1007/s007060170063.

(236) Laligant, Y.; Calage, Y.; Torres-Tapia, E.; Greneche, J. M.; Varret, F.; Ferey, G. Crystal Structure of the Inverse Weberite ZnFeF5(H2O)2, Magnetic and Mossbauer Study of the Antiferromagnet ZnFeF5(H2O)2 and Ferrimagnet MnFeF5(H2O)2. **1986**, *61*, 283–290.

(237) Hall, W.; Kim, S.; Zubieta, J. O. N.; Walton, E. G.; Brown, D. B. Structure of a Mixed-Valence Iron Fluoride, Fe2F5*2H2O. *Inorg. Chem.* **1977**, *16* (8), 1884–1887.

(238) Bartel, C. J.; Weimer, A. W.; Lany, S.; Musgrave, C. B.; Holder, A. M. The Role of Decomposition Reactions in Assessing First-Principles Predictions of Solid Stability. *npj Comput. Mater. 2019 51* **2019**, *5* (1), 1–9. https://doi.org/10.1038/s41524-018-0143-2.

(239) Verscharen, W.; Babel, D. Röntgen- Und Neutronen-Strukturbestimmung Des Na2MnFeF7-Typs: Eine Trigonale Weberit-Variante. *J. Solid State Chem.* **1978**, *24* (3–4), 405–421. https://doi.org/10.1016/0022-4596(78)90034-8.

(240) Dey, U. K.; Barman, N.; Ghosh, S.; Sarkar, S.; Peter, S. C.; Senguttuvan, P. Topochemical Bottom-Up Synthesis of 2D- and 3D-Sodium Iron Fluoride Frameworks. *Chem. Mater.* **2019**, *31* (2), 295–299. https://doi.org/10.1021/acs.chemmater.8b04010.

(241) Koch, J.; Hebecker, C. *Neue Verbindungen Vom Weberit-Typ Mit Der Zusammensetzung Na2MIIMIIIF7 Und AgzMIIMInF7*; Springer-Verlag, 1984; Vol. 365.

(242) Boireau, A.; Gravereau, P.; Dance, J. M.; Tressaud, A.; Hagenmuller, P.; Soubeyroux, J. L.; Welsch, M.; Babel, D. Structural and Magnetic Properties of Several Cobalt(II) Weberites. *Mater. Res. Bull.* **1993**, *28* (1), 27–38. https://doi.org/10.1016/0025-5408(93)90005-X.

(243) Dahlke, P.; Babel, D. Die Kristallstrukturen Der Weberite Na2CuScF7 Und Na2ZnAlF7. *Zeitschrift für Anorg. und Allg. Chemie* **1994**, *620* (10), 1692–1697. https://doi.org/10.1002/zaac.19946201005.

(244) Peschel, B.; Babel, D. Die Kristallstrukturen Der Vanadium-Weberite Na2MIIVIIIF7 (MII = Mn, Ni, Cu) Und von NaVF4. *Zeitschrift für Anorg. und Allg. Chemie* **1997**, *623* (10), 1614–1620. https://doi.org/10.1002/zaac.19976231022.

(245) Marinel, S.; Pollet, M.; Desgardin, G. Sintering of CaZrO3-Based Ceramic Using Mixed Conventional and Microwave Heating. *J. Mater. Sci. Mater. Electron.* **2002**, *13* (3), 149–155. https://doi.org/10.1023/A:1014381300373/METRICS.

(246) Santos, J. L.; Marçal, R. L. S. B.; Jesus, P. R. R.; Gomes, A. V.; Lima, E. P.; Monteiro, S. N.; de Campos, J. B.; Louro, L. H. L. Effect of LiF as Sintering Agent on the Densification and Phase Formation in Al2O3-4 Wt Pct Nb2O5 Ceramic Compound. *Metall. Mater. Trans. A Phys. Metall. Mater. Sci.* **2017**, *48* (10), 4432–4440. https://doi.org/10.1007/s11661-017-4271-y.

(247) Jouanneau, S.; Dahn, J. R. Influence of LiF Additions on Li [Ni x Co1 − 2x Mn x] O 2 Materials: Sintering, Structure, and Lithium Insertion Properties. *J. Electrochem. Soc.* **2004**, *151* (10), A1749. https://doi.org/10.1149/1.1793712.